RUHR-UNIVERSITÄT BOCHUM

Lingyun Li

On the hydromechanical behaviour of loess and its effect on slope stability under rainfall infiltration

Bochum 2022

Heft 74

Schriftenreihe des Lehrstuhls für
Bodenmechanik, Grundbau und Umweltgeotechnik

Herausgeber: Torsten Wichtmann

ISSN 2699-1020

Hydromechanical behaviour of loess and slope stability Lingyun Li 74

ISSN 2699-1020

Ruhr-Universität Bochum
Schriftenreihe Bodenmechanik, Grundbau und Umweltgeotechnik
Heft 74

Herausgeber:
Prof. Dr.-Ing. habil. Torsten Wichtmann
Ruhr-Universität Bochum
Fakultät für Bau- und Umweltingenieurwissenschaften
Lehrstuhl für Bodenmechanik, Grundbau und Umweltgeotechnik
44801 Bochum
Telefon: 0234/ 3226135
Telefax: 0234/ 3214236
Internet: www.bgu.ruhr-uni-bochum.de

ISSN 2699-1020

© 2022 der Herausgeber

On the hydromechanical behaviour of loess and its effect on slope stability under rainfall infiltration

Dissertation

as a requirement of the degree of
Doktor-Ingenieur (Dr.-Ing.)

at the Faculty of
Civil and Environmental Engineering
Ruhr-Universität Bochum

submitted by
Lingyun Li
from Shaanxi, China

Reviewers
Prof. Dr.-Ing. habil. Torsten Wichtmann
Prof. Dr. Maria Datcheva
Prof. Dr. Snehasis Tripathy

Bochum, July 2023

This work is dedicated to my beloved parents.

Preface of the editor

Loess soils are characterized by a loose structure stabilized by capillary effects and cementation bonds. In case of water infiltration the suction in the soil decreases and cementation bonds weaken, potentially leading to a collapse of the structure accompanied by the development of excess pore water pressure, loss of shear strength and large deformations. Such effects have frequently caused slope failures in thick loess deposits due to heavy rainfall. Investigations on the slope stability under such conditions necessitate a deep understanding of the hydro-mechanical behaviour of loess, as well as its description by sophisticated constitutive models for numerical simulations in more complicated cases.

Previous experimental studies have been mainly performed on remoulded loess, which differs significantly from undisturbed loess with respect to structure. Furthermore, earlier studies were restricted to monotonic hydro-mechanical processes, while subsequent rainfall events in combination with evaporation are associated with a cyclic wetting and drying of the soil. Therefore, the experimental program performed by Lingyun Li concentrates on the comparison of the hydro-mechanical behaviour of undisturbed and remoulded samples of a loess from China, as well as on the effect of wetting and drying cycles. The thorough experimental investigation on unsaturated and saturated samples of a loess from China included tests on compressibility, shear strength, hydraulic conductivity, soil water characteristic curve (SWCC) and collapse behaviour under water infiltration. Amongst others, oedometer tests with controlled suction or water infiltration at a certain mechanical stress, single- and multi-phase direct shear tests, drained and undrained monotonic triaxial tests, and measurements of the SWCC during several drying and wetting cycles and under different net normal stresses were performed.

Based on her experimental data Lingyun Li has calibrated an established constitutive model for unsaturated soils (Barcelona Basic Model), which was subsequently applied in finite element simulations of a soil column and a slope considering thermo-hydro-mechanical coupling. Lingyun Li has inspected the influence of the atmospheric boundary conditions on parameters like pore water pressure or suction, temperature and stress within the soil. The back analysis of a real slope failure case in China delivered useful insights into the driving mechanisms.

Lingyun Li has performed a large number of high-quality laboratory tests with great care, which is particularly important when handling the sensitive undisturbed loess as

well as testing soils in unsaturated states. The test results were evaluated with respect to various soil properties and represent the most complete set of data for this special kind of soil published so far. The data can serve as a valuable basis for the development and calibration of constitutive models for loess soils. The numerical simulations considering atmospheric boundary conditions give a deeper insight into the thermo-hydro-mechanically coupled processes in loess soils potentially leading to slope failure under heavy rainfall events. The dissertation of Lingyun Li contributes to an enhanced understanding of the hydro-mechanical behaviour of loess soils as well as the driving mechanisms of slope failure in such soils.

Prof. Dr.-Ing. habil. Torsten Wichtmann Bochum, 19.07.2023

Acknowledgements

This research was carried out in the Chair of Soil Mechanics, Foundation Engineering and Environmental Geotechnics, Ruhr-Universität Bochum. First and foremost, I would like to thank my supervisor Prof. Tom Schanz who gave me a chance to start my study in RUB and provided me a lot of precious scientific support during my research work. His wisdom and personality deeply impressed and will always inspire me. I am sorry that he has not lived to see me graduate. His enthusiasm, ultimate support, vast knowledge, memories and thoughts will be with me forever.

I would like to thank Prof. Dr.-Ing. habil. Torsten Wichtmann for supervising this dissertation with his precise advices, priceless comments and suggestions.

I would also like to express my gratitude to Prof. Maria Datcheva (Bulgarian Academy of Sciences) for her continuous help and lots of constructive comments and suggestions on my PhD work when Prof. Schanz passed away unexpectedly. Her kindness and hospitality during my research stay in Bulgarian Academy of Sciences impressed me as well.

My sincere gratitude also goes to Dr. Wiebke Baille and Dr. Diethard König, for their continuous help and lots of constructive suggestions during my research work, which guided me through the long academic puzzlement to a sudden enlightenment.

I gratefully thank Prof. Dr. Snehasis Tripathy (Cardiff School of Engineering, United Kingdom) for acting as reviewer of my thesis. His critical and constructive comments significantly improved this work.

My gratitude should also be extended to Michael Skubisch, Joachim Blazytko, Werner Müller (Soil Mechanics Laboratory) for supporting me during my experimental work.

I also would like to appreciate the financial support by the China Scholarship Council and RUB research school for providing me the financial support during my PhD study. The years in RUB are the most meaningful time in my life so far. The precious experience with them has rooted in my mind forever.

Last but not least, I sincerely thank my family and friends for their endless love and amazing support during my PhD study.

Bochum, July 2023 Lingyun Li

Abstract

Thick layers of loess cover large areas in China. Loess is a problematic and moisture sensitive soil, which makes loess slopes vulnerable to failure when subjected to rainfall. During the rainy season, many landslides used to occur in the past causing loss of lives and an enormous amount of damage on the economy. Hence, the landslide risk assessment has become one of the most important geotechnical issues in projects involving loess slopes. Therefore, the main objective of this thesis is to thoroughly investigate landslides in loess areas induced by rainfall.

In the experimental part of the thesis, the hydro-mechanical behaviour of loess encountered in the Shannxi region of China was studied both in undisturbed and remolded states. For this purpose, loess samples were collected in situ and from them a number of undisturbed and remolded specimens for laboratory testing were prepared. Firstly, in order to account for the cyclic infiltration processes that take place on the surface of the loess slopes in the considered region of China, the effect of hydraulic loading path on the hydro-mechanical loess behaviour has been studied. Next, the influencing factors such as microstructure and stress path on the collapse properties and hydro-mechanical behaviour of loess were investigated over a wide range of suction. Hydraulic characteristics of the loess under different hydraulic loading paths were studied by three different techniques. Specifically, the branches of the soil water characteristic relationship, such as main wetting, main drying and scanning curves were experimentally determined. Furthermore, different empirical models were used to fit the soil water characteristic relationship data and the quality of the fit by the selected models was evaluated. In order to obtain the unsaturated permeability, firstly, the falling head test was used to measure the permeability in the saturated state. Analytical and statistical functions of the soil water characteristic curve were then considered to predict the permeability of the unsaturated soil. The suction-controlled oedometer testing was used to study the coupled hydro-mechanical behaviour under various stress paths. This allowed for the investigation of the resulting volumetric and saturation-desaturation behaviour.

The finite element software CODE_BRIGHT with the Barcelona Basic Model (BBM) was applied to analyze the stability of a selected loess slope under atmospheric boundary conditions. A soil water characteristic model with hysteresis considering entrapped air was employed to reproduce the hysteretic unsaturated flow phenomenon. The parameters of the constitutive and hydraulic models were calibrated based on the experimental data.

The results of the finite element simulation of a real case loess slope under atmospheric boundary conditions are presented and discussed. Emphasis is given on the distribution of pore water pressure and plastic strain in the slope under various atmospheric boundary conditions. The stress distribution and its change influenced by the atmospheric factors have been analyzed. Furthermore, the main mechanism of slope instability has been identified.

Zusammenfassung

Ausgedehnte Gebiete in China sind von mächtigen Lößschichten bedeckt. Löß ist ein problematischer und feuchtigkeitsempfindlicher Boden, der anfällig für Erdrutsche infolge von Regenfällen ist. Während der Regenzeit haben sich in der Vergangenheit wiederholt Erdrutsche ereignet, die Menschenleben gekostet und enorme wirtschaftliche Schäden verursacht haben. Daher ist die Bewertung des Risikos von Erdrutschen zu einer der wichtigsten geotechnischen Fragen bei Projekten geworden, die Lößhänge betreffen. Das Hauptziel dieser Arbeit ist daher eine eingehende Untersuchung von Erdrutschen in Lößgebieten, die durch Niederschläge ausgelöst werden.

Im experimentellen Teil der Arbeit wurde das hydromechanische Verhalten von Löß aus der Region Shannxi in China sowohl im ungestörten als auch im aufbereiteten Zustand untersucht. Zu diesem Zweck wurden Lößproben im Feld entnommen, aus denen eine Reihe von ungestörten und aufbereiteten Probekörpern für Laborversuche hergestellt wurden. Unter Berücksichtigung der zyklischen Infiltrationsprozesse, die an der Oberfläche der Lößhänge in der betrachteten Region Chinas stattfinden, wurde zunächst die Auswirkung des hydraulischen Belastungspfades auf das hydromechanische Verhalten des Lößes untersucht. Anschließend wurde der Einfluss verschiedener Faktoren wie der Mikrostruktur und des Belastungspfades auf die Kollapseigenschaften und das hydromechanische Verhalten von Löß in einem weiten Bereich von Saugspannungen quantifiziert. Die hydraulischen Eigenschaften des Lößes unter verschiedenen hydraulischen Belastungspfaden wurden unter Einsatz von drei verschiedenen Techniken untersucht. Insbesondere wurden die verschiedenen Abschnitte der charakteristischen Bodenwasserkennlinie (“Soil water characteristic curve,,), wie die Hauptbefeuchtungskurve, die Haupttrocknungskurve und die dazwischenliegenden übergangskurven („scanning curves“) experimentell bestimmt. Darüber hinaus wurden verschiedene empirische Modelle verwendet, um die Daten der charakteristischen Bodenwasserkennlinie zu approximieren, und die Qualität der Anpassung durch die ausgewählten Modelle wurde bewertet. Um die ungesättigte Durchlässigkeit zu ermitteln, wurde zunächst die Durchlässigkeit des gesättigten Bodens mit dem Versuch mit fallender Druckhöhe ermittelt. Anschließend wurden analytische und statistische Funktionen der charakteristischen Bodenwasserkennlinie zur Vorhersage der Durchlässigkeit des ungesättigten Bodens herangezogen. Zur Untersuchung des gekoppelten hydromechanischen Verhaltens unter verschiedenen Beanspruchungspfaden wurde der ödometerversuch mit kontrollierter Saugspannung eingesetzt. Dies ermöglichte die Untersuchung des resultierenden volumetrischen und Bewässerungs-Entwässerung-Verhaltens.

Die Finite-Elemente-Software CODE_BRIGHT und das Barcelona Basic Modell (BBM) wurden eingesetzt, um die Stabilität eines ausgewählten Lößhangs unter atmosphärischen Randbedingungen zu analysieren. Ein Modell der charakteristischen Bodenwasserkennlinie mit Hysterese, das die eingeschlossene Luft berücksichtigt, wurde verwendet, um das Phänomen der hysteretischen ungesättigten Strömung zu reproduzieren. Die Parameter der konstitutiven und hydraulischen Modelle wurden auf Basis der experimentellen Daten kalibriert. Die Ergebnisse der Finite-Elemente-Simulation eines realen Lößhangs unter atmosphärischen Randbedingungen werden vorgestellt und diskutiert. Der Schwerpunkt liegt dabei auf der Verteilung des Porenwasserdrucks und der plastischen Dehnung innerhalb der Böschung unter verschiedenen atmosphärischen Randbedingungen. Die Spannungsverteilung und ihre Veränderung in Abhängigkeit von den atmosphärischen Faktoren wurden analysiert. Außerdem wurde der maßgebende Mechanismus, der zur Hanginstabilität führt, identifiziert.

Contents

Nomenclature

α_{il}	Parameter for elastic thermal strain
α_i	Parameter for elastic thermal strain
α_{sp}	Expansive index for TEP model regarding pressure
α_{ss}	Expansive index for TEP model
β	Parameter controlling the rate of increase in stiffness with suction
β_a	Adjust for significance of observation data and parameters information
β_g	Humidity term
$\gamma_{d-initial}$	Initial dry density
γ_g	Gas pressure term
γ_l	Liquid leakage coefficient
$\delta_{\mathbf{ij}}$	Kronecker's tensor
δ	Parameter for smoothing the seepage condition boundary condition
ϵ	Random error
ϵ^e	Elastic strain
ϵ^p	Plastic strain
ϵ^{T-e}	Strain due to temperature change
$\epsilon^{\sigma-e}$	Strain induced by net stress
ϵ^{s-e}	Strain induced by suction
η_a	Wind velocity
θ_l^w and θ_g^w	Volumetric water content in liquid phase and gas phase
θ	Volumetric water content
Θ	Normalized volumetric water content
θ_r	Residual volumetric water content
θ_s	Saturated volumetric water content
κ	Compressibility coefficient for elastic behaviour
κ_i and κ_s	Elastic volumetric strain parameters for TEP model
κ_{i0} and α_i	Thermal-elasto-plastic model parameters in TEP model

κ_{s0}	Elastic stiffness parameter when changing suction at zero net stress
λ	Shape parameter for retention curve
$\lambda(0)$	Stiffness parameter for saturated virgin compressibility
$\lambda(s)$	Stiffness paramter for unsaturated virgin compressibility
$\lambda(T)$	Parameter for soil thermal conductivity
λ_{dry}	Parameter for soil thermal conductivity in the dry state
λ_{sat}	Parameter for soil thermal conductivity in the saturated state
μ_l	Dynamic viscosity of the pore liquid
ρ	Density
ρ_d	Dry density
ρ_g	Gas density
ρ_{ga}	Atmospheric gas density
ρ_s and ρ_l	Solid and liquid densities
ρ_v	Vapour density
σ	Stress tensor
$\sigma_{\mathbf{ij}}$	Total stress tensor
$\sigma'_{\mathbf{ij}}$	Effective stress tensor
σ'	Effective vertical stress
σ_n	Total normal stress
σ^{sd}	Standard deviation
σ_v	Vertical stress
σ_{vm}	Maximum pre-consolidation pressure
$\widetilde{\sigma}_0$	Yield stress
σ_1	Total axial stress in conventional triaxial test
σ_3	Total confining stress in conventional triaxial test
τ	Tortuosity in molecular diffusion law
τ_f	Shear stress on the failure plane at failure
υ	Specific volume
ϕ	Stability factor
ϕ'	Effective angle of internal friction
ϕ_0	Reference porosity
χ	Bishop's coefficient
ψ	Total suction
ψ_{aev}	Air entry value
ψ_{wev}	Water entry value

ψ_m	Matric suction
ψ_o	Osmotic suction
ψ_r	Residual suction
ω^v	Mass fraction of the vapour
ω_k	Weighting factor for each serial measurement
ω_{tm}	Weighting factor for each measurement
A	Cross-sectional area
A_d	Dry albedo
A_w	Wet albedo
b	Body forces
$\mathbf{b}$	Vector of body forces
c'	Effective cohesion
C_C	Coefficient of concavity
C_c	Compression index
C_r	Swelling or rebound index
C_U	Coefficient of uniformity
D_m	Diffusion coefficient of vapour
e	Void ratio
e_f	Final void ratio
e_0	Initial void ratio
E	Evaporation
f^Q	Internal/external energy supply
f^w	External supply of water
g	Gravity acceleration
g^g_{best}	Global best of the objective function
G_s	Specific gravity
H_r	Relative humidity
i	Non-advective mass flux
i_c	Energy flux due to conduction
I_c	Collapse potential
i_e	Conductive heat flux
I_n	Cloud index
i^w_g	Vapour non-advective flux
i^a_i	Air non-advective flux

J	Deviatoric stress tensor
j	Total mass flux
j_e	Heat flow rate
j_E	Energy fluxes due to mass motion
j_g	Gas flow rate
j_l	Liquid flow rate
$\mathbf{k}$	Tensor of intrinsic permeability
K_a	Dielectric constant
k_{evap}	Factor with which evaporation is multiplied
k_{rl}	Relative permeability
k_r	Relative conductivity
k_{rain}	Factor with which rain is multiplied
k_{rad}	Factor with which radiation is multiplied
K_w	Coefficient of permeability
n	Porosity
p	Mean stress
p'	Mean effective stress
p^c	Reference mean stress
p_g	Gas pressure
p_{ga}	Atmospheric gas pressure
p_l	Pore water pressure
$\triangle p_l$	Prescribed increment of p_l during the time step (MPa)
p^{net}	Mean net stress
P_{rain}	Rainfall
P_0	Model parameter for SWCC
p_0	Pre-consolidation pressure
p_0^*	Pre-consolidation pressure for saturated condition
q	Flow rate
q_g	Gas advective flux
q_l	Liquid advective flux
r	Compressibility coefficient for high values of suction in Barcelona Basic Model
R	Radius of curvature
R_n	Radiation
S_e	Effective degree of saturation
S_g	Degree of saturation of gaseous phases
S_l	Degree of saturation of liquid phases

S_{ls}	Maximum degree of saturation
S_r	Degree of water saturation
S_{rl}	Residual degree of saturation
SS	Scaled sensitivity
S_{r0}	Initial degree of saturation
T	Temperature
T_a	Atmospheric temperature
t_a	Annual gap
t_d	Daily gap
t_m	Time at noon (s)
T_{ref}	Reference temperature
T_s	Surface tension
t_s	Time when autumn starts (s)
u	Solid displacements
$\mathbf{u_a}$	Air pressure
$\mathbf{u_w}$	Water pressure
u_{v0}	Saturated vapour pressure
V_a	Volume of air
V_v	Volume of voids
V_w	Volume of water
w	Gravimetric water content
w_g^w	Mass fraction of the water in the gas phase
w_l^h	Solute concentration
w_l^h	Mass fraction of solute
w_l^a	Mass fraction of air
$\mathbf{x}$	Vector of model parametres
x_a	Annual amplitude
x_d	Daily amplitude
x^{norm}	Normalisation of the parameter
x_m	Annual mean
$\mathbf{y}$	Vector of model response
z_a	Screen height
z_0	Roughness length

1 Introduction and motivation

1.1 Background and motivation

Loess is an aeolian sediment which was formed during the quaternary period through the commutative evaporation and rainfall leading to sedimentation of silt-sized particles. One main feature of the sedimentation of loess in China is that it occurred over a large area of about 640,000 km^2 with large layer thickness. Loess slopes located in this arid region are stable for a long time, however, during the rainy season, in the past landslides happened in the loess plateau and caused an enormous amount of damage to the economy and people's lives. The loess landslides induced by continuous heavy rainfall are one of the most important geotechnical engineering problems in the loess plateau region in Northwest China. The annual rainfall is usually concentrated in a short period of several weeks and relatively large. Under the continuous heavy rainfall, the rainwater infiltrates into the loess slope, causing a matric suction reduction and a decrease in the shear strength of the unsaturated loess. The landslide in the Baqiao area in the year 2011 caused 32 casualties due to the prolonged rainfall event. Seasonal intensive rainfall and rainstorm were recognised to be the biggest triggering factor of landslides in the loess area. The main features of the climate condition is the alternating evaporation and precipitation leading to a cyclic wetting and drying in the soil at shallow depth from the surface of the slope.

Studying the mechanism of rainfall-induced loess landslides becomes imperative when these landslides are increasingly exposed to extreme climatic conditions. Field monitoring and physical modeling are both used in a complementary way to study rainfall-induced landslide mechanisms. To these have to be added the numerical simulations, which are a frequently used tool nowadays in geotechnical engineering to investigate the stability of loess slopes under rainfall. It should be noted that in terms of numerical simulations, it is of great importance that the magnitude and spatial variation of pore water pressure is considered and advanced constitutive models are used to simulate the specific behavior

of the involved soil material.

Loess is a problematic and moisture-sensitive soil, it has a meta-stable structure and suffers a dramatic decrease of stiffness and strength during wetting. From the microstructural aspect, the natural loess is characterized by a honeycomb structure, which is built by the clay cementations among the interaggregate pores and grain particles. Cyclic wetting and drying can alter the loess microstructure, specifically the arrangement and size of pores, the fractal dimension and structure of aggregates, the contact between particles and aggregates and the connectivity of pores, which further can change the hydraulic and mechanical behaviour of loess, including its shear strength, permeability, compressibility, water retention capacity and bearing capacity. Ultimately, all these factors and these changes in the properties of loess soils adversely affect the stability of loess slopes.

When considering loess landslides under significant variation in the climatic conditions, it is very important that the characteristics of the loess both for the unsaturated state and the saturated state to be well and fully understood. The coupled hydro-mechanical behaviour of loess was studied in the past, for instance the loading influence on the water retention characteristics, and the suction hardening behaviour. The soil initial state, sample preparation, the boundary and initial conditions of the tests and the soil stress history, they all are factors influencing the water retention properties, unsaturated shear strength and the soil deformation behavior. However, to this point, the hydraulic path effect on soil hydraulic and mechanical behavior was rarely studied so far. The constitutive models were mostly developed based on data of remolded loess samples. There is less work considering undisturbed loess. Due to the specific precipitation process that determines the structural properties of the undisturbed loess, its microstructure is different before the test and during the test may also undergo changes different from those of the remolded loess samples. It is thus necessary to conduct independent studies on undisturbed loess samples.

1.2 Objectives and scopes

The general objective of this study is to investigate the hydro-mechanical behaviour of both initially undisturbed and remolded loess in the context of loess-slope stability affected by atmospheric conditions. An adequate constitutive model for unsaturated soil is used to model the slope under atmospheric boundary conditions by fully coupled thermo-

hydro-mechanical simulations. One focus is on the thorough experimental investigation of the loess soil originating from China. This investigation enabled a detailed characterization of the material as well as to deduce parameters for the numerical modelling using both HM and THM models.

The scopes of the investigation are explained in detail as follows:

- Thorough characterization of the basic geotechnical properties and micro-structural investigation of disturbed and undisturbed loess using scanning electron microscopy (SEM) and mercury intrusion porosimetry (MIP).
- To investigate experimentally the influencing factors on collapsibility of loess. To qualitatively explain the relationship between collapse index and vertical pressure by performing both single oedometer and double oedometer tests. To investigate the relationship between structural properties and collapsibility of loess.
- Study of the influencing factors on the shear strength parameters cohesion and internal friction angle of the undisturbed and remolded loess. Single-stage and multi-stage shear tests at different water contents and applied vertical stresses were used for this purpose.
- To evaluate the variations of the hydraulic properties of the loess motivated by the data from the literature that the boundary conditions in which the considered unsaturated loess slope is located represent an alternating process of wetting and drying. To present an analysis of the studies to date related to the alternative wetting and drying process and its influence on the swelling-shrinking potential, water content, void ratio and particle cementation of loess soils. Examination of the influence of alternative wetting and drying, representing realistic field conditions on the hydraulic behaviour of remolded and undisturbed loess specimens. Including hysteresis in cyclic wetting-drying paths in terms of water content and volumetric changes.
- Experimental investigation of the hydro-mechanical behaviour of the undisturbed and remolded loess was performed under (a) suction-controlled wetting and drying process and (b) at constant suction but increasing and decreasing net stress. Because of the non-uniqueness of water retention under different boundary conditions, the major of the objectives is to quantity the effect of stress state and stress paths on the water retention behavior including deformation and yield characteristics, and to determine the parameters needed for modelling of behaviour in the framework of an elasto-plastic constitutive model for unsaturated soils (Barcelona basic model).

- Assessment of the effect of hysteresis in water retention behaviour and of consideration of atmospheric boundary conditions in thermo-hydraulic numerical simulations using the finite element software CODE_BRIGHT.
- Numerical investigation of the Baqiao loess slope failure with a thermo-hydro-mechanical analysis considering both the hydraulic hysteresis model and the atmospheric boundary conditions. The effect of atmospheric variables on deformation, pore pressure, shear stress distribution and the resulting failure mechanism will be analyzed.

1.3 Organization

This thesis is composed of 8 chapters. Chapter 1 outlines the background and motivations, the objectives and scopes of this research, as well as the organization of the thesis.

Chapter 2 gives the state of the art, which covers the current knowledge regarding loess, its formation, its microstructure, and the chemically and physically based collapse mechanisms. This chapter gives an overview about types of loess slopes and the classification of rainfall-induced loess landslides. In order to investigate the hydro-mechanical characteristics, the concept of suction in unsaturated soils, pre-consolidation pressure, and yield surface are explained. The actural state of the art on water retention behaviour, unsaturated permeability and their models are shown. An extended overview of the constitutive model used (BBM-TEP) to study the hydro-mechanical behaviour of unsaturated loess is presented. Besides, background, theory, and the main variables of the models are discussed. A review of relevant aspects regarding volume change in loess due to applied mechanical loading paths and applied suctions is discussed. The last part of the second chapter deals with the main issues regarding slope stability.

The sampling site, basic physical, and chemical properties of the material used in this study are introduced in Chapter 3. Detailed material characteristics are presented, including results of microstructural investigations. The experimental program carried out in this work is described in the second part of Chapter 3.

Chapter 4 introduces the experimental methodology used to investigate the hydraulic and mechanical properties of unsaturated loess under different boundary conditions and stress paths. Special attention is given on the suction-controlled testing procedures ap-

plied to study the coupled hydro-mechanical behaviour.

Chapter 5 presents and discusses the experimental results, including the effect of initial sample and loading conditions on shear strength, one-dimensional compression behaviour and collapse potential of remolded and undisturbed loess. The experimental results regarding the water retention behaviour are presented. Both analytical and statistical water retention models were used for the determination of the SWCC-fitting parameters. Based on the SWCC curve, unsaturated shear strength and coefficient of unsaturated permeability were predicted. Results from the SWCC-test, unsaturated compression tests, and direct shear tests are used to deduce the parameters needed for the numerical modelling.

Chapter 6 presents the theoretical framework contained in the applied THM analysis. A simulation of element tests has been used to validate the constitutive model and to calibrate model parameters. A model taking into account air entrapment is introduced to reproduce the hysteretic unsaturated flow phenomenon. A one-dimensional column is used to study the influence of the atmospheric boundary condition variables on pore water pressure and temperature distribution.

Chapter 7 presents simulations of a real loess slope under atmospheric boundary conditions. Emphasis is given on the distribution of pore water pressure and plastic strain under antecedent rainfall events. Finally, the shear reduction technique is used to analyze the loess slope stability.

Chapter 8 summarizes the outcomes of the present work and provides suggestions and recommendations for further studies in this field.

2 State of the art

This chapter provides an overview of the behavior of loess, with a focus on various aspects such as its formation, distribution, microstructure, and collapse mechanisms. The chapter also addresses the distribution and types of failure of loess landslides. Further, the basic concepts of unsaturated soil mechanics, including suction, effective stress, and stress state variables are described together with factors that influence soil water characteristics, including deformation and stress paths and the hysteresis phenomenon of soil water retention behaviour. Finally, the chapter introduces the constitutive modeling of volume change behavior of unsaturated soils and the common methods used in studies of slope stability under rainfall.

2.1 Loess soil

2.1.1 Occurrence, geological description and classification of loess soil

This section explores the physical and mechanical properties of loess soil, which are unique and distinct. Loess, a windblown sediment, covers approximately 10% of the world's surface, as reported by Pécsi (1990). The majority of loess deposits are found in North Africa, Northwestern Europe, the Middle East, and Central Asia, including countries such as France, Germany, Belgium, Ukraine, Russia, Thailand, and Algeria, as noted by Smalley (1995); Smalley et al. (2001); Smalley and Jary (2005); Dijkstra et al. (1995); Lin (1995); Phien-Wej et al. (1992); Nouaouria et al. (2008). The global distribution of loess deposits is shown in Fig. 2.1. Typically, loess deposits are located in dry continental zones at middle latitudes. In China, loess covers an area of 640,000 m^2, equivalent to approximately 7% of China's land area.

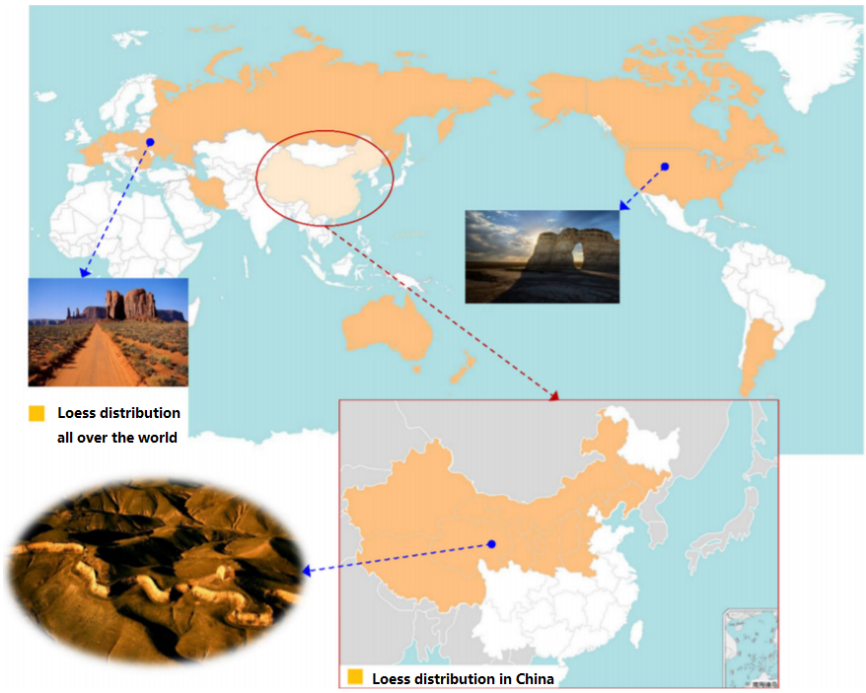

Figure 2.1: Loess distribution in the world and China (Qiu et al., 2018).

From a geological perspective, loess is a sedimentary deposit of wind-blown aeolian silt that dates back to the Pleistocene epoch. The formation of loess is associated with the Mongolian-Siberian anticyclone, which is generated by the continental ice sheet and the high-pressure center above the desert, as explained by Li et al. (2019). Over time, the parent rock of loess weathers into stones, sand, and clay of different sizes. Loess is distributed along with the wind transport from the Caspian Sea to Central Asia, crossing the Qinghai-Tibet Plateau, and moving from the North and Northwest of Gansu, Ningxia, and the Mongolian Plateaus towards Central Asia and other arid desert areas to the Southeast. When the wind is weakened or obstructed by the Qinling Mountains, the sedimentation process halts. After several hundred thousand years of accumulation, the Loess Plateau is formed.

China has the world's most extensive, complete, and thickest loess deposits, which are mainly distributed in Shandong, Hebei, Henan, Shanxi, Shaanxi, Gansu, Qinghai, Ningxia, and Xinjiang provinces or autonomous regions. Loess is concentrated in the middle part of the Yellow River, between 30° and 49° north latitude and between 34° and 39° east longitude. The sedimentation process of loess in China is illustrated in Fig. 2.2. The thickness of loess sedimentation in China ranges from 30 to 200 m and can reach up to 500 m in Jingyuan, Gansu Province.

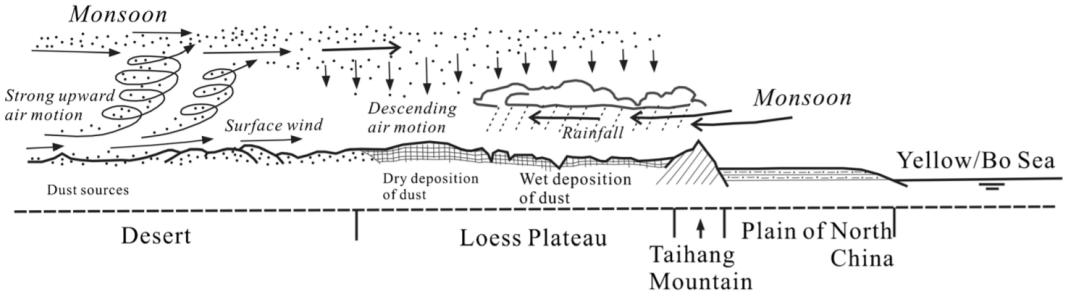

Figure 2.2: Schematic representation of loess-forming processes in the Chinese Loess Plateau (Derbyshire et al., 2000).

Loess is predominantly found in areas with continental arid and semi-arid climates, where evaporation rates exceed rainfall. The formation of loess is closely related to changes in climatic conditions, which have oscillated between dry and cold to hot and humid. Loess particles were deposited during both dry and cold climates, whereas wet particles were carried to valleys and formed alluvial fan soils (Frechen et al., 2003).

The aeolian deposits found in the loess plateau in Shaanxi originate from the vast inland deserts of northwest China. The northwest winter monsoonal winds, flowing from the Siberian-Mongolian region, carry aeolian material onto the loess plateau (An et al., 1991). The landform is located in the central part of the Guanzhong Basin and comprises different terrain types, including flood plains, loess tablelands, and proluvial fans. Due to the intermittent neotectonic movement, lifting, and river erosion, the plain area is divided into a floodplain and the first, second, and third terraces (Shi et al., 2016).

Loess in China can be classified into four types based on different sedimentary environments: Wucheng loess (Q_1), Lishi loess (Q_2), Malan loess (Q_3), and Holocene modern loess (Q_4) (Pécsi, 1990). Wucheng loess (Q_1) was deposited during the early Pleistocene, which corresponds to the first glacial period. Q_1 is mainly distributed in the high terrace with a relatively large thickness, roughly equivalent to the semi-rock stratum. Lishi loess (Q_2) was deposited during the Middle Pleistocene, which marks the second glacial period and was characterized by a drier climate. Q_2 is distributed in the high terrace loess tableland and loess platform. The accumulation of Lishi loess was widespread, and the soil layers are thus quite thick. During the late Pleistocene, the third glacial period was marked by a more dry and cold climate, which led to the formation of Malan loess (Q_3)

(Porter, 2001). Although the thickness of Q_3 is relatively small, it has a wide distribution range and is characterized by a loose structure and the development of vertical joints (Porter, 2001). With the onset of the Holocene, the climate became warmer and more humid. The deposited Holocene modern loess (Q_4) layer is also loose and mainly distributed in large valleys, covering the valley surface and forming a second bottom, second stage terrace, or new alluvial fans. When flowing water erodes the Q_4 deposited area, it forms a surface with both vertical and horizontal gullies.

2.1.2 Microstructure of loess

Loess is a type of fine-grained, silty soil that typically appears yellow, brownish yellow, or light brown, depending on its water and clay content. Its parent rock composition is mainly feldspar, mica, and quartz, which undergo glacial grinding or cold climate weathering (Rogers et al., 1994). The silt particles have sharp, acute angles, with a particle size between 0.005 and 0.05 mm. X-ray analysis has identified illite as the primary clay mineral in loess, along with a small amount of montmorillonite (Guo-rui, 1984).

Various methods and techniques have been used in the past to study the microstructure characteristics of loess. The scanning electron microscope (SEM) is commonly used to provide microscopic images, while mercury intrusion porosimetry (MIP) is used to quantitatively study the pore size distribution. Comparative studies have also been conducted between remolded and undisturbed samples to gain knowledge of the natural structural loess and its specific properties.

The type and degree of cementation in loess play a crucial role in the formation of a loose structure with a relatively large void ratio (Rogers, 1995). Cementation can occur through various chemical agents such as iron oxide, calcium carbonate, clay minerals, as well as other water-soluble salts and humus (Lefebvre, 1995; Rogers, 1995; Klukanova and Frankovska, 1995).

The primary difference between as-compacted and undisturbed loess is in their pore size distribution. As-compacted loess has a more homogeneous pore size distribution, while undisturbed loess has a more heterogeneous distribution that includes at least two pore families due to cement bonding between aggregates or grain solids. The microstructural evolution of undisturbed samples is dependent on the stress level and stress path, and factors such as the climate during loess sedimentation (Derbyshire and Mellors, 1988) de-

termine the structure of undisturbed loess. Due to rainfall-evaporation cycles during loess deposition, loess forms a flocculation structure with large pores, and its microstructure reduces to a collection of bonding bridges, inter-aggregates, and intra-aggregates (Houston et al., 2001). Periodic short precipitation infiltrations dissolve soluble salts in the soil between particles and agglomerates.

However, in long-term arid conditions, the capillary forces generated by evaporation cause soluble salts or clay minerals to concentrate at the connection points between grain solids, as shown in Fig. 2.3. This concentration leads to the formation of a cementitious bond between the flocculated solid skeleton, increasing shear resistance and incompressibility. Natural loess is a macroporous material, with well-developed vertical jointing (Ng et al., 2016). Cementing materials are often added after deposition or dissolved and re-precipitated at particle contacts. The microstructure of loess includes bonding bridges, intra-aggregates, and inter-aggregates, as well as the arrangement of these various elements, as shown in Fig. 2.4. The flocculation structure formed by clay particles reduced collapse deformation caused by saturation (Haeri et al., 2017). The structure of undisturbed loess can change due to saturation and loading. As vertical load increases, the cement bonding between intact loess solid particles and agglomerates is damaged, and large inter-aggregate pores transform into small intra-aggregate pores. These pores are flatter but still randomly oriented (Munoz-Castelblanco et al., 2011; Delage et al., 2008).

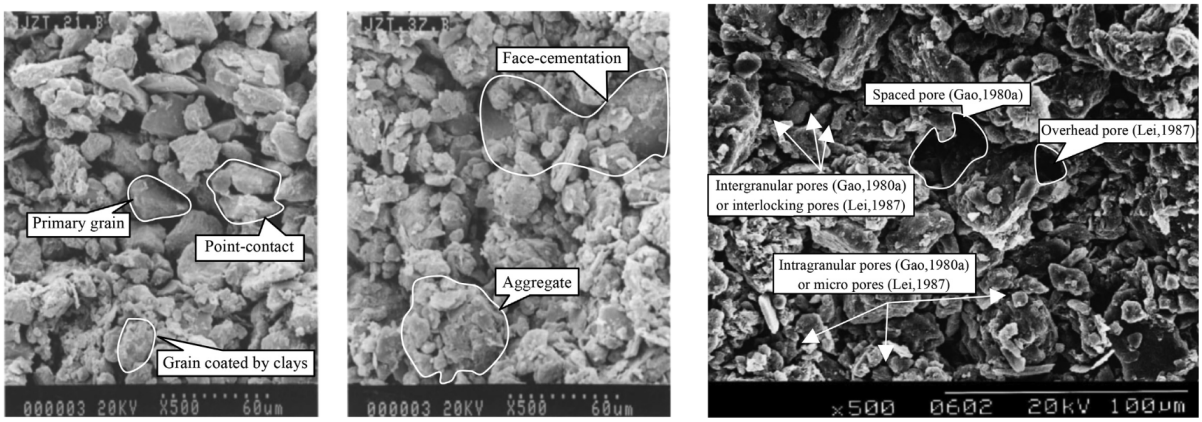

(a) (b)

Figure 2.3: Typical SEM photographs of loess (a) Solid-phase morphology, and (b) Pore system elements (Dijkstra et al., 1994).

The microstructure of remolded loess is primarily determined by the water content and vertical load during the sample preparation process, as well as the compaction technique

used. As the water content of loess increases, the structure tends to become softer, making it easier for clumps to form between the particles. In addition, the structure of remolded loess is relatively isotropic, meaning that its properties are similar in all directions.

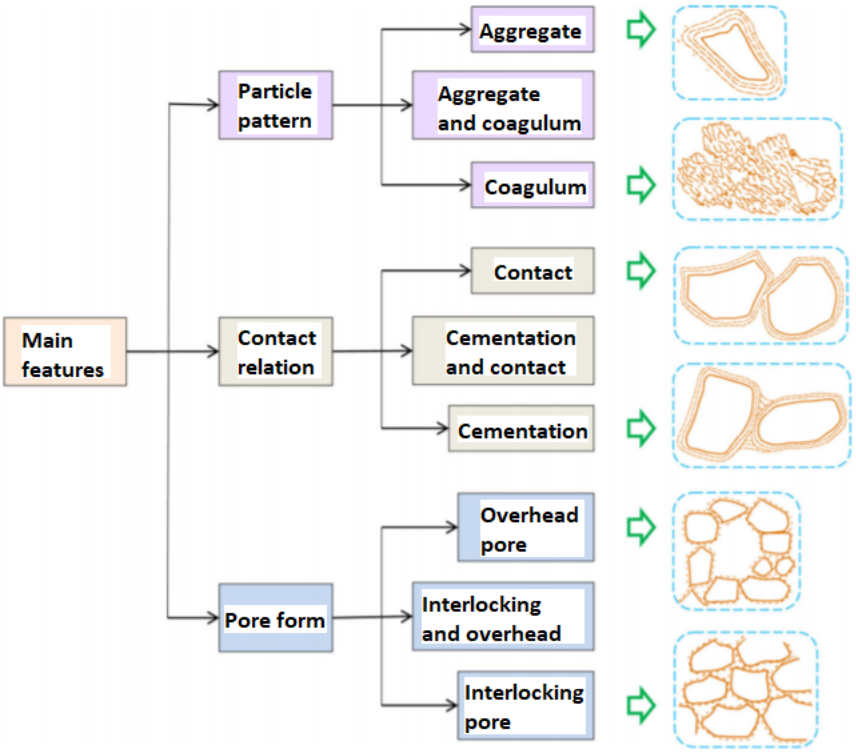

Figure 2.4: Main features of the loess microstructure (Guo-rui, 1984; Guorui, 1994).

From a physical standpoint, the dominant inter-aggregate pores in remolded samples can be controlled through the compaction process. This results in a similar arrangement of granular particles and aggregates to that of granular materials (Jiang, Zhang and Hu, 2014). Capillary suction typically provides the metastable bonding. With the addition of water, the aggregates increase in volume and the clay particles absorb the water, resulting in a softening effect. Remolded loess samples exhibit mechanical properties similar to those of fine granular materials. The main factor causing collapse deformation in these samples is the decrease in capillary forces resulting from wetting.

2.1.3 Collapse mechanism of loess

The most significant geotechnical property of loess soil is its collapsibility, which means that it can move as a weakly cemented mass of material and fail along interconnected

joint systems simultaneously. Some scholars (Liu et al., 2015) have proposed that the collapsibility of loess is caused by the formation of a flocculation structure between particles and agglomerates. From a macroscopic perspective, the destruction of these cementation bonds and flocculation structures is mainly due to the dissolution of the cementing material and external disturbances (Guorui, 1994).

Natural loess is characterized by a microstructure composed of fragments and aggregate grains connected by crystalline carbonate. However, this structure is very unstable and easily displaced or deformed at the contact points when wetted under pressure, leading to collapse. Cementation and bonding are destroyed during the wetting process, as the dissolved bonding between inter-particle, inter-aggregate or intergranular contacts fails in shear. This results in significant collapse deformation on the macro structure level. The wetting action of water film can also release the inherent swelling and shrinking potential of the soil. When the crystalline carbonate in loess is leached out, clay becomes the primary bonding agent, leading to the formation of an interlocking arrangement structure. Under higher water content and smaller external loading, the intrinsic structure can be destroyed. However, for soil with lower water content, a larger external load is needed to destroy the intrinsic structure.

Loess can also exhibit characteristics of a cohesionless particulate material that can flow in both dry and moist conditions. This collapsibility is caused by the under-compaction of the porous fabric of the soil (Houston et al., 2001; Tadepalli and Fredlund, 1991). As the degree of saturation increases, the capillary forces in the soil decrease, which can cause a reduction in the inter-aggregate pore volume. However, in undisturbed samples, the swelling of clay particles under certain stress states counteracts collapse and reduces the collapse potential.

Some scholars have observed that the collapsible deformation of remolded soil is closely related to the initial void ratio. During the wetting process, the structure of recompacted soil significantly influences the deformation behavior, and the initial micro-structure is primarily determined by the specimen preparation (Sivakumar Babu et al., 2006). When less energy is applied during specimen preparation, the void ratio and the compression at subsequent loading increase. Conversely, if the compaction energy during preparation is large enough, the tight pore structure can reduce or eliminate the collapsible deformation. The engineering behavior of remolded loess samples is primarily determined by the size and distribution of inter-aggregate and intra-aggregate pores, rather than the con-

centration and distribution of solids. Furthermore, increasing compaction effort leads to a reduction in inter-aggregate voids, but has little effect on intra-aggregate voids (Burton et al., 2014). The swelling or collapsing deformation of compacted soils due to wetting results from the combined effects of swelling in the intra-aggregate pores and collapsing of the inter-aggregate pores.

There is an alternative interpretation of the collapse mechanism in remolded soil versus undisturbed soil. In undisturbed soil, collapse is often caused by cementation joints, while in remolded soil, it is usually due to the reduction of matric suction resulting from wetting. According to Dijkstra et al. (1994), the microstructure of undisturbed loess, which consists mainly of a particle skeleton and interparticle bonds, is a major cause of large collapsibility. This structure is inherently unstable, especially when subjected to applied mechanical stress during water infiltration. Both carbonate and soluble salts can lead to sudden large deformations due to dissolution. Even when the void ratios of as-compacted and undisturbed samples are the same, the pore size distributions often differ significantly, which can be attributed to the presence of carbonate bonding.

The particle arrangement in loess soils is influenced by various climate factors (Beckwith and Hansen, 1982; Lin and Liang, 1982). Different scholars have analyzed the causes of loess collapse from different perspectives, including the clay content, the proportion of macropores, the soluble salt content, and the inter-particle association form. The collapsibility of loess upon immersion in water is determined by the degree of water swelling in the microstructure and pore deformation in the macrostructure. Following collapse deformation, macro-pores are transformed into micro-pores, and the connection between particles and agglomerates becomes denser and more stable. According to Feda et al. (1995), collapsible deformation can occur at both the microscopic and macroscopic levels.

The microscopic structure of soil can contribute to collapsible deformation through cementation joint failure, debonding, grain crushing, and fabric transition. At the macroscopic level, collapse deformation may result from soil sample loading, wetting, creep, and softening. Unsaturated soil mechanics theory explains that collapsible deformation occurs due to the decrease of matric suction between pores. In collapsible soils, inter-aggregate pores are significantly larger than intra-aggregate pores. Inter-aggregate pore volume can be controlled during the compaction process, while intra-aggregate voids are usually small and less affected by compaction.

2.1.4 Special features of structural loess

Loess soils typically have a high proportion of silt particles, followed by clay, while sand is present in relatively small amounts. However, particle size distribution may vary slightly with soil depth. Plasticity characteristics of loess are generally low to medium plastic, with a plastic limit (w_P) of about 25-35%, sometimes reaching 45%, and a plasticity index in the range 5-22%, making it very sensitive to changes in moisture. The primary minerals in loess are quartz, feldspar, and calcite, with low levels of mica and hornblende. Clay minerals detected in loess include montmorillonite, illite, chlorite, and kaolinite. Chemical composition analysis reveals the presence of Na^+, K^+, Ca^{2+}, Mg^{2+}, SO_4^{2-} (sulphate), Cl^- (chlorate), and calcium carbonate.

Undisturbed loess is often treated as over-consolidated soil due to the structure formed during the sedimentation process. This means that the actual loading is less than the pre-consolidation pressure. The bonding within the undisturbed loess induces effects that are similar to those of real overconsolidation. Suction-controlled compression tests and constant loading drying tests are commonly used to study the structural properties of undisturbed loess. The difference in mechanical properties between remolded and undisturbed samples can provide valuable information about the structural properties and their influencing factors.

Various mechanical tests have been conducted on loess soils, including direct shear tests with different vertical loads (Li et al., 2019), water retention tests (Ng et al., 2016), salt solution tests (Zhang et al., 2013 and Wen and Yan, 2014), dynamic strength tests (Qiu et al., 2018 and Hu et al., 2001), one-dimensional compression tests (Luo et al., 2018), and penetration tests (Li and Li, 2017). The shear strength of undisturbed loessial soil arises from intrinsic cohesion, adsorption cohesion, and friction. Specifically, the structural strength of the cemented structure, combined with intrinsic cohesion, adsorption cohesion, and friction, constitutes the structural strength of undisturbed loess. The loss of structural strength can be due to applied loads, changes in water content, and disturbance effects (Wen and Yan, 2014). The external load can lead to the destruction of the cemented joints in undisturbed loess and rearrangement of the particles.

During the process of the disappearance of the structural strength of undisturbed loess, both the water content and the external load play a coupling role (Jiang, Zhang and Hu, 2014) (Fig. 2.3). An increase in the water content leads to the dissolution of the

cementation bonding, resulting in the collapse of the open structure and denser packing structure. This increase in water content also results in an increase in the thickness of the water film surrounding the grains, which reduces the adsorption force and matric suction. In the case of undisturbed samples, any disturbance of sufficient intensity can destroy the cementing bonding between the particles (Fig. 2.3). External loading can also change both the arrangement of particles and bonding characteristics. Saturation can resolve and weaken the chemical constituents, which reduces the cohesion strength.

Various empirical models have been proposed by scholars to represent the behavior of undisturbed loess, which includes structural parameters. For instance, Liu and Carter (2002) introduced structural parameters into the Modified Cambridge model to reflect the compressive properties of structural clay, while Suebsuk et al. (2010) used an elastoplastic model with structural parameters to reflect the mechanical properties of undisturbed loess. The structural properties of the undisturbed loess are quantitatively described by macroscopic conventional samples to emphasize their structural strength in comparison to remolded loess. Chinese scholars have proposed different empirical formulas for the structural parameters of the model, which are derived from element tests based on damage mechanics due to their rich experimental experience. These tests include the dynamic triaxial tests utilized by Luo et al. (2004), suction-controlled compression tests used by Hu et al. (2005), and true triaxial tests employed by Chen et al. (2007) and Deng et al. (2012). Additionally, damage mechanics and energy change were introduced to differentiate the unique structural characteristics of undisturbed loess from the remolded loess soil.

Although various hypotheses have been proposed to explain the structural properties of undisturbed loess using microscopic quantitative indicators, accurately determining the damage ratio of soil under certain stress and different water content remains controversial. One approach is to use structural parameters that can represent the structural properties synthetically under various strain and moisture conditions. However, the different approaches vary in how they identify these structural parameters and the physical meaning behind them.

2.2 Loess slope instability under rainfall infiltration

2.2.1 Landslides in loess formations in China

The loess slopes typically have a steep angle and remain stable in dry conditions, but they have a high potential for instability during wetting. The bedrock is situated beneath the alluvial deposits of silty clay and pebbles and was deposited during the tertiary period. Loess landslides are distributed in strip clusters along the Yellow River Gorge and Luliang, and the Shanxipo in North China, and in a linear cluster along the north shore of the Baoji River and the west of Liupan Mountain. The internal initiation and development of loess landslides are responses to three necessary factors: pore water pressure, steep slope, and large deposition thickness (Guorui, 1988; Zhang and Liu, 2010). External factors that can cause loess landslides include earthquakes, rainfall, excavation (Huang et al., 2008; Wang et al., 2011; Liu et al., 2012), rising groundwater levels, human activities, and cyclic freezing-thawing (Derbyshire et al., 2000).

Changes in groundwater level can affect the pore water pressure in loess slopes, while excavation can alter the stress state inside the slope. Rainfall, on the other hand, can change the shear strength of the slope material. Field investigations have revealed the presence of joint fissures in the upper section of loess slopes, as well as tensile cracks on the back of the slope caused by tension. Groundwater levels on loess slopes are often buried deep, with the loess layer overlaying bedrock and continuously covering basins, slopes, hills, valleys, and terraces, resulting in present-day topographic relief that is consistent with the underlying terrain.

In large areas of North China, it is common to observe very steep slopes that remain stable for long periods of time. However, even very gentle loess slopes can experience large-scale landslides after the monsoon season (Tu et al., 2009). This suggests that the stability of loess is sustained over large areas mainly because of the dry climate that maintains unsaturated conditions. The climate in the loess area is characterized by a wide annual range of temperature and precipitation, and it is monsoonal to continental in nature. According to statistics, one-third of all landslides in China occur in the loess area, and with the increase in economic development and engineering activities in western China, the incidence of geological disasters has increased rapidly. Loess landslides pose a serious threat to the safety of habitation and construction in cities and towns in loess regions. Historical records show that the Bailu tableland has experienced slope failure

phenomena (Xu and Liao, 2007). The Bailu tableland has an extra-tropical monsoon climate with four distinct seasons, characterized by the combined effects of the southeast monsoon and cold, dry air from the Mongolia plateau in the Northwest.

Loess landslides can be classified into four types based on the composition of the slide mass and the situation of the failure plane: bedrock contact landslides, palaeosol contact landslides, mixed landslides, and slides within loess (Qiu et al., 2016 and Peng et al., 2018). Various models have been proposed to explain the mechanism of loess landslides, including those caused by runoff erosion or rises in groundwater levels, shallow loess landslides due to precipitation, landslides due to cut slopes or irrigation, and progressive failure loess landslides due to external loads.

The form of mass movement determines the mode of loess slope failure, which can be classified into toppling, falling, cracking-sliding, sliding, peeling, and caving (see Fig.2.5, Li and Mo, 2019). Cracking-sliding failure is the most common mode of failure in the Malan Loess region. Cracking-sliding failures in loess slopes are typically caused by sliding of the slope material along the lower part of the failure plane (Peng et al., 2016). While these failures may be small in volume, they can result in considerable disaster and sometimes even fatalities. In fact, over the past two decades, more than 2000 cracking-sliding failures have been recorded, causing an average of more than 100 fatalities per year (Wang et al., 2013).

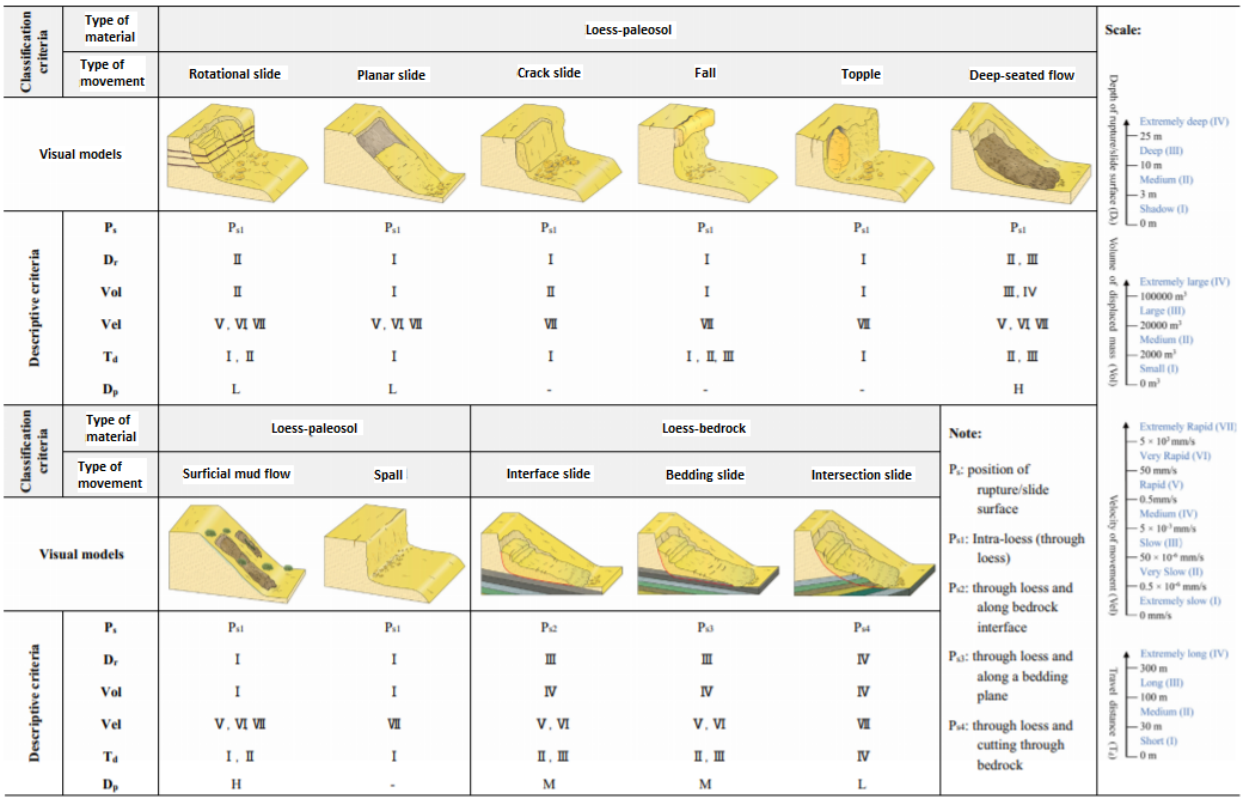

Figure 2.5: Unified loess landslide classification system (Li and Mo, 2019).

Unlike flows or slides as defined by Cruden and Varnes (1996), cracking-sliding failures are characterized by a composite failure plane. The upper part of the plane typically develops vertically from the crown of the slope down to a depth of one to several meters, and is formed by tensile cracking. A slope can remain stable for a long time with these cracks before eventually failing. The lower part of the failure plane is generally inclined at an angle ranging from 15 to 60 degrees.

2.2.2 Slope instability under rainfall

It is well established that water plays a significant role in triggering landslides, including those in the loess area. Recent landslide occurrences in the area have shown a strong correlation with average monthly precipitation, whether in the form of rainfall, surface water, or groundwater. This is evident from the distribution map of loess landslides that occurred between 1980 and 2010, as shown in Fig. 2.6. The highest occurrence of landslides in the loess area is in regions with high rainfall, where the annual and monthly average rainfall is 584.9 mm and 53.7 mm, respectively. The maximum annual

and monthly rainfall are 1132 mm and 259 mm, respectively, and 97.3% of the landslides occurred between May and October. As seen in Fig. 2.6, areas with precipitation up to 200 mm/year are more prone to landslides.

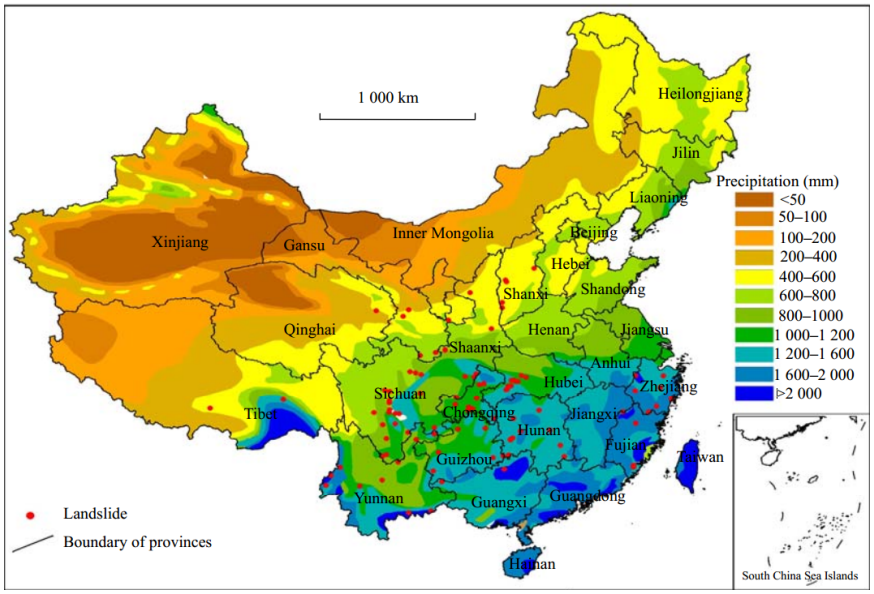

Figure 2.6: The average annual precipitation for previous years in China and locations of landslides (Huang and Li, 2011).

According to Zhou et al. (2002), loess slopes are formed by the deposition of aeolian dust, and the distribution of landslides is related to the structure, lithology, and geological conditions of the loess. The causes of instability in loess slopes include natural factors, such as the steep topography, geological structure, and seismic activity, as well as human activities, such as construction, deforestation, and irrigation.

Regarding the classification of rainfall-induced shallow landslides, Crosta and Frattini (2008) reviewed different methods used by various studies. More recently, Cascini et al. (2010) and Cruden and Varnes (1996) classified these landslides based on the acceleration of the failed mass as slide, slide to flow, and flowslide. They defined the failure stage as the formation of a continuous shear surface throughout the soil mass, with the post-failure stage represented by the rapid generation of large plastic strains and the consequent sudden acceleration of the failed soil mass.

Furthermore, Fell et al. (2008) and Cascini et al. (2010) divided the process of slope slip under rainfall into early instability and late instability. Early instability refers to the gradual instability process of the sliding zone soil and the formation process of the

interconnection of the sliding zone, while late instability refers to the formation of large plastic deformation and the accelerated sliding process of the soil.

Various approaches have been employed to study the mechanism of rainfall-induced loess slope failure, including saturated triaxial tests, unsaturated shear tests, in-situ immersion tests, and indoor seepage tests. For instance, Peng et al. (2018) used in-situ surveys to analyze the sliding mechanism of loess landslides in the Heifangtai area, while Xu et al. (2011) used field experiments to study the infiltration properties of artificially excavated loess slopes under rainfall. Sliding models to explain debris flow generated on loess slopes during rainfall were proposed by Peng et al. (2016), Miao et al. (2002), and laboratory tests were conducted by Wu et al. (2017) to study the deformation of loess slopes under rainfall conditions. Deformation and stability of loess slopes with red mudstone interlayers were monitored using artificial rainfall by Baoping et al. (2005), and Shi et al. (2016) analyzed the structural characteristics, landslide type, and formation mechanism of loess slope along the Weihe River in the Baoji area. In addition, laboratory tests have been used to study the erosion properties of loess, combined with the loss of surface soil and the infiltration of rain on a certain slope, as seen in the work of Acharya et al. (2011). Several studies, such as Xiaokun et al. (2018) and Wang et al. (2002), have focused on studying the effect of seepage on pore water pressure and groundwater level in the slope, while others, such as Xu et al. (2012) and Cui et al. (2018), have investigated loess landslides caused by irrigation. Peng et al. (2015) and Wang et al. (2014), have studied the stability of loess slopes under rainfall and excavation conditions using limit equilibrium and finite element strength reduction methods. Additionally, some studies have divided loess landslides under rainfall into different modes based on the geological development of the loess slope, as done by Tang et al. (2015).

It is widely accepted that rainfall-induced landslides are primarily triggered by changes in pore water pressures and seepage forces (Gerscovich et al., 2006; Zhu and Anderson, 1998). The causes of rainfall-induced loess landslides are generally divided into two mechanisms (Collins and Znidarcic, 2004). In the first mechanism, rainwater infiltration is hindered by impervious soils and soils with low permeability, such as bedrock and paleosol, leading to an increase in excess pore water pressure in the overlying loess and eventually causing slope instability. This type of instability typically leads to soil liquefaction at the contact surface of the two soils and is characterized by high sliding speed, long sliding distance, and large sliding soil (Wang and Sassa, 2001). The in situ stress path of soil can be described by a constant shear stress path (Anderson and Sitar, 1995).

Traditional slope stability analyses typically account for the effects of rainfall by assuming changes in groundwater flow patterns due to increasing pressure heads or rising groundwater tables. However, it is important to note that a rising groundwater table is not always a factor, especially in cases of shallow failures where evidence of such a rise is lacking (Fourie et al., 1999). In an effort to better understand landslides resulting from increased groundwater levels in loess slopes in the Fuyang and Heifengtai areas, Zhang et al. (2014) developed a numerical simulation model.

The second mechanism of loess landslides occurs when the soil is in an unsaturated state and rainfall infiltrates the ground. This causes a reduction in soil suction, which in turn decreases both unsaturated shear strength and unsaturated stiffness (Fourie et al., 1999; Fredlund and Rahardjo, 1993). Failures in this mechanism are mainly attributed to the advance of a wetting front and reduced shear strength due to decreased matric suction in the unsaturated soil (Rahardjo et al., 1995). As a result, traditional approaches may not be appropriate for analyzing such failures (Fourie, 1996). Most research on loess landslides involves in-situ wetting tests and indoor soil tests to explain the formation mechanism of these landslides.

The change in shear strength of loess slope material due to rainfall can be explained through the unsaturated soil mechanics. During rainfall infiltration, the unsaturated shear strength of the material decreases as a result of the decrease in matric suction. Some scholars have conducted unsaturated tests to study the unsaturated properties of loess and explain loess landslides based on soil mechanics (Derbyshire et al., 1994). Others, such as Wen and Yan (2014) have used direct shear tests with different water content to study the unsaturated shear strength of loess soil and analyze its effect on landslides. Wang et al. (2015) used the strength reduction method combined with shear strength tests to analyze the mechanism of shallow and deep landslides under rainfall. Additionally, shear tests have been used to study the residual strength of the slip zone soil.

In summary, research on the analysis of loess slopes under rainfall has mainly focused on model tests and laboratory tests, with limited literature exploring the use of numerical modeling methods to study loess landslides under rainfall. However, with advancements in numerical techniques, numerical simulations are becoming increasingly popular in slope stability analysis. Numerical methods allow for the use of complex material models and

boundary conditions to simulate stress and strain development in soils, without the need to assume the location of the sliding surface in advance.

2.3 Fundamentals of unsaturated soil mechanics

2.3.1 Soil suction

The term unsaturated soil refers to a soil which is not completely dry or completely saturated, but has a degree of water saturation at any value between 0 and 1. This implies to consider the soil as a three-phase system consisting of soil solids, water and air, where the behaviour is additionally controlled by the interfacial properties of the air-water and water solid interfaces. The total suction of soil reflects the free energy state of water in the soil related to the aggregate (potential) of free water, which can be expressed through the partial vapor pressure, as shown in Equ. 2.1.

$$\psi = \frac{RT}{V} \cdot \ln \frac{RH}{100} \tag{2.1}$$

ψ is the total suction, R is the universal gas constant, T is the absolute temperature, V is the molar volume of the water $V = \upsilon_{w0} \cdot w_\upsilon$, RH is the relative humidity with $= \frac{P}{P_0}$, P is the partial pressure of the water vapor, and P_0 is the saturation pressure of water vapor over a flat surface at the same temperature.

The total suction (ψ) of soil comprises matric suction (ψ_m) and osmotic suction (ψ_o), as shown in Equ. 2.2.

$$\psi = \psi_m + \psi_o \tag{2.2}$$

Capillary effects, short-range adsorption and osmotic effects are the main mechanisms decreasing the potential of pore-water in soils. Capillary effects are unique to unsaturated states, whereas short-range adsorption reflecting soil solid-pore water interaction and osmotic effects occur in both saturated and unsaturated conditions. The combined effects of capillary and short-range adsorption are grouped under the term matric suction, while osmotic effects are the result of dissolved solutes in the pore water with solutes either being externally introduced or naturally occurring (e.g., as exchangeable cations in clays). Matric suction is determined by the curvature of the water-air interface according to the Young-Laplace equation. The value of matric suction is influenced by capillary

action between the solid and gas-liquid interface, as shown in Equ. 2.3.

$$\psi = u_a - u_w = T_s \cdot \left(\frac{1}{R_1} + \frac{1}{R_2} \right) \tag{2.3}$$

T_s is the surface tension of the liquid phase, R_1 and R_2 are the radii of curvature of the membrane in two orthogonal directions.

Surface tension dominates capillarity, producing an internal water potential that is related to pore size and pore size distribution, controlling small suction and large water content. Matric suction equals the difference between pore water pressure (u_w) and pore gas pressure (u_a) only when matric suction is greater than the cavitation pressure of soil water.

2.3.2 Soil-water characteristic curve (SWCC)

The soil-water characteristic curve (SWCC) describes the ability of soil to retain or absorb water at a given suction. It plays a fundamental role in understanding the flow behavior of water in unsaturated soil. It is also referred to as the suction-water content or capillary pressure-saturation relationship. Under energy equilibrium conditions, the SWCC is a constitutive relationship between the total potential energy and the soil water content. The potential energy can be defined in terms of relative humidity, water head, or matric suction, while the water content can be represented by the degree of saturation, gravimetric water content, or volumetric water content.

The SWCC is the relationship between suction and water content or degree of saturation for an initially saturated sample during drying to dry condition and subsequent re-wetting to zero suction. The term SWCC is employed in this work also for suction-water content relationships of more than the initial drying and main wetting paths. Fig. 2.7 illustrates the variation of possible paths of a SWCC and the terms to designate it. Independent of soil type the SWCC has a characteristic shape and parameters describing the water-retention behaviour of a soil are deduced.

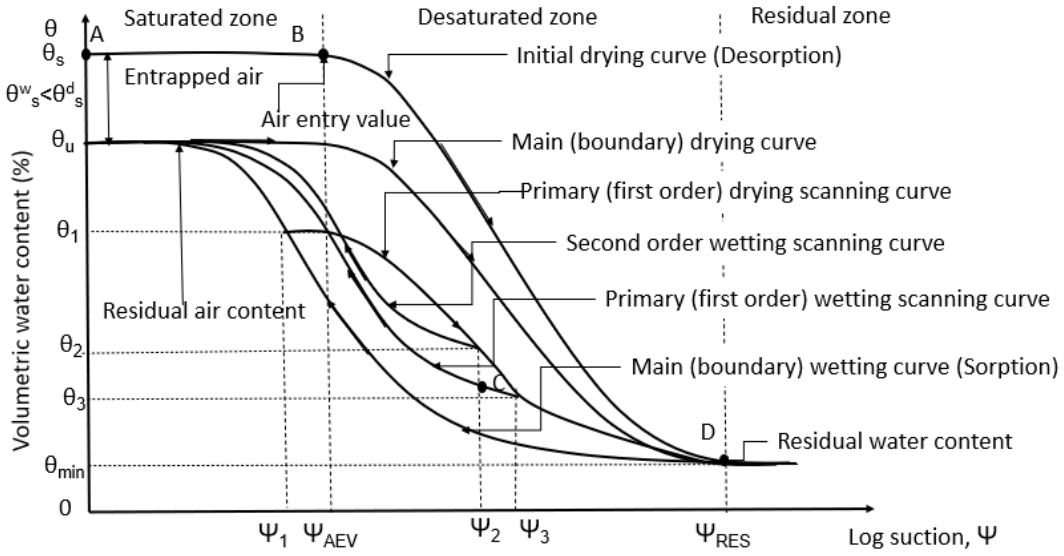

Figure 2.7: The main characteristics of a hysteretic SWCC (Pham et al., 2005).

The air entry value (ψ_{aev}) is the point of transition between the saturated and unsaturated states along a drainage path. In the drying curve, the air entry value represents the minimum matric suction required for air to replace water in the macropores. Similarly, the water entry value is the soil suction at which water starts to displace air and enters the soil pores during the wetting process (Yang et al., 2004).

Once the residual suction (ψ_{res}) is reached during drying no further decrease in water content takes place. This minimum value of water content is usually named residual water content (θ_r). In the illustration in Fig. 2.7, it is named θ_{min}. The drying scanning curves and wetting scanning curves are located inside the main drying and wetting loop.

Based on the distribution of pore water in the soil and the connection of pore water, the SWCC is divided into three stages: the saturated zone, the transitional zone, and the residual zone (Fig. 2.7). In the saturated zone ranging from $\psi = 0$ to $\psi = \psi_{AEV}$, really all pores are filled with water and the water phase is therefore continuous. Only discontinuous air-bubbles exist. In the transition zone large pores followed by smaller pores drain until reaching θ_r. The inclination of the transitional zone is determined by pore-size distribution. Both the water and air phase are continuous in this regime where capillary effects play the major role. In the residual zone the air phase is continuous and the water phase is discontinuous and the water exists in form of thin firms around the soil grains which are not interconnected.

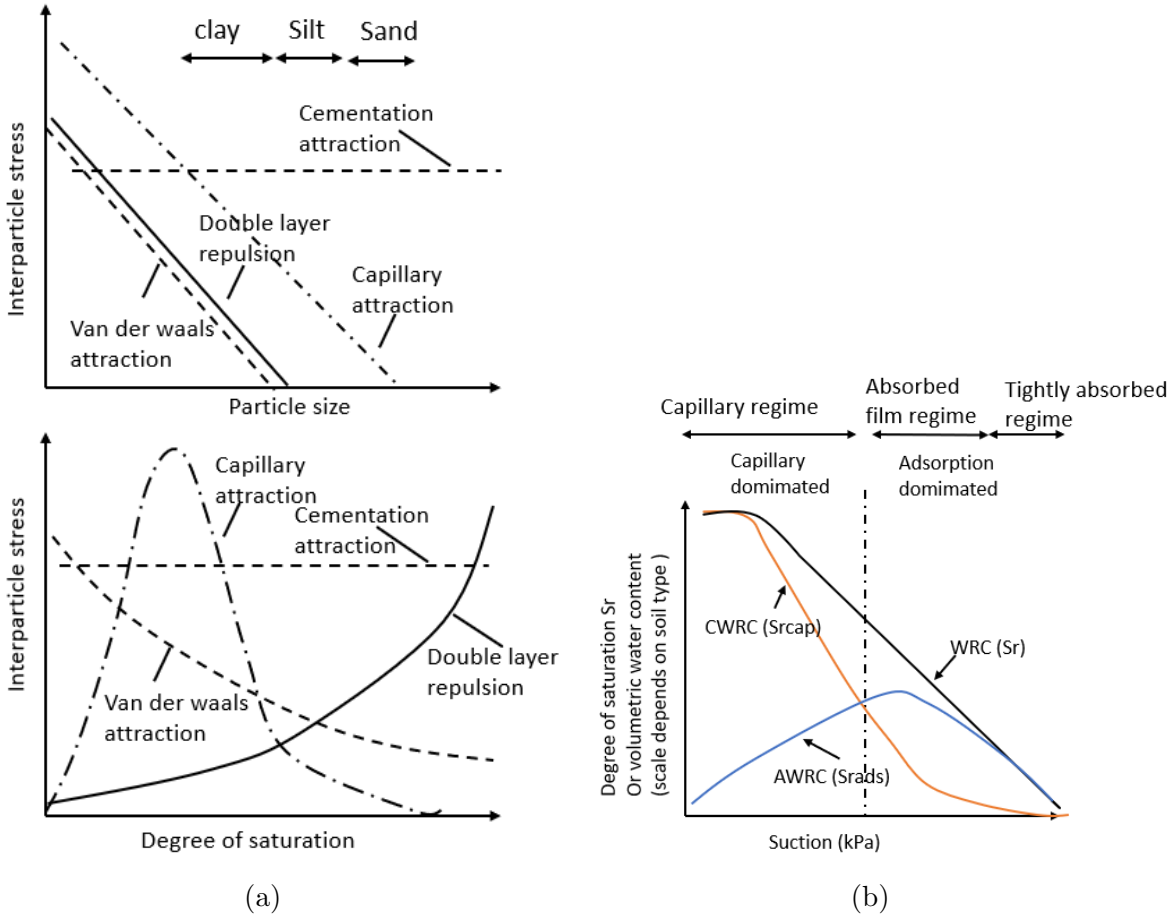

Figure 2.8: (a) Schematic diagram for the relation between interparticle stress and degree of saturation considering both capillarity and adsorption. (b) Schematic physical characteristic of SWCC (Lu, 2004).

According to the characteristics and determining role of matric suction and osmotic suction, the SWCC can be divided into three parts: the tightly adsorptive regime, the adsorptive film regime, and the capillary regime (Fig. 2.8(a) lower part). In the tightly adsorptive regime, only a small amount of free water exists, and most of the water is adsorbed in the interlamellar space. Clay minerals can intensively adsorb water on the surface of solid particles, resulting in high intermolecular forces between water and the soil particles (Fig. 2.8(a) upper part).

2.3.3 Hysteresis phenomenon in water retention behaviour

Hysteresis is a commonly observed phenomenon in SWCC of soils, which means there is no unique relationship between the degree of saturation and suction. As also visible in Fig.

2.7 more water is retained during drying than is adsorbed by the system during wetting. The degree of saturation may also vary with applied stress and depend on historic suction values. Due to the large number of experimental evidence showing a hysteretic water retention curve on the main drying and wetting curves, there is widespread agreement in the literature regarding the relevance and phenomenological background of hysteresis in the soil-water characteristic curve. The phenomenon of hysteresis was first detected and reported by Haines (1930), and it has been confirmed through both experimental and theoretical experiences since then (Topp, 1969; Poulovassilis, 1970; Pavlakis and Barden, 1972; Mualem, 1984; Nimmo, 1992; Iwata, 1995; Pham et al., 2003).

As can be seen in Fig. 2.7, in the conceptual model of a hysteretic SWCC, under free volume conditions, there are typically three types of curves: (i) initial drying boundary curves, (ii) main drying or wetting curves after different numbers of cycles, and (iii) countless scanning curves. The main drying curve and main wetting curve form the main loop, resulting in numerous cycles. The scanning curves are located within the main SWCC loop. The initial drying curve is unique for a given soil and is irreversible (Al-Mukhtar et al., 1999; Marcial et al., 2002; Fleureau et al., 2002). For fine-grained soils, the relationship between the degree of saturation and suction of the initial drying curve of the soil starts from the saturated slurry state at a water content higher than its liquid limit. Cui et al. (2002) conducted tests on FoCa7 clay specimens to study their drying and wetting behavior. A distinct almost horizontal residual branch was not found in this study.

Due to the presence of entrapped air, the minimum suction required for air bubbles to enter the maximum pore on the drying path is larger than the maximum suction of water into the maximum pore, which is the water entry value along the wetting path. To model the hysteresis SWCC, a new parameter, the water entry value, is introduced to differentiate the wetting and drying curves for different hydraulic loading paths. Existing hysteresis models require only the boundary curves, and the scanning curve can be predicted from the boundary curves. Several model concepts and formulations have been developed to approximate the hysteresis loop in SWCC.

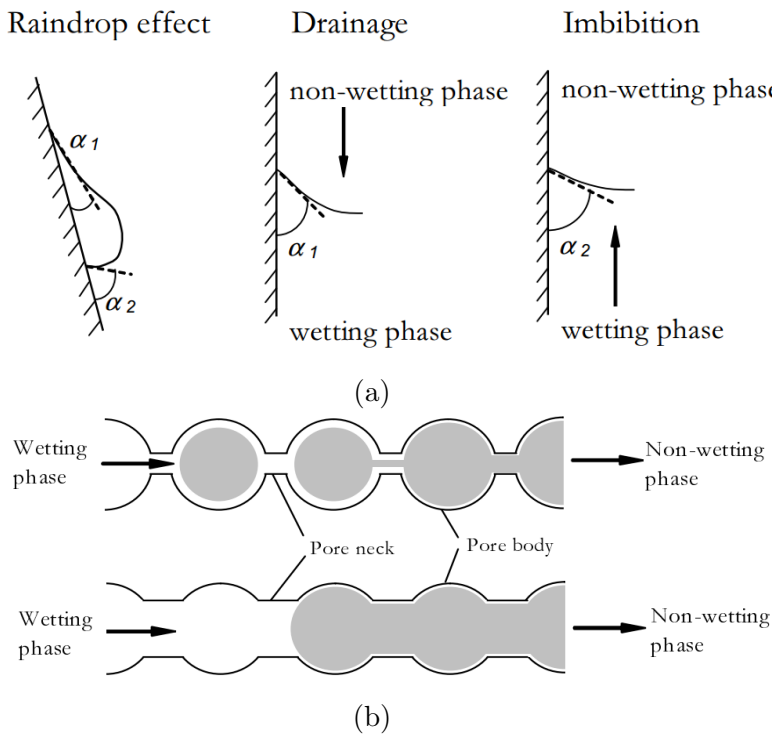

Figure 2.9: (a) Raindrop effect visualized by a drop running down a homogeneous surface and in tubes during drainage and imbibition process (Bear and Braester, 1972), and (b) Influence of the pore geometry on the inclusion of a fluid caused by snap-off effect (Chatzis and Dullien, 1983).

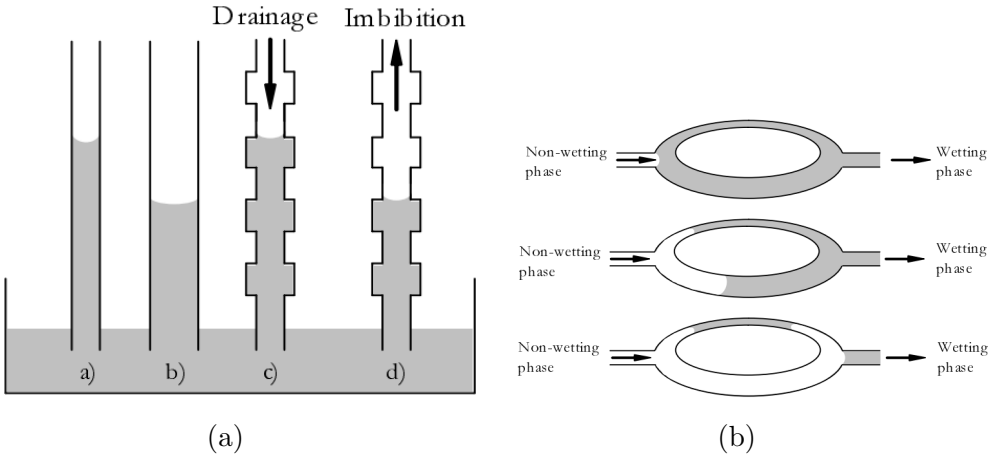

Figure 2.10: (a) Capillary rise depending on the tube diameter and drainage process and imbibition in variable diameter tubes (Haines, 1930, Miller et al., 1988). (b) Influence of the pore geometry on the fluid placement caused by by-passing effect (Chatzis and Dullien, 1983)

The hysteresis phenomenon in soil water retention curves is caused by several factors, including the rain drop effect (Bear and Braester, 1972), ink-bottle effect (Haines, 1930; Miller et al., 1988), snap-off effect, and by-passing effect (Chatzis and Dullien, 1983), as shown in Figs. 2.9 and 2.10. During the initial drying process, occluded air bubbles, redistribution of the pore system, or closed pores prevent water from filling all pores at the end of the main wetting path. This results in a difference in the maximum degree of saturation between the drying and wetting paths. Several factors, including bulk density, particle size distribution, pore size distribution, vertical loading, temperature, mineralogic composition, initial pore structure, and hydraulic loading path, affect the cyclic hysteresis of wetting and drying curves. The hysteresis phenomenon of loess has been experimentally studied by various researchers (Muñoz-Castelblanco et al., 2013; Ng et al., 2016). The water content at a given suction can differ under different hydraulic loading paths and suction history, which can also cause differences in the mechanical properties of soils (Lins, 2010). Studies of the soil water retention curve can be useful to predict other unsaturated soil properties, including unsaturated shear strength, deformation behavior, and seepage.

2.3.4 Factors influencing SWCC

The relationship between suction and water content is influenced by various internal and external factors. Internal factors encompass particle gradation, pore size and pore size distribution, density, and the type and mineralogy of soil solids (Richards and Weaver, 1944, Croney and Coleman, 1954, Salter and Williams, 1965, Reeve et al., 1973). The pore-size distribution is the primary factor affecting the shape and slope of the SWCC. In a poorly graded soil, the slope of the SWCC is steep since water can be discharged within a narrow range of soil suction. In contrast, a well-graded soil has a relatively flat SWCC slope due to evenly distributed pores at different scales.

External factors include stress state and ambient temperature. Additionally, several other factors have been taken into account to create water retention curve models, such as deformation during wetting and drying, density, confining pressure, and a bi-modal pore size distribution. The void ratio has an impact on pore structure and size distribution. Nuth and Laloui (2008) postulated an intrinsic SWCC for a nondeforming soil, which can shift along the logarithmic suction axis when soil deformation occurs. Numerous studies have been conducted on the factors that influence the SWCC of loess, such as Liang et al. (2018), Jiang et al. (2017), Huang et al. (2010) and Luo et al. (2014).

The soil-water characteristic curve (SWCC) for sand is characterized by a limited residual zone due to the small surface area and surface charge density of sand particles. In contrast, silt has a larger range of soil suctions and can absorb more pore water due to its smaller pore size range, significant surface area, and surface charge density. The air-entry pressure and water-entry pressure are primarily controlled by the fraction of the larger pores, while the small pores have a minimal effect on the air entry value. The total specific surface area of the soil gradually increases from sand to clay, with clay having the highest surface area and surface charge density, resulting in the highest water absorption capacity. The SWCC of clay covers a wide range of suctions, with a gradual decrease in total pore volume, increasing air entry value, and stronger water retention capacity.

The behavior of expansive soils is strongly affected by various factors, including osmotic suction, temperature, clay content, salt solution ions, and more. In materials that contain a high percentage of water-sensitive minerals, factors related to osmotic suction, such as temperature and salt solution, significantly impact the soil water retention curve. Conversely, less cohesive materials like loess are less affected by salt solutions, and their SWCC is primarily determined by the pore size distribution resulting from the breakage of cementation bonding, rather than the electric double-layer effect.

Noncohesive materials are typically treated as non-deformable. In collapsible soils, such as loess, the void ratio changes during wetting and drying, which need to be taken into account for an accurate determination of SWCC in terms of the degree of saturation or volumetric water content. Depending on the deformation, the change in air entry value can be determined inversely. Thus, an SWCC model not considering deformation-related parameters cannot reflect the non-uniqueness of the degree of saturation for a given suction value. To account for the influence of boundary conditions, confining stress, and void ratio on the SWCC, several methods have been proposed. One method involves implementing the relationship between the air-entry value parameter and the void ratio (e) (Gallipoli et al., 2003), as shown in Equ. 2.4. Another approach involves introducing the concept of elasto-plastic deformation into the simulation of the soil water characteristic curve, with the degree of saturation (S_e) viewed as the result of two variables: deformation and suction (Nuth and Laloui, 2008).

$$S_e = \left(1 + \left(\frac{e^{\phi} * \psi}{w}\right)^{n}\right)^{-m} \tag{2.4}$$

e is void ratio, ψ is suction, w, ϕ, n and m are model parameters.

2.3.5 Experimental methods to determine SWCC

In order to obtain a soil water characteristic curve, there are two main approaches. The first involves using instruments that can control suction, and the water content is measured when the suction is in equilibrium. The sensor must be in good contact with the soil during measurement, and isothermal balances between the sensor's internal temperature, the environment, and the soil temperature are necessary. The second approach involves measuring suction during the dynamic change process of the water content. However, if the hydraulic characteristics of the material are related to the equilibrium duration, and the SWCC is affected by the rate of suction change, the SWCC obtained by these two methods may differ. Furthermore, different methods have their own limitations and suction measurement range, as shown in Fig. 2.11. In order to obtain the SWCC over the full range of suction, multiple measurement methods may need to be used in the experiment.

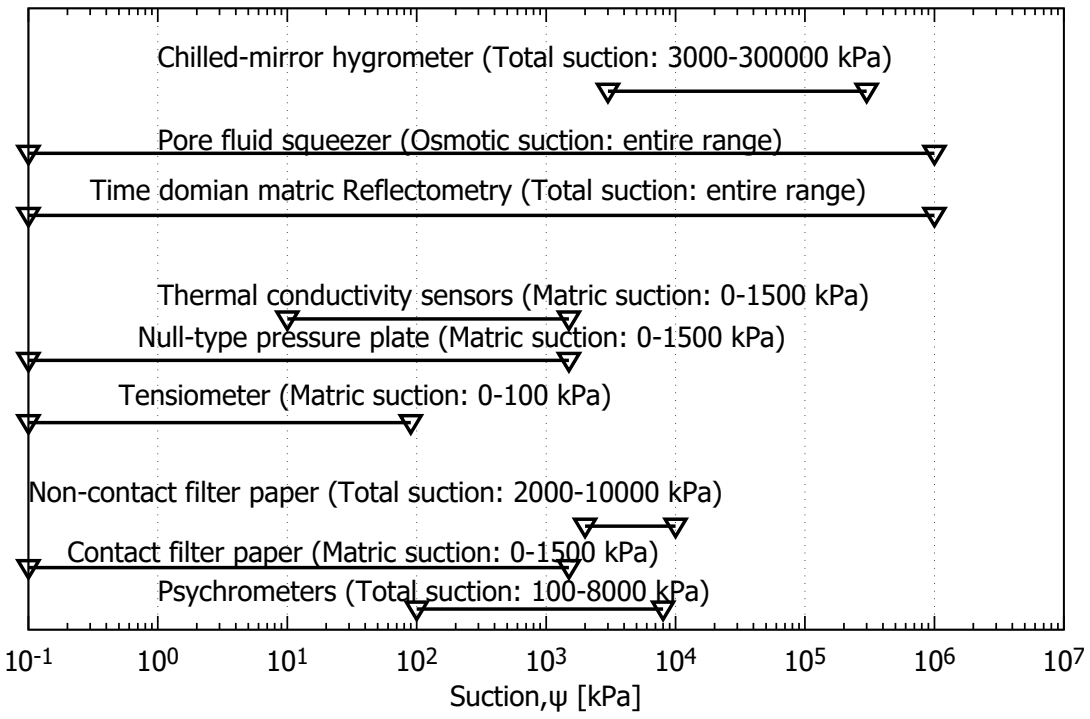

Figure 2.11: Soil suction measurement techniques and measuring range.

2.3.6 Unsaturated permeability

The permeability of unsaturated soils depends on the pore structure (void ratio and porosity), the pore fluid properties (density and viscosity), and the relative amount of water in the system (water content and degree of saturation). The gradient in total potential of soil pore water, commonly expressed as total suction or total head, is the driving mechanism for seepage in unsaturated soil, thus, the flow of liquid water. Neglecting transport of water through vapour, the flow of water may only occur through the continuous liquid water phase in the soil pores. Therefore, the water flow and resulting coefficient of permeability strongly depend on the degree of saturation and the corresponding soil structure. The unsaturated permeability function relates to the saturated coefficient of permeability k in forms of the relative amount of pore water head $k(h)$, suction, and degree of saturation $k(S_r)$. The unsaturated permeability function can be assumed to have the same shape of the soil-water characteristic curve as $\theta(\psi)$ or $S_r(\psi)$.

The unsaturated permeability coefficient can be indirectly obtained by analyzing the soil-water characteristic curve (SWCC). Capillary theory is used to establish the relationship between the unsaturated coefficient of permeability and the SWCC. The unsaturated coefficient of permeability ($k(\psi)$) is usually normalized by dividing it with the saturated coefficient of permeability k_{sat}. The relative permeability is then denoted as $k_r = \frac{k(\psi)}{k_{sat}}$ and may have values between zero and one.

There are three main approaches to model the relationship between saturation and permeability: (i) empirical models, which utilize experimental data of unsaturated infiltration to fit a corresponding formula, such as those developed by Richards (1931), Gardner (1958), and Brooks and Corey (1964*b*); (ii) macro models; and (iii) statistical models.

Macro models assume that the flow of water is laminar on microstructural level and obeys Darcy's law at macroscopic level. By considering pore connectivity and using pore distribution equations, the pore channel model is established using probabilistic methods. The soil-water characteristic curve is used as an indirect indicator to reflect the pore channels, as demonstrated by the works of Childs and Collis-George (1950), Burdine (1953), and Mualem (1976).

2.3.7 Effective stress and stress state variables in unsaturated soil framework

Constitutive relations integrate material features and state variables. State variables are unaffected by the characteristics of the material. For both saturated and unsaturated soils, effective stress is defined as the stress that physically describes the stress acting on the soil skeleton. In saturated soil, the effective stress (σ') is well defined as the difference between total stress σ and the pore-water pressure u_w (see Equ. 2.5) known as Terzaghi's equation.

$$\sigma' = \sigma - u_w \tag{2.5}$$

Terzaghi's definition of effective stress is congruent with the concepts of multiphase continuum mechanics (Fredlund and Rahardjo, 1993). In unsaturated soil, the air pressure u_a and the matric suction as difference between air and water pressure $(u_a - u_w)$ must be taken into account as acting on the soil skeleton. Bishop (1955) extended Terzaghi's effective stress as shown by Equ. 2.6:

$$\sigma' = (\sigma - u_a) + \chi(u_a - u_w) \tag{2.6}$$

In Equ. 2.6, also known as Bishop's equation, the effective stress is expressed in terms of a single stress state variable, and is formulated as the sum of the net stress $(\sigma - u_a)$ and the product of suction $(u_a - u_w)$ with the effective stress parameter χ. When using a single-variable approach in a constitutive model, the effective stress parameter (χ) is required to be properly defined. Firstly, the effective stress parameter was assumed to be equal to the degree of saturation S_r (see Equ. 2.6, with $\chi = S_r$). χ was used to describe the stress state of an unsaturated soil by involving the soil property (S_r), so violating the basic distinction between state variables and constitutive relations. When attempting to account for phenomena like nonlinearity and hysteresis, including soil characteristics in the description of stress state imposes considerable inflexibility (Jennings and Burland, 1962). Subsequent experiments have revealed that there is no unique relationship between the two variables (χ and S_r). Later, more sophisticated approaches for determining χ were introduced (Khalili et al., 2004). Khalili et al. (2008) introduced a novel correlation between the effective stress parameter and the ratio of matric suction to air entry value (ψ_{aev}), as shown in Equ. 2.7.

$$\chi = \begin{cases} 1 & \psi < \psi_{aev} \\ \left(\frac{\psi}{\psi_{aev}}\right)^{\gamma} & \psi \geq \psi_{aev} \end{cases} \tag{2.7}$$

A best-fit value of the exponent is $\gamma = -0.55$. This exponent is a material-independent constant, which was suggested to represent the behavior of different soil types. The correct determination of the parameter χ is still a matter of research.

Coleman (1962) and Fredlund and Morgenstern (1977) suggested the use of independent stress state variables, namely the net normal stress $(\sigma - u_a)$ and matric suction $(u_a - u_w)$, to describe stress-strain relationships. By employment of two variables the distinction between state variables and constitutive behavior can be kept (Sheng et al., 2008). Using two variables requires distinguishing two types of deformation, namely suction induced and net stress induced deformation. The variation in soil deformation brought on by changing net stress and matric suction, which is exclusively correlated with the degree of saturation. It is important to note that the scales of the two variables are different; net stress is a macroscale variable, while matric suction is a microscale variable (see Fig. 2.12).

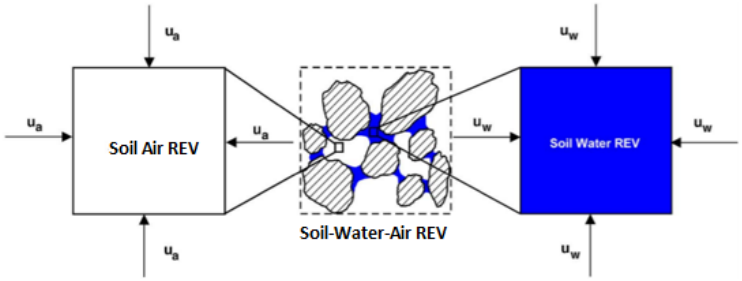

Figure 2.12: Illustration of scale definition difference among air-water-solid REV, soil water REV, and soil air REV (Lu, 2008).

The next approach in defining an effective stress in unsaturated soil mechanics is through introducing a new variable named suction stress (Lu et al., 2008; Lu, 2004), which is effective in describing the shear behavior of unsaturated soils over the full range of degrees of saturation. The suction stress is a part of the effective stress in unsaturated soils, and it represents the tensile strength of the soil resulting from the Van der Waal's attractive force, double-layer repulsive force, surface tension, and solid-liquid interface forces due to pore water pressure that contribute to the interaction energy at the soil particle surface (see Fig. 2.8). The effective stress defined using the suction stress is given

by Equ. 2.8.

$$\sigma' = (\sigma - u_a) - \sigma_S \tag{2.8}$$

The suction stress of soils can be measured in the laboratory either through tensile strength tests or by deducing it from shear strength tests. Additionally, it can be calculated from theoretical considerations using the suction stress characteristic curve (SSCC). The SSCC describes the relationship between suction stress and water content, degree of saturation, or suction, and can be established from the soil water characteristic curve (SWCC) (Lu et al., 2010). For example, in sandy soils, suction stress is zero at the saturated condition, and under a certain value of matric suction, suction stress reaches its maximum magnitude, resulting in an increase of effective stress.

The magnitude of suction stress in unsaturated soil is equivalent to the magnitude of the effective stress under the condition of no external stress, as they both result from the interparticle forces. However, the difference between suction stress and Terzaghi's skeleton stress is that the forces contributing to suction stress are self-balanced at the inter-particle level and do not arise from the total stress that passes from one particle to another, as is the case for the Terzaghi's skeleton stress.

2.3.8 Wetting-induced collapse deformations in unsaturated soil

Wetting-induced deformation, also named collapse, is a common occurrence in compacted soils (Lawton et al., 1992) or natural soil deposits of various types. The two primary requirements for collapse to be possible are a loose soil structure (large void ratio) and a water content below the saturated state. At dry state, the grains or aggregates are kept in place by a material or a force which evades at inundation and subsequent water infiltration. Numerous researchers have reported that soil compacted at the dry side of optimum water content typically exhibits collapse behavior upon wetting, while soil compacted at the wet side of optimum water content condition does not (Barden et al., 1973; Lawton et al., 1989, Lawton et al., 1992; Tadepalli and Fredlund, 1991; Vanapalli et al., 1996). When the initial water content of remolded compacted soil is higher than the optimum moisture content, the soil has a more dispersed fabric than a soil compacted at dry side with a flocculated aggregated fabric. The collapse deformation of compacted soil is mainly determined by the large pore structure between the agglomerates.

The collapsible of loess is a sudden, large, and irreversible process characterized by non-continuous deformation. Cui et al. (2005) concluded that the collapsibility of loess soil in northern France is significantly sensitive to changes in water content. The meta-stable structure of loess leads to a large abrupt collapse deformation that is irreversible under cyclic wetting and drying. The deformation characteristics of loess are similar to those of silty soil and low plastic clay.

The collapse potential is typically determined for a specific vertical load. Two test methods are commonly used to quantify the collapse potential: the single oedometer test and the double oedometer test (see Fig. 2.13b). In single-oedometer tests (Fig. 2.13a), a sample with specific initial void ratio and water content is loaded to a defined vertical stress and then subjected to liquid water. The resulting change in sample height is measured. Subsequently, the saturated sample is further loaded to maximum target vertical stress followed by unloading. Multiple single-oedometer tests for a given initial condition are needed in order to capture the effect of applied vertical stress at the moment of inundation. Fig. 2.13(b) illustrates typical double oedometer experimental results for collapse behaviour. The collapse potential is defined as the difference in void ratio between the compression curves of an unsaturated sample and a saturated sample. Al-Obaidi (2015), amongst others has conducted suction-controlled oedometer tests to investigate collapsible materials. Within the framework of unsaturated soil mechanics, the collapse settlement is caused by the decrease in suction. The collapse curve can be divided into three parts based on the inclination of the curve between deformation and suction, as shown in Fig. 2.14. For a soil with initial water content close to residual water content, the evolution of volume change (see curve collapse behaviour in Fig. 2.14) can be related to the respective residual, transition and saturated zone of the wetting SWCC-curve. Only a small part of deformations occurs in the pre-collapse phase. Once the saturated zone is reached, no further deformations occur in the post-collapse phase.

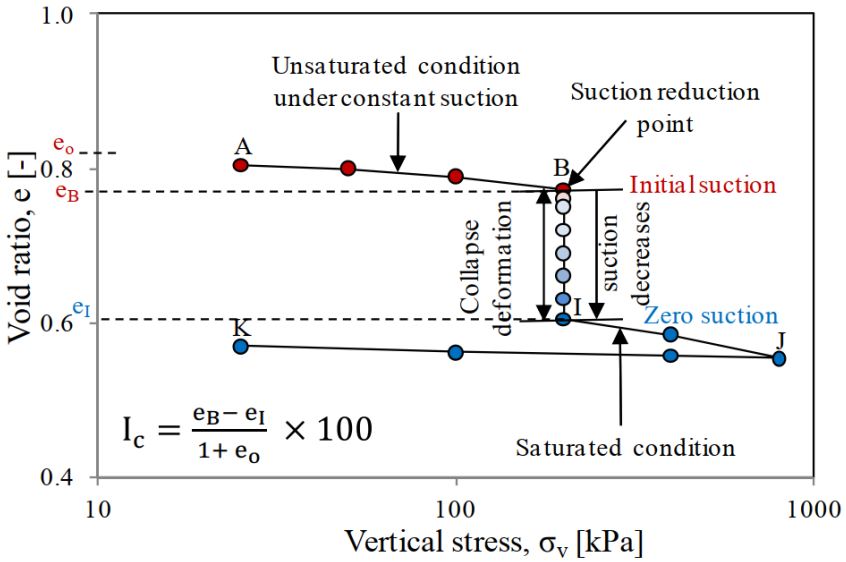

(a)

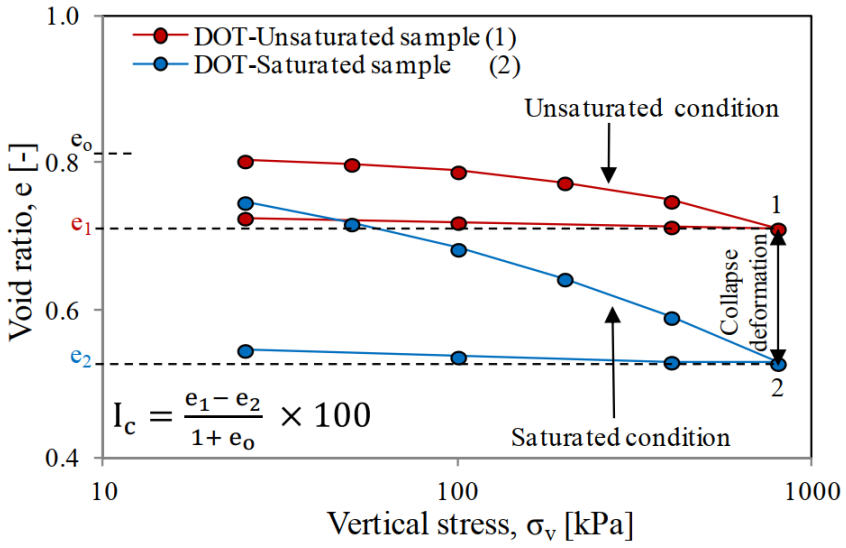

(b)

Figure 2.13: (a) Collapse deformation defined in single oedometer test. (b) Collapse deformation defined in double oedometer test (Al-Obaidi, 2015).

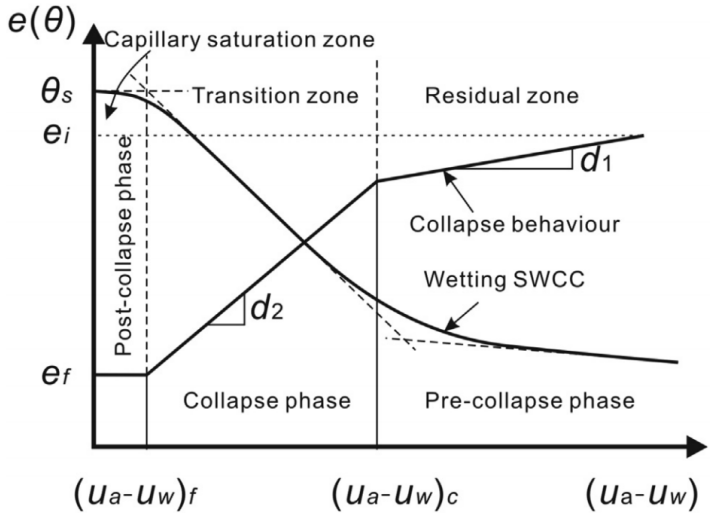

Figure 2.14: Collapse deformation due to wetting at a given net mean stress (Vanapalli et al., 1996).

Previous studies have identified several controlling factors for collapse mechanisms. From a physical standpoint, these factors include clay content, salt content, and pore structure. From a mechanical standpoint, controlling factors include matric suction, applied stress, and stress path. For compacted samples, the initial structure is related to the compaction energy, but the structure is a dynamically changing system that is further related to the SWCC. The applied loading during testing simulates the stress state of the soil in the field. Additionally, the collapse deformation of remolded soil is determined by the dry density and initial water content.

In order to predict the deformation of the collapsible soil, different empirical models were used. Fredlund and Gan (1995) gave formulations of collapse deformation based on suction and vertical loading. Rodrigues and Vilar (2006) and El-Ehwany and Houston (1990) proposed a model that used the final collapse void ratio as the reference value. Depending on the relationship between the wetting-induced deformation curve and the soil water characteristic curve, Xie and Li (2018) used the soil water characteristic curve to indirectly calculate the collapse deformation. The prediction of the void ratio is based on the assumption that the collapse strain has the same pattern as the soil water retention curve.

2.4 Constitutive modelling of unsaturated collapsible soil

2.4.1 Modelling of SWCC

To model the SWCC, three main approaches are used: empirical, statistical, and physical approach. Empirical methods involve proposing mathematical equations that have a similar shape to the SWCC curve and fitting the measured SWCC data to obtain the model parameters. These methods can be further divided into those that consider hysteresis and those that do not.

- Modelling without considering hysteresis

Equations with two or three parameters have been proposed by researchers such as Gardner (1958), Brooks and Corey (1964*b*), Campbell (1974), Van Genuchten (1980) and Fredlund and Xing (1994).

The parameters of the empirical equations are typically associated with the air-entry value and the investigated soil's rate of desaturation. The Brooks and Corey exponential model (Brooks and Corey, 1964*b*) relies on the pore size distribution's main characteristic. A smooth and closed model was proposed by Van Genuchten (1980). However, the van Genuchten model, see Equ. 2.9 is meant to fit experimental data to the residual saturation phase.

$$S_e = \frac{S_w - S_{res}}{S_{sat} - S_{res}} = \left(\frac{1}{1 + (a\psi)^n} \right)^m \tag{2.9}$$

where S_{res} is the residual degree of saturation, n and m are fitting parameters related to the pore size distribution. The fitting parameter a is related to the air entry value. The air entry value characterizes the corresponding suction value when the air begins to enter the maximum pore in the soil. ψ is the suction value, S_e is the effective degree of saturation, and S_{sat} is the saturated degree of saturation. Most often the model is used in its two-parameter form assuming $m = 1 - 1/n$.

The Fredlund and Xing models (Fredlund and Xing, 1994, see Equ. 2.10) artificially specify the maximum and minimum suction ranges for expressing the relationship between suction and degree of saturation.

$$\theta = C\left(\psi\right) \frac{\theta_s}{\left\{\ln\left[\mathrm{e} + \left(\frac{\psi}{\mathrm{a}}\right)^{\mathrm{n}}\right]\right\}^m} \tag{2.10}$$

a is the curve-fitting parameter related to the air-entry value, while n as well as m are curve-fitting parameters related to the shape of the curve. ψ is the suction, ψ_r is the residual suction, and ln is the natural logarithm. $C(\psi)$ is a correction function, which gives the suction equal to 10^6 kPa when the water content is zero. $C(\psi)$ is defined as:

$$C(\psi) = -\frac{\ln(1 + \frac{\psi}{\psi_\mathrm{r}})}{\ln[1 + (\frac{10^6}{\psi_\mathrm{r}})]} + 1 \tag{2.11}$$

The model proposed by Brooks and Corey (1964*b*) considers the branch of the SWCC for suction values larger than the air entry value as a line $S = 1$ (see Equ. 2.12).

$$\theta = \left(\frac{1}{1 + a\psi}\right)^{\lambda} \tag{2.12}$$

The equations proposed by Gardner (1958), Van Genuchten (1980), Fredlund and Xing (1994) employ sigmoidal functions.

The physical approach to determine the dependence of the degree of saturation on suction employs the pore size distribution and particle gradation characteristics of the soil. The soil can be categorized into independent and non-independent domains based on its spatial distribution. Poulovassilis and Childs (1971) used non-independent domain and Main hysteresis loop family of scanning curves. The soil air injection curve (SAIC) concept utilizes the mercury intrusion method to measure two sets of ratios (Prapaharan et al., 1985): the non-wetting ratio, which is the difference between the injected non-wetting fluid and solid volumes, and the water ratio, which is the difference between the water and solid volumes.

- Modelling of SWCC considering hysteresis

Some researchers, such as Hanks et al. (1969), Dane and Wierenga (1975), Jaynes (1984), and Pham et al. (2003), have presented empirical equations that consider the hysteresis in the soil-water characteristic curve. Two categories of models are commonly used to predict hysteretic SWCC: physically based models and empirical models (Pham et al., 2005). Physical models based on domain theory have been introduced by researchers such as Topp (1971), Mualem (1974), Beliaev and Hassanizadeh (2001), Mualem and Beriozkin (2009), and Maqsoud et al. (2012). In contrast, empirical models were developed by researchers such as Kool and Parker (1987), Feng and Fredlund (1999), Kawai et al.

(2000), Li (2005), Stoimenova et al. (2006), and Canone et al. (2008). Empirical models employ regression analysis to fit the experimental data, and two sets of parameters are used to simulate and distinguish the two main curves.

In order to obtain an SWCC model that can reflect the hysteresis effect, mathematical methods such as the mathematical scale method and the regional method can be applied. In the scale method, as used by Zhou et al. (2012), one main curve is used to predict another one and the scanning curves, requiring only one set of parameters. Additionally, independent domain theories for modelling hysteresis as a physical phenomenon in soil science have been presented by Everett and Whitton (1952) and Everett and Smith (1954). Empirical hysteresis concepts have also been developed to account for non-wetting phase trapping resulting from drainage and imbibition cycles and have been verified with SWCC data measured in the laboratory (Parker et al., 1987; Meyer et al., 1990; Gerhard and Kueper, 2003). Mathematical methods are used to generate countless scanning curves to simulate the random hydraulic loading paths.

2.4.2 Elasto-plastic modelling of unsaturated soil

The coupled hydro-mechanical process of collapse deformation in unsaturated soil mechanics involves a reciprocal relationship between mechanical loading affecting soil water retention behavior, and hydraulic loading influencing pre-consolidation stress (Khoshghalb and Khalili, 2013). Various researchers have proposed the use of the elasto-plastic framework to describe the collapse phenomenon for any soil showing collapse, including undisturbed unsaturated soils (Alonso et al., 1990 and Chiu and Ng, 2003). The constitutive model for unsaturated soil must take into account the impact of suction on the elasto-plastic mechanical parameters.

One such model is the Barcelona Basic Model (BBM) (Alonso et al., 1990), which is based on the Modified Cam Clay (MCC) model (see Fig. 2.15) and is often used for unsaturated soil. The BBM incorporates the net stress and matric suction to capture the influence of suction on the yield surface by introducing the suction increase (SI) yield surface and the loading collapse (LC) surface (see Fig. 2.16). It accounts for the effects of suction on the compressibility, pre-consolidation pressure, and yield surface.

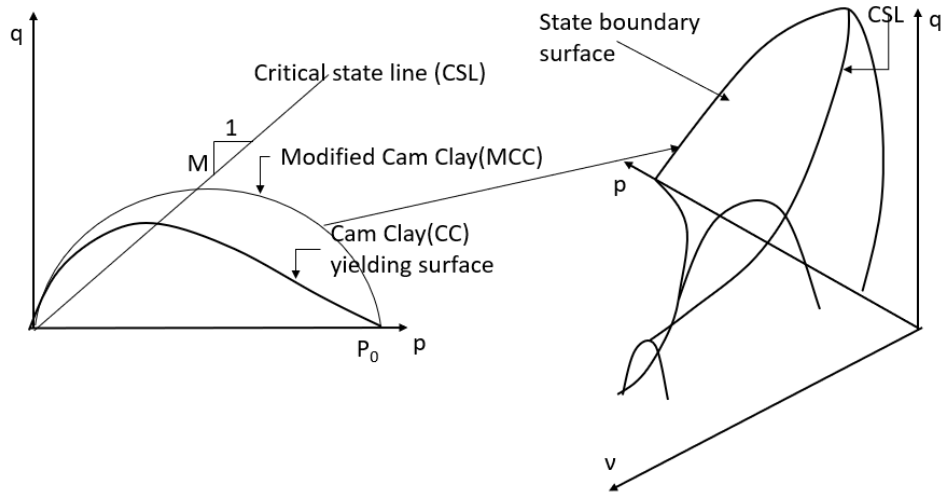

Figure 2.15: Yield function of Cam Clay model and Modified Cam Clay model.

To establish the unsaturated yield surface, the yield stress under different matric suctions must be determined. Yield points are obtained in the $p-s$ quadrant (see Fig. 2.16), and the resulting yield line is fitted with a mathematical formula. The model reflects the conditions where an increase in net stress or a decrease in suction exceeds the LC-yield stress, leading to plastic deformation and expansion of the LC-yield surface. Corresponding, an increase in suction to a value greater than the maximum past suction results in irreversible deformations and an upwards shift of the SI-yield line. The region enclosed by the LC- and SI-yield lines and the two axes is the elastic zone. The elastic parameters are assumed to be not affected by a suction change. Collapsibility decreases with increasing initial water content due to the expansion of the plastic range with decreasing suction. Wetting induced deformation is dependent on the initial state, dry density and water content of the sample, the stress path, and the LC curve. If the stress path remains within the elastic region, no significant deformation occurs. Das and Thyagaraj (2018) studied the influence of initial moisture content, dry density, initial consolidation pressure, and compaction pressure during sample preparation on the loading collapse line. Experimental results were used to analyze the tendency of the collapse potential governed by the overlying stress.

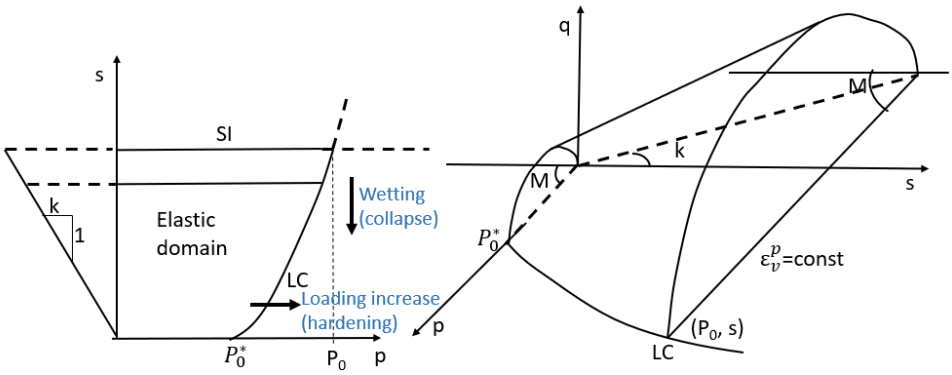

Figure 2.16: Yield surface in suction-net stress plane (left), and in three-dimensional (p-q-s) space (Alonso et al., 1990).

Some aspects of soil behaviours that are not considered in BBM are the irreversible results of expansion in swelling clays, the decrease in collapse potential when the confining stress becomes larger than a threshold value and the non-linear shape of the strength envelope (Alonso et al., 1990; Wheeler and Sivakumar, 1995). To address this, Sun and colleagues conducted wetting tests on compacted kaolin clay with varying initial densities (Sun, Sheng and Xu, 2007; Sun et al., 2008; Sun, Sheng and Sloan, 2007). They found that wetting-induced collapse deformations primarily depend on the initial void ratio and net mean stress under which the soil is wetted, regardless of the initial matric suction. Sun et al. (2006) also found that volume decrease due to wetting is more sensitive to changes in degree of saturation than suction. These findings suggest that wetting-induced collapse behavior can be predicted by means of the degree of saturation, which is independent of initial matric suction. However, the measurement or control of the degree of saturation during suction controlled compression tests is still a topic of debate.

Khalili and Khabbaz (1998) proposed an explanation for the observed collapse deformation based on effective stress as the single variable. They argued that matric suction affects both the pre-consolidation pressure and effective stress in collapsible soil. During wetting, the pre-consolidation pressure decreases more than the effective stress, leading to plastic deformation. A mathematical relationship between effective stress parameters and suction ratio can be obtained through curve fitting, but no clear physical explanation is provided for this effective stress parameter.

2.4.3 Aspects of suction history and hysteresis

The role of suction history in volume and water content changes has been widely investigated in the literature (Fleureau et al., 1993; Gens et al., 1995; Romero et al., 1999). It has been observed that the deformation of the soil is influenced by the saturation path, as the deformation under a mechanical loading-unloading test after an applied drying path is different from the deformation after an applied wetting path at the same net stress. Several researchers have investigated the effect of the hydro-mechanical stress path on stiffness, shear strength, deformation, dilatancy, and soil water retention behaviour. In particular, the yield point during isotropic loading at a given value of suction was found to be reduced by a preceding cycle of wetting and drying, as consistently observed by Sharma (1998).

Furthermore, the relationship between suction and degree of saturation is influenced by the past loading-unloading paths due to the hysteresis phenomenon. Experimental studies have found that different degrees of saturation can result in different absorption stresses under the same matric suction (Likos and Lu, 2004), which can further affect the effective stress parameters (Khalili and Zargarbashi, 2010), small deformation shear modulus (Khosravi et al., 2016), compression modulus (Ng et al., 2009), and other deformation (Guan et al., 2009) and strength properties. Due to hysteresis, the shear strength obtained in the drying path is greater than the shear strength obtained under the wetting path. Wetting softens the stress-strain behavior of the sample and reduces its strength, and it can also produce plastic deformation during the wetting procedure.

The hysteresis behaviour can be modeled in various ways. One way is to use a hysterestic model for the soil water retention curve. For example, Gallipoli et al. (2003) proposed a modified expression for the water retention curve that considers the impact of volumetric strains on the SWCC. Romero and Vaunat (2000) investigated the effects of volumetric strains and hydraulic hysteresis on the variation of the degree of saturation. Another approach is to introduce an additional parameter, such as volumetric water content or degree of saturation, as a new constitutive variable in the model to capture the hydraulic loading path. Wheeler et al. (2003) introduced the concept of bulk water and meniscus water to represent the two parts of water in the soil, instead of using water content as a single variable. The constitutive model proposed by Vaunat et al. (2000) addresses the irreversible behavior of unsaturated soils during wetting and drying, including hydraulic hysteresis. However, this model is not coupled with the load-collapse yield surface, which

limits its applicability. To address this limitation, Gallipoli et al. (2003) proposed a simplified approach in which the load-collapse yield surface is represented as a vertical straight line in the space of Bishop mean stress versus suction, and the suction-increase and suction-decrease yield surfaces resulting from hydraulic hysteresis are represented as horizontal straight lines in the same space. All three yield surfaces are fully coupled, meaning that movement in one will cause the other two to move. These models are presented in different stress spaces but can be seen as variants of the framework given by Alonso et al. (1990).

2.4.4 Shear strength of unsaturated soil

The shear strength of a soil being saturated or unsaturated can be defined as the maximum internal resistance per unit area the soil can sustain along the failure plane under external or internal stress loading (Lu, 2004). The Mohr-Coulomb failure criterion (see Eq. 2.14) relates the material variables ϕ' and c' (effective friction angle and effective cohesion) to the effective stress represented by the stress state variable $(\sigma - u_w)$ in case of saturated soils. Based on experimental evidence obtained by suction-controlled direct shear tests on unsaturated soils, Fredlund et al. (1978) introduced the additional variable ϕ^b to capture the increase in shear strength with increasing matric suction.

The shear strength (τ) of unsaturated soil can be discussed with respect to either the peak shear strength or the residual strength reached at large strains. The peak shear strength consists of three components: the effective cohesion (c'), the strength provided by the friction angle (ϕ'), and the strength provided by suction.

An extend Mohr-coulomb failure criterion was introduced by Fredlund et al. (1978), where the failure envelope is a plane surface in the space of the stress state variables and shear stress τ (see Fig. 2.17) is defined by Eq. 2.15. It is to be noted that the internal friction angle ϕ' is independent of matric suction, as shown by parallel failure lines for different suction shear stress vs. net stress plots. In case of triaxial tests it is also possible to formulate the extended M-C criterion in terms of principal stresses (see Eq. Fredlund and Rahardjo, 1993). There are limitations of the validity of Eq. 2.15 when considering the full range of suction from saturated to residual state. One main point is that the internal friction angle associated with matric suction ϕ^b is a highly non-liner function of matric suction (e.g. Vanapalli et al., 1996). For suction near zero, ϕ^b is equal or close to ϕ', but can have values of 0° or even negative values for suctions in the residual saturation state.

This conceptual relationship between the unsaturated shear strength envelope and the soil water characteristic curve was highlighted by Vanapalli et al. (1996). In this sense, they suggested an approach for the prediction of shear strength of an unsaturated soil using shear strength parameters of the saturated state and soil water characteristic curve, as shown in Eq. 2.13.

$$\tau = c' + (\sigma_n - u_a)\tan(\phi') + \left(\frac{\theta - \theta_r}{\theta_s - \theta_r}\right)(u_a - u_w)\tan(\phi') \tag{2.13}$$

In Eq. 2.13, θ_s is maximum volumetric water content, θ_r is the residual volumetric water content.

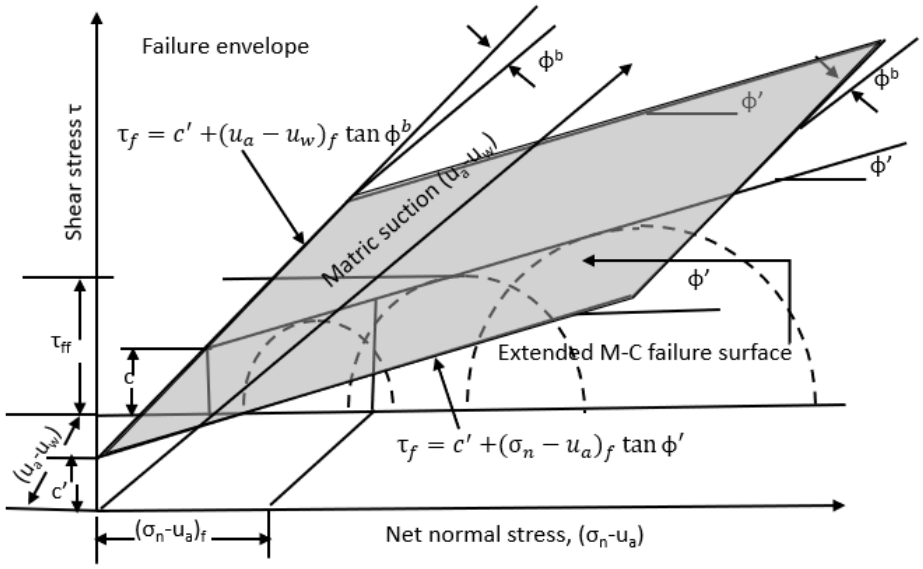

Figure 2.17: Extension of Mohr-Coulomb failure model for unsaturated soil (Fredlund and Rahardjo, 1993).

Another approach to describe unsaturated shear strength is the use of the effective stress approach (Bishop, 1955). It consists in substituting the effective stress σ' in the traditional Mohr-Coulomb failure criterion.

$$\tau_f = c' + \sigma' \cdot \tan(\phi') \tag{2.14}$$

With the Bishop effective stress definition

$$\sigma' = (\sigma - u_a) + \chi(u_a - u_w) \tag{2.15}$$

the effective stress parameter (χ) is equal to the effective volumetric water content, this yields in

$$\tau = c' + \left[(\sigma_n - u_a)_f + \chi_f (u_a - u_w)_f\right] \tan(\phi') \tag{2.16}$$

As presented in Section 2.3.7, the determination of effective stress parameters is difficult. However, several approaches have been suggested (see Section 2.3.7).

Besides peak shear strength, many scholars have studied the effects of suction on the critical state, residual strength, and dilatancy angle. Most scholars use mathematical methods to fit the curve between the matric suction and the respective investigated parameters and obtain certain empirical equations. However, empirical equations often have limited physical meaning, and it is therefore difficult to explain these relationships in terms of soil mechanics.

Undisturbed loess is known to have higher strength values than as-compacted loess samples under the same conditions. Various scholars have proposed a structure parameter to represent this strength difference between remolded and undisturbed samples. Studies are ongoing to investigate the effect of water content on this strength difference. It has been observed that the shear strength of loess increases with an increase in dry density and decreases with an increase in water content below the critical matric suction. The critical matric suction has a negative relationship with the vertical loading. Beyond the critical matric suction, the matric suction no longer has an influence on shear strength or even has a reverse influence. The difference in shear strength between remolded and undisturbed loess decreases with an increase in water content. The contribution of matric suction to the friction angle is relatively small compared to that of dry density or confining pressure. The most commonly used test methods for measuring shear strength in loess are direct shear and triaxial compression tests.

2.5 Numerical modelling

The literature review reveals that rainfall-triggered loess landslides are prevalent. To predict accurate material behavior, the finite element method can utilize complex constitutive models. This section presents an introduction to numerical simulation, specifically using the finite element method, in solving slope stability issues. The finite element method has gained popularity in slope analysis due to its ability to analyze deformation and stress

distribution without assuming the location of the potential sliding surface under varying boundary conditions.

The first part of this section introduces the constitutive model used in numerical simulation to study slope stability under rainfall. The second part discusses the impact of atmospheric conditions, particularly rainfall and evaporation, on slope stability. Finally, the third part describes the various methods used for slope stability analysis, including the conventional limit equilibrium method that acquires safety factors and slip surfaces, and the development and expansion of plastic zones.

2.5.1 Basic processes and material models in slope stability numerical simulations

The stability of slopes under rainfall has been analyzed using various techniques. The distribution and change of pore water pressure under rainfall conditions is a critical factor due to its influence on the unsaturated shear strength. The distribution of pore water pressure plays a crucial role in indicating the instability of the slope, which is influenced by both the hydraulic and mechanical properties of the materials. The infiltration of rainwater into the slope soil creates a seepage field, which constantly changes with the rainfall. The pore water pressure generated by the seepage field alters the stress field inside the soil, resulting in soil deformation. As effective stress decreases, soil porosity reduces, causing weaker seepage of rainwater in the pores, and ultimately affecting the seepage field. The seepage field and stress field constantly interact with each other by changing the permeability, with pore water pressure being the primary factor affecting the stress field.

The evolution of slope stability can be explained by analyzing the distributions of pore water pressure or degree of saturation. Many studies have compared the calculated results of hydraulic-only and coupled hydro-mechanical models. Numerical analysis used a coupled hydro-mechanical constitutive model to consider the influence of the hydraulic property of the material on the deformation was still rarely found in the literature.

The governing partial differential equation for water flow in unsaturated soil in three-dimensional space can be described based on Darcy's law and mass conservation (Fredlund and Rahardjo, 1993 and Richards, 1931.

Infiltration can occur from various sources, such as rainfall, irrigation, pipe leakage, or other sources, and typically begins at the surface. However, it is important to note that evaporation also plays a crucial role in the distribution of pore water pressure, as shown in Fig. 2.18. Neglecting the effect of evaporation on the pore water pressure can lead to an overestimation of slope safety. Studies on slope stability often consider evaporation as part of atmospheric boundary conditions.

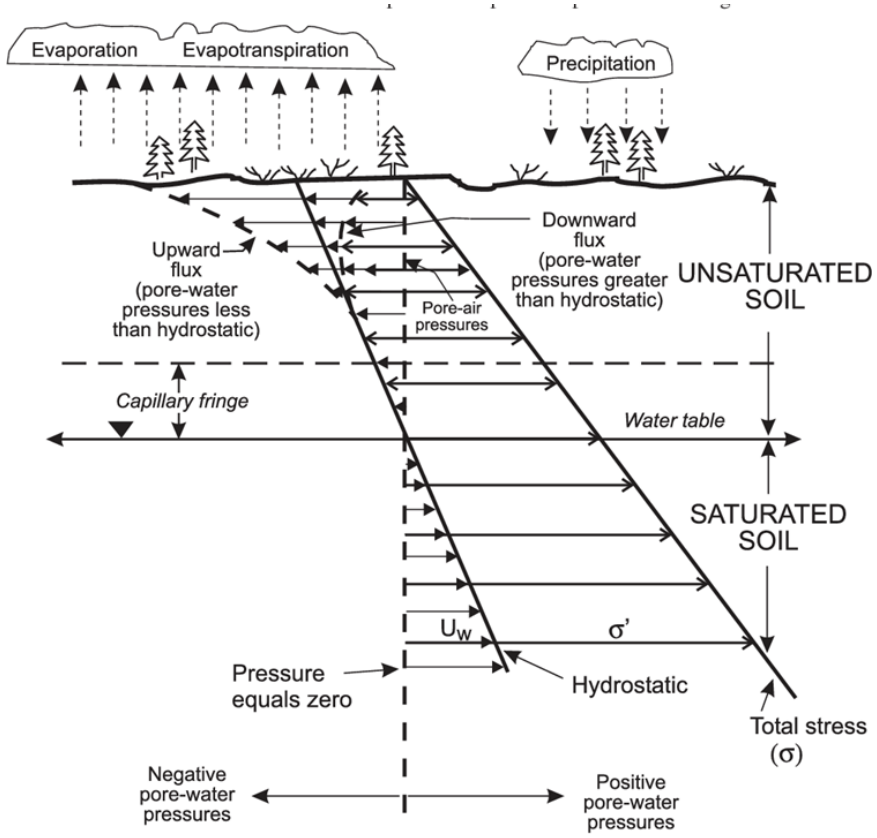

Figure 2.18: Distribution of pore water pressure vs. in a ground depth (Fredlund, 2000).

Hysteresis is important when wetting-drying circles are considered. Researchers have incorporated soil water characteristic curves (SWCC) with hysteresis characteristics into hydraulic models (Hu et al., 2018). In their numerical simulations, Chen et al. (2017) considered the hysteretic SWCC model to study the effect of rainfall on the slope. Using a hysteretic soil water characteristic curve in numerical simulations of a slope can lead to more reliable results. Neglecting the hysteresis effect of SWCC in soils can overestimate the safety of slopes (Ebel et al., 2010).

In the field of slope stability analysis, researchers have studied the effects of hystere-

sis on pore water pressure, deformation, and slope stability through a combination of experiments and numerical simulations. For example, Brideau et al. (2011) conducted experiments and numerical simulations to investigate these effects, while Zhang and Wang (2007) used the hysteretic SWCC in their study of the stability of heterogeneous slopes under cyclic evaporation and rainfall. These studies demonstrate the importance of considering SWCC hysteresis in slope stability analysis, and provide valuable insights into the behavior of slopes under various hydraulic and environmental conditions.

When simulating slope stability, it is generally acknowledged that coupled hydro-mechanical models are more accurate than hydraulic-only calculations. Over the years, researchers have developed a range of coupled hydro-mechanical models with increasing complexity to deal with problems related to flow in both saturated and unsaturated soil systems, and the mechanical interaction resulting from changes in soil suction (LLoret and Alonso, 1980; Olivella et al., 1996).

For instance, Xiong et al. (2014) used a finite element-finite difference scheme with three-phase coupling to simulate the stability of a slope under rainfall, and incorporated a hysteresis water retention model in the calculation. This allowed for more accurate simulation of the coupled hydro-mechanical behavior of the slope, taking into account the interactions between water flow and mechanical deformation. Such advanced models can provide valuable insights into the behavior of slopes under different conditions, and aid in the assessment of slope stability and the design of effective mitigation measures.

In their study, Cho and Lee (2001) investigated the process of rainfall-induced infiltration into a soil slope. They employed a two-dimensional finite-element model to analyze the flow-deformation coupled problem and studied the mechanical behavior of the slope material. The stress-strain relationship was formulated using elastic modeling.

Cascini et al. (2011) and Cascini et al. (2010) utilized the GeHoMadrid code to perform coupled hydro-mechanical analysis of the spatial and temporal occurrence of rainfall-induced shallow landslides of flow type. Their analysis employed the elasto-plastic constitutive model with the Mohr-Coulomb yield criterion.

Several studies on slope instability involving special materials have demonstrated the need to incorporate their specific material properties such as those of expansive soil (Qi and Vanapalli, 2016; Lu et al., 2006) and residual soil (Rahardjo et al., 2005; Gasmo

et al., 2000) into the model. The Barcelona Basic Model (BBM) is often used to simulate the coupled hydro-mechanical behavior of soils when the slope stability is addressed. For example, Qi (2017) used the BBM model to analyze the stability of an expansive soil slope under rainfall, while Askarinejad (2015) studied the failure mechanisms in unsaturated silty sand slopes triggered by rainfall. Furthermore, Xu et al. (2018) utilized the BBM model to investigate the deformation and stability of the ground when the groundwater level rises. Kim et al. (2012) incorporated the alteration of the rainfall pattern to investigate its influence on the instability of partially saturated soil slopes.

The finite element software CODE_BRIGHT, whose constitutive models library includes the BBM, is commonly used in the analysis of slopes or dams due to its ability to consider the coupled thermo-hydro-mechanical problems. Recently, CODE_BRIGHT was enhanced with the opportunity to consider the climate boundary conditions (Mahinroosta et al., 2015; Tsiampousi et al., 2017). Several studies have used CODE_BRIGHT to investigate the behavior of soil under different scenarios. For example, Zandarín et al. (2009) examined the tailing dam's saturation zone and water level changes during construction, while Alonso et al. (2003) studied the stress distribution, plastic zone development, pore water pressure distribution, and safety factor of expansive soil under rainfall. In addition, Alonso et al. (2016) evaluated the distribution of pore water pressure during and after the reservoir water level drop calculation, and Pinyol et al. (2012) investigated the distribution of pore water pressure in levees subjected to fluctuating water levels. Furthermore, Hoffmann et al. (2014) and Hamrouni et al. (2015) analyzed the changes in pore water pressure on one-dimensional slopes during rainfall.

2.5.2 Atmospheric conditions

Rainfall infiltration is a common trigger for landslides, as it can lead to soil wetting at a shallow depth (Sassa et al., 2005; Wang et al., 2010; Zhuang et al., 2017; Sorbino and Nicotera, 2013). However, atmospheric factors such as relative humidity, wind speed, radiation, and temperature can also affect the distribution and change of surface pore water through evaporation, in addition to infiltration. In-situ monitoring experiments have shown that these factors have an impact on the water content of the slope (Rahardjo et al., 2008), but they are often not considered in slope stability analysis. As reviewed by Elia et al. (2017), the effect of climate on the topsoil of the slope is a multi-factor, long-term, and iterative process of infiltration and evaporation. While studies have in-

vestigated the influence of rainfall on slope stability (Xu and Zhang, 2010; Zhou et al., 2014; Chen et al., 2018), their simplified approach does not fully consider the influence of the atmospheric conditions. In numerical simulations using SEEP/W finite element software, the effect of evaporation on the slope is typically only considered through the use of negative infiltration rates.

For example, the computer code NOSAT was developed within the state surface framework and used in monitoring and modeling of slope response to climate changes (Ledesma et al., 1996, Rahardjo et al., 2008 and Rahardjo and Rezaur, 2008). The NOSAT code can be used for coupled unsaturated flow-deformation analysis (Ledesma et al., 1996). Cardoso et al. (2012) used the CODE_BRIGHT finite element code to simulate the influence of seasonal variations in rainfall and evaporation on embankment deformation, while Alonso and Pinyol (2008) studied the deformation behavior of pavements under different climate conditions.

A number of studies have explored the impact of evaporation on slope stability. For example, Alonso et al. (2003) investigated the deformation and stability of an over-consolidated clay slope under rainfall, while Griffiths and Lu (2005) found that the safety factor increased with increasing level of evaporation and decreasing level of infiltration. Capparelli and Versace (2011) used actual transpiration and evaporation models to estimate their impact on suction in summer, while Le et al. (2012) and Van Asch and Malet (2009) demonstrated the significant impact of evaporation in the unsaturated zone on groundwater recharge and resulting levels, which in turn affects slope stability.

Arnone et al. (2011) developed a comprehensive model that considers soil infiltration, evaporation, groundwater fluctuation, and initial soil conditions to simulate rainfall-induced landslides. Other studies have linked shallow surface run-off models with soil water characteristic curves to establish infinite slope models under spatially distributed evaporation, as demonstrated by Casadei et al. (2003), or have investigated changes in pore water pressure caused by atmospheric evaporation and precipitation, as shown by Tsiampousi et al. (2016).

Rahardjo et al. (2013) highlights the significance of evaporation effects when studying rainfall-induced slope stability. However, the effects of evaporation and infiltration on slope stability are complex. High infiltration can result in a reduction of the safety factor, while incorporating evaporation into the analysis can produce an intermediate safety

factor value corresponding to specific infiltration or evaporation states. Therefore, it is essential to investigate the development of soil slope instability under varying climatic conditions. To simulate the effects of climate on pore water pressure changes more accurately and realistically, it is necessary to consider both rainfall and evaporation in the analysis.

2.5.3 Slope stability analysis approaches and slope failure criteria

Slope stability is influenced by various external factors, including rainfall infiltration, which weakens the shear strength of the slope while increasing self-gravity stress. To assess the stability of the slope, the factor of safety is used as a criterion. The most commonly used methods for slope stability analysis are the limit equilibrium method and the finite element strength reduction method. In the limit equilibrium method, the safety factor is computed based on the assumed sliding surface. Since this method is based solely on the condition of limit equilibrium, it does not provide information about the stress and displacement state of the slope.

Furthermore, the limit equilibrium method neglects the effects of stress history on slope stability. The pore water pressure distributions used as input data in limit equilibrium slope stability analysis can be obtained through three methods: (i) calculated pore water pressure distribution from numerical seepage analysis (Tsaparas et al., 2002), (ii) assumed pore water pressure distribution based on the wetting front concept (Chen et al., 2009), and (iii) actual field-measured pore water pressures (Gasmo et al., 2000). The limit equilibrium method considers a multiple potential failure surfaces and uses computing the safety factor for each surface (Bishop, 1955; Price and Morgenstern, 1965; Spencer, 1967).

It is important to consider the stress state at the potential failure location when analyzing slope stability. The potential slip surface search method is used to determine the critical slip surface of the slope, and it is essential to examine all possible surfaces, including plane, cylindrical, cycloidal, and other shapes. Huat et al. (2006) developed stability charts for slope stability analysis under rainfall conditions using finite-element seepage and limit equilibrium stability analyses. These charts provide geotechnical engineers with a useful tool to quickly assess the safety factor in response to a rainfall event. For example, the safety factor for the slip surface at depth H of an infinite slope is given by

Duncan et al. (2014):

$$F_s = \frac{c'}{\gamma_{sat} H \sin\beta \cos\beta} + \frac{\tan\phi'}{\tan\beta} - \frac{m\gamma_w \tan\phi'}{\gamma_{sat} \tan\beta} \tag{2.17}$$

where F_s is the safety factor, c' is the effective cohesion, ϕ' is the effective friction angle, β is the slope angle, γ_{sat} is the saturated unit weight of the soil and m is the distance from the groundwater table to the slip surface.

Based on the extended Mohr-Coulomb failure criterion (Fredlund et al., 1978), the safety factor of an unsaturated soil slope is expressed by Cho and Lee (2002):

$$F_s = \frac{c' + (u_a - u_w)\tan\phi^b + (\sigma_n - u_a)\tan\phi'}{\gamma_t H \sin\beta \cos\beta} \tag{2.18}$$

where γ_t is the total unit weight of the soil, u_a is the pore air pressure, u_w is the pore water pressure, $u_a - u_w$ is the matric suction, σ_n is the total normal stress, σ_n-u_a is the net normal stress on the slip surface and ϕ^b is the soil internal friction angle associated with matric suction.

Lu and Godt (2008) developed an analytical framework for the stability of infinite slopes under steady unsaturated seepage conditions with the suction stress (σ^s) included (Lu and Griffiths, 2004).

$$F_s = \frac{c'}{\gamma_{sat} H \sin\beta \cos\beta} + \frac{\tan\phi'}{\tan\beta} - \frac{\sigma^s \tan\phi'}{\gamma_{sat} H}(\tan\beta + \cot\beta) \tag{2.19}$$

With the rapid development of computer technology, the application of the finite element method to the analysis of geotechnical engineering problems is becoming more and more common. This finite element analysis can provide both stability analysis and deformation results. The slope instability is evaluated based on the plastic strain and plastic deformation area, and the strength reduction on finite element with nonlinear iterative convergence is used as the criterion for instability assessment. In a study by Pham and Fredlund (2003), the dynamic programming method was combined with finite element calculations to analyze the stability of two-dimensional slopes.

The strength reduction method is a useful technique for simulating slope instability and plastic deformation processes in finite element analysis. This method involves computing the factor of safety of the slope after considering the coupling behaviour of transient seepage field and stress field, and then analyzing the overall stability of the slope.

Coupled hydro-mechanical modeling can be used to calculate the stress state and pore water pressure in slopes, as noted by Alonso et al. (2003). Based on the resulting stress field from numerical modeling, a local safety factor at a particular point or a global safety factor for a specified slip surface can be easily calculated to assess the slope stability, as demonstrated by Cho and Lee (2001). The factor of safety is typically determined by a shear strength reduction factor, which is the ratio of the actual strength to the reduced strength necessary for the elasto-plastic finite-element analysis to converge within a specified number of iterations, as described by Cai and Ugai (2004). By reducing the strength parameters such as cohesion and friction angle, the possible failure surface of a slope can be identified through deformation analysis. $\phi - c$ reduction method is widely used by researchers worldwide, for instance Dawson et al. (1999), Griffiths and Lane (1999), Brinkgreve and Bakker (1991), Cheng et al. (2007), Crosta et al. (2006), and Isakov and Moryachkov (2013).

The ability of finite element simulations to determine the actual stress state gives it an advantage over the limit equilibrium method in slope stability analysis. In addition, the finite element method can accommodate complex boundary conditions and material models, making it a versatile tool for analyzing slope stability.
In addition to the factor of safety, which is commonly used to evaluate slope stability, the progressive development of the plastic zone and continuous sliding surface is another important consideration. This approach involves monitoring of the development of strain and shearing forces within certain areas of the sliding surface. When the strain exceeds a certain value or the shearing force surpasses the peak shear strength of the soil, the slope material enters the softening stage, and the shear stress decreases. The development of the shear zone in the slope reflects the progressive failure of the landslide, which usually involves the softening and dilatancy of the soil during the shearing process (Ye et al., 2005). This approach can provide important insights into the behavior of slopes and can help improve our understanding of slope stability. If this process continues to develop, it may form a local failure zone, which eventually causes failure of the slope. This phenomenon is known as the progressive cumulative failure process of the slope.

During rainfall, the plastic zone initially appears near the toe of the slope and gradually extends upward along the slope. This is due to the decrease or even disappearance of matric suction and the increase of soil mass caused by rainfall infiltration, which further expands the plastic zone inside the slope. As rainfall continues, the plastic zone on the slope surface extends further upwards and inwards along the slope, while its area and

connectivity increase (see Fig. 2.19, Lin et al., 2008). This progressive development of the plastic zone is a key factor in the slope instability process under rainfall conditions.

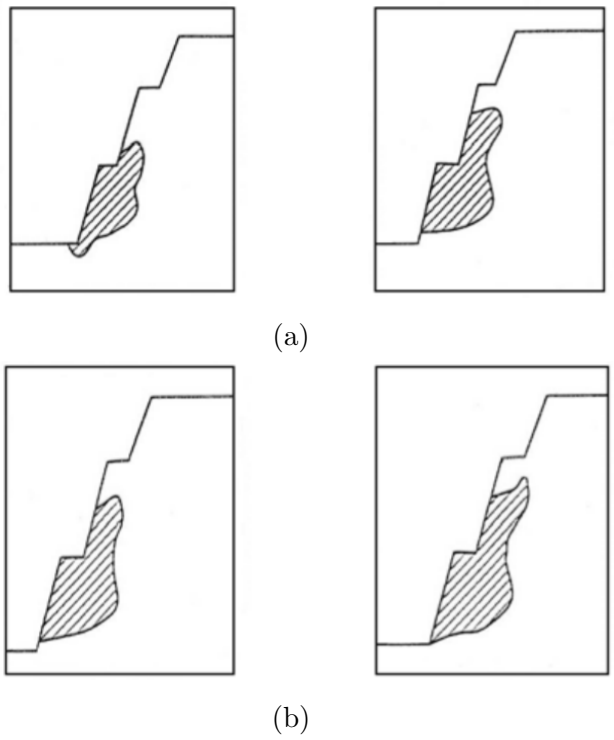

Figure 2.19: Enlargement of the plastic state zone in the slope according to water content increase (Lin et al., 2008). (a) Initial water content and w=18%. (b) w=22% and saturated state

The plastic zone is continuous and has the largest distribution area within the slope, which is extremely unfavorable for the overall stability of the slope. The plastic zone extends further into the slope under the continuous action of rainfall, and even after the rainfall stops, the rainwater in the transient saturation zone of the slope continues to infiltrate and exit the slope, enlarging the plastic zone area on the slope surface, although not significantly. Rainwater infiltration also widens the distribution of the plastic zone in the deeper parts of the slope, forming a distribution zone with a penetrating plastic zone that provides objective conditions for the potential sliding surface of the slope. It is reasonable to judge the failure criterion of the overall instability of the slope based on the plastic deformation from the foot to the top of the slope. If the stress concentration zone where plastic deformation occurs, the slope may experience overall instability in the plastic zone that penetrates each other, resulting in slope failure. The position of the

plastic shear band of the model and its stress path are calculated to evaluate the failure. Once the stress path at this point reaches the critical state line, failure occurs.

2.6 Summary

This chapter provides an overview of the distribution and formation of loess and loess slopes, as well as the current understanding of unsaturated loess behavior. Through a review of the literature, insights into the unique characteristics of loess are gained. The fundamental concepts of constitutive models for unsaturated soils and the numerical methods used for analyzing rainfall-induced slope instability are also discussed. Based on this discussion, the following conclusions can be drawn:

- The nature of loess as a soil presents various challenges, primarily its propensity to collapse. Collapsible loess is characterized by a metastable structure, high void ratio, and low density. Numerous studies have examined the microstructural properties of loess and factors that influence it, such as clay components, void shape, and cementation bonding. As the focus is on the unsaturated natural loess, studies have primarily concentrated on undisturbed loess as opposed to remolded loess, where cementation bonds and softening of soil fabric differ significantly.
- In addition, loess is known to have a high potential for collapse, which can lead to unfavorable consequences, such as a significant increase in compressibility and decrease in shear strength when it gets wet. As a result, the soil mass becomes denser than its original metastable structure due to the reduction in volume. Various factors such as initial water content, dry density, and sampling methods are believed to influence the degree of collapsibility. Common methods for measuring the collapse potential include single oedometer and double oedometer tests.
- The chapter also discusses the advances in investigating the hydraulic properties of unsaturated soil, with a focus on the soil water characteristic curve (SWCC). Various techniques for obtaining the SWCC, such as the pressure plate, axis translation, and dewpoint methods, were presented. The chapter also covers the different approaches used to determine the unsaturated permeability of soils, including the use of empirical equations, analytical solutions, and numerical simulations. The effects of soil structure, pore size distribution, and pore connectivity on unsaturated hydraulic properties were also discussed. The knowledge gained from this chapter

can be applied in various geotechnical engineering applications, such as the design of landfills, embankments, and foundation systems.

- Both mechanical and hydraulic factors play a significant role in the deformation properties of loess. The deformation of collapsible loess is the result of the coupling of hydro-mechanical behaviour, which is not fully understood in many aspects. Unsaturated soil mechanics is an effective tool for investigating the behaviour of collapsible loess. An elastic-plastic model within the framework of unsaturated soil mechanics was introduced. Longitudinal studies have shown that the governing variables, such as mechanical and hydraulic stress, as well as stress path, can have a significant impact on the final deformation.
- In Section 2.5, recent studies on rainfall-induced slope instability, the methods used, and the results obtained were analyzed, as well as the limitations of these studies. Various factors contributing to loess landslides and different approaches to their investigation were discussed. There are many constitutive models for unsaturated soil with different degrees of complexity available in the literature, and it is crucial to select a model that can accurately represent the relevant deformation and failure mechanics in the field for slope simulations. The Barcelona Basic Model is rarely employed in slope analyses, and previous research has not examined the impact of atmospheric boundaries on loess slopes, unlike the artificial assumption of rainfall.

However, despite the extensive literature review, there remain some unresolved questions regarding collapsible loess and loess slopes. For instance, the difference between remolded and undisturbed loess requires further investigation. Additionally, the coupled hydro-mechanical behaviour of natural loess is not yet fully understood. The hysteresis phenomenon in the water retention curve of loess is another area that has not been thoroughly explored, and this has inspired the research objectives of this thesis.

3 Material and experimental program

3.1 Origin and sampling of the loess material

The samples used in the study were taken from Yangling, located at coordinates 34 °16'53.8″N 108 °05'24.4″E (shown as a red dot in Fig. 3.1), which is approximately 91.2 km from Xi'an, the capital city of Shaanxi province in China. Yangling is situated on the north side of the Wei River valley in the southern part of the plateau. The Wei River is the largest tributary of the Yellow River and originates from the north of the Niaoshu Mountain in Wuyuan county, Gansu province.

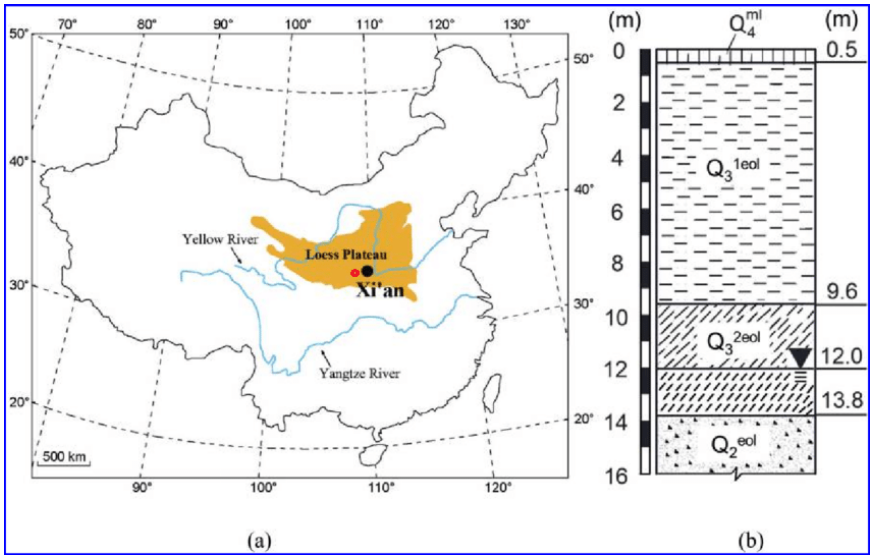

Figure 3.1: Soil profile (Liu et al., 2015), the red dot on the map to the left indicates the sampling location.

The region has a mean annual temperature of 13 °C and an average annual precipitation of 650-700 mm, with most of the rainfall occurring in the summer and autumn months. Precipitation is concentrated in the months of July, August, and September, as

shown in Fig. 3.2. The rainfall from April to September accounts for 77% of the total annual rainfall, indicating a large variation in precipitation throughout the year.

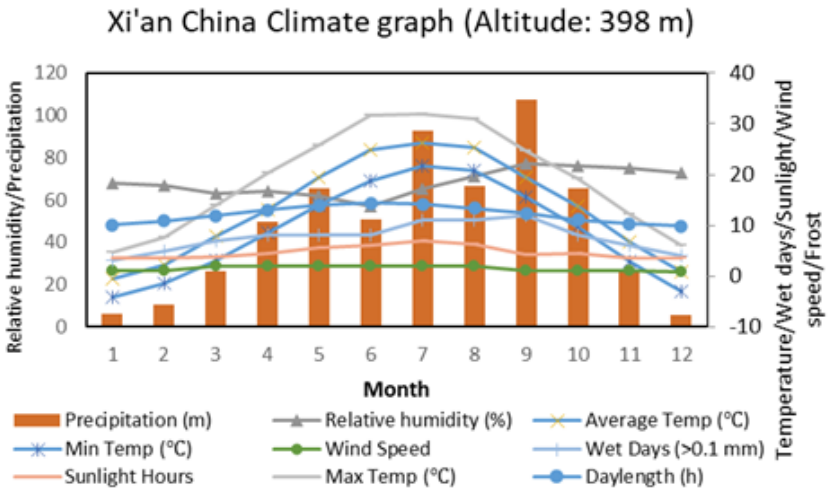

Figure 3.2: Precipitation distribution during the year.

The Cenozoic Quaternary era is divided into two parts, the Holocene (Q_4) and the Pleistocene ($Q_1 - Q_3$), as shown in Fig. 3.1. The Pleistocene era is further divided into early, middle, and late periods, represented by Q_1, Q_2 and Q_3. The main loess layer is composed of the Wucheng loess (Q_1), the Lishi loess (Q_2), and the Malan loess (Q_3). The Q_2 loess layer is buried below the Malan loess and is relatively denser than Q_3 and Q_4 loess in the upper part. It is generally believed that Q_2 loess has only a certain degree of collapsibility under high pressure. In contrast, the Q_3 formation is known for its significant collapse potential, and most studies on loess have focused on Q_3 loess. The soil tested in this study belongs to the Q_3 loess layer.

The undisturbed block samples and additional disturbed loess material samples were collected near an artificial slope with an approximate inclination of 30° at a depth of 3 meters below the original ground surface (see Fig. 3.3(a) and Fig. 3.3(b)). The groundwater table is located deeply below the ground surface. The color of the loess is affected by the water content, appearing dark rusty yellow at high water content and light yellow at low water content.

(a) (b)

Figure 3.3: (a) Sampling site. (b) Example of undisturbed loess samples taken at the site.

Two block samples, measuring approximately 17*17*17 cm, were obtained using a shovel and spade, along with additionally 20 kg of undisturbed material. Some visible roots and wormholes were observed on the sample surface. The block samples had visible large pores and vertically developed joints. The samples were carefully wrapped in plastic and double plastic bags and transported to the laboratory of the Civil and Environmental Engineering department at Ruhr Universität Bochum, Germany, for experimental testing.

3.2 Physical and chemical properties of loess

The soil samples were analyzed for physical and chemical characteristics, including specific gravity, particle size distribution, Atterberg's limits and Proctor density. The undisturbed block samples were used to determine the natural water content and density.

The water content was measured using oven drying at 105 °C according to standard ASTMD2216 (2010). The actual density was determined using standard ASTMD2937 (2000). The specific gravity was determined according to standard ASTMD854 (2010), and the Atterberg's limits, including liquid limit (w_L) and plastic limit (w_P), were measured based on standard ASTMD4318 (2000), see Table 3.1 and Table 3.3.

The particle size distribution was determined using sedimentation method (ASTMD422, 1963). It has been found that the loess sample is mainly composed of silt sized grains ranging from 0.002 mm to 0.075 mm diameter (Fig. 3.4 (a)). According to the Unified Soil Classification System (USCS), the material used in this study is clayey silt (Fig. 3.4 (b)). In Table 3.2 the material is classified as clayey silt.

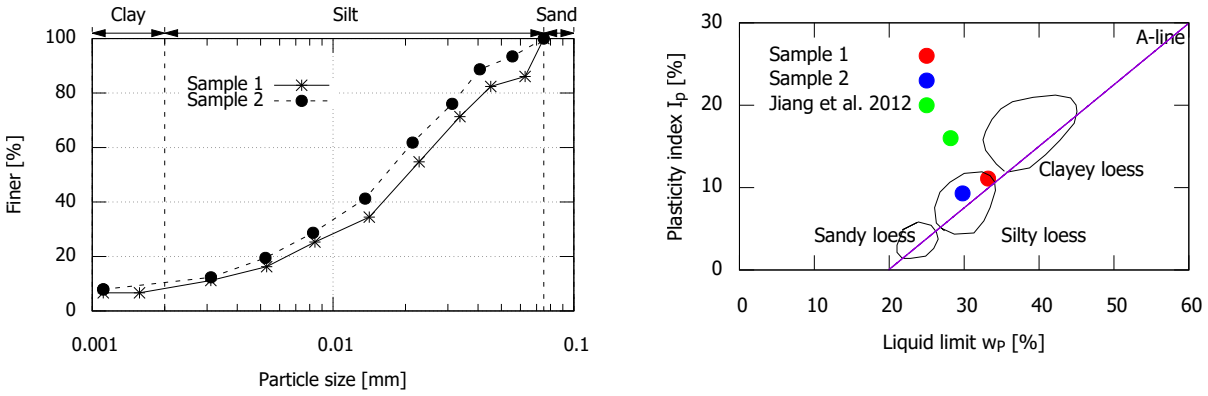

(a) (b)

Figure 3.4: (a) Particle size distribution, and (b) Plasticity chart including loess types after Gibbs and Holland (1960) for the loess samples.

Table 3.1: Summary of physical soil properties of the undisturbed block samples.

	Natural water content	Specific gravity	In place dry density	Field void ratio
	w_0	G_s	ρ_{dfield}	e_{field}
	[%]	[-]	[g/cm^3]	[-]
Sample 1	11.2	2.69	1.240	1.170
Sample 2	22.7	2.67	1.214	1.199

Table 3.2: Particle size analysis

	d_{10}	d_{30}	d_{60}	Passing sieve	Passing sieve	Classification
	[mm]	[mm]	[mm]	0.125 mm [%]	0.075 mm [%]	
Sample 1	0.0031	0.0084	0.228	1	86.1	clay silt
Sample 2	0.0031	0.0083	0.214	1	93.5	clay silt

Table 3.3: Atterberg limit values of loess

	Liquid limit [%]	Plastic limit [%]	Plasticity index [%]
Sample 1	33.2	22.1	11.1
Sample 2	29.8	20.5	9.3

The content of $CaCO_3$ in the loess sample was determined to be 13.2 g/kg using the standard DIN18129 (1996). $CaCO_3$ serves as a cementing agent in the loess and is an important component of its structure, providing a bridge between aggregates and grains.

Structural investigations using scanning electron microscopy (SEM) and mercury intrusion porosimetry (MIP) have been performed on an undisturbed sample from block 1 and on a remolded loess sample with a dry density close to that of the undisturbed sample. The MIP test (as shown in Fig. 3.5 and Fig. 3.6) provides a representation of the distribution of different pore sizes in the soil sample. The equivalent diameter corresponding to the intrusion pressure is used to obtain a quantitative pore size distribution curve for the soil. The undisturbed sample has three dominant pore groups (see Fig. 3.5), while the remolded sample (see Fig. 3.6) has two dominant pore groups, with the larger pore group splitting into a group with medium size after disturbance. Pores with sizes ranging from 40 to 0.01 μm have an absolute predominating role in the undisturbed sample, accounting for about 85% of the total pore volume. The pore system is mainly composed of large pores with a pore diameter from 40 to 0.2 μm, accounting for 65% of the total pore volume. After disturbance, the percentage of the pore group ranging from 40 to 0.2 μm changes significantly, and the volume of micropores with a diameter of around 17.5 μm drops and stabilizes at a low value. The adjustment in pore size is not the same for each pore group, only the larger pores adjust drastically, causing a breakage in the original pore distribution and the formation of a new one.

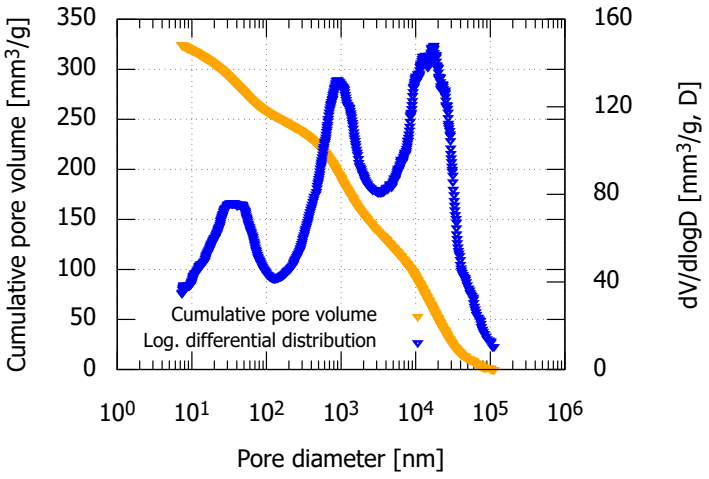

(a)

Figure 3.5: Pore size distribution of the undisturbed sample.

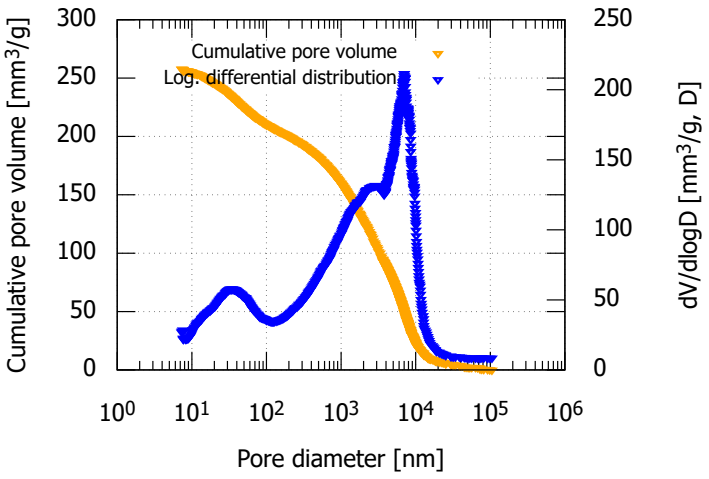

(a)

Figure 3.6: Pore size distribution of the remolded loess sample.

The following Figs. 3.7 (a) to (d) shows SEM figures of the undisturbed loess. The magnification of the SEM images increases in the order of the Figs. 3.7 (a) to (d). The well-structured nature of the undisturbed sample can be clearly recognized. Fig. 3.7 (a) and Fig. 3.7 (b) show large pores with diameters of about 150 to 350 μm, marked in yellow. In Fig. 3.7 (c), pores in the range from 20 to 100 μ dominate (in green colour). In Fig. 3.7(b), pores of diameters up to about 15 to 20 μm are found. The undisturbed

sample has an open flocculated structure (Fig. 3.7(b)). The number of contact points is small. In the undisturbed sample, there are macropores that are visible to the naked eye (Fig.3.7(b)). The orientation of the particle is irregular, in the order of the Figs. 3.7 (a) to (d), which have large diameters and do not interconnect. Most of the pores are circular or elliptical (Fig. 3.7(d)).

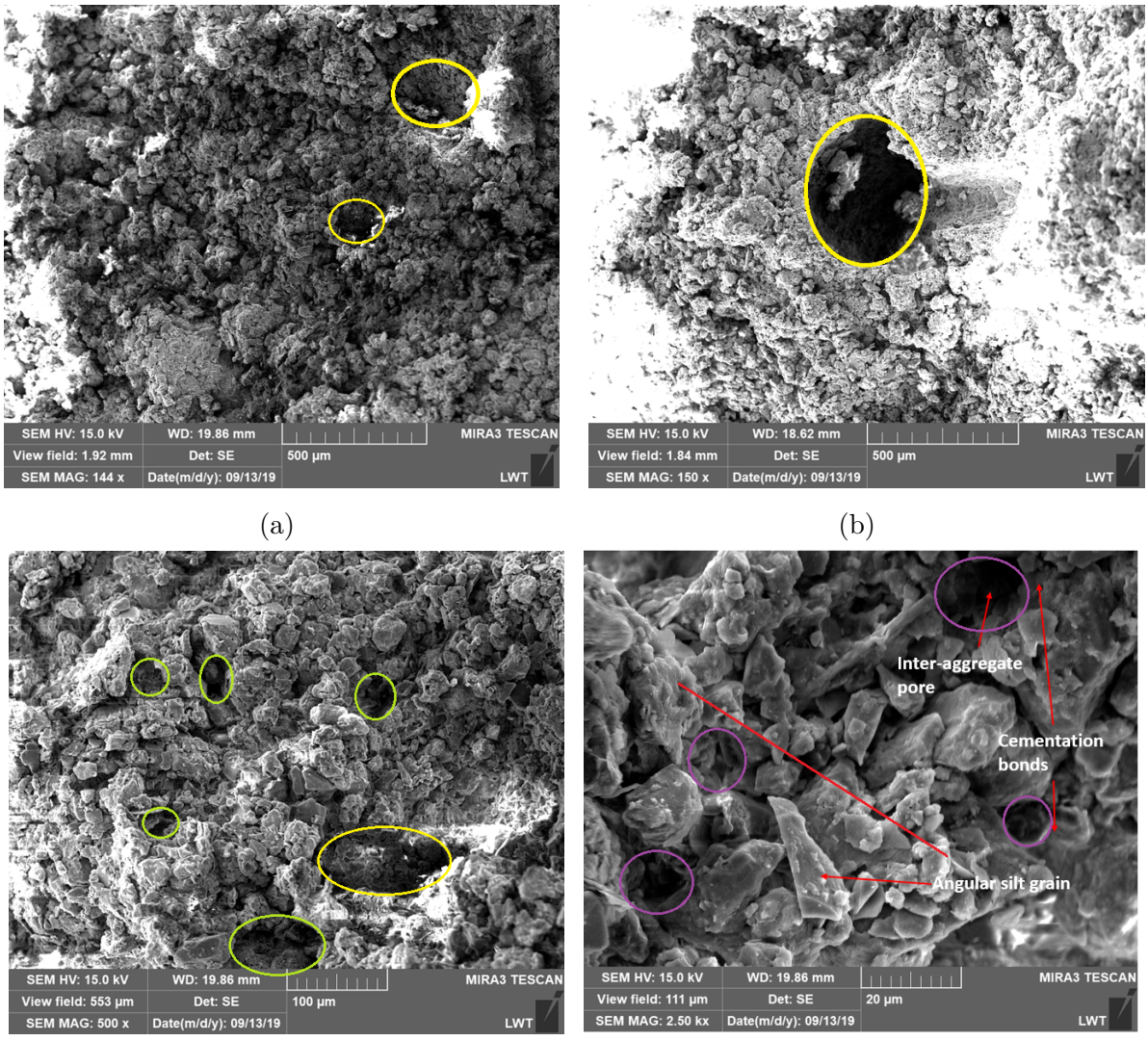

Figure 3.7: SEM images of the undisturbed loess sample from block 1 at magnification (a) 144x, (b) 150x; (c) 500x; and (d) 2500x.

The SME pictures of the remolded sample are shown in Fig. 3.8 (a) to (d). In Fig. 3.8(d), mainly angular grains from about 2 μm up to 20 μm diameters or length can be distinguished from coated aggregates. The detailed quantitative structural analysis including

both SEM and MIP data of the undisturbed and remolded loess sample is presented in Section 3.2.

The SEM pictures of the remolded loess are provided in Figs. 3.8 using two different magnifications. Comparing the SEM pictures of the undisturbed states, one can see that the dominating pore type inside the remolded loess sample are the intra-aggregate pores (Fig. 3.8(a)). In contrast, in the undisturbed sample, the dominating pore type are the inter-aggregate pores, in the order of the Figs. 3.7 (a) to (d).

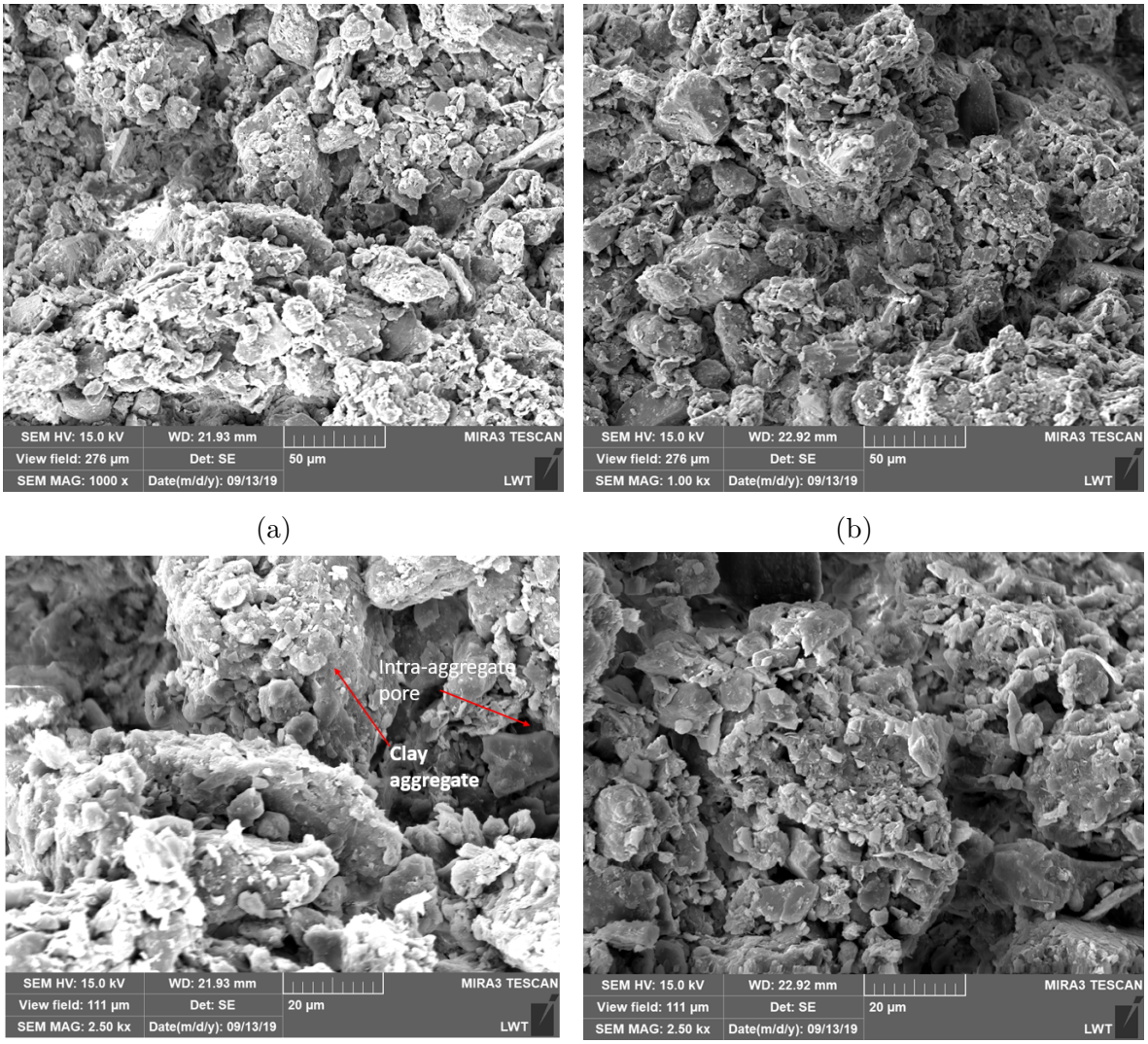

Figure 3.8: SEM images of the remolded loess sample from block 1 at magnification (a) 1000x, (b) 1000x; (c) 2500x; and (d) 2500x.

3.3 Experimental program

Several tests were carried out to study the mechanical behaviour of undisturbed and remolded loess, such as collapsibility testS, direct shear tests and triaxial tests. The hydro-mechanically coupled behaviour of loess was studied by suction-controlled oedometer tests using different loading paths. SWCC tests under different hydraulic loading paths were carried out to study the water retention characteristics of loess. The detailed test program will be presented in the following sections, including the initial conditions and applied boundary conditions for all samples tested. The details of sample preparation and of the different test procedures are given in Chapter 4.

3.3.1 Collapse tests

The study aimed to investigate the effect of initial water content, soil state (undisturbed or remolded), and the applied vertical stress at inundation on the collapse potential of loess soil using a conventional oedometer device. Both double oedometer (DO) tests and single oedometer (SO) tests were conducted, with six different applied vertical stresses at inundation and two initial water content levels selected for the SO tests, see Table 3.4 and Table 3.5.

Table 3.4: Single oedometer tests

No.	Sample type	$\rho_{d,initial}$ [g/cm^3]	$w_{initial}$ [%]	$e_{initial}$ [-]	Applied vertical stress at inundation [kPa]
SOU11, SOU12, SOU13, SOU14, SOU15, SOU16	Undisturbed	1.24	11.2	1.17	25, 50, 100 200, 400, 800
SOU21, SOU22, SOU23, SOU24, SOU25, SOU26	Undisturbed	1.214	22.7	1.199	25, 50, 100 200, 400, 800
SOC11, SOC12, SOC13, SOC14, SOC15, SOC16	Remolded	1.24	11.2	1.17	25, 50, 100 200, 400, 800
SOC21, SOC22, SOC23, SOC24, SOC25, SOC26	Remolded	1.214	22.7	1.199	25, 50, 100 200, 400, 800

SOU represents a single oedometer test on an undisturbed sample, SOC represents a single oedometer test on a remolded sample.

Table 3.5: Double oedometer tests

No.	Sample type	$\rho_{d,initial}$ [g/cm^3]	$w_{initial}$ [%]	$e_{initial}$ [-]	Vertical loading [kPa]
DOU1	Undisturbed	1.24	11.2	1.17	25-800
DOU2	Undisturbed	1.214	22.7	1.199	25-800
DOC1	Remolded	1.24	11.2	1.17	25-800
DOC2	Remolded	1.24	18	1.17	25-800
DOC3	Remolded	1.214	22.7	1.199	25-800

DOU represents a double oedometer test on an undisturbed sample, DOC represents a double oedometer test on a remolded sample.

3.3.2 Shear strength tests

3.3.2.1 Single stage direct shear test

Direct shear tests were performed on undisturbed and remolded loess samples with different initial water contents to investigate their strength properties. The tests were carried out with a small vertical load to study the shear strength of shallow loess under unsaturated conditions. Table 3.6 lists the samples tested and their initial state parameters.

Table 3.6: Single stage direct shear tests

No.	Sample type	$\rho_{d,initial}$ [g/cm^3]	$w_{initial}$ [%]	$e_{initial}$ [-]	Vertical loading [kPa]
SSU11	Undisturbed	1.24	11.2	1.17	50
SSU12	Undisturbed	1.24	11.2	1.17	100
SSU13	Undisturbed	1.24	11.2	1.17	150
SSU21	Undisturbed	1.214	22.7	1.199	50
SSU22	Undisturbed	1.214	22.7	1.199	100
SSU23	Undisturbed	1.214	22.7	1.199	150
SSU31	Undisturbed	1.24	Saturated	1.17	50
SSU32	Undisturbed	1.24	Saturated	1.17	100
SSU33	Undisturbed	1.24	Saturated	1.17	150
SSC11	Remolded	1.24	11.2	1.17	50
SSC12	Remolded	1.24	11.2	1.17	100
SSC13,	Remolded	1.24	11.2	1.17	150
SSC21	Remolded	1.24	16	1.17	50
SSC22	Remolded	1.24	16	1.17	100
SSC23	Remolded	1.24	16	1.17	150
SSC31	Remolded	1.24	18	1.17	50
SSC32	Remolded	1.24	18	1.17	100
SSC33	Remolded	1.24	18	1.17	150
SSC41	Remolded	1.214	22.7	1.199	50
SSC42	Remolded	1.214	22.7	1.199	100
SSC43	Remolded	1.214	22.7	1.199	150
SSC51	Remolded	1.24	Saturated	1.17	50
SSC52	Remolded	1.24	Saturated	1.17	100
SSC53	Remolded	1.24	Saturated	1.17	150

SSU represents a single stage direct shear test on an undisturbed sample, SSC represents a single stage direct shear test on a remolded sample.

3.3.2.2 Multistage direct shear test

Some of the direct shear tests were conducted as multi-stage direct shear tests, in which multiple vertical stress values were applied to the same sample. The conditions of the tested samples are provided in Table 3.7.

Table 3.7: Multistage direct shear tests

No.	Sample type	$\rho_{d,initial}$ [g/cm^3]	$w_{initial}$ [%]	$e_{initial}$ [-]	Vertical loading [kPa]
MSU1	Undisturbed	1.214	22.7	1.199	50, 100, 150, 200
MSU2	Undisturbed	1.24	Saturated	1.17	50, 100, 150, 200
MSC1	Remolded	1.24	11.2	1.17	50, 100, 150, 200
MSC2	Remolded	1.24	16	1.17	50, 100, 150, 200
MSC3	Remolded	1.214	22.7	1.199	50, 100, 150, 200
MSC4	Remolded	1.24	Saturated	1.17	50, 100, 150, 200

MSU represents a multistage direct shear test on an undisturbed sample, MSC represents a multistage direct shear test on a remolded sample.

3.3.2.3 Triaxial compression test

Both drained and undrained triaxial compression tests were conducted. Undrained tests were performed because in a natural loess slope, an impermeable layer may impede drainage, and excess pore water pressure may build up, causing a decrease in effective stress and a reduction in strength. The testing program for the triaxial tests is presented in Table 3.8.

Table 3.8: Triaxial compression tests

No.	Soil sample	Test type	$\rho_{d,initial}$ [g/cm^3]	$w_{initial}$ [%]	$e_{initial}$ [-]	Effective confining pressure [kPa]
CDU11	Undisturbed	CD	1.214	22.7	1.199	50
CDU12	Undisturbed	CD	1.214	22.7	1.199	100
CDU13	Undisturbed	CD	1.214	22.7	1.199	150
CDC41	Remolded	CD	1.214	22.7	1.199	50
CDC42	Remolded	CD	1.214	22.7	1.199	100
CDC43	Remolded	CD	1.214	22.7	1.199	150
CUC41	Remolded	CU	1.214	22.7	1.199	50
CUC42	Remolded	CU	1.214	22.7	1.199	100
CUC43	Remolded	CU	1.214	22.7	1.199	150

CDC represents a consolidated drained triaxial compression test on a remolded sample, CDU represents a consolidated drained triaxial compression test on an undisturbed sample, CUC represents a consolidated undrained triaxial compression test on an undisturbed sample.

3.3.3 Deformation tests under hydro-mechanical loading paths

The compressibility of loess was investigated under different hydro-mechanical loading paths. The first part of the experimental program involved compression loading and unloading at constant applied suctions in oedometers (refer to Table 3.9). In the second part of the program, the net stress was maintained constant, while the suction was stepwise reduced from an initial value (wetting) and subsequently increased (drying path) (refer to Table 3.10).

The axis translation technique was used for suction control in the low range, and the vapor equilibrium technique was used in the large suction range. The effect of various combinations of applied suction and net stress on deformation and water content were measured for different loading paths. The impact of soil suction on stiffness during loading and unloading, as well as yielding, was studied.

Table 3.9: Suction controlled oedometric compression tests

Sample No.	Sample type	Suction [kPa]	Net vertical stress [kPa]	Technique
SCC1	Remolded	20	25-50-100-200-400-800	ATT
SCU1	Undisturbed		-400-200-100-50-25	
SCC2	Remolded	50	25-50-100-200-400-800	ATT
SCU2	Undisturbed		-400-200-100-50-25	
SCC3	Remolded	80	25-50-100-200-400-800	ATT
SCU3	Undisturbed		-400-200-100-50-25	
SCC4	Remolded	100	25-50-100-200-400-800	ATT
SCU4	Undisturbed		-400-200-100-50-25	
SCC5	Remolded	200	25-50-100-200-400-800	ATT
SCU5	Undisturbed		-400-200-100-50-25	
SCC6	Remolded	2500	25-50-100-200-400-800	VET
SCU6	Undisturbed		-400-200-100-50-25	
SCC7	Remolded	334050	25-50-100-200-400-800	VET
SCU7	Undisturbed		-400-200-100-50-25	

SCC represents a suction controlled oedometric compression test on a remolded sample, SCU represents a suction controlled oedometric compression test on an undisturbed sample.

The deformations obtained from multistage wetting tests at specific net stresses were compared with the deformations observed during one-step wetting using liquid water in the single oedometer tests. Moreover, the hydro-mechanical tests enabled the determination of the water retention curves at different mechanical loadings.

Table 3.10: Constant loading wetting drying tests

Sample No.	Sample type	Net vertical stress [kPa]	Suction [kPa]	$w_{initial}$ [%]	$\rho_{d,initial}$ [g/cm^3]
LWDC1	Remolded	50	800-600-400-200-50-		
LWDU1	Undisturbed		0-50-200-400-800		
LWDC2	Remolded	100	800-600-400-200-50-	11.2	1.24
LWDU2	Undisturbed		0-50-200-400-800		
LWDC3	Remolded	150	800-600-400-200-50-		
LWDU3	Undisturbed		0-50-200-400-800		
LWDC4	Remolded	200	800-600-400-200-50-		
LWDU4	Undisturbed		0-50-200-400-800		

LWDC represents a constant loading wetting drying test on a remolded sample, LWDU represents a constant loading wetting drying test on an undisturbed sample.

3.3.4 Drying-wetting tests on the determination of SWCC

The soil water retention curves under unconfined boundary conditions (zero net stress) under various hydraulic loading paths were determined. The samples used in the tests were categorized into two types: initially compacted and initially undisturbed samples. To determine the water content-suction relationship of the loess over a wide suction range, it was necessary to use different methods to induce suction. For suctions less than 1 MPa, the axis translation technique (ATT) was used, and for suctions greater than up to 300 MPa, the vapor equilibrium technique (VET) together with suction measurements using chilled mirror hygrometer (CMH) at given time steps was used. The initial suction of the undisturbed samples was measured using chilled mirror hygrometer. The suction values controlled by the axis translation technique (ATT) were 0, 50, 100, 200, 400, 600, and 1000 kPa. The drying paths started from a saturated state, and the wetting path started from 1000 kPa suction. In VET, the samples were placed in a desiccator with 12% relative humidity ($\approx$ 300 MPa suction) for the drying path and 98% relative humidity ($\approx$ 2.3 MPa suction) for the wetting path. A detailed description of the various hydraulic paths of the SCWW measured is prescribed in Section 4.4.2.3. Table 3.11 shows the number of

samples and the tests performed to obtain the soil water retention curve.

Table 3.11: Water retention curve tests

Sample type		Path of SWCC	Suction	Technique
Remolded	Undisturbed		[kPa]	
S1	US1	Scanning	1000-0	ATT
S2, S3, S4, S5, S6, S7, S8, S9	US2		2000	VET or CMH
ID1	UID1	Initial drying	0-1000	ATT
ID2, ID3, ID4, ID5, ID6, ID7, ID8, ID9	UID2		2000	VET or CMH
MW1	UMW1	Main wetting	0-1000	ATT
MW2, MW3, MW4, MW5, MW6, MW7, MW8, MW9	UMW2		2000	VET or CMH
MD1	UMD1	Main drying	1000-0	ATT
MD2, MD3, MD4, MD5, MD6, MD7, MD8, MD9	UMD2		2000	VET or CMH
SD1	USD1	Second wetting	0-1000	Pressure plate
SD2, SD3, SD4, SD5, SD6, SD7, SD8, SD9	USD2		2000	VET or CMH
SW1	USW1	Second drying	1000-0	ATT
SW2, SW3, SW4, SW5, SW6, SW7, SW9	USW2		2000	VET or CMH
TW1	UTW1	Third wetting	0-1000	ATT
TW2, TW3, TW4, TW5, TW6, T7, TW8, TW9	UTW2		2000	VET or CMH

ATT represents the axis translation technique, VET represents the vapor equilibrium technique, and CMH represents the chilled mirror hygrometer.

3.3.5 Hydraulic conductivity test

The saturated hydraulic conductivity of loess was measured under different vertical loads using the variable head permeability method based on standard ASTMD5084 (2007) to determine the permeability coefficient, see Table 3.12.

Table 3.12: Hydraulic conductivity tests

No.	Soil sample	$\rho_{d,initial}$ [g/cm^3]	$w_{initial}$ [%]	$e_{initial}$ [-]	Vertical net stress [kPa]
PU1	Undisturbed	1.24	22.7	1.17	50
PU2	Undisturbed	1.24	22.7	1.17	100
PU3	Undisturbed	1.24	22.7	1.17	150
PC1	Remolded	1.24	22.7	1.17	50
PC2	Remolded	1.24	22.7	1.17	100
PC3	Remolded	1.24	22.7	1.17	150

PC represents a hydraulic conductivity test on a remolded sample, PU represents a hydraulic conductivity test on an undisturbed sample.

4 Experimental equipment and methods used

This chapter provides an overview of the experimental techniques used in the study, including their theoretical basis, equipment components, and operational challenges. This chapter explains the calibration process of the equipment and provides detailed information about the experimental procedures used in each test conducted in the study. This includes the sampling process and the stress path applied to the samples, which are illustrated in detail.

4.1 Collapse behaviour

4.1.1 Single oedometer tests

The single oedometer test simulates the loading-wetting process of a collapsible soil. The test involves stepwise mechanically loading the specimen at the initial water content until a target vertical stress is reached, followed by flooding the specimen with liquid water to achieve saturation (ASTMD5333, 1996). Each load increment lasts overnight or until primary consolidation is completed (ASTMD2435, 1996). After wetting, stepwise loading continues until a maximum vertical stress of 800 kPa is reached, followed by unloading to a vertical stress of 400 kPa. The loading path is illustrated in Fig. 4.1. The difference between the deformation before and after saturation represents the amount of collapse deformation at the specified stress level, and the collapse potential can be calculated using Equ. 4.1.

$$I_c = \left[\frac{d_f - d_0}{h_0} - \frac{d_i - d_0}{h_0}\right] \times 100 = \left[\frac{d_f - d_i}{h_0}\right] \times 100 \tag{4.1}$$

d_0 represents the initial dial gauge reading under seating stress, measured in mm. d_i represents the dial gauge reading under a particular stress before wetting, also in mm.

d_f represents the dial gauge reading under a particular stress after wetting, in mm. h_0 is the initial height of the specimen in mm. The term $\frac{d_f - d_0}{h_0}$ represents the strain under a particular stress after wetting, while $\frac{d_i - d_0}{h_0}$ represents the strain under a particular stress before wetting.

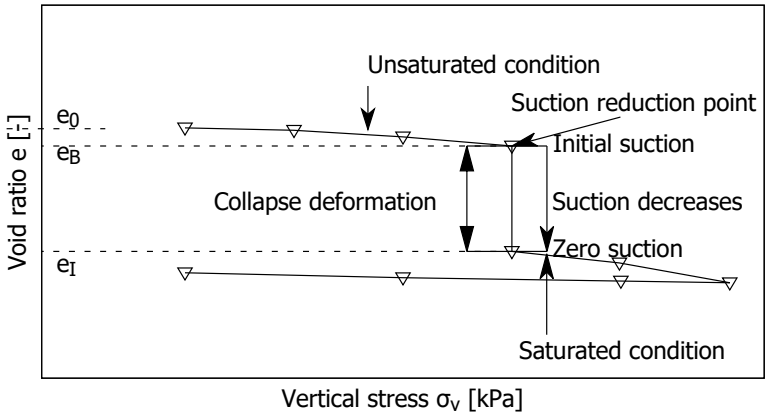

Figure 4.1: Single oedometer test.

Equ. 4.2 and Equ. 4.3 are equivalent expressions to Equ. 4.1 for the calculation of collapse potential.

$$I_c = \frac{\triangle h}{h_0} \times 100 \tag{4.2}$$

$\triangle h$ refers to the change in specimen height due to wetting, measured in mm.

$$I_c = \frac{e_B - e_I}{1 + e_0} \times 100 \tag{4.3}$$

e_B represents the void ratio under a particular stress before wetting, while e_I represents the void ratio under the same stress after wetting. e_0 represents the initial void ratio.

4.1.2 Double oedometer tests

The double oedometer test method, introduced by Jennings (1957), assumes that the sequence of loading and wetting has no effect on the wetting-induced collapse deformation. This method involves preparing two identical soil samples with the same initial void ratio and water content and testing them separately on two oedometer devices. Before applying the first load step, one of the samples is saturated with water, while the other sample is

left unaltered.

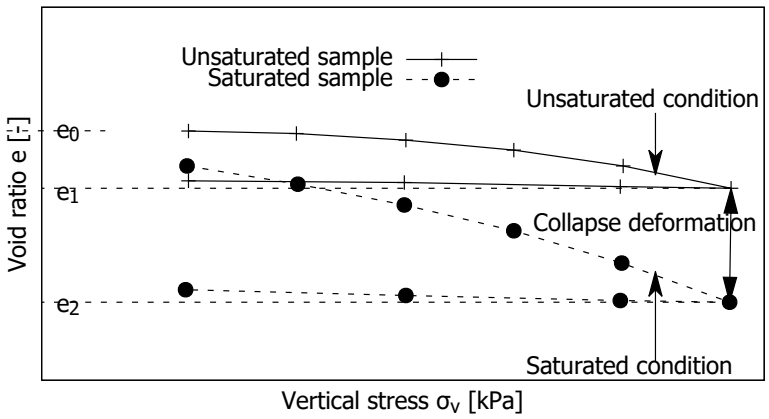

Figure 4.2: Double oedometer test.

After saturating one sample and leaving the other unaltered, the two samples are loaded stepwise until a maximum vertical stress is reached and then unloaded to a small value of vertical stress. The loading and unloading processes for both samples are performed according to the one-dimensional consolidation test described in standard ASTMD2435 (1996), as shown in Fig. 4.2. In the double oedometer test, the collapse deformation is defined as the difference in the void ratio of the two samples under the same vertical load.

4.2 Direct shear tests

The single stage direct shear test method, based on standard ASTMD3080 (2011), involves using a shear box with dimensions of 60 mm width, 60 mm length, and 19.65 mm height. Multiple specimens are used to conduct the shear tests under different vertical loading conditions. The shear rate in this test is 0.036576 mm/min.

Multistage shear tests were first introduced by Taylor (1951) to study the unsaturated shear strength of undisturbed silty clay using the triaxial technique, with pore water pressure measurements. In this testing method, using the direct shear apparatus, different values of vertical stress are applied, and the corresponding shear phases are performed

on the same sample. This approach is especially advantageous for testing undisturbed soils, where sampling of multiple identical samples is difficult and costly. Multistage shear testing can eliminate the variability in initial sample properties, and the time required for sample preparation is less than in single-stage testing, leading to lower costs. However, some researchers have noted that this technique may not be appropriate for soils with a sensitive structure.

The multistage test involves consolidating and shearing the same soil specimen multiple times in a direct shear box, with saturation and specimen preparation identical to the traditional single stage direct shear test. Saturation and consolidation to the first vertical stress are completed in the first stage, followed by the first shearing stage. When the slope of the shear stress versus time decreases significantly and the curve runs almost horizontally, the specimen is released from shear stress, then subjected to the second vertical stress, and allowed to consolidate before the second shearing stage, see Fig. 4.3. This procedure is repeated for the third test stage, in which the sample is then sheared up to the maximum horizontal displacement. During first and second shear phase, the horizontal displacement was 2 mm, while in the final stage, the sample was sheared until about 3 mm.

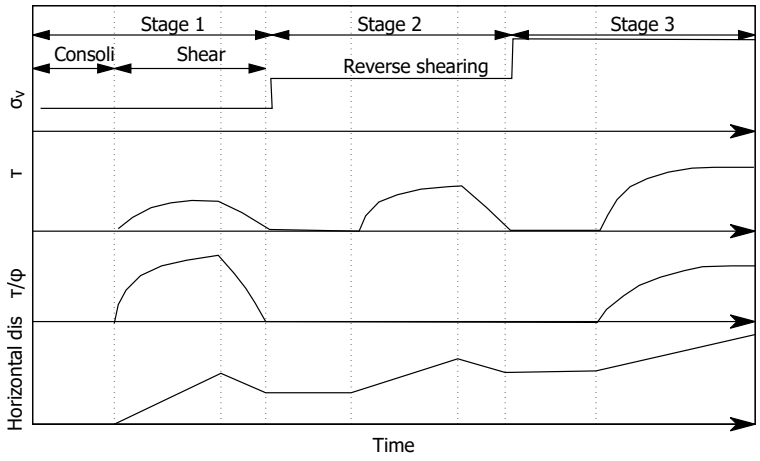

Figure 4.3: Prodedure of multistage direct shear tests.

In the present study, the multi-stage shear test involved three stages of shearing for each sample. In a multi-stage direct shear test on an unsaturated, undisturbed sample, the test should be stopped before reaching the peak shear stress to preserve the sample to not enter the softening phase.

4.3 Drained and undrained triaxial compression tests

Both remolded and undisturbed loess samples were subjected to both consolidated undrained compression (CU) and consolidated drained compression (CD) tests in a conventional triaxial device. To prepare the sample for testing, it was mounted into the cell and then saturated through three steps. First, CO_2 was percolated through the sample, followed by de-aired water. The final step of the saturation procedure was backpressure saturation, which was performed at a cell pressure of 200 kPa, with 200 kPa back pressure.

The specimens used in the triaxial tests had a diameter of 40 mm and an initial height of 80 mm. Saturation was confirmed by obtaining a B-value greater than 0.95, according to Skempton, 1954. After saturation, the specimens were isotropically consolidated under a specific cell pressure and then sheared using the strain-controlled method by increasing the vertical stress. The effective confining stress levels at which consolidation and testing were conducted were 50, 100, and 150 kPa. The axial strain was increased at a rate of 0.0063 mm/min, and shearing was stopped when the axial strain reached 30%. The procedures used in the testing followed the standards ASTMD7181 (2011) and ASTMD7181 (2011).

4.4 Determination of the SWCC

4.4.1 Types of equipment used for determination of SWCC

To determine the water content-suction relationship of the loess for both drying and wetting paths over a wide range of suction, different methods for inducing suction were used. The axis translation technique (ATT) (Hilf, 1956) was used to apply matric suction in the range $<$ 1500 kPa. The vapor equilibrium technique (VET) was used in combination with intermediate measurements of suction in the chilled-mirror hygrometer (CMH), for a suction range of 2-300 MPa (Seiphoori and Ferrari, 2014). Additionally, the chilled-mirror hygrometer was used to determine the initial total suction of the soil specimens.

4.4.1.1 Pressure plate apparatus

The axis translation technique artificially increases both the gas pressure and the water pressure, with the water pressure being positioned greater than zero, thus avoiding cavitation (Gardner, 1956). The limits of application and problems of the axis translation technique were discussed in detail by Agus (2005). The underlying assumption of the axis translation technique is that the curvature of menisci remains consistent under high gas pressure.

Fig. 4.4 illustrates the pressure plate equipment, which uses a water-saturated ceramic plate as a semi-permeable membrane that only permits the liquid phase to pass through, while blocking the gas phase as long as the gas pressure is below the ceramic's air entry value. Prior to testing, the ceramic plate must be completely saturated with distilled de-aired water.

The soil sample is positioned on the ceramic plate, with its water phase in contact with the ceramic plate's water phase. Due to the high gas pressure in the chamber, some gas may dissolve into the water. When the water passes through the ceramic plate and the pressure dissipates, the dissolved gas can be released from the water. As time passes, the gas accumulates beneath the ceramic plate, resulting in a decrease in hydraulic conductivity, particularly along the wetting path (Delage and Tarantino, 2008). It is essential to pay close attention to this wetting path.

The pressure chamber shown in Fig. 4.4 is linked to an air pressure regulator for the application of air pressure (u_a). The base of the pressure plate is joined to a high-precision burette with a volume of 25 cm^3 and a scale resolution of 0.05 cm^3, which is used to apply water pressure (u_w) to the soil samples. The resulting matric suction, which is the difference between the air pressure (u_a) and water pressure (u_w), is represented by ψ_m, i.e., $\psi_m = u_a - u_w$.

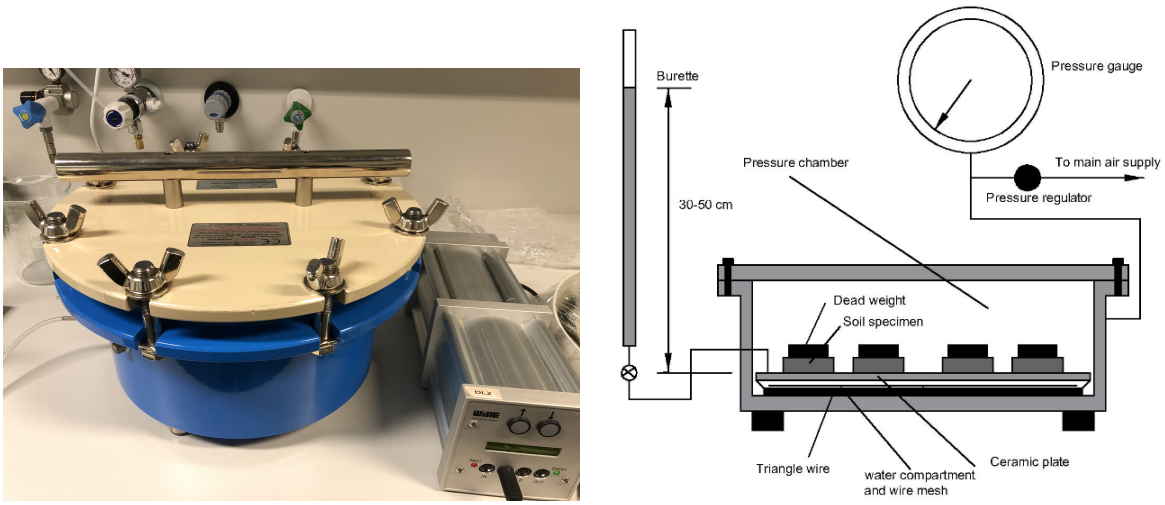

(a) (b)

Figure 4.4: (a) Photograph and (b) Schematic plot of the pressure plate equipment.

The ATT method was employed to impose suction values of 0, 50, 100, 200, 400, 600, and 1000 kPa. The drying path of the water retention curve commences with a suction value of 50 kPa, which is the smallest suction value applied during the test. The wetting path started at a suction value of 1000 kPa. To ensure that the water phase remains continuous within the sample, it is important to follow a predesigned hydraulic loading path and to carefully control the air pressure during the wetting process.

4.4.1.2 Vapour equilibrium technique (VET)

The total suction in the range greater than 2000 kPa is applied using desiccators containing different concentrations of saline solutions (Greenspan, 1977; Hovarth, 1985; Lide, 1994; ASTME104, 1997). Saline solutions were prepared by mixing salts and distilled water to achieve a constant desired relative humidity (RH) in the desiccator (see Fig. 4.5). The RH of the saline solutions was calibrated using the chilled-mirror hygrometer technique at the beginning and end of the test. The experiment was conducted in a temperature-controlled room with a constant temperature of 22°C $\pm$ 0.5°C, which allowed keeping the applied suctions constant (Agus and Leong, 2003). The results of the experiment, including the values controlled by VET and corresponding saline solutions, are listed in Table 4.1.

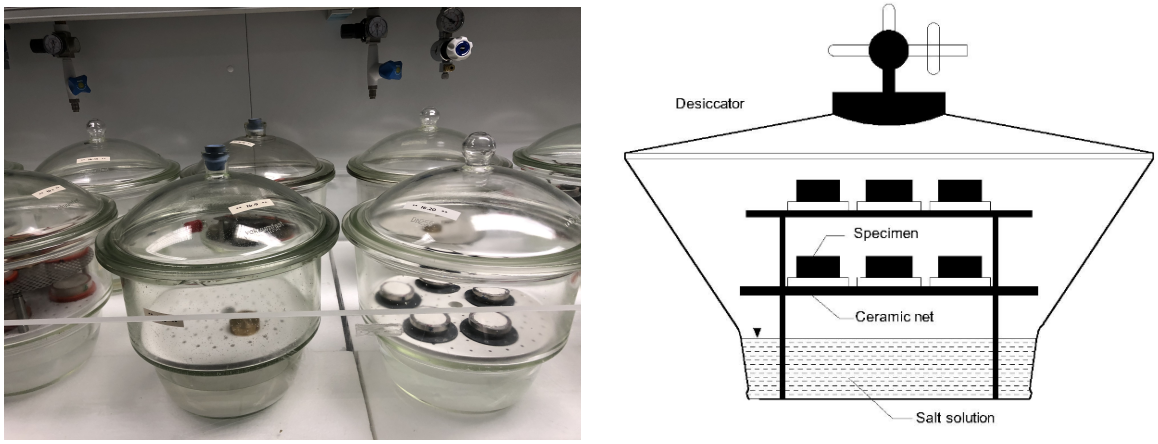

(a) (b)

Figure 4.5: (a) Photograph, and (b) Schematic plot of the dessicator.

Table 4.1: Relation between humidity and corresponding suction values of the saturated salt solutions used for the VET method (as determined at the end of the test).

Solution	K_2SO_4	KNO_3	KCl	NaCl	$Mg(NO_3)_2$	$MgCl_2$	LiCl	NaOH
Solubility (g/l)	111.1	316	347	359	420	542	832	1090
Relative humidity, RH (-)	0.982	0.934	0.852	0.753	0.54	0.362	0.158	0.095
Total suction (MPa)	2.5	9.5	22.27	39.47	85.62	151.53	256.98	334.05

4.4.1.3 Chilled mirror hygrometer (CMH)

The device used in the study to measure relative humidity is a chilled-mirror hygrometer (CMH) of type 3TE (see Fig. 4.6), made by Decagon Devices, Inc., Pullman, WA. The relative humidity and temperature is measured by the CMH, after the liquid phase of water inside the sample reaches equilibrium with the vapor phase in the closed air space around the sample at a prescribed ambient temperature. A small fan circulates the air in the sensing chamber to accelerate vapor equilibration.

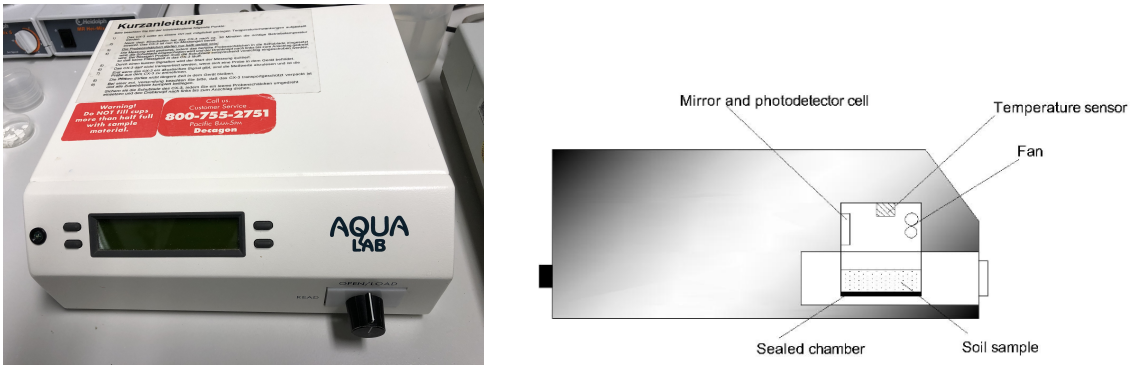

(a) (b)

Figure 4.6: (a) Photograph and (b) Schematic drawing of the chilled mirror hygrometer.

The chilled mirror hygrometer includes a Peltier cooling device that cools the mirror until dew forms, an optical sensor detects the dew formation, the corresponding dew point temperature is measured by the thermocouple attached to the chilled mirror. The relative humidity is calculated as the ratio of the saturated vapor pressure at the ambient soil sample temperature (u_v) to the saturated vapor pressure at the dew point temperature ($u_{v,sat}$) (Lu, 2004). The CMH is a useful tool for rapid measurement of total suction, with measurement time of less than 10 minutes.

The Kelvin's equation (see Equ. 4.4) is the thermodynamic equation used to calculate total soil suction using the measured RH-value at the prescribed ambient temperature. The equation is as follows (Lu, 2004, Leong et al., 2003 and Bulut, 2008).

$$\psi_m + \psi_o = \psi = -\frac{RT}{\nu_{w0} w_v} \cdot \ln \frac{u_v}{u_{v0}} \tag{4.4}$$

where ψ is the total suction (kPa), R is the universal (molar) gas constant (8.31432 J/(mol K)), T is the absolute temperature (i.e. $T = (273.16 + t°C)$ K), t is the temperature in $°C$, ν_{w0} is the specific volume of water or the inverse of the density of water (i.e. $1/\ \rho_w$ m^3/kg), ρ_w is the density of water (i.e. 998 kg/m^3 at $t = 20°C$), w_v is the molecular mass of water vapour (i.e. 18.016 kg/kmol), u_v is the partial pressure of pore water vapour (kPa), and u_{v0} is the saturation pressure of water vapour over a flat surface of pure water at the same temperature (kPa). The term $u_v = u_{v0}$ is called the relative humidity (RH) and is entered as a fraction (i.e. water activity) in the equation.

4.4.2 Procedure for determining SWCC

4.4.2.1 Sample preparation for SWCC measurement

To prepare the remolded soil samples, the material was sieved through 2 mm sieves and its water content was measured by oven-drying according to the standard procedure described in ASTMD2216 (2010). The remolded soil was then mixed with a pre-determined amount of water to achieve four different initial water content values of 11.2%, 16%, 18%, and 22.7%.

The soil water characteristic curve was determined for both undisturbed and remolded samples, where the initial water content of the undisturbed block sample was 11.2%. Undisturbed samples were obtained by cutting them from the block using metal rings with a cutting edge.

After mixing, the soil was left in an air-tight container for one week to reach equilibrium. The specimens were then compacted into plastic rings with a diameter of 50 mm and a height of 15 mm, with an initial dry density of 1.24 g/cm^3 and a target water content of 11.2%. The device shown in Fig. 4.7 was used for static compaction of the samples.

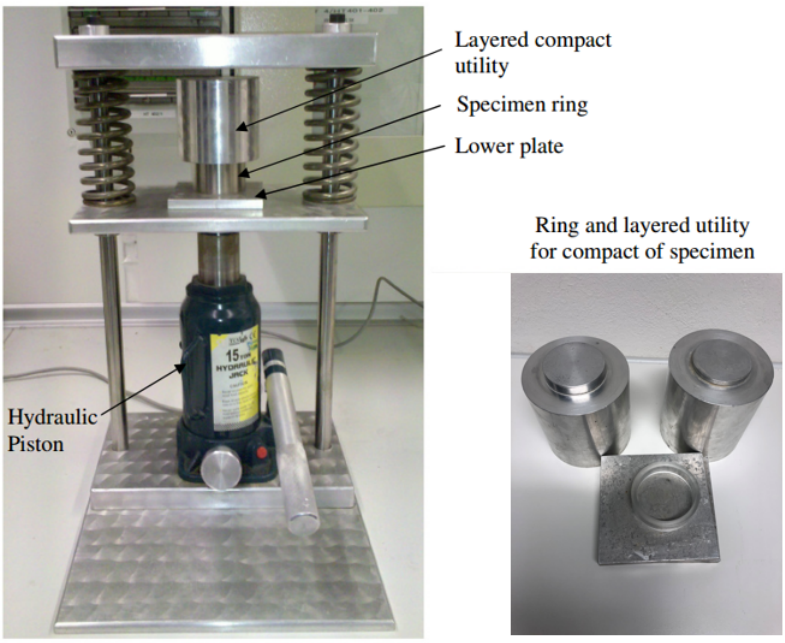

Figure 4.7: Static compacting device.

4.4.2.2 Transient technique for measuring SWCC using VET and CMH

The conventional method for determining the soil water characteristic curve (SWCC) involves measuring the equilibrium soil water content corresponding to a given applied suction. For the drying path, suctions are stepwise applied from an initially saturated or low suction state, while for the wetting path, suctions are stepwise decreased from an initially dry state of the sample. At each step of applied suction, the soil sample requires time to reach equilibrium, which can result in very long test durations, particularly for high plasticity clays or for investigating cyclic drying-wetting behavior, as performed in this study.

The transient method using VET and CMH-measurements was used to shorten the experimental SWCC-testing duration. This method was applied for suctions ranging from 3 to 300 MPa during both wetting and drying. The drying path involves subjecting the sample to the maximum possible suction in VET (334 MPa), while for the wetting path, the sample is initially dry and subjected to a low suction of 2.5 MPa using the vapour equilibrium technique. Intermediate suction states and corresponding water contents are captured during the equilibration time using repeated measurements of total suction in the chilled-mirror hygrometer and measurements of actual water content by weighing the sample.

Figure 4.8: Microcell components.

To host the soil sample during the transient drying and wetting paths, a special cell called microcell was constructed (Seiphoori and Ferrari, 2014; Seiphoori et al., 2016). This cell is made of brass, has an inner height of 7 mm and a diameter of 30 mm, and can provide constant volume conditions during the hydration process. The dimensions of

the soil sample were designed to fit snugly into the measurement chamber of the chilled-mirror-hygrometer. The microcell also has holes on the top and bottom that allow for relative humidity equalization between the soil sample and the atmosphere inside the measurement chamber of the CMH. A photograph of the microcell and soil sample is shown in Fig. 4.8.

4.4.2.3 Experimental program and hydraulic paths applied for SWCC

The following paragraphs explain the detailed experimental program, which was summarized in Table 3.11. As described in Section 4.4.2.1, the samples investigated were either undisturbed or compacted to a dry density of 1.24 g/cm^3 at 11.2% water content, with initial suction values of 10124 kPa and 10213 kPa, respectively. The samples were divided into seven groups based on their hydraulic loading paths: scanning curve (S), initial drying (ID), main wetting (MW), main drying (MD), second wetting (SW), second drying (SD), and third wetting (TW). Figs. 4.9 to 4.13 provide a graphical representation of each group's loading path.

- Scanning path

Samples S2 to S9 were placed in desiccators with specified suctions, while samples S1 and US1 were stepwise wetted using ATT in pressure plates. The undisturbed sample US2, which had an initial suction of around 10 MPa, was subjected to a suction of 2.53 MPa for wetting, and the transient suction values were measured using a chilled mirror hygrometer. Samples S1 and US1 were incrementally wetted using the ATT method in pressure plates, starting at a suction of 1000 kPa and gradually decreasing to 0 kPa in steps of 200 kPa. More information on the suctions and samples can be found in Fig. 4.9.

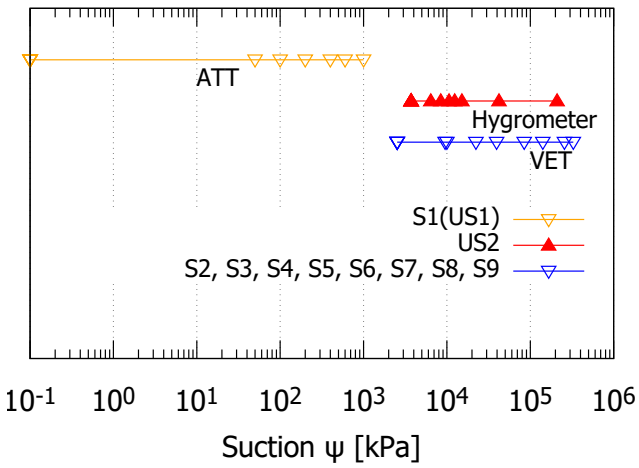

Figure 4.9: Hydraulic path for scanning curve.

- Initial drying path

Fig. 4.10 shows the hydraulic loading for the initial drying path. The remolded samples (ID1 to ID9) and undisturbed samples (UID1 and UID2) were saturated by placing them on inundated porous stones in a saturation tray for a day after the sampling process. The specimens were kept in a ring during saturation to prevent distortion. After saturation, the specimens were placed separately into the pressure plate or desiccators. The initial suction value of the pressure plate was set to 50 kPa. The undisturbed sample (UID2) was placed into the desiccator with a total suction of 328.16 MPa, and the transient suction and water content values were measured by CMH and weighing, respectively.

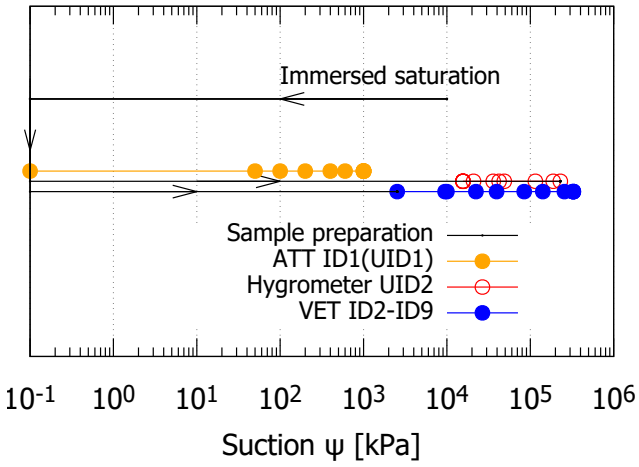

Figure 4.10: Hydraulic path for initial drying curve.

- Main wetting path

Fig. 4.11 shows the hydraulic paths for the main wetting. After the sampling process, the remolded loess samples (MW1 to MW9) and undisturbed samples (UMW1 and UMW2) were dried in the oven for one day. Samples MW1 and UMW1 were then subjected to a wetting path in the pressure plate. The undisturbed sample UMW2 was placed in a desiccator with a total suction of 2.53 MPa, and the transient suction and water content values were measured. The sampling preparation procedure of MW2 to MW9 was similar as in case of UMW2.

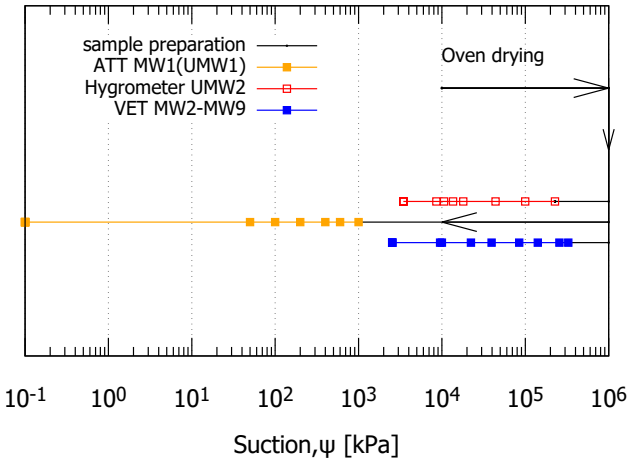

Figure 4.11: Hydraulic paths for main wetting curve.

- Main drying path and second drying path

A wetting and drying cycle was performed by placing the sample on saturated immersed porous stones for seven days and then drying it in the oven for one day. A second saturation was then performed. Afterwards, samples MD1 and UMD1 were subjected to suction that increased from 50 kPa to 1000 kPa. Samples MD2 to MD9 were each subjected to suction between 2.5 and 334 MPa until equilibrium was reached. Sample UMD2 was subjected to a suction of 1000 MPa, and the transient suction and water contents were measured.

The paths applied for the main drying are shown in Fig. 4.12(a). The corresponding paths for the second drying (SD) with one additional cycle of oven drying and one step saturation prior to suction-controlled second drying are illustrated in Fig. 4.12(b). Samples SD1 and USD2 were dried stepwise in the pressure plate, and samples SD2 to SD9 were each subjected to a suction between 2.5 and 334 MPa in VET. Sample USD2 was tested using transient VET with CMH measurements.

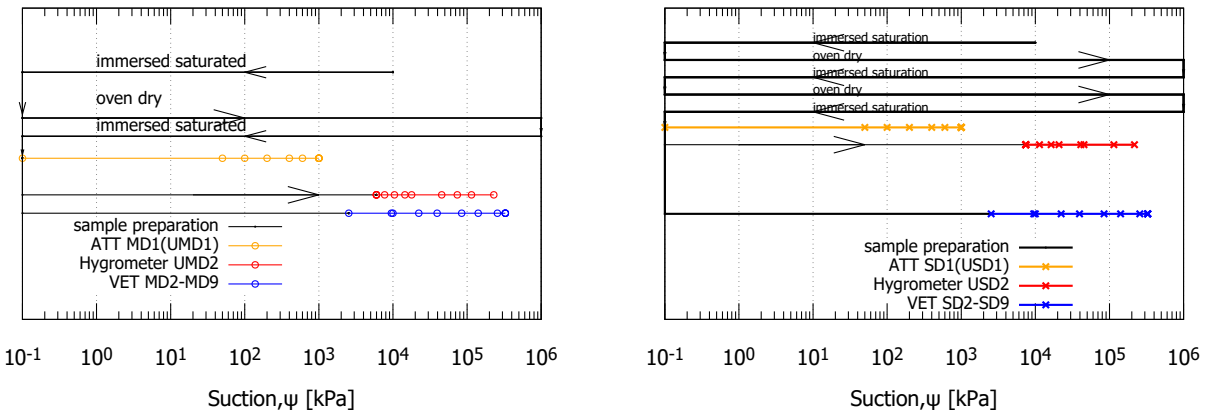

(a) (b)

Figure 4.12: Hydraulic paths for (a) main drying curve and (b) second drying curve.

- Samples for the second and third wetting path

The relevant hydraulic routes are depicted in Fig. 4.13(a) and Fig. 4.13(b). As shown in Fig. 4.13, the samples for the second and third wettings were prepared by a corresponding number of preceding drying-wetting cycles. Similarly to the previous hydraulic path, samples SW1, USW1, TW1, and UTW1 were wetted stepwise in the pressure plate, while samples USW2 and UTW2 were tested using the transient technique with VET and CMH measurements. Remolded loess samples SW2 to SW9 and TW2 to TW9 were tested using VET in the high suction range.

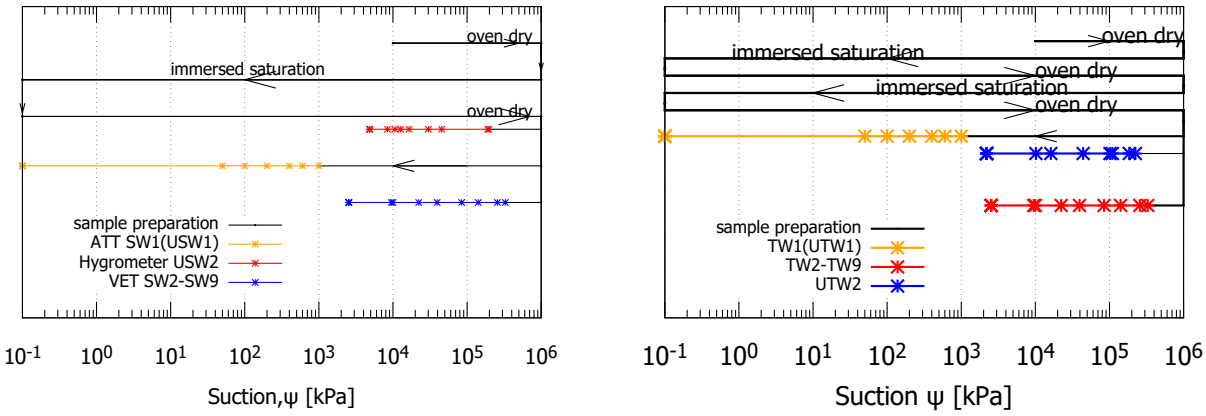

(a) (b)

Figure 4.13: Hydraulic paths for (a) second wetting curve and (b) third wetting curve.

The drying process caused a slight decrease in the volume of the samples. The samples were weighed using a precise balance with an accuracy of 0.001 g. The water content of the pressure plate samples was determined by measuring the mass after the sample reached equilibrium based on the water content versus time graph.

4.5 Volumetric behaviour under controlled suction

4.5.1 Types of equipment used in suction controlled oedometer tests

The Barcelona cell is a one-dimensional compression oedometer developed in 1999 at the Universitat Politecnica de Catalunya (UPC) in Barcelona, Spain (Romero et al., 1999). In this study, the Barcelona cell was used to perform compression-decompression tests under constant suction and a wetting-drying test under constant loading to evaluate the impact of net stress on the soil-water characteristic curve.

4.5.1.1 UPC-Barcelona cell

The whole system includes the cell itself, an air-pumping system, and a burette. The cell consists of a bottom pedestal, a main cell, and a rubber membrane. In this study, the matric suction was applied by ATT for a suction range < 1500 kPa. For this, a high-air entry ceramic plate is installed on the bottom pedestal below the soil specimen. To ensure a continuous pathway of liquid, the ceramic disk must be water saturated and flushed with liquid de-aired water before the test. The air pressure for suction control is applied through a separate connection, named air pressure or vapour pressure control in Fig. 4.13. A flexible membrane can separate the application of vertical net stress and matric suction.

To apply the target values of vertical stress and air pressure, two air-pressure regulators were employed. The valve at the top of the cell was used to regulate the vertical stress, while the side face valves were used to control the suction. The net stress is the total vertical stress minus the gas pressure applied to the soil pore system. A dial gauge with a minimum possible reading of 0.001 mm is connected to the top of the cell to measure the specimen's deformation. A burette attached to the ceramic plate's bottom measures the change in water volume inside the soil sample. The burette's entire volume was 25 cm^3, and the resolution was 0.05 cm^3. The diameter of the specimen was 50 mm

and the height was 20 mm. Fig. 4.14 (a) shows a photograph of the cell, while Fig. 4.14 (b) shows a schematic drawing of the cell.

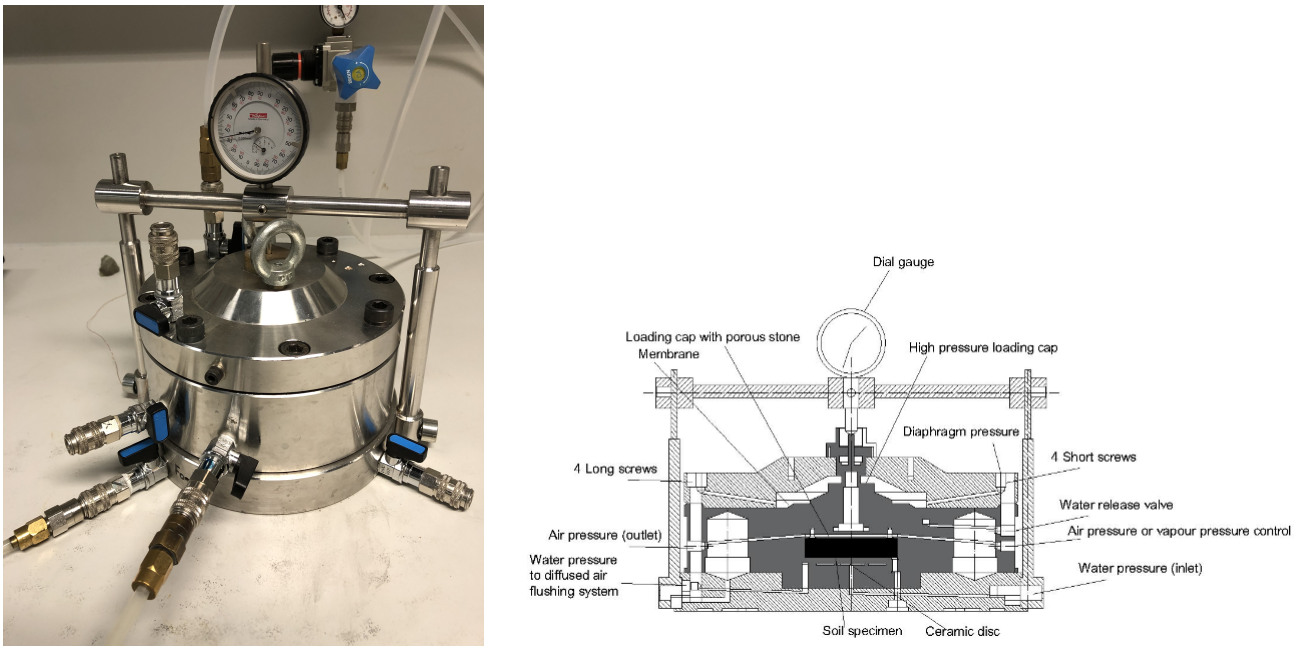

(a) (b)

Figure 4.14: (a) Setup of the Barcelona cell and (b) Scheme of a Barcelona cell setup.

4.5.1.2 UPC-Isochoric cell

The Isochoric cell was developed and manufactured at Universitat Politecnica de Catalunya (UPC), Barcelona, Spain (Romero et al., 1999). The Isochoric cell was designed to test the swelling pressure of expansive soils during wetting under constant volume conditions. The soil volume change caused by suction variation was measured using a modified Isochoric cell (Al-Badran, 2011, Lins, 2010, Nguyen-Tuan, 2014, Al-Obaidi, 2015, and Agus, 2005).

The isochoric cell was employed in this work, together with an oedometer loading frame, to perform suction-controlled compression-decompression testing and wetting-drying experiments at a high suction range (suctions $>$ 2000 kPa). A vertical load can be applied to the sample and the corresponding displacement can be measured by replacing the cell's original top cap. The isochoric cell, loading frame, and vapour circulation system are all part of the overall system. The isochoric cell is made up of three parts: a porous stone pedestal, a flexible top cap, and the main cell. With a circulating pump setup, VET was

employed to apply suction to the soil sample. An air pump and a flask filled with saline solution are part of the vapour circulation system.

Rubber tubes connect the flask, the top, and the bottom of the soil specimen, see Fig. 4.16. The air pump supports the vapor circulation inside the whole system to achieve suction equilibrium between the atmosphere of the saline solution in the bottle and the soil sample. Because molecular diffusion controls the vapor movement, the VET method is very time-consuming, which is a disadvantage of the method, which was discussed in Pintado and Lloret (2009). The temperature was always measured to calculate the total suction of the system. The diameter of the specimen is 50 mm, and its height is 20 mm. Figs. 4.15 and Fig. 4.16 show the design of the isochoric cell and the vapour circulation system.

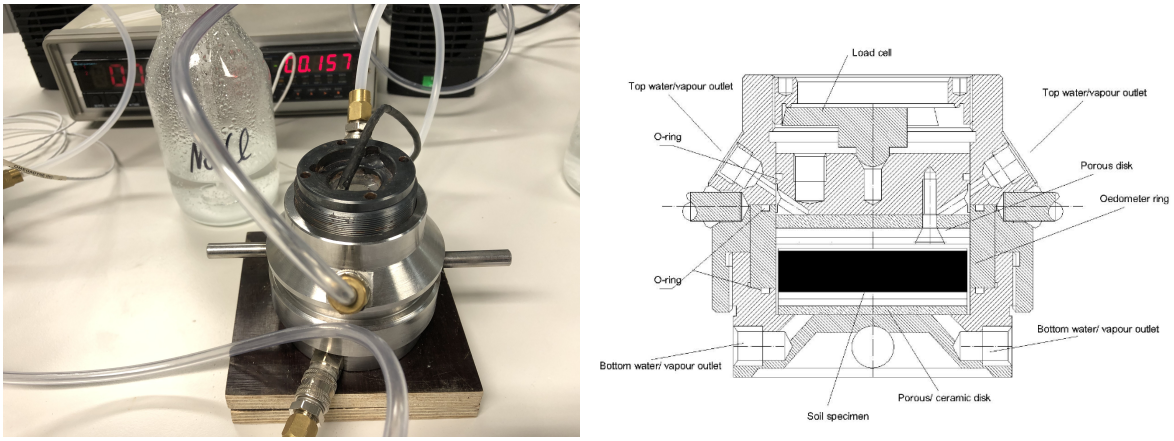

(a) (b)

Figure 4.15: (a) Setup of the Isochoric cell, and (b) Schematic drawing.

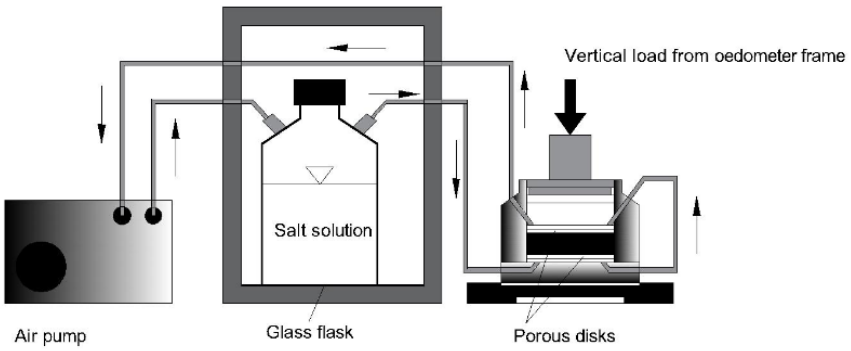

Figure 4.16: Isochoric cell, with vapour circulation system.

4.5.1.3 Modified pressure plate apparatus

In this study, the modified pressure plate apparatus (Lins et al., 2009 and Lins, 2010) was used to investigate the one-dimensional compression and rebound behaviour of the loess soils under controlled suction (Fig. 4.17). The oedometer is made up of a black cell body in which a soil sample is placed on a ceramic disk that is attached to a burette. Air pressure is delivered from the top of the cell to the sample via a porous stone. Vertical stress can be imposed using a weighted loading frame on a level system.

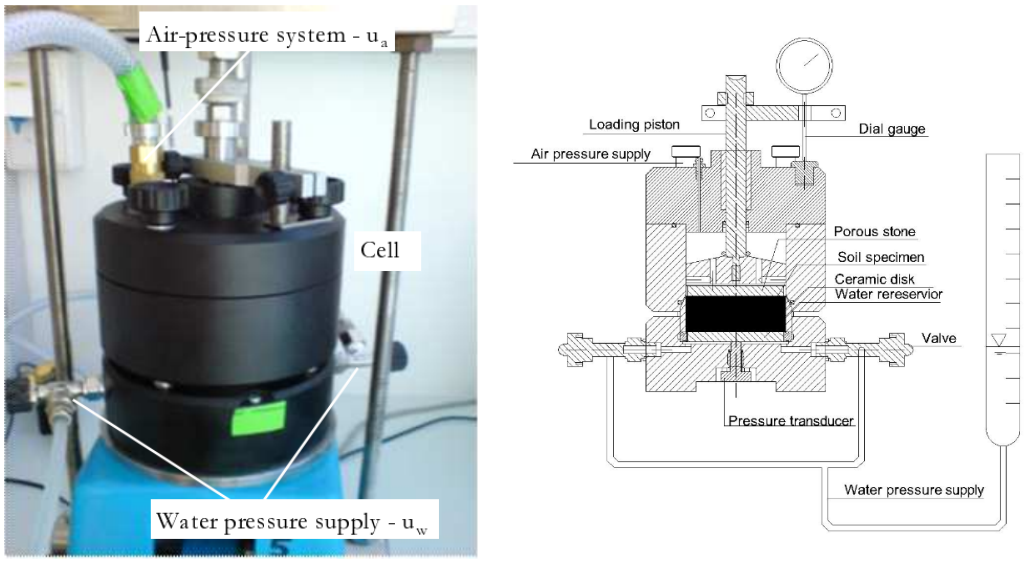

(a) (b)

Figure 4.17: Setup of the modified pressure plate apparatus (Lins et al., 2009 and Lins, 2010) (a) Photograph, (b) Scheme of setup.

To maintain controlled suction values, ATT was utilized. A ceramic disk with an air entry value of 100 kPa was placed above a water reservoir, with a burette connected to measure inflow and outflow volumes during loading and unloading. The burette has a total volume of 25 cm^3 and a resolution of 0.05 cm^3. Volume changes in the specimen were measured with a dial gauge on the loading piston. Air bubbles were periodically removed to ensure continuity between pore water and the water pressure line. The specimen ring had an inner diameter of 70 mm and a height of 20 mm.

4.5.2 Constant suction oedometer tests

The modified pressure plate apparatus, and the Barcelona cells were used with ceramic plates having different air entry values to test different suction ranges. In the modified pressure plate apparatus suctions below 100 kPa and in the Barcelona cell suctions between 0 and 1000 kPa were applied. In the modified isochoric cell suctions greater than 2 MPa were applied using VET. The study focused on four high suction values for the constant suction compression test, controlled via VET using four saline solutions: 2.5 MPa (potassium chlorate KNO_3), 35 MPa (sodium hydroxide NaOH), 9.6 MPa (sodium chloride), and 334.05 MPa (calcium chloride) were used to apply higher suction, respectively. Loess, a non-expansive soil, has a dominant suction range of less than 3 MPa.

The remolded specimens were compacted into a ring while the undisturbed specimens were cut from a larger block using a metal ring. The initial state and suction equilibrium are crucial for constant suction-compression tests (Sivakumar, 2000), and the initial total suction was measured using a chilled-mirror hygrometer following standard ASTMD6836 (2008). The total initial suction for undisturbed loess with initial water content is 11.1 MPa in this study.

The test procedure includes suction equilibration, loading, and unloading stages. The soil specimen is loaded until it reaches the target net vertical stress under constant induced suction. The one-dimensional compression test follows standard ASTMD2435 (1996). The the soil specimen's suction and stress conditions are depicted in Fig. 4.18.

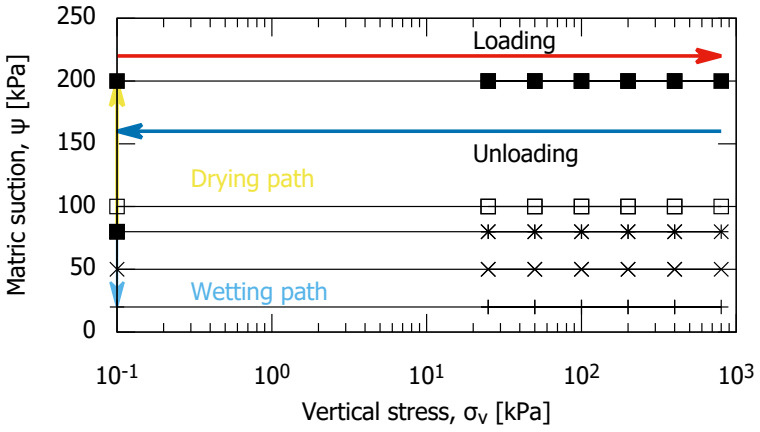

Figure 4.18: Suction controlled compression tests using ATT.

4.5.3 Wetting and drying tests at constant load

The wetting-drying experiments were conducted on an unsaturated soil sample with suction-controlled wetting-drying cycles under constant net stress. The soil specimen was initially loaded to a certain vertical total stress at an initial suction (11.2 MPa). The suction was then gradually reduced at a constant vertical net stress until it reached zero. The initial and boundary conditions of the soil samples were the same for all tests.

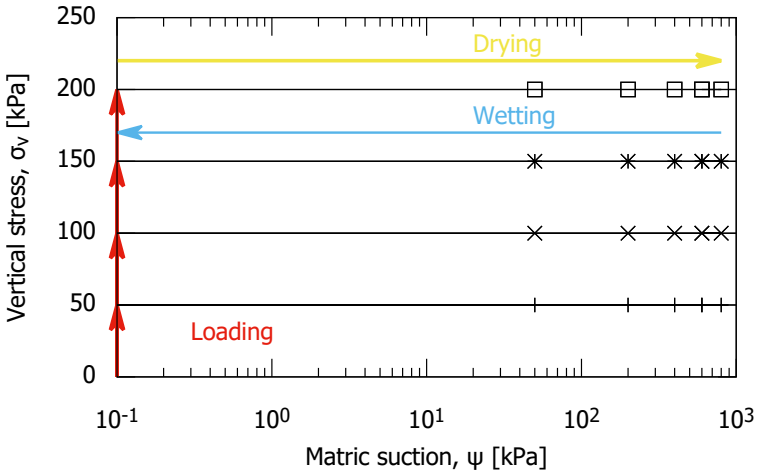

Figure 4.19: Tests with wetting and drying under constant net vertical stress using ATT

The Barcelona cell with axis translation technique was applied for suctions up to 800 kPa, and the Isochoric cell with VET was used to test remolded loess samples under vertical loading of 150 kPa at four different suction values. Stress paths are shown in Fig. 4.19, and collapse potential was calculated at the end of each suction level using Equ. 4.2. Changes in soil specimen volume and water content were measured throughout the test.

5 Experimental results

This chapter presents the experimental data obtained from the laboratory program and the related discussions of the results. The data are analyzed with emphasis on the comparison between remolded and undisturbed soil samples. The first section discusses the results of the single and double oedometer tests, with focus on the observed collapse behaviour for remolded and undisturbed samples. The subsequent section presents the results of shear strength investigations, by direct shear tests and triaxial tests for remolded and undisturbed samples. The third part of this chapter presents the determined soil-water characteristic curves, with a focus on the effect of cyclic drying and wetting on the SWCC. The fourth part of the chapter discusses the volumetric behavior of loess samples using results of suction-controlled oedometer tests. Finally, the obtained experimental data were used to determine the constitutive model parameters.

5.1 Collapse behaviour

5.1.1 Collapse potential as function of applied vertical stress determined from single and double oedometer tests

This section provides information about the collapse behaviour of samples at two different initial water contents and for a range of applied vertical stresses at inundation. Figs. 5.1 (a) and (b) illustrate the relationship between void ratio and applied vertical stress for single oedometer tests with various applied vertical stresses at inundation of the remolded loess soil, with initial water contents of 11.2% and 22.7%, respectively. The void ratio decrease before inundation in Fig. 5.1 indicates the compression due to mechanical loading at an unsaturated state. As seen in Fig. 5.1(a), this void ratio decrease before inundation is relatively small. Solely the curve of the sample flooded at a vertical stress of 800 kPa

shows an increased slope at higher stresses indicating that yield stress was reached before flooding.

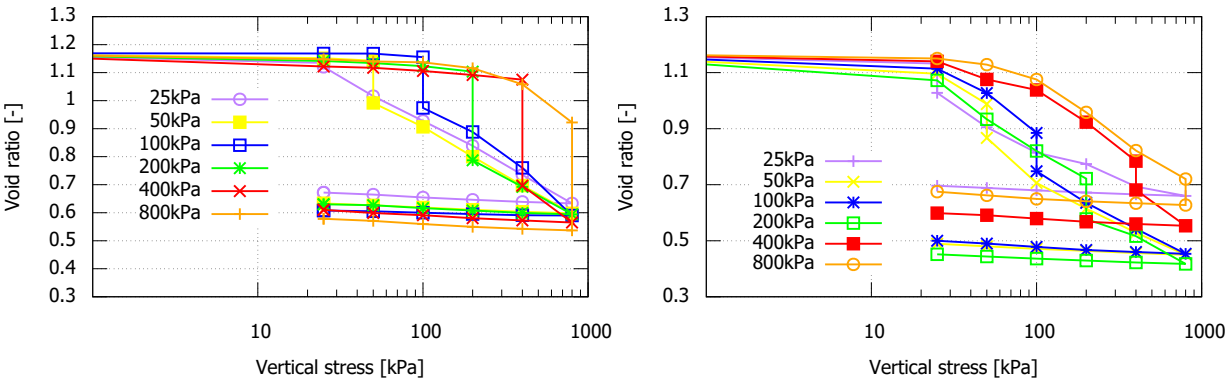

(a) (b)

Figure 5.1: Vertical stress vs. void ratio from single oedometer tests on remolded samples at two initial water contents (a) w_0=11.2%, and (b) w_0=22.7%.

Fig. 5.1(b) presents the collapse test results for an initial water content of 22.7%. The figure indicates that samples inundated at vertical stresses ranging from 50 kPa to 800 kPa enter the plastic zone before inundation. The differences in the compression curves can be attributed to variations in the initial water content (11.2%-43%) and degree of saturation, and in different degrees of saturation reached after wetting. Fig. 5.1(b) shows that initial void ratio was rather idential for all tested samples. The initial degree of saturation was different, due to variations in the initial water content. Different durations for wetting and loading stages can be a reason.

Figs. 5.1(a) and (b) show that loess shows collapse deformation in response to wetting at all values of applied vertical stress at the time of inundation. This collapse deformation is characterized by a sudden decrease in void ratio upon inundation. During inundation, the air phase is replaced by liquid water, and supporting capillary forces disappear, causing the collapse of macropores. The rate of collapse deformation is dependent on the rate of water access, which is influenced by the permeability of the loess.

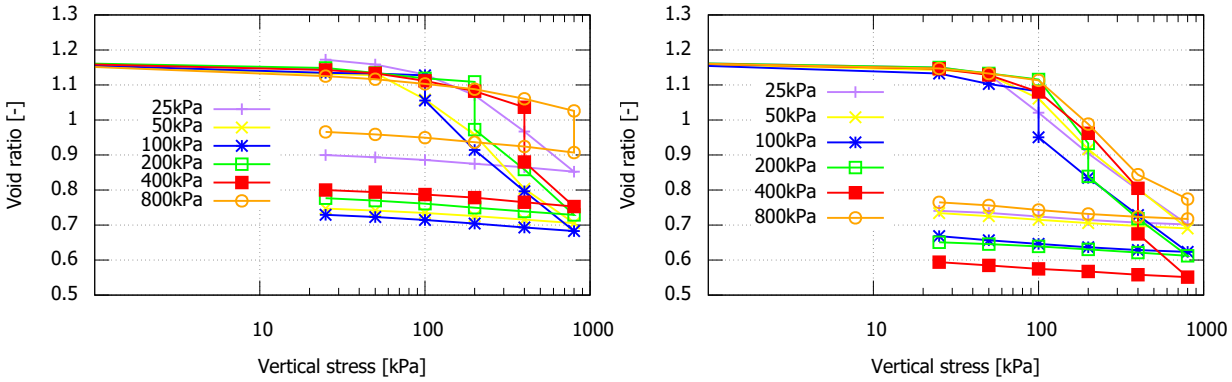

(a) (b)

Figure 5.2: Vertical stress vs. void ratio from single oedometer tests on undisturbed samples at two initial water contents (a) w_0=11.2%, and (b) w_0=22.7%.

Fig. 5.2 illustrates the respective results for the undisturbed loess soil samples. Only the samples wetted at applied vertical stress of 25 kPa and 50 kPa (as listed in Table 3.4) exhibited swelling deformation upon wetting, whereas all other samples at both initial water contents demonstrated collapse deformation. Upon wetting, water percolated through the samples, leading to a reduction in capillary tension and to the softening of the bonds and dissolving the aggregates assembly (Xie et al., 2018). With increasing water access, the structure's strength, contributed by the cementing bonding, decreases sharply and nearly approaches zero (Houston et al., 2001; Jiang, Li, Hu and Thornton, 2014; Derbyshire and Meng, 1995).

The degradation of inter-particle contacts is a major contributing factor to the collapse deformation. The destruction of bonding due to inundation is proportional to the degree of both heterogeneity and bonding (Dijkstra et al., 1995; Kie, 1988). In addition to the gravitational forces, there is also shear stress acting among soil particles, which cause smaller particles to slip into larger pore spaces, leading to the collapse of soil structure and deformation (Lawton et al., 1989). Under collapsed conditions, the particles attempt to rearrange themselves and compact into a new structure (Klukanova and Sajgalik, 1994). Eventually, after wetting the soil reaches a new equilibrium state. If the vertical stress is lower than the saturated pre-consolidation pressure for the sample, swelling deformation may occur. This was the case for the undisturbed samples at smaller water content of 11.2 %. Maximum collapse is observed when inundation occurs at an applied vertical stress close to the pre-consolidation pressure of the natural loess sample.

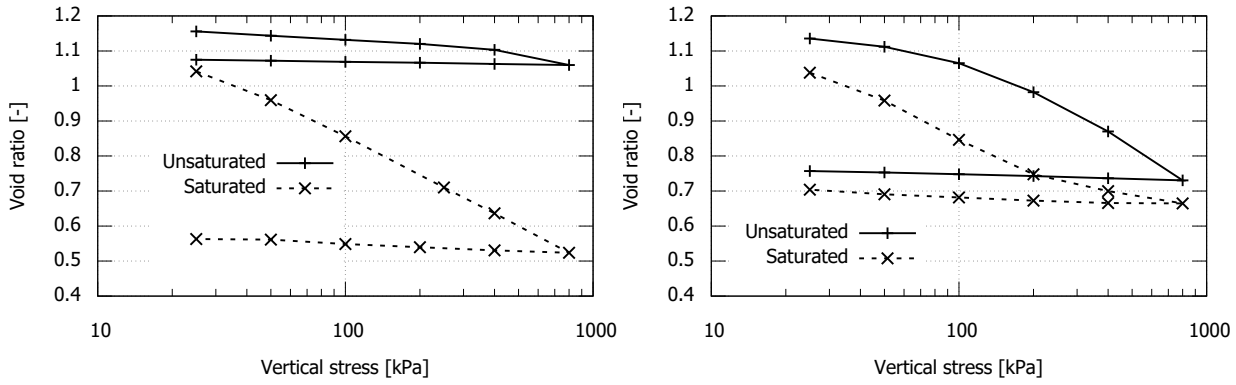

(a) (b)

Figure 5.3: Vertical stress vs. void ratio from double oedometer tests on remolded samples, for (a) w_0=11.2% and (b) w_0 =22.7%.

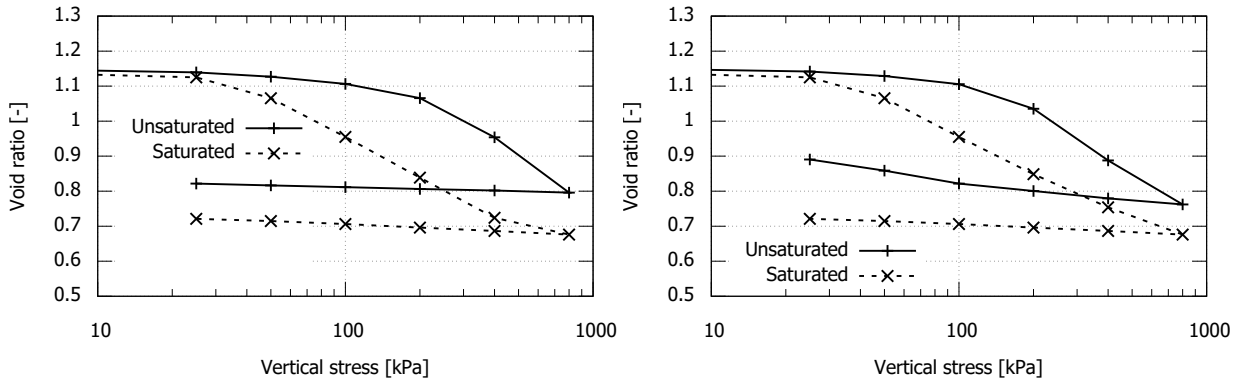

(a) (b)

Figure 5.4: Vertical stress vs. void ratio from double oedometer tests on undisturbed samples, for (a) w_0=11.2% and (b) w_0=22.7%.

The double oedometer tests (DOT) for both remolded and undisturbed samples at two different initial water contents are presented in Figs. 5.3 and 5.4. The collapse potentials obtained from SOT and DOT are compared in Fig. 5.5, and summarized in Table 5.1. It should be noted that the saturated sample in case of DOT was wetted after installation in the oedometer devices under zero vertical loading stress.

The collapse potential obtained from the double oedometer test is systematically larger than that obtained from the single oedometer test regardless of sample type and test conditions, as shown in Fig. 5.5(a) and Fig. 5.5(b). Fig. 5.5a further reveals that, in the case of remolded loess at smaller water content of 11.2%, the collapse potential increased with increasing the vertical stress for both test types (DOT and SOT). However, for the remolded sample with water content of 22.7%, the collapse potential exhibited a maximum at approximately 200 kPa for both single and double oedometer tests.

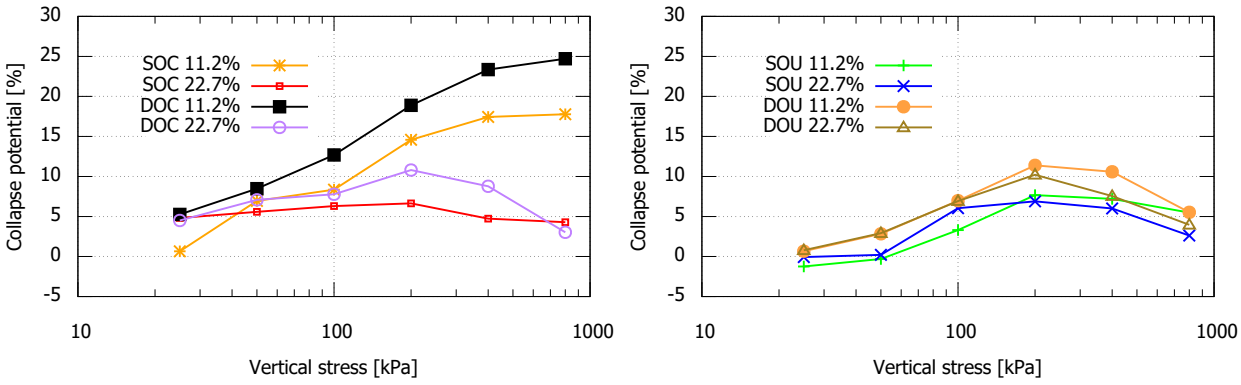

(a) (b)

Figure 5.5: Vertical stress vs. collapse potential of (a) remolded and (b) undisturbed samples at two initial water contents w_0=11.2%, and w_0=22.7%.

Table 5.1: Collapse potential (I_c[%]) of remolded and undisturbed samples

Sample type	w_0[%]	Test type	Vertical stress, $\sigma_v(kPa)$					
			25	50	100	200	400	800
Remolded	11.2	SOT	0.65	6.95	8.35	14.58	17.43	17.77
		DOT	5.26	8.48	12.69	18.89	23.35	24.71
	22.7	SOT	4.82	5.58	6.3	6.64	4.73	4.28
		DOT	4.51	7.08	7.72	10.81	8.77	3.03
Undisturbed	11.2	SOT	-1.24	-0.31	3.3	7.67	7.2	5.48
		DOT	0.67	2.84	6.97	11.39	10.59	5.52
	22.7	SOT	-0.067	0.21	6.04	6.89	6.01	2.61
		DOT	0.78	2.92	6.93	10.21	7.55	3.97

SOT: single oedometer test; DOT: double oedometer test.

For all undisturbed samples irrespective of their initial water content (Fig. 5.5b), the collapse potential determined from both the single and double oedometer tests initially increased until a maximum was reached at approximately 200 kPa applied vertical stress, after which it slightly decreased.

Overall, the SOT and DOT results demonstrate similar trends, as shown in Fig. 5.5. Specifically, the collapse potential of the remolded loess sample at a water content of 11.2% continuously increased with the applied vertical stress, while for remolded samples at a water content of 22.7% and undisturbed samples at both water contents, the collapse potential first increased to a maximum value and then decreased. This behavior can be attributed to the fact that remolded samples at a water content of 11.2% have higher resistance to deformation in the unsaturated state, resulting in a higher collapse potential at high applied stresses.

Both the unsaturated sample for the DOT and the sample for the SOT were prepared in the same manner. The soil structure before immersion was only affected by the applied vertical pressure. In the SOT, the collapse deformation of the unsaturated sample was caused only by water immersion at a given vertical applied stress. Under prior loading, the degree of saturation changed in case of the SOT, and the collapse deformation was affected by both pressure and water saturation.

In the double oedometer test, the initially saturated sample was loaded stepwise. Due to the long period of water immersion and resulting consolidation process, the double oedometer test's collapsibility coefficient was larger than that of the single oedometer test.

5.1.2 Effect of initial water content

This subsection presents and discusses only results of double oedometer tests on remolded samples. Fig. 5.6 illustrates the effect of the initial water content on the collapse potential, showing the calculated collapse potential for remolded samples with initial water contents of 11.2%, 18% and 22.7% under vertical applied stresses of up to 800 kPa. It shows that the collapse potential at a low initial water content of 11.2% increases continuously with increasing applied vertical stress, while for samples with initial water contents of 18% and 22.7%, a maximum collapse potential is reached at 200 kPa, which decreases with further stress increase.

In the DOT, there is no wetting induced saturation occurring. The observed behavior may be due to the high initial suction of the unsaturated sample with w_0=11.2%, which results in a much larger pre-consolidation pressure than for the samples with w_0=18% and w_0=22.7%. The smaller pre-consolidation pressure of the samples with w_0=18% and w_0=22.7% leads to greater deformation at the unsaturated state under larger stresses, thereby reducing the collapse potential. Additionally, the higher initial degree of saturation in samples with w_0=18% and w_0=22.7% explains their smaller collapsibility, see Table 5.2.

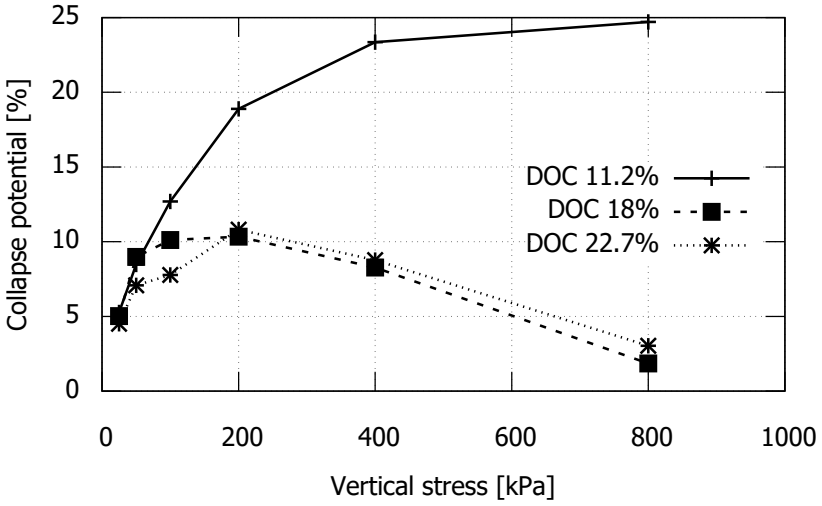

Figure 5.6: Vertical stress vs. collapse potential (%) of the remolded samples for various values of the initial water content.

Table 5.2: Collapse potential [%] of remolded samples

Sample type	w_0[%]	Test type	Vertical stress, $\sigma_v(kPa)$					
			25	50	100	200	400	800
Remolded	11.2	DOT	5.26	8.48	12.69	18.89	23.35	24.71
	18	DOT	5.03	8.98	10.11	8.27	8.27	1.85
	22.7	DOT	4.51	7.08	7.72	10.81	8.77	3.03

5.1.3 Effect of sample structure

Fig. 5.7 and Fig. 5.8 compare the relationships between the collapse index and the applied vertical stress at inundation for remolded and undisturbed samples, showing the data for double oedometer tests and single oedometer tests with two different initial water contents.

Both figures demonstrate that the remolded samples with $w_0 = 11.2\%$ exhibit a greater collapse potential than the respective undisturbed samples. For higher initial water content of 22.7% the remolded samples show the higher collapse index only in a stress range up to 100 kPa.

The undisturbed samples underg less collapse upon wetting then the remolded samples. The collapse index increases with increasing stress up to a certain applied vertical stress at inundation, which depends on the stress history and sedimentation process. Especially the low collapse index at small stresses indicates that the bonding in the undisturbed samples only partially breaks down under wetting at lower stresses.

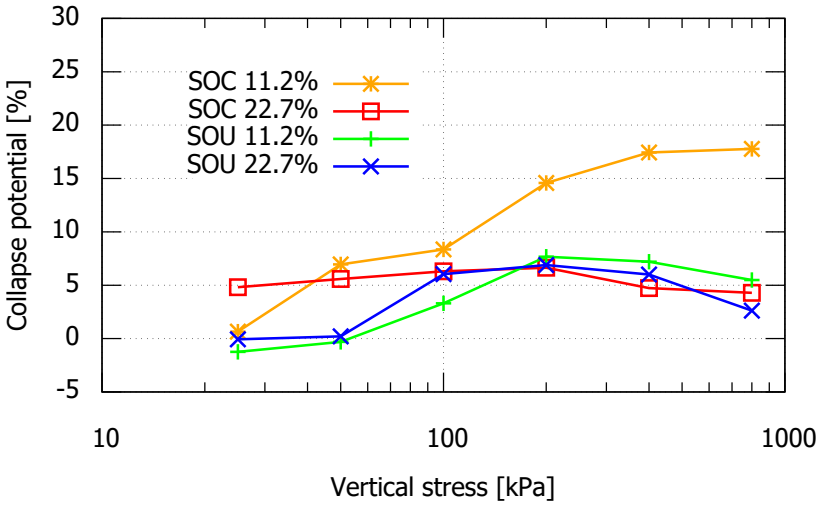

Figure 5.7: Vertical stress vs. collapse potential from single oedometer tests (noted as SOC for remolded sample and SOU for undisturbed sample).

In general, the stronger bonding in undisturbed samples leads to less collapsibility, while the weaker particle arrangement in remolded samples results in greater collapsibility. This is because the undisturbed samples have been subjected to higher levels of vertical stress in their history, which has resulted in long-term bonding during the sedimentation

process. This bonding helps to resist the collapse of the sample upon wetting (Osipov and Sokolov, 1995, Assallay et al., 1997, and Feda et al., 1995).

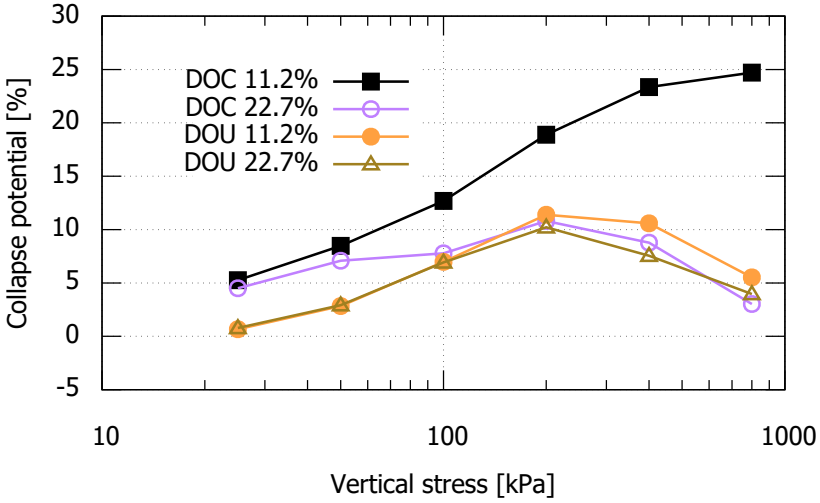

Figure 5.8: Vertical stress vs. collapse potential from double oedometer test (noted as DOC for remolded sample and DOU for undisturbed sample).

The interconnectivity between silt particles is provided by clay particles, humus colloids, and soluble salts, which further enhance the structure of the loess soil (Dijkstra, 2001). This underlying structure is responsible for the peak collapsible loading of undisturbed loess, even under low initial water content. When an external force destroys the natural structure of unsaturated loess, the bonding force due to cementation gradually relaxes. As a result, the difference between the compression curves of remolded and undisturbed loess samples gradually disappears with increasing stress (see Fig. 5.8).

However, for high initial water content, the collapsibility coefficient of undisturbed loess and remolded compacted loess is almost equal (Fig. 5.8). This is because as the initial water content increases, a weaker cementation is observed in the undisturbed loess, resulting in significant plastic compressive deformation accompanied by considerable destructuration. During the subsequent saturation, the undisturbed loess undergoes collapse deformation similar to that of remolded loess (Fig. 5.8).

5.2 Shear strength

The shear strength of both undisturbed and remolded loess samples was investigated using single-stage and multi-stage direct shear tests and triaxial tests. Essentially, the effects of initial water content, sample state (undisturbed vs. remolded) and testing technique employed (single-stage vs. multi-stage direct shear tests) on the shear strength are discussed in this section.

5.2.1 Single-stage direct shear tests: effect of initial water content and sample state

Figs. 5.9 to 5.13 display the results of single-stage direct shear tests conducted on remolded soil samples with different initial water content values (11.2%, 16%, 18%, 22.7% and about 43% corresponding to saturated condition). Details of the initial test conditions can be found in Tables 3.6 and 3.7 in Section 3. The graphs show the relationship between shear stress and horizontal displacement (Figs. 5.9(a) to 5.13(a)) and between vertical and horizontal displacement (Figs. 5.9(b) to 5.13a(b)), with positive values of vertical displacement indicating dilation and negative values indicating contractive behavior during shear. The graphs illustrate the effect of normal stress on the shear behavior for samples with different water content. Samples with water contents between 11.2% and 18% subjected to low normal stress (50 kPa) exhibited softening behavior with dilatant volumetric deformation whereas the samples subjected to 100 kPa and 150 kPa normal stress showed contractive behaviour. This is consistent with observations reported by Cui and Delage (1996) and Hossain and Yin (2010). Samples with a water content of 22.7% and the saturated samples exhibited hardening behavior accompanied by volume reduction for all values of the applied normal stress.

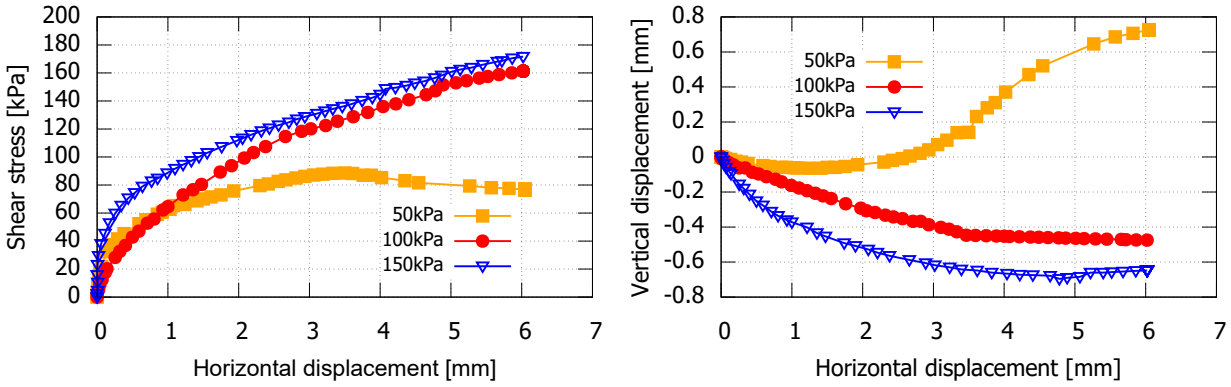

(a) (b)

Figure 5.9: Single-stage direct shear tests on remolded samples with w_0=11.2%, (a) shear stress vs. horizontal displacement, and (b) vertical vs. horizontal displacements.

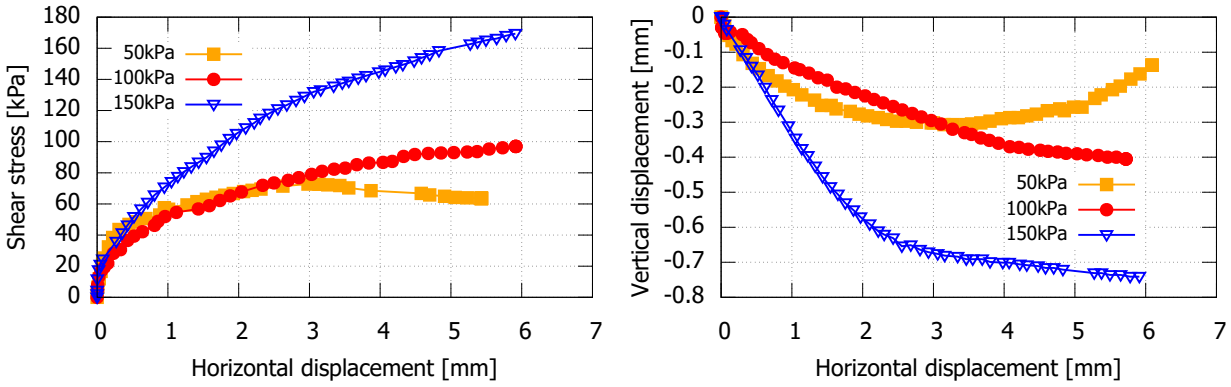

(a) (b)

Figure 5.10: Single-stage direct shear tests on remolded samples with w_0=16%, (a) shear stress vs. horizontal displacement, (b) vertical vs. horizontal displacements.

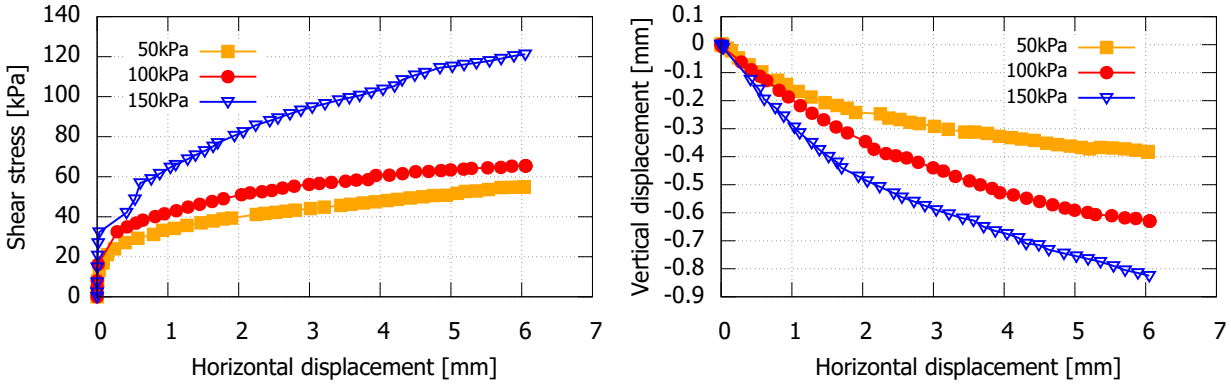

(a) (b)

Figure 5.12: Single-stage direct shear tests on remolded samples with w_0=22.7%, (a) shear stress vs. horizontal displacement, (b) vertical vs. horizontal displacements.

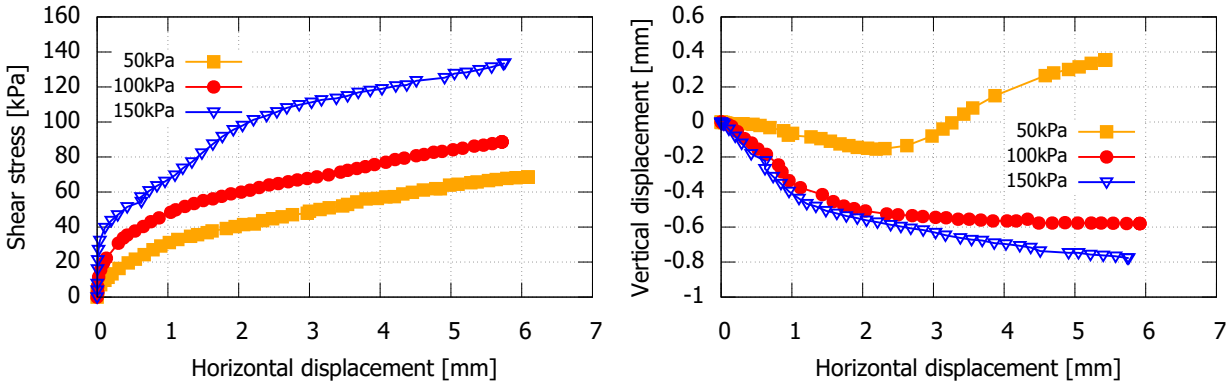

(a) (b)

Figure 5.11: Single-stage direct shear tests on remolded samples with w_0=18%, (a) shear stress vs. horizontal displacement, (b) vertical vs. horizontal displacements.

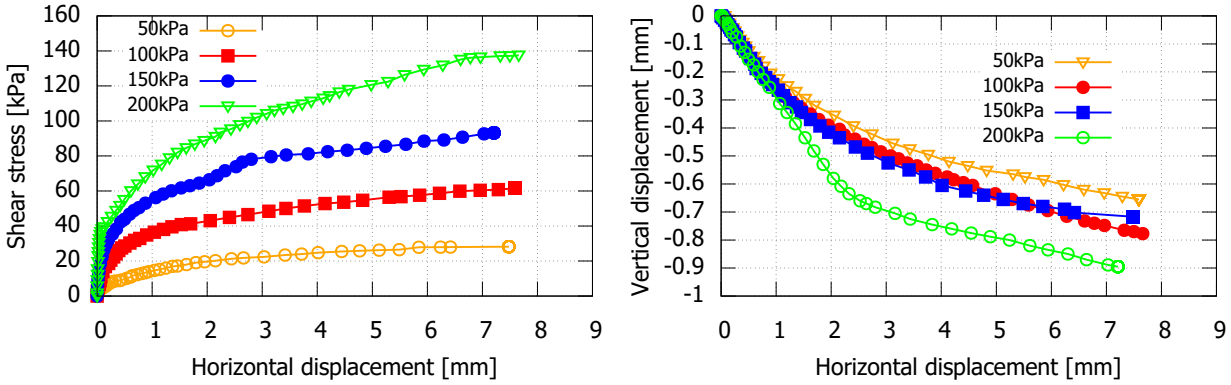

(a) (b)

Figure 5.13: Single-stage direct shear tests on the saturated remolded samples, (a) shear stress vs. horizontal displacement, (b) vertical vs. horizontal displacements.

The results of the tests depicted in Fig. 5.9 to Fig. 5.13 reveal that both the vertical stress and water content have significant impacts on the shear strength of unsaturated loess soil. In general, at a given normal stress, the peak shear stress decreased with increasing water content. The effect of initial water content on the volumetric behaviour was most pronounced for the samples at 50 kPa normal stress, where the observed behaviour changed from dilative to contractive with increasing water content.

The residual shear strength is typically assumed to be reached when there are no further changes in both volume and shear stress during the shearing process. However, the

results of this study suggest that residual state may not have been achieved, as dilation or contraction were still observed even at horizontal displacements as large as 7 mm. In other studies (Kayadelen et al., 2007 and Alsherif and McCartney, 2016), similar observations were made. They found that the residual state could not be achieved for compacted silt that was sheared at high suctions, thus, low water content resulting in a hardening type of failure.

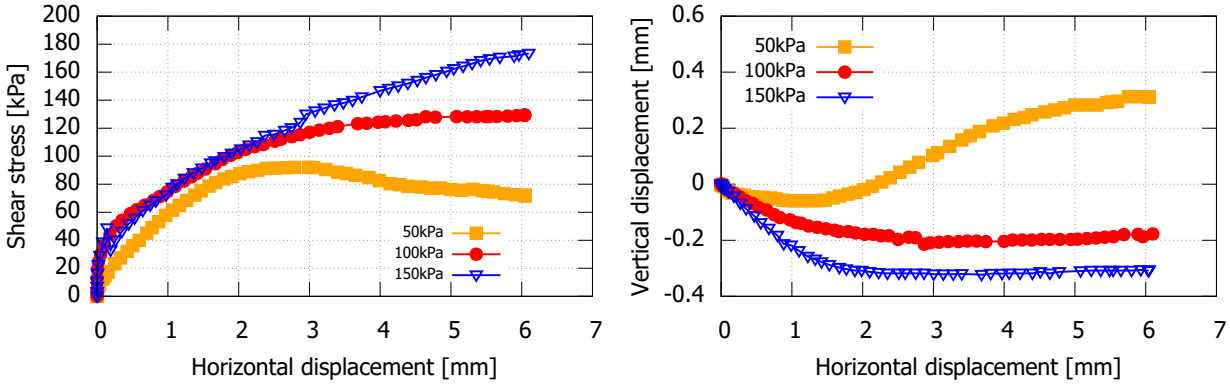

(a) (b)

Figure 5.14: Single-stage direct shear tests on undisturbed samples with w_0=11.2%, (a) shear stress vs. horizontal displacement, (b) vertical vs. horizontal displacements.

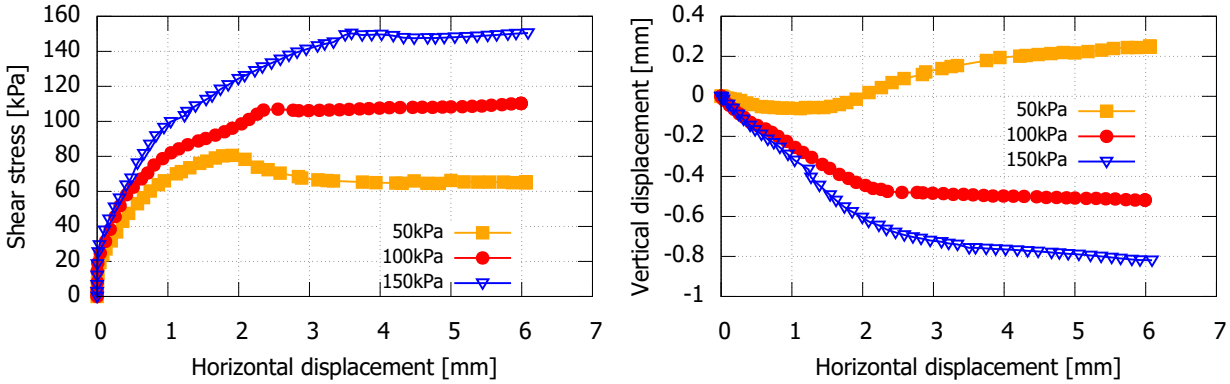

(a) (b)

Figure 5.15: Single-stage direct shear tests on undisturbed samples with w_0=22.7%, (a) shear stress vs. horizontal displacement, (b) vertical vs. horizontal displacements.

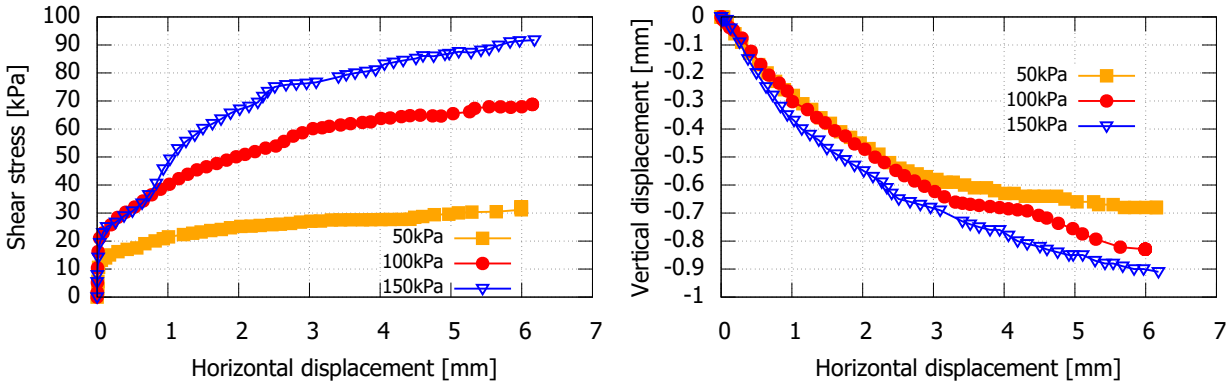

(a) (b)

Figure 5.16: Single-stage direct shear tests on saturated undisturbed samples, (a) shear stress vs. horizontal displacement, (b) vertical vs. horizontal displacements.

Fig. 5.14 to Fig. 5.16 illustrate the single-stage test results on the undisturbed samples for water contents of 11.2%, 22.7% and for the saturated state with about 43% water content. Fig. 5.14(a) to Fig. 5.16(a) show the shear stress vs. horizontal displacement, while Fig. 5.14(b) to Fig. 5.16(b) show the vertical vs. horizontal displacements. In general, the trends are similar to the remolded samples: at normal stresses of 100 and 150 kPa contractive behaviour with hardening was observed at unsaturated and saturated states, whereas at low normal stress of 50 kPa dilative behaviour with softening occured for the unsaturated states (Figs. 5.14 and 5.15) and changing to contractive behaviour for the saturated state. However, the undisturbed sample with w=22.7% sheared at 50 kPa still exhibited dilative behaviour (Fig. 5.15) whereas the remolded sample with the same water content showed already contractive behaviour (Fig. 5.12). When the sample is subjected to large vertical loading (100 and 150 kPa), the applied normal stress is greater than the pre-consolidation pressure, and the soil follows a normally consolidated behavior. The primary structure is destroyed by prior consolidation and a new structure is formed. During shearing, the soil sample is compressed, which is reflected in a relatively smooth increase in shear stress with increasing horizontal displacement, as shown in Fig. 5.16a. When undisturbed loess soil is subjected to a small load of 50 kPa, this load is not enough to change its original structure and the consolidation deformation before shearing is small.

The observed effect of water content on the type of shear behaviour was interpreted such that increasing suction, thus decreasing water content, leads to stronger particle contacts, resulting in more brittle behaviour (Jotisankasa and Mairaing, 2009).

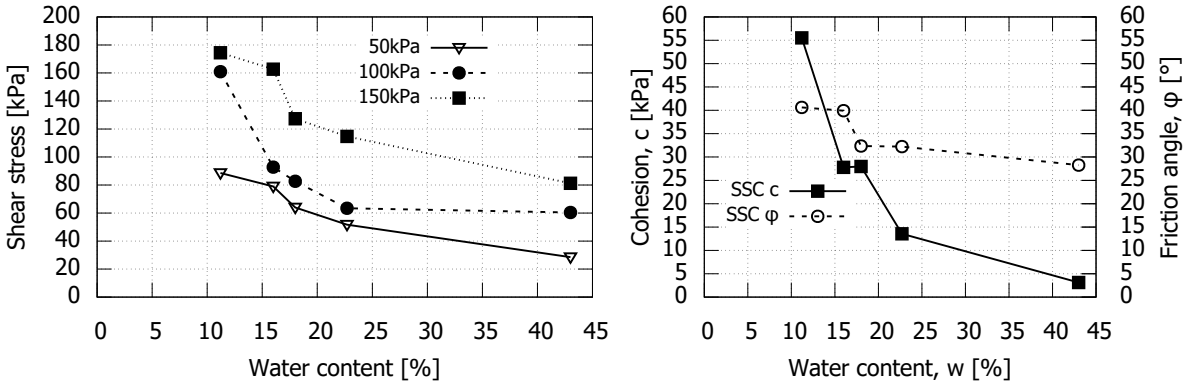

(a) (b)

Figure 5.17: Single-stage shear tests on remolded samples, (a) peak shear stress vs. water content, and (b) shear strength parameters vs. water content.

Fig. 5.17(a) displays the maximum shear stress reached in the tests versus water content, while Fig. 5.17(b) shows the cohesion and friction angle deduced for each test series for the remolded samples. The corresponding values are summarized in Tables 5.3 and 5.4. As shown in Fig. 5.17(a) and (b), both the maximum shear stress and the shear strength parameters decrease as the initial water content increases. However, the effect on cohesion is more significant than that on the friction angle. This is because a higher initial moisture content in the soil sample leads to the dissolution of cementation substances and thicker water film between the loess particles, thus reducing cohesion.

Table 5.3: Shear strength [kPa] of remolded samples from single-stage shear tests.

Water content (%)	Vertical loading, σ_v (kPa)		
	50	100	150
11.2	88.6	160.9	174.4
16	79.0	92.8	162.7
18	64.0	82.7	127.3
22.7	51.7	63.4	114.7
43	28.5	60.41	81.2

Table 5.4: Shear strength parameters of remolded samples from single-stage shear tests.

Water content (%)	Cohesion, c' (kPa)	Friction angle, ϕ' (°)
11.2	55.5	40.6
16	27.8	39.9
18	28.0	32.4
22.7	13.6	32.2
43	4.0	27.8

In comparison to the fully saturated state, unsaturated loess soil exhibits higher shear strength due to the matric suction, which increases as water content decreases. This results in an increase in the apparent cohesion of the soil, ultimately leading to a higher shear strength. Studies with unsaturated shear tests confirm this trend, showing an increase in both peak and residual shear strength as water content decreases (Section 2.4.4).

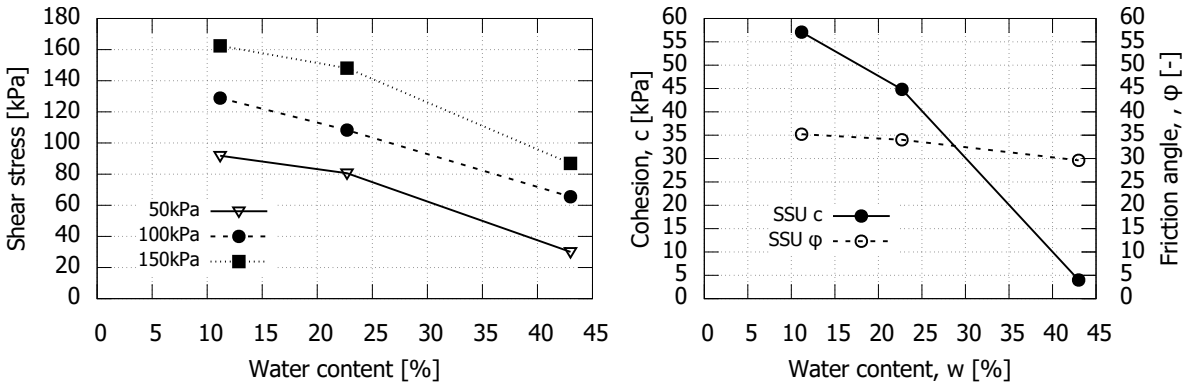

(a) (b)

Figure 5.18: Single-stage shear tests on the undisturbed samples, (a) peak shear stress vs. water content, and (b) shear strength parameters vs. water content.

Fig. 5.18 shows the test results for the undisturbed samples, revealing how the water content affects the peak shear strength under different levels of applied vertical loading and the shear strength parameters. The corresponding values are summarized in Tables 5.5 and 5.6. The data indicates that both cohesion and friction angle decrease as the water content increases. Although the decrease in friction angle is less significant than that of cohesion, it is still noticeable.

Comparing the shear strength parameters obtained for the undisturbed (Tab. 5.6) and the remolded (Tab. 5.4) samples, the cohesion and friction angle of both sample types are very similar in the water-saturated state (see Fig. 5.19). At the water content 11.2%, the friction angle of the remolded sample ($\phi' = 40.6°$) was larger than the one of the undisturbed sample ($\phi' = 35.2°$), while cohesion did not differ much (55.5 and 57.1 kPa). At $w_0 = 22.7\%$, the friction angle of the undisturbed sample was only slightly greater (34.0° vs. 32.2°), whereas the cohesion of the undisturbed sample (44.8 kPa) significantly exceeded the corresponding value of the remolded one (13.6 kPa).

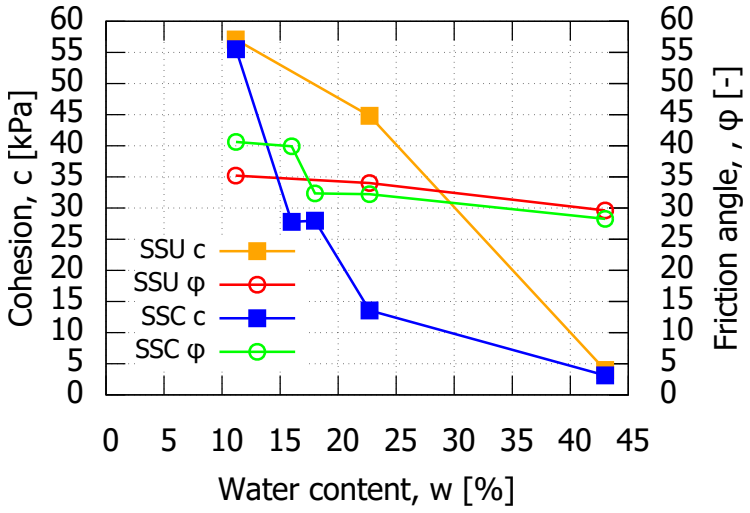

Figure 5.19: Shear strength parameters vs. water content from the single-stage shear tests on the remolded undisturbed samples.

Table 5.5: Peak shear strength [kPa] of the undisturbed samples from single-stage shear tests.

Water content (%)	Vertical loading, σ_v (kPa)		
	50	100	150
11.2	91.8	128.9	162.4
22.7	80.6	108.3	148.1
43	30.1	65.5	87.0

Table 5.6: Shear strength parameters of undisturbed samples from single-stage shear tests.

Water content, w_0 (%)	Cohesion, c' (kPa)	Friction angle, ϕ' (°)
11.2	57.1	35.2
22.7	44.8	34.0
43	3.9	29.6

5.2.2 Multi-stage direct shear test results: effect of initial water content and sample state

Results of multi-stage tests on saturated and unsaturated remolded samples are presented in Figs. 5.20 to 5.23. During all loading stages in the multi-stage shear tests only contractive behaviour with hardening was observed. The figures demonstrate that there is no evidence of shear softening with dilatant behaviour during the loading stage at 50 kPa. This is due to the limited horizontal displacement allowed during shear. Comparing Fig. 5.20(b) to Fig. 5.9(b), it is visible that for the single-stage test (Fig. 5.9(b)), dilation started at a horizontal displacement of 1.8 to 2 mm, whereas in the multi-stage test (Fig. 5.20(b)), the shear phase was stopped before dilation could occur.

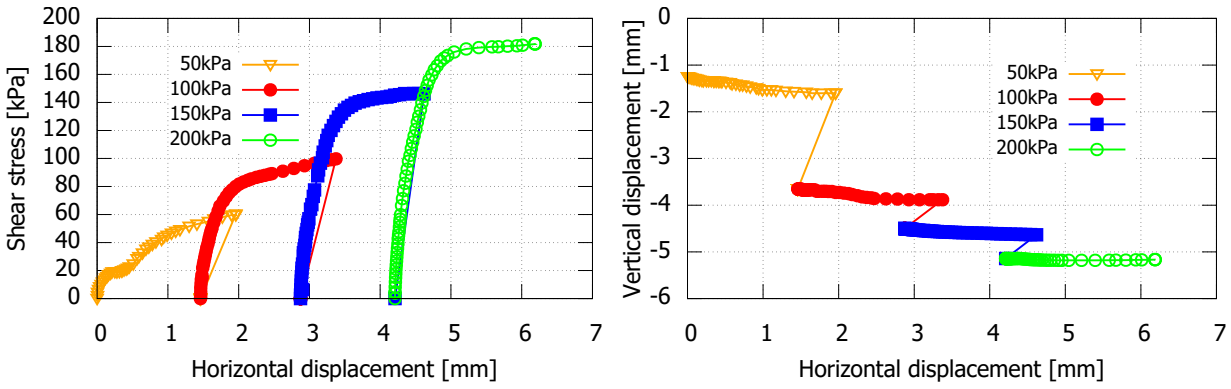

(a) (b)

Figure 5.20: Multi-stage direct shear tests on remolded samples with $w_0 = 11.2\%$, (a) Shear stress vs. horizontal displacement, and (b) vertical vs. horizontal displacements.

Table 5.7 and Table 5.8 summarize the maximum shear stress and the shear strength parameters derived from the multi-stage shear tests for the remolded samples.

Figs. 5.24 and 5.25 present the results of the multi-stage tests conducted on the undisturbed loess samples. The plots of shear stress versus horizontal displacement for different normal stresses are shown in Figs. 5.24(a) and 5.25(a), while Figs. 5.24(b) and 5.25(b) display the plots of vertical versus horizontal displacements. All the curves exhibit strain hardening behavior accompanied by compression.

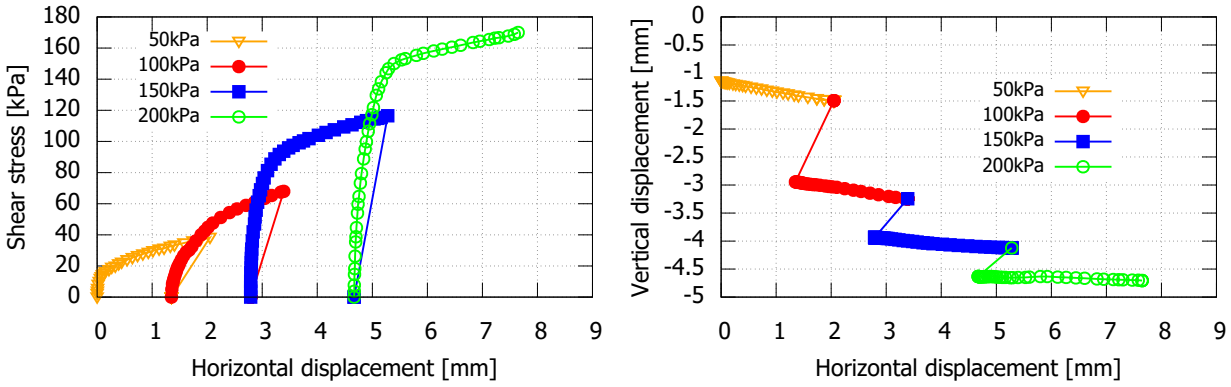

(a) (b)

Figure 5.21: Multi-stage direct shear tests on remolded samples with $w_0 = 16\%$, (a) Shear stress vs. horizontal displacement, (b) vertical vs. horizontal displacements.

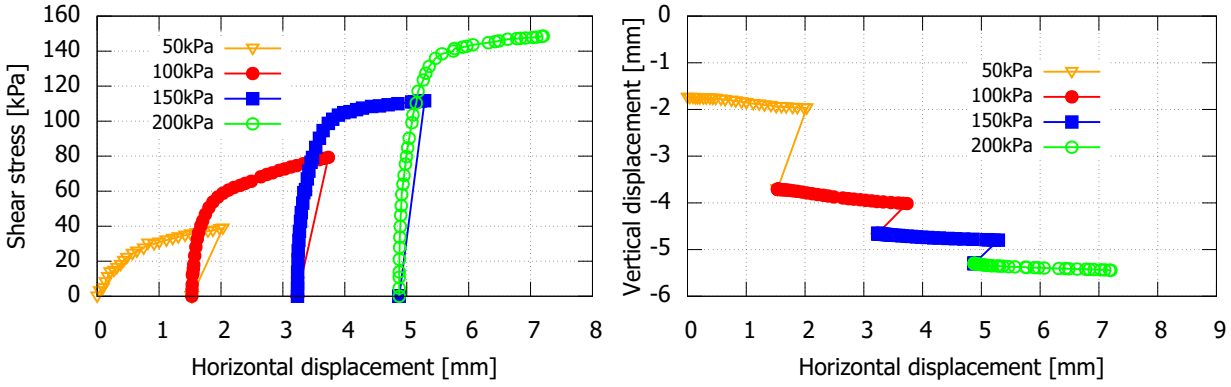

(a) (b)

Figure 5.22: Multi-stage direct shear tests on remolded samples with $w_0 = 22.7\%$, (a) Shear stress vs. horizontal displacement, (b) vertical vs. horizontal displacement.

Table 5.7: Shear strength (kPa) of remolded loess from multi-stage shear tests.

Water content (%)	Vertical loading, σ_v (kPa)			
	50	100	150	200
11.2	78.3	107.9	156.5	208.8
16	60.3	99.7	146.1	181.9
22.7	37.6	79.3	111.7	140.6
43	26.2	52.0	69.1	99.7

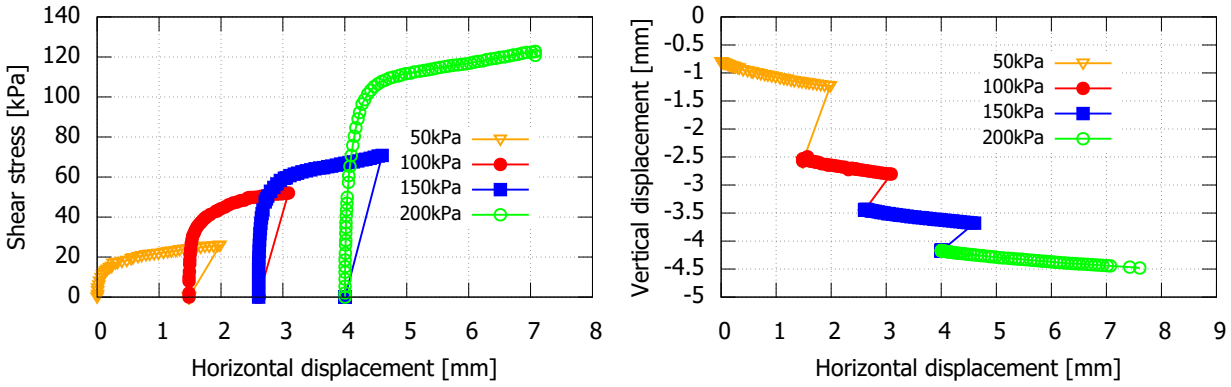

(a) (b)

Figure 5.23: Multi-stage direct shear tests on saturated remolded samples with $w_0 = 43\%$, (a) Shear stress vs. horizontal displacement, (b) vertical vs. horizontal displacements.

Table 5.8: Shear strength parameters of remolded loess from multi-stage shear tests.

Water content, w_0 (%)	Cohesion, c' (kPa)	Friction angle, ϕ' (°)
11.6	27.9	41.3
16	19.2	39.4
22.7	7.0	34.3
43	2.4	25.4

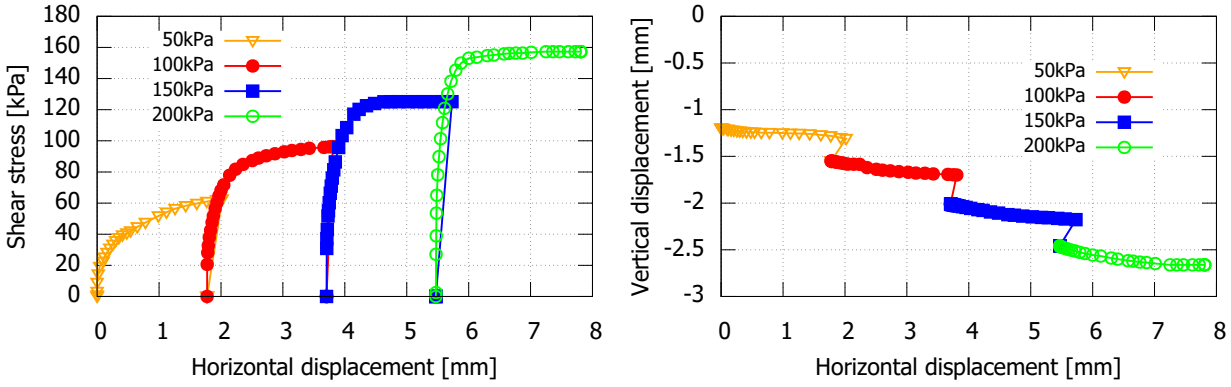

(a) (b)

Figure 5.24: Multi-stage direct shear tests on undisturbed samples with $w_0 = 22.7\%$, (a) Shear stress vs. horizontal displacement, (b) vertical vs. horizontal displacements.

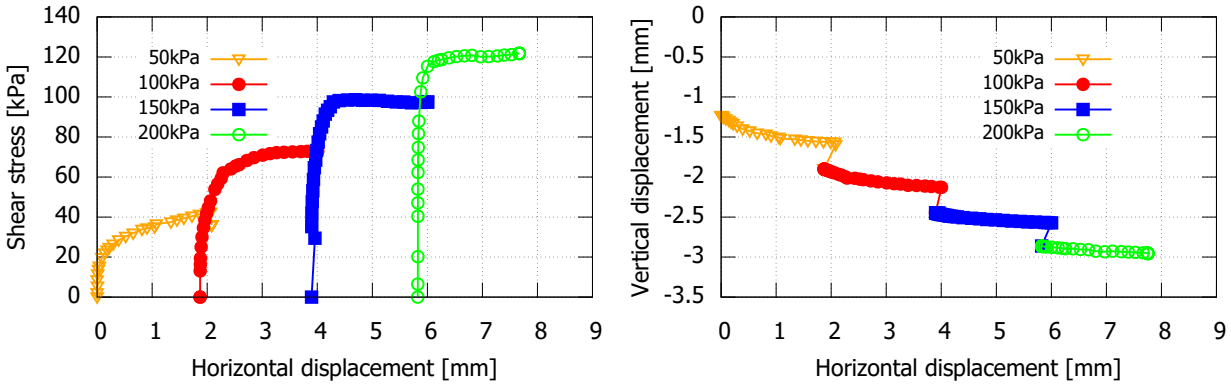

(a) (b)

Figure 5.25: Multi-stage direct shear tests on saturated undisturbed samples, (a) Shear stress vs. horizontal displacement, (b) vertical vs. horizontal displacements.

The failure shear stress was determined at the end of each shearing phase, corresponding to a horizontal displacement of approximately 2 mm, as shown in Figs. 5.24(a) and 5.25(a). The values as well as the shear strength parameters derived from the multi-stage tests on undisturbed samples are summarized in Tables 5.9 and 5.10.

Table 5.9: Peak shear strength of the undisturbed loess from multi-stage shear tests.

Water content	Vertical loading, σ_v (kPa)			
	50	100	150	200
22.7	36.0	72.9	97.5	121.8
43	62.5	96.3	125.2	157.3

Table 5.10: Shear strength of undisturbed loess from multi-stage shear tests.

Water content, w_0 (%)	Cohesion, c' (kPa)	Friction angle, ϕ' (°)
22.7	32.03	32.05
43	11.55	29.41

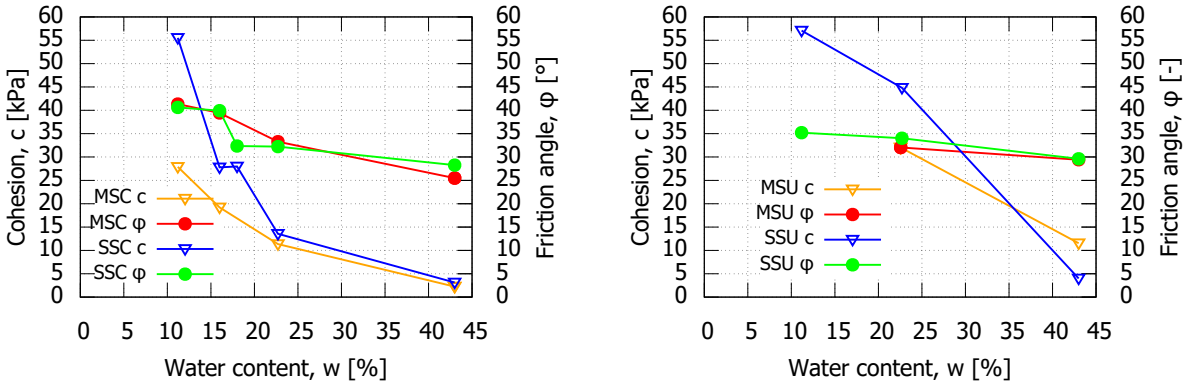

Figure 5.26: Shear strength parameters as function of water content from multi-stage (MSC) and single stage (SSC) shear tests, (a) Remolded loess, (b) Undisturbed loess.

Fig. 5.26 compares the values of cohesion and friction angle obtained from the single- and multi-stage shear tests for different water contents and sample types (remolded or undisturbed). The diagrams show that the multi-stage direct shear test results exhibit lower cohesion compared to the single-stage shear test results for both remolded and undisturbed loess samples at low water content (11.2% - 22.7%). This difference in cohesion may be attributed to the soil microstructure, characterized with relict joints and discontinuities that are sensitive to the disturbances inherent in the primary stage of multi-stage shear testing. The cementation bonding of the undisturbed loess is gradually broken down over successive shearing stages. In contrast, Fig. 5.26 reveals that the values of friction angle obtained from the single- and multi-stage tests are quite similar, independently of the water content and the sample type (remolded or undisturbed).

5.2.3 Evaluation of direct shear tests using suction stress concept

The suction stress can be calculated by determining the point at which the shear stress envelope intersects the horizontal axis in the shear stress-normal stress coordinate system, as depicted in the upper diagram of Fig. 5.27. The single-stage direct shear tests on the remolded samples at varying water contents, corresponding to varying degrees of saturation, were used to determine the suction stress of the samples. Suction stress represents the effective stress of a sample at zero external applied stress (see Section 2.3.7). Once determined, the suction stress of each sample is plotted against its initial

degree of saturation, as illustrated in the lower diagram of Fig. 5.27. The magnitude of suction stress continuously decreases with increasing degree of saturation.

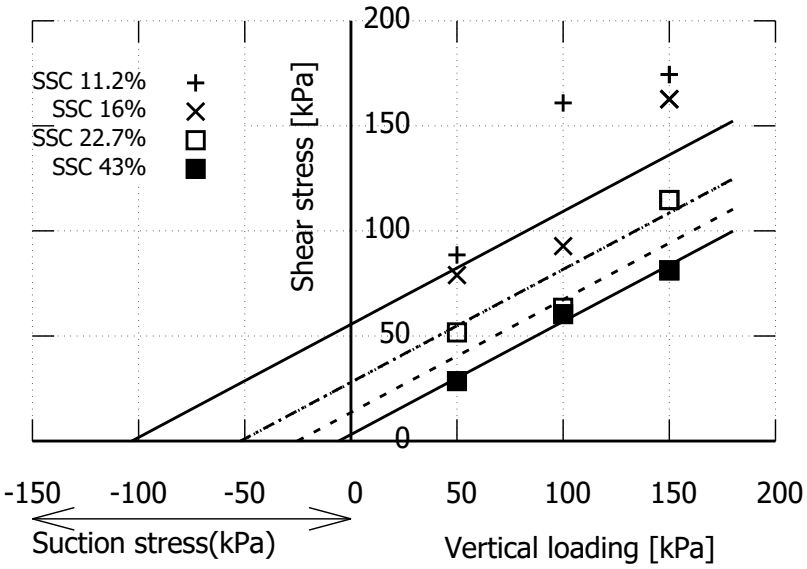

(a)

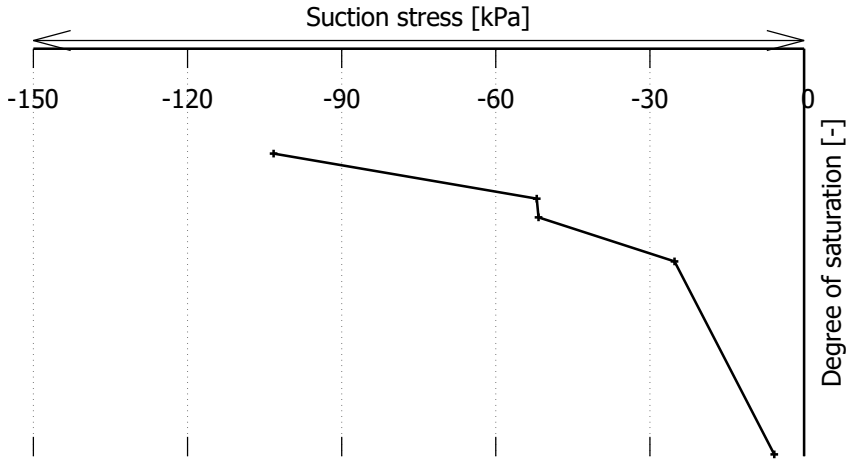

(b)

Figure 5.27: Suction stress and shear strength.

5.2.4 Shear strength from drained triaxial tests

Figs. 5.28 and 5.29 illustrate the results of consolidated drained triaxial tests on remolded loess samples corresponding to sample Nos. CDC41, CDC42 and CDC43 in Table 3.8. The initial void ratio and water content were 1.12 and 22.7%, respectively. The samples were saturated prior to shearing. Fig. 5.28(a) shows that the stress-strain curves are significantly influenced by the confining pressure in the consolidated drained tests. As the initial mean effective stress increased, so did the peak deviator stress. At all three confining stresses the samples show contractive behaviour, as visible in the curves of volumetric versus axial strain in Fig. 5.28(b).

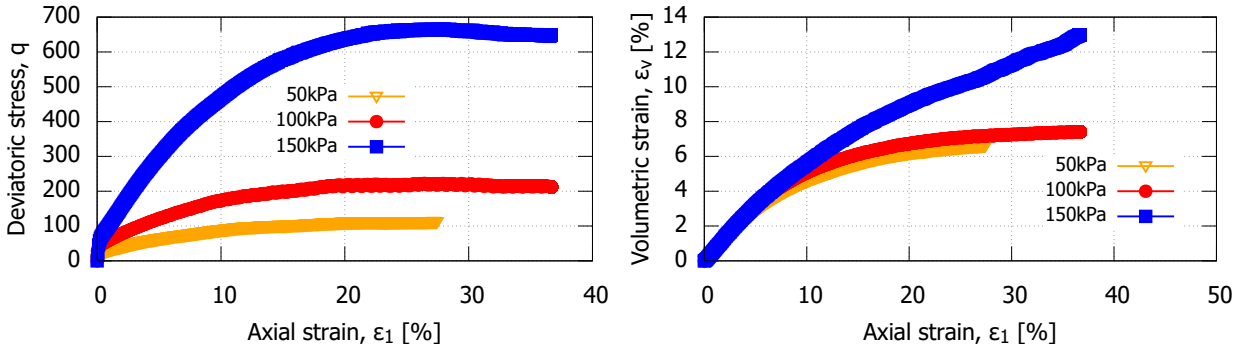

(a) (b)

Figure 5.28: Results of drained triaxial compression tests on remolded loess samples, (a) Deviatoric stress vs. axial strain, and (b) Volumetric strain vs. axial strain.

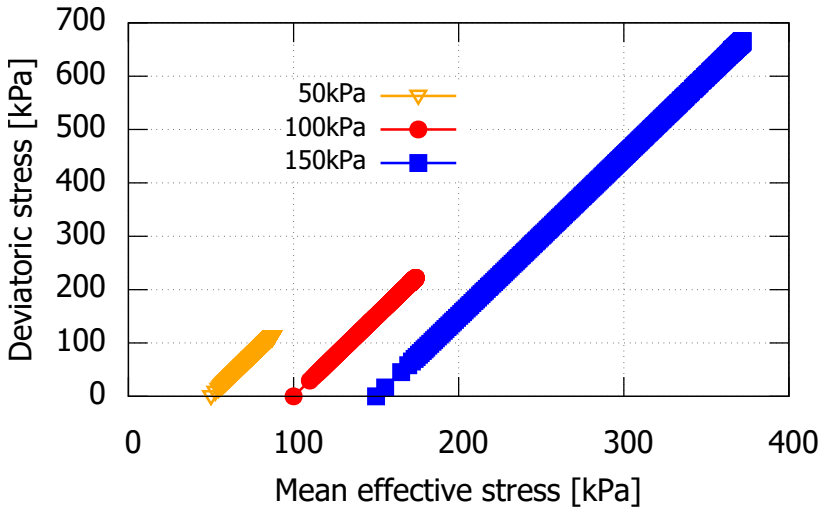

Figure 5.29: Deviatoric stress vs. mean effective stress - remolded loess samples.

The results of the drained triaxial compression tests on the undisturbed samples CDU11, CDU12, and CDU13 (Table 3.8) are presented in Figs. 5.30 and 5.31. The deviatoric stresses reached at 50 kPa and 100 kPa effective confining stress are significantly greater than for the corresponding remolded samples. At all three confining stresses, the samples exhibit contractive volumetric behaviour with similar magnitudes of volumetric strains (Fig. 5.30(b)). Further, they show hardening behavior, followed by plastic failure after obvious yielding and plastic deformation.

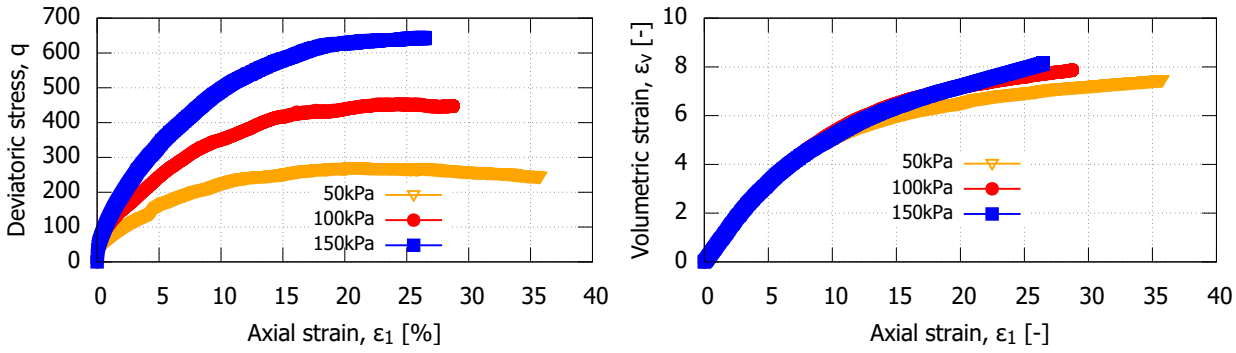

(a) (b)

Figure 5.30: Results of drained triaxial compression tests on undisturbed loess samples, (a) Deviatoric stress vs. axial strain, and (b) Volumetric strain vs. axial strain.

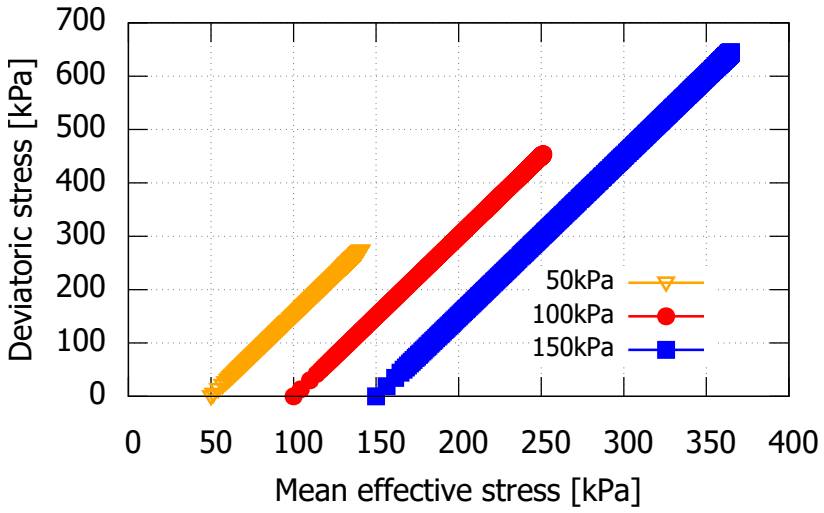

Figure 5.31: Mean effective stress vs. deviatoric stress - undisturbed loess samples.

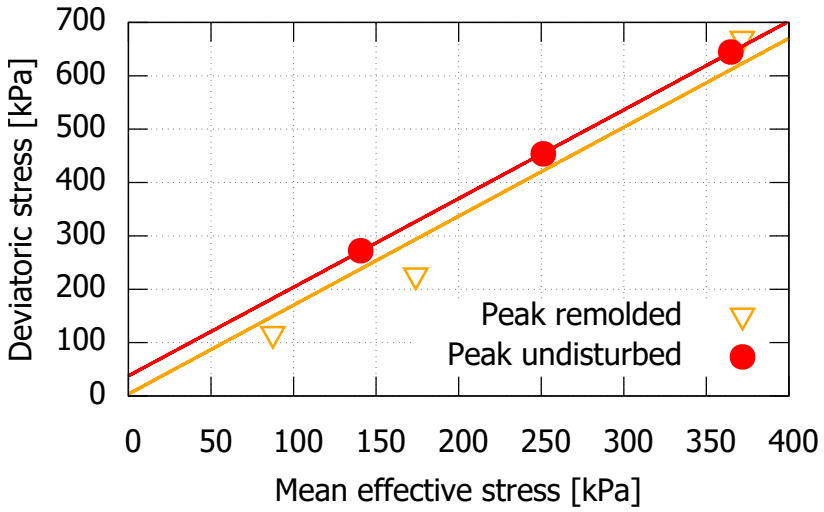

Figure 5.32: Peak shear stress from drained triaxial compression tests on remolded (CDC) and undisturbed samples (CDU).

Table 5.11: Deviatoric stress q (kPa) and corresponding mean effective stress p' (kPa) at peak stress and critical state (CS) from drained triaxial compression tests.

		Sample state	Initial mean effective stress, p'_0 (kPa)		
			50	100	150
Peak	$p';q$	Remolded	87.47; 112.42	174.01; 222.04	371.79; 665.38
Peak	$p';q$	Undisturbed	140.71; 272.12	251.24; 453.72	364.82; 644.46
CS	$p';q$	Remolded	87.34; 112.02	170.74; 212.23	366.04; 648.11
CS	$p';q$	Undisturbed	131.75; 245.24	249.11; 447.32	364.11; 642.33

Table 5.12: Shear strength parameters from drained triaxial compression test.

Sample	Cohesion, c' (kPa)	Friction angle, ϕ' (°)
Remolded at CS	0.00	40.66
Undisturbed at CS	10.73	41.69
Remolded at peak	0.00	41.13
Undisturbed at peak	19.41	40.59

The values of the deviatoric stresses and the corresponding mean effective stresses reached at peak and at critical state and the deduced shear strength parameters effective cohesion

and effective friction angle are provided in Table 5.11 and Table 5.12. Figure 5.32 compares the peak states of the undisturbed and remolded samples reached during shearing in a q-p' diagram. The data reveals higher peak strength values for the undisturbed samples at low to intermediate mean effective stresses, while both types of samples show similar peak values at larger mean effective stress. The higher strength of the undisturbed sample at lower stress levels is also reflected by the higher value of effective cohesion visible in Table 5.12.

5.2.5 Undrained shear behaviour from triaxial tests

Fig. 5.33 displays the results of undrained triaxial compression tests on saturated undisturbed loess samples in terms of deviatoric stress versus axial strain (Fig. 5.33(a)) and pore-water pressure versus axial strain (Fig. 5.33(b)). The results show that at the initial stage of loading, the deviatoric stress and pore pressure increase as the axial strain increases. The deviatoric stress reaches its maximum at a small strain (about 2%), then it slightly decreases. After the axial strain reaches approximately 18%, the pore water pressure and deviatoric stress reach a steady state. Fig. 5.34 shows the respective effective stress paths of the undrained triaxial compression tests. At low initial confining stress of 50 kPa after a slight increase, the mean effective stress continuously decreases during undrained shear. At the maximum deviatoric stress of the sample sheared from $p'_0 = 50$ kPa, the instability line is defined. The measured deviatoric and mean effective stress at maximum axial strain correspond to the critical state. The stress path of sample the test with $p'_0 = 50$ kPa is similar to a typical stress path of a liquefied sample. The samples sheared from 100 and 150 kPa initial mean effective stress show a final reincrease in mean effective stress after the deviator stress has passed a first maximum in q followed by a temporary minimum deviator stress. This behaviour is also termed limited liquefaction.

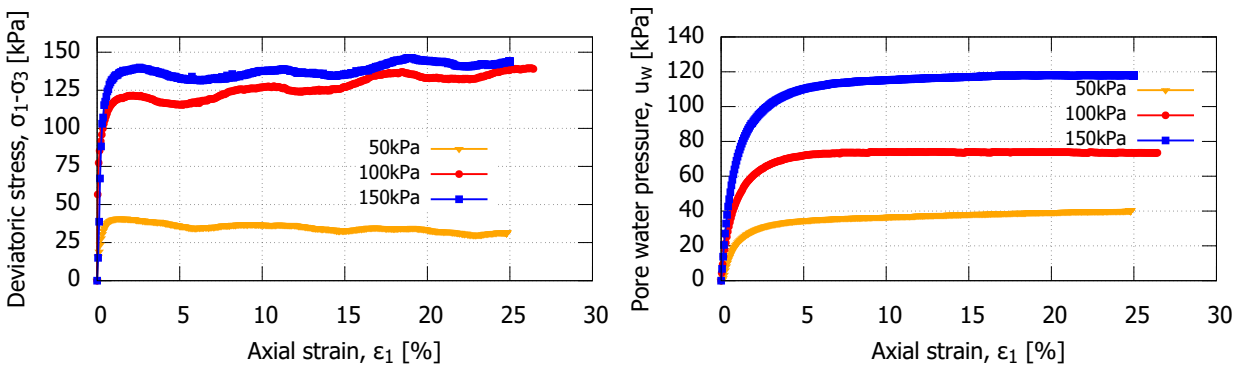

(a) (b)

Figure 5.33: Undrained triaxial test results of the undisturbed samples, (a) Deviatoric stress vs. axial strain, (b) Pore water pressure vs. axial strain.

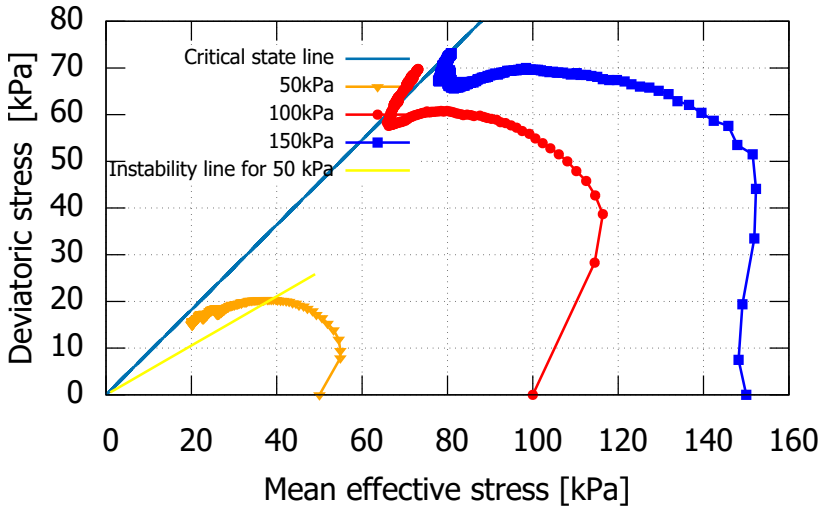

Figure 5.34: Effective stress paths from the undrained triaxial compression tests on undisturbed loess samples.

The excess pore pressure required to bring the soil to the potentially unstable region under static loading is much smaller than that required to bring the soil to the steady-state line (SSL). Hence, for a soil that is already in or near an unstable state, blocking the drainage channel may cause instability depending on the initial stress state and groundwater level.

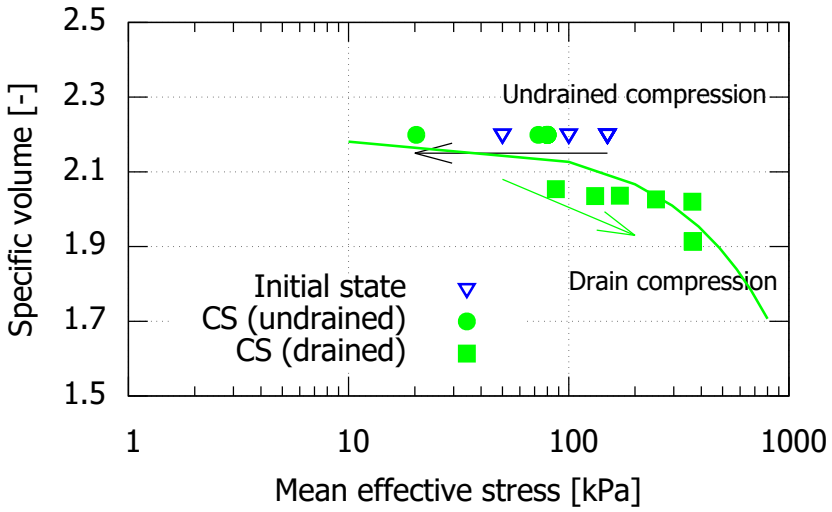

Figure 5.35: Steady state line in $\nu - p'$ space.

Research studies by Castro (1975), Castro (1977), Poulos (1981), and Poulos et al. (1985) have established a relationship between the void ratio and the mean effective stress in the critical-state, which is referred to as critical-state line (CSL) or steady-state line (SSL). This line is typically plotted in a specific volume-log p' plane and can be assumed to be linear. The critical state is reached when for continuous axial deformation no further changes in deviator stress and pore water pressure occur. Fig. 5.35 illustrates the correlation between the specific volume of the sample and the effective stress, as determined from undrained tests. During testing, the void ratios at start of shearing of the specimens ranged from 0.99 to 1.05, due to the applied consolidation stress prior to shear, which is lower than the in-situ value of 1.199. Since all three initial states are located above the critical state they tend to reach the CSL during undrained shear by an overall decrease in effective stress, thus liquefaction or limited liquefaction type of behaviour. Critical state data from the drained triaxial tests have been added in Fig. 5.35, approximately revealing a unique critical state line for both drainage conditions.

5.3 Determination of SWCC with emphasis on cyclic drying-wetting behaviour

This section focuses on the analysis of the results of the experiments conducted to determine the soil water retention curves of loess under different hydraulic loading paths. The

drying-wetting paths of both remolded and undisturbed loess samples were determined. To cover the range of suction relevant to loess, different methods were used to induce suction in the samples. The paths applied on both undisturbed and remolded samples were initial drying (ID), main wetting (MW), main drying (MD), secondary wetting (SW), secondary drying (SD), and tertiary wetting (TW).

5.3.1 Effect of sample structure

Fig. 5.36(a) and Fig. 5.36(b) show the relationship between the degree of saturation and applied suction of the remolded and undisturbed loess for the initial drying and the main wetting paths, respectively. The as prepared condition of the undisturbed sample had a suction of 10.1 MPa with a degree of saturation of 6.2%. As suction increases, the degree of saturation is significantly reduced. Samples subjected to the main wetting path showed an increase in degree of saturation from the residual state up to approximately 80%. Hysteresis was observed for both the remolded and undisturbed samples, with the loop between first drying and main wetting paths being more narrow for the remolded loess.

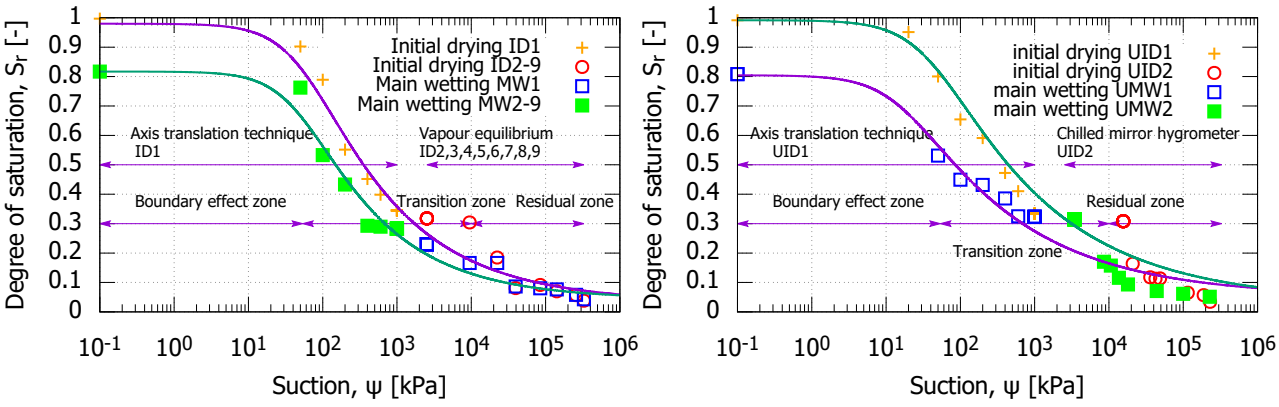

(a) (b)

Figure 5.36: Initial drying and main wetting curves for (a) remolded and (b) undisturbed loess samples.

The air entry value is a measure of the suction value at which air begins to enter the largest pores in the soil. For the remolded loess sample, the air entry value during the initial drying curve is approximately 53.8 kPa. Another important point is the residual water content, which is the point at which it becomes difficult to drain water from the soil

by increased suction. At this point, only evaporation can effectively decrease the degree of saturation. The residual degree of saturation measured in the experiments seems to be much lower than 11%, as shown in Fig. 5.36. The residual water content of loess is related to soil properties.

Fig. 5.37, Fig. 5.39, and Fig. 5.41 compare the degree of saturation vs. suction relationships of the remolded and undisturbed samples for the applied drying and wetting paths, separately. During main wetting, for a given suction value the degree of saturation for the remolded loess sample is larger than that of the undisturbed loess sample. After cyclic wetting and drying, the structure of the undisturbed loess sample becomes more homogeneous, while the structure of the remolded loess sample does not change (Jiang, Zhang and Hu, 2014). The difference between the two types of loess samples becomes less noticeable as the number of cycles increases. For the low suction range of the wetting paths (Fig. 5.37(b), Fig. 5.39(b), Fig. 5.41(b)), for the same suction values the degree of saturation for the remolded sample is larger than that of the undisturbed loess sample. This difference is due to the difference in the pore size distribution. In the high suction range ($\geq$1 MPa), the degree of saturation for the undisturbed loess sample is slightly larger than that of the remolded loess sample. The difference in the SWCC between the remolded and undisturbed loess is small for the initial drying and main wetting curves (Fig. 5.37), but it becomes larger for the second wetting curve (Fig. 5.39).

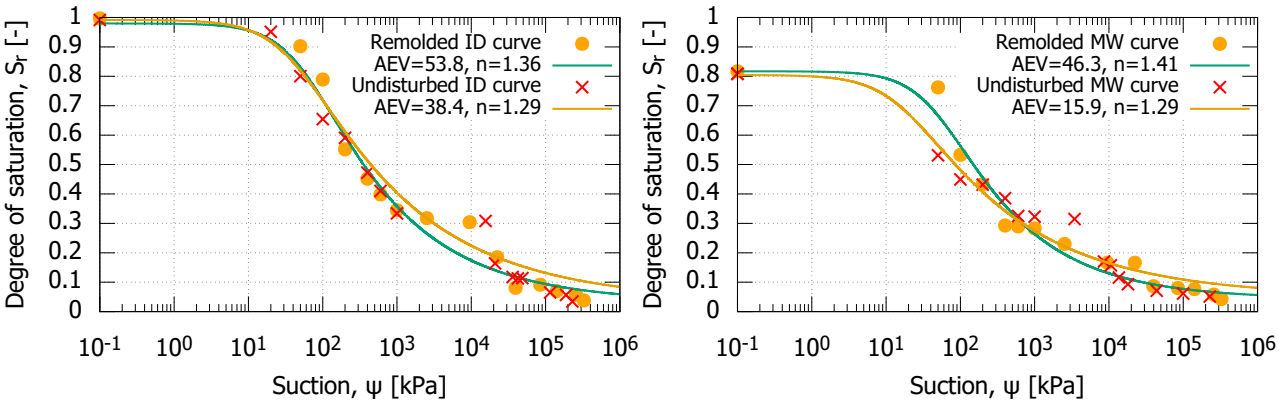

(a) (b)

Figure 5.37: $S_r - \psi$ relationship for (a) Initial drying curve (ID), and (b) Main wetting curve (MW).

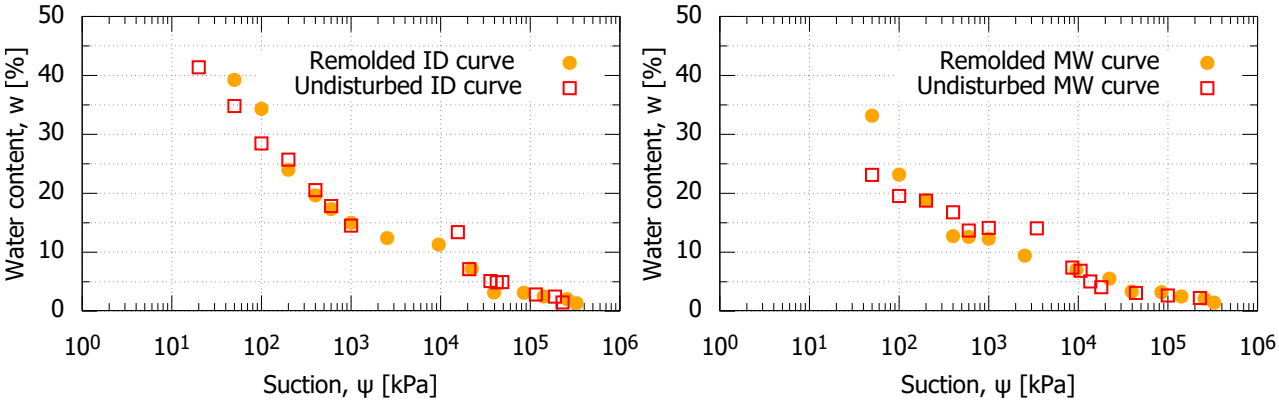

(a) (b)

Figure 5.38: w$-\psi$ relationship for (a) Initial drying curve (ID), and (b) Main wetting curve (MW).

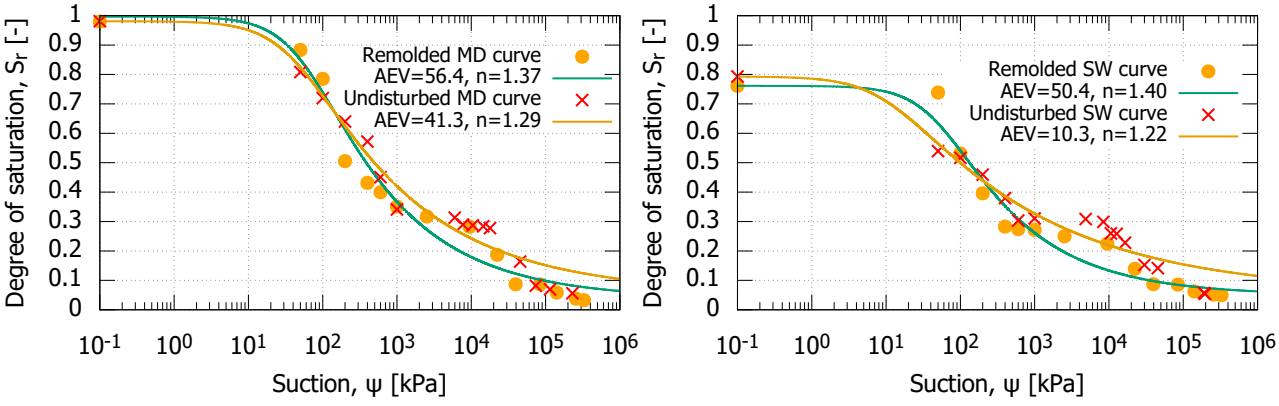

(a) (b)

Figure 5.39: $S_r - \psi$ relationship for (a) Main drying curve (MD), and (b) Secondary wetting curve (SW).

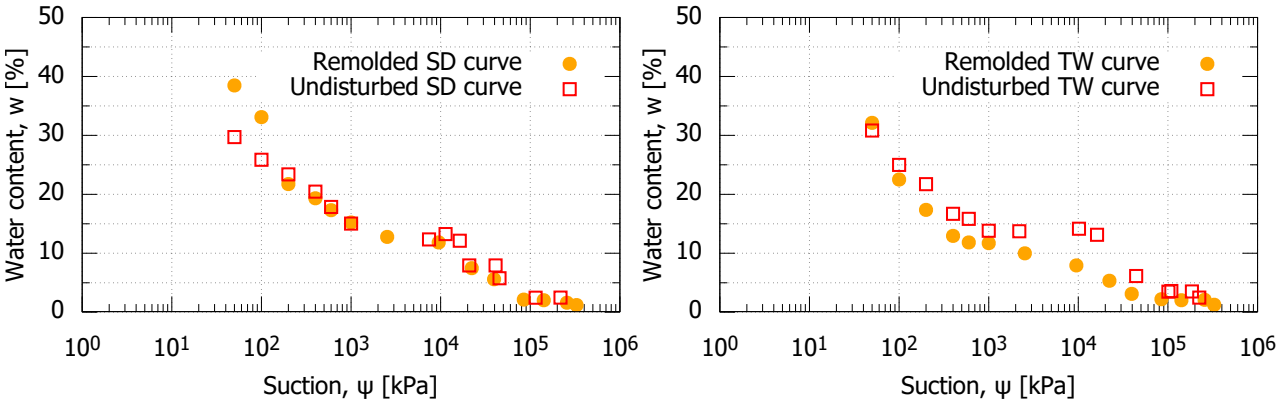

(a) (b)

Figure 5.42: $w - \psi$ relationship for (a) Secondary drying curve (SD), and (b) Tertiary wetting curve (TW).

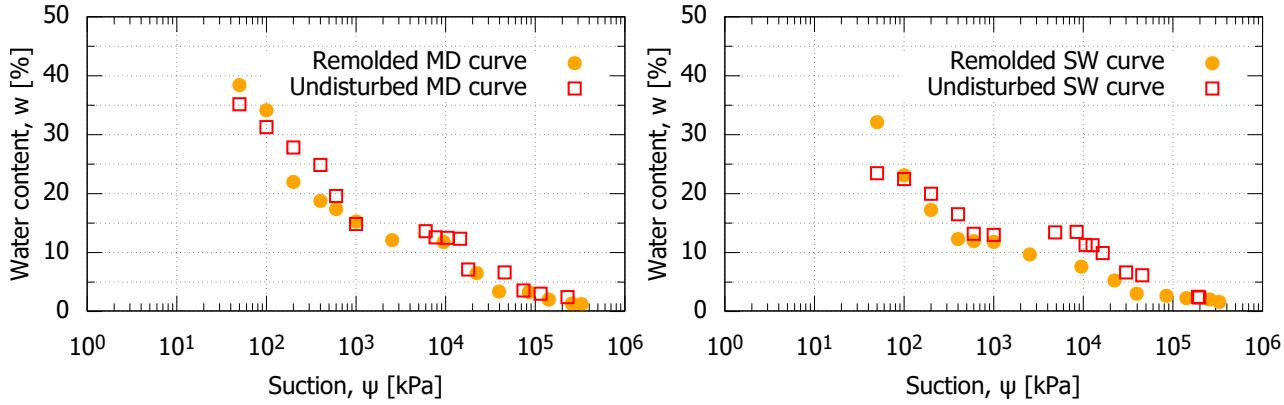

(a) (b)

Figure 5.40: $w-\psi$ relationship for (a) Main drying curve (MD), and (b) Secondary wetting curve (SW).

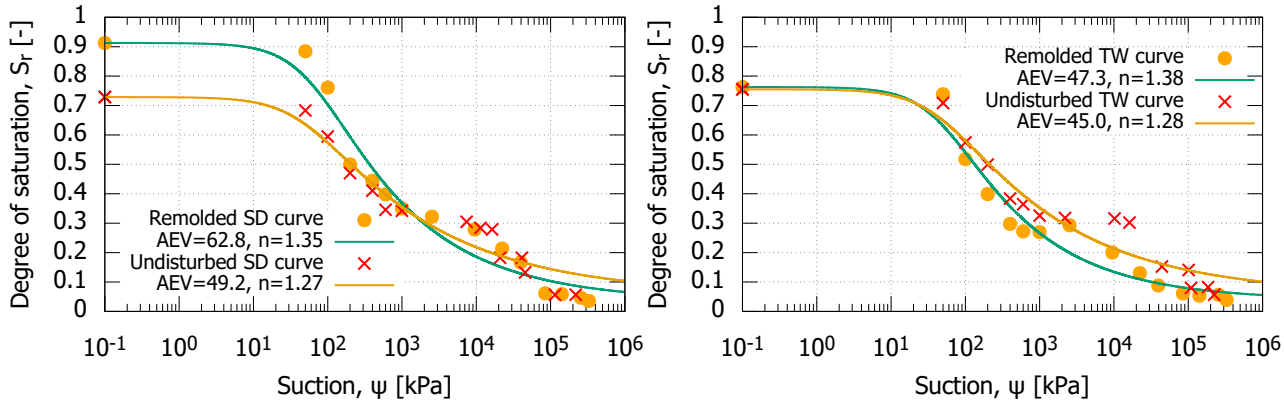

(a) (b)

Figure 5.41: $S_r - \psi$ relationship for (a) Secondary drying curve (SD), and (b) Tertiary wetting curve (TW).

The effect of volume change on the water retention characteristics was not considered, since volume changes due to shrinkage or swelling were very small. Further, in the transient wetting and drying method, the sample was installed inside the microcell, which did not allow volumetric expansion during wetting. The remolded loess is characterized with a double pore structure, i.e., intra-aggregate and inter-aggregate pores. Under a low water content, wetting causes an increase in the amount of absorbed water in the small intra-aggregate pores, and the suction is mainly controlled by the inter-aggregate pores. When the water content of the soil is larger, wetting causes the amount of water both in

the inter-aggregate pores and the intra-aggregate pores to increase. The intra-aggregate pores have already been saturated, and the suction is mainly controlled by the large inter-aggregate pores.

Regarding the drying paths shown in Fig. 5.38, Fig. 5.40 and Fig. 5.42, when the suction is less than 1000 kPa, the water content decrease was steep. Again, beyond the suction value of 10 MPa, the water content decreased until residual values. After the water content is smaller than the residual water content, the SWCCs of different structured remolded and undisturbed loess are close to each other, that is, the SWCCs in this suction range tend to be similar for both sample types.

Van Genuchten model (Van Genuchten, 1980) was used to fit the SWCC experimental data. From the SWCCs, it can be observed that the air-entry value (AEV) and residual suction value (ψ_r) bound a relatively low range of suction values, which indicates a small clay content and a dominant silt fraction. The AEV of remolded and undisturbed loess samples under the initial drying path were 53.8 kPa and 38.4 kPa, respectively. Beyond the residual suction, a further decrease in suction does not induce a significant decrease in the degree of saturation.

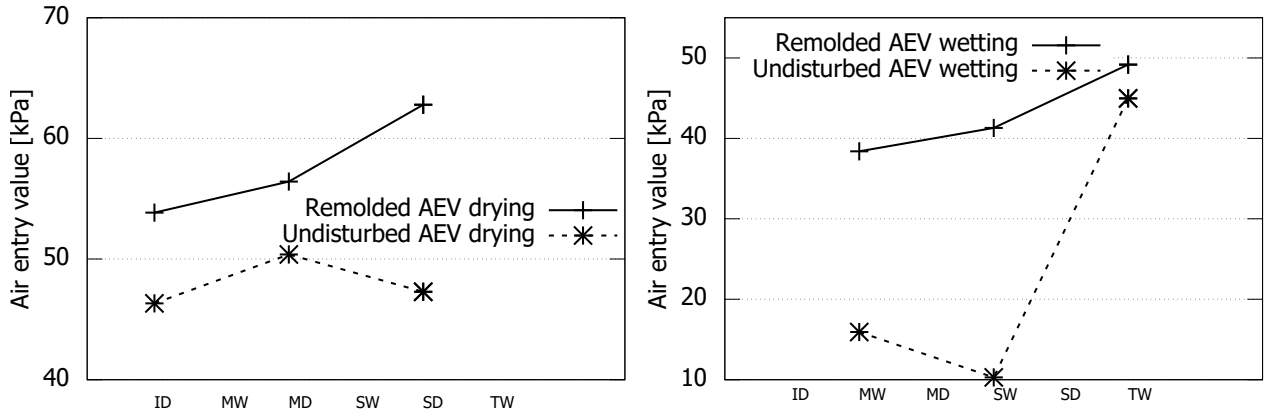

Figure 5.43: Air entry values after cyclic wetting and drying on (a) drying paths, (b) wetting paths.

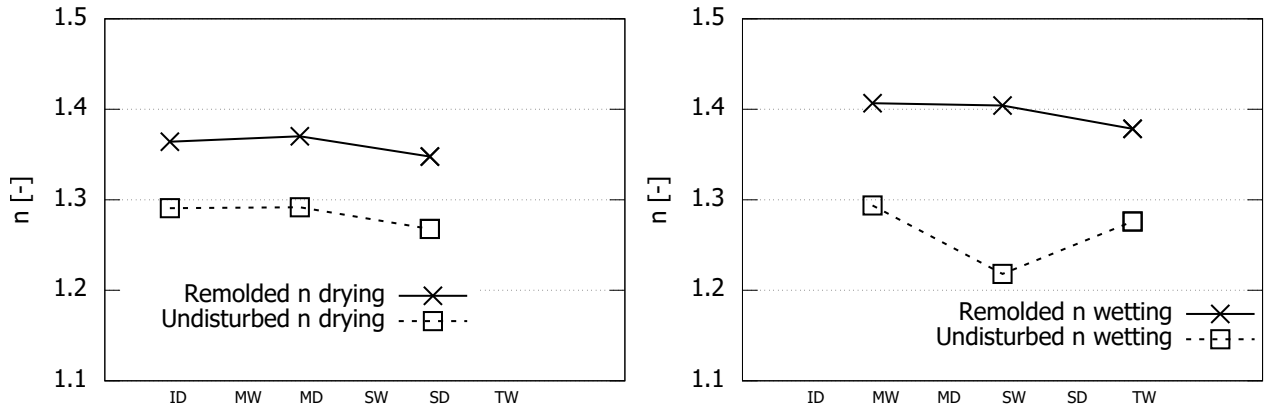

Figure 5.44: Slope of SWCC after cyclic wetting and drying on (a) drying paths, (b) wetting paths.

As can be seen from Fig. 5.44(b), the values of the parameter n, controlling the slope of the SWCC of remolded and undisturbed loess samples are similar, while the air entry values show a difference. A possible reason is that for remolded loess, the pore size distribution is more homogeneous after the metastable intact loess structure is destroyed during the sample preparation process. One of the main factors controlling the SWCC is the pore size distribution. The double peak pore structure typical for undisturbed loess (Jiang, Zhang and Hu, 2014), with the macro pores, leads to a larger rate of drainage and smaller air entry value as compared to the remolded loess.

After remolding the loess soil, the size of the large pores is reduced, so that the radius of curvature of the meniscus in the pores is reduced, and the matric suction is increased, so the pressure required for the air to enter the pores of the soil increases, and the air entry value also increases (Fig. 5.43)(a). From the soil water retention curve, it is visible that the air entry value of the undisturbed loess sample after several cycles increases, and the water retention curve becomes flatter.

Considering the MIP pictures in Section 3.2, the undisturbed loess sample has a trimodal pore-size distribution, where the smallest pore size was around 36.5 nm, the intermediate pore size was 901 nm, and the largest pore family had a diameter of 17.5 μm. The remolded loess sample posseses a bi-modal pore-size distribution with a suppressed intermediate pore size peak, and a micro-pore family with a peak at about 7 μm. Further, the cumulative pore volume of the remolded loess sample was found to be smaller than

the one of the undisturbed loess. These findings are consistent with the smaller AEV observed for the undisturbed loess sample as compared to the remolded one.

From the MIP results, it is known that the pore size of the undisturbed loess is larger than that of the remolded loess. Under the same suction, the water content of the soil sample with larger pores is lower. Without confining, the cyclic wetting-drying is similar to a leaching process. The cyclic wetting and drying process has less influence on the remolded loess, while for the undisturbed loess, the leaching process will dissolve the cementation, which constitutes the macropores. The multi-modal pore size distribution of the undisturbed loess will reduce to two or a single peak shape and homogenize after several wetting and drying cycles.

It can be seen that the influence of the number of cycles on the soil-water characteristic curve of loess under unconfined conditions is mainly reflected in the influence on the parameters related to the air entry value and the residual water content, while the number of cycles has little effect on the parameter related to the moisture reduction rate.

5.3.2 Effect of hydraulic loading path

The initial drying and main wetting curves obtained from the SWCC measurements of undisturbed and remolded loess samples are shown in Figs. 5.45 and 5.46. The different main paths obtained from the drying and wetting curves of the degree of saturation versus suction relationships signify hysteresis in the hydraulic behaviour of the undisturbed and remolded loess samples. The results show hysteresis behaviour with a low magnitude, visible as the enclosed gap between the drying path and wetting path.

In Fig. 5.45(b), Fig. 5.46(b) to Fig. 5.49(b), the difference in the degree of saturation between drying and wetting paths under certain suction is becoming less with the increase of suction. At suctions higher than the residual suction, where the soil is dominated by the absorption mechanisms, the hysteresis behaviour is negligible. The hydraulic hysteresis of the SWCC is related to the fabric and affinity for water inside soils. Any change to particles and pore size arrangements allows the hydraulic hysteresis to take place (Fleureau et al., 1993). The difference in the water retention curve is controlled by

the pore size distribution, which becomes more homogeneous with an increasing number of cycles.

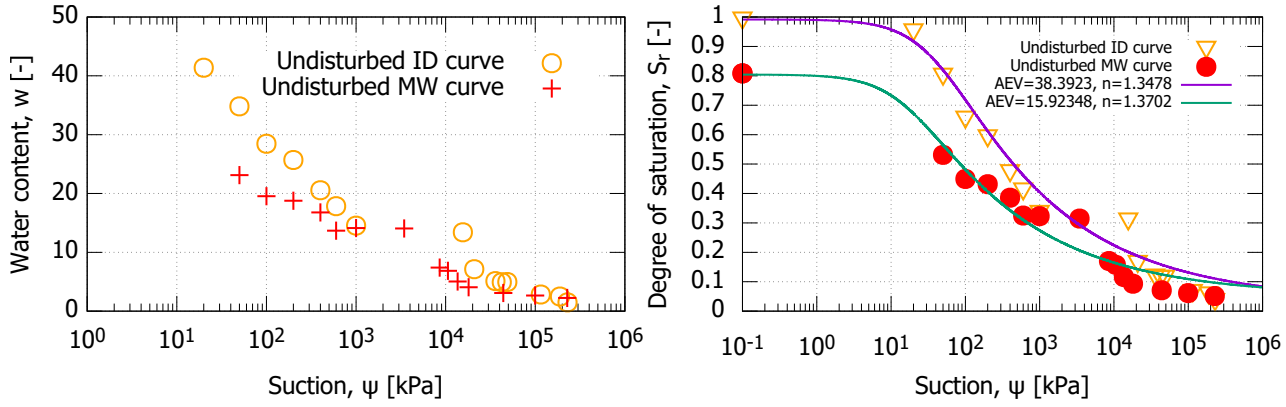

(a) (b)

Figure 5.45: Initial drying and main wetting paths of undisturbed loess sample, (a) $w-\psi$ relationship, and (b) $S_r-\psi$ relationship.

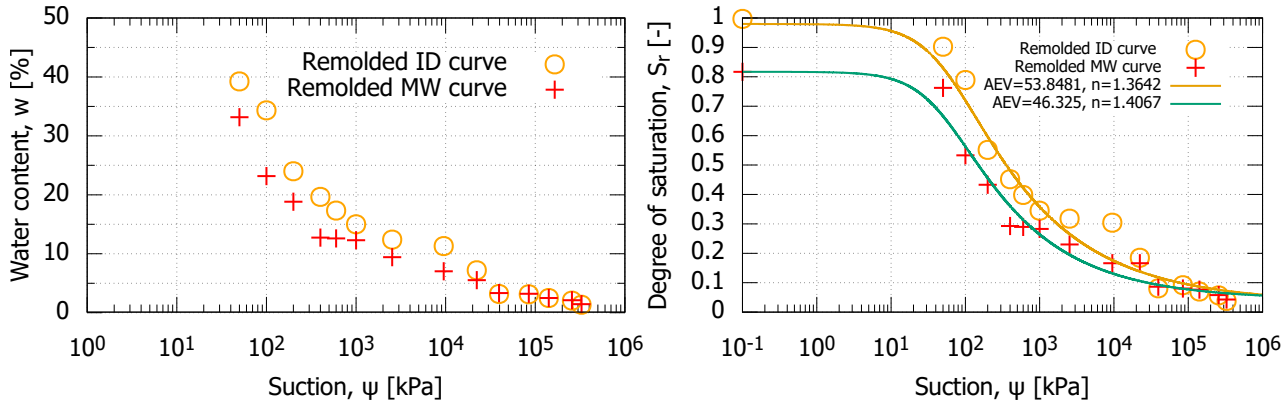

(a) (b)

Figure 5.46: Initial drying and main wetting paths of remolded loess sample, (a) $w-\psi$ relationship, and (b) $S_r-\psi$ relationship.

The maximum degree of saturation of the specimens subjected to subsequent drying-wetting cycles is less than that of the sample under the initial drying path. The air-entrapped value is the difference between the maximum degree of saturation for the drying and wetting curve, which decreases with the increase in the number of cycle for undisturbed loess samples (Fig. 5.45(b)). The hysteresis for the undisturbed loess sample is larger than that of the remolded loess sample (Fig. 5.46(b)). The hysteresis phenomenon is more obvious in the low suction range. After two cycles of wetting and drying, the

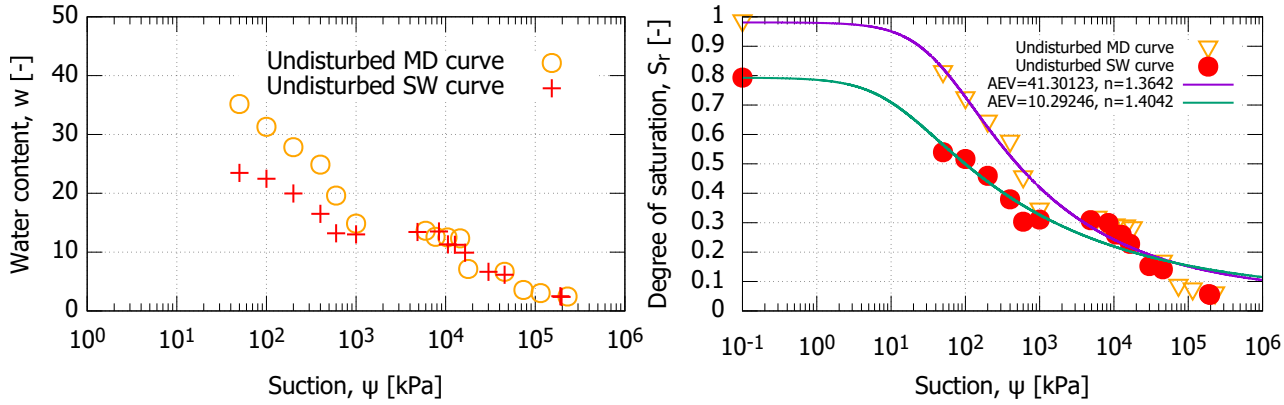

(a) (b)

Figure 5.47: Main drying and secondary wetting paths of undisturbed loess sample, (a) $w - \psi$ relationship, and (b) $S_r - \psi$ relationship.

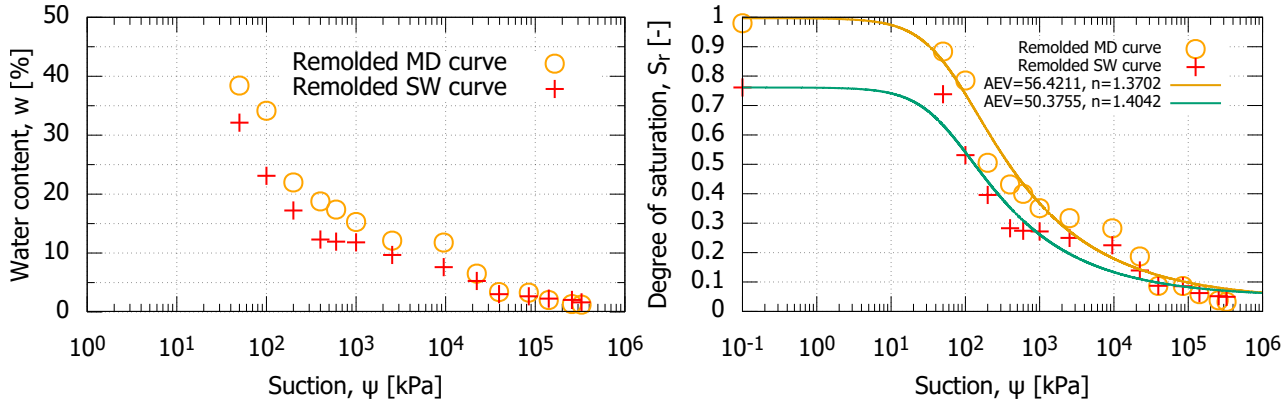

(a) (b)

Figure 5.48: Main drying and secondary wetting paths of remolded loess sample, (a) $w - \psi$ relationship, and (b) $S_r - \psi$ relationship.

hysteresis on the undisturbed loess sample has vanished (Fig. 5.49(b)), but there is still hysteresis behaviour in the remolded loess sample (Fig. 5.50(b)). Because there is only a small content of water-sensitive minerals, the suction is mainly controlled by the capillary forces, which means the pore size distribution controls the matric suction-dominated range, which is related to the shape and curvature of the water-air interface. Ink-bottle effects and other physical-based mechanisms contribute to hysteresis, which is related indirectly to the capillary forces. The parameter $D_{d/w}$ quantifying the difference in the degrees of saturation between the drying path and the subsequent wetting path was cal-

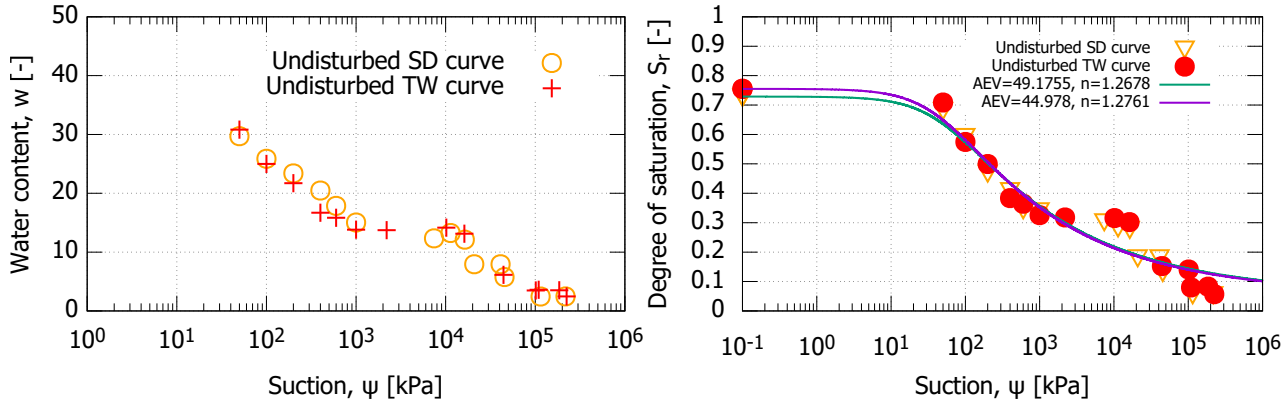

(a) (b)

Figure 5.49: Secondary drying and tertiary wetting paths of undisturbed loess sample, (a) $w - \psi$ relationship, and (b) $S_r - \psi$ relationship.

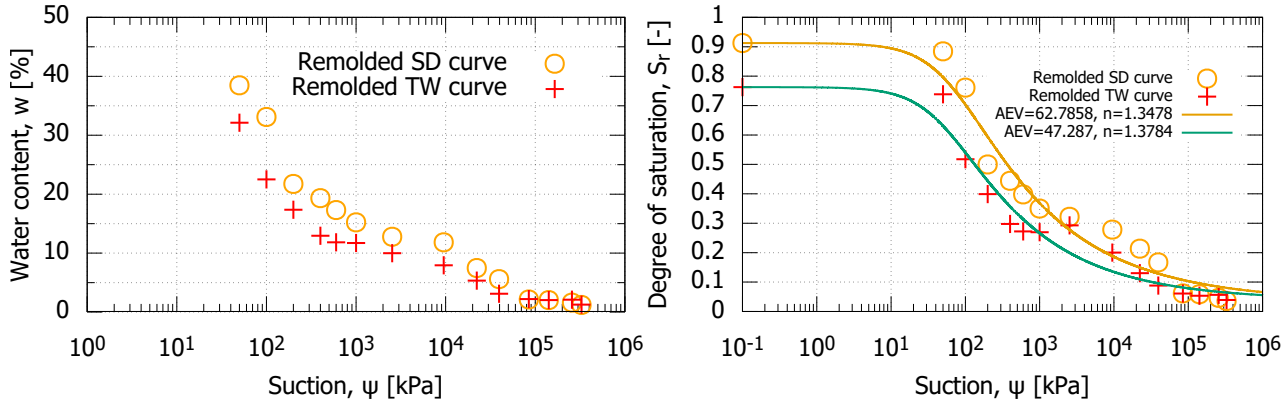

(a) (b)

Figure 5.50: Secondary drying and tertiary wetting paths of remolded loess sample, (a) $w - \psi$ relationship, and (b) $S_r - \psi$ relationship.

culated according to:

$$D_{d/w} = \frac{S_d - S_w}{S_{ds} - S_{dr}} \tag{5.1}$$

For the same value of suction, S_d is the degree of saturation of the drying path, S_w is the degree of saturation of the wetting path, S_{ds} is the maximum degree of saturation of the drying path, and S_{dr} is the residual degree of saturation of the drying path.

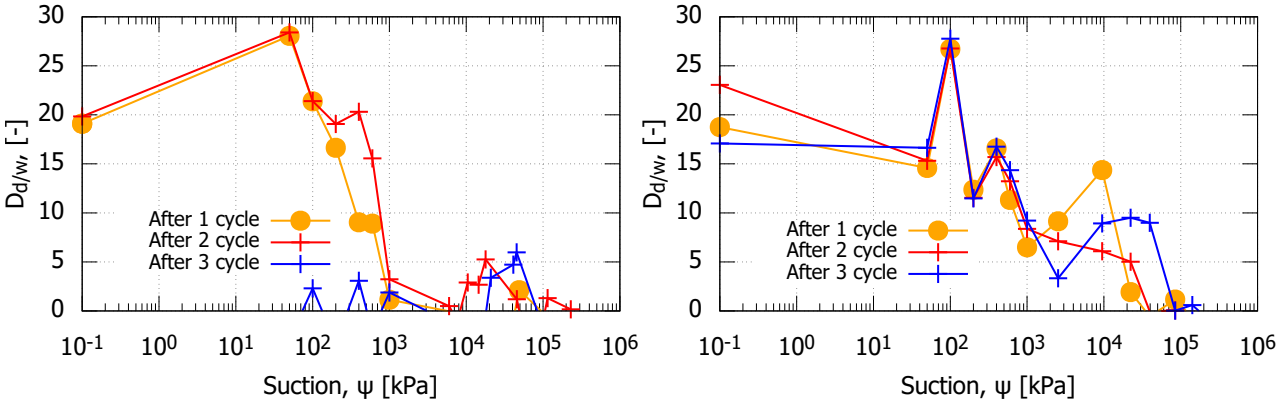

Figure 5.51: Hysteresis's magnitude of (a) Undisturbed and (b) Remolded loess samples.

Fig.5.51 illustrates the relationship between $D_{d/w}$ and suction, with each drying and wetting cycle displaying a hysteresis loop. Notably, the wetting curve consistently falls below the drying curve, and the hysteresis loop formed during the first cycle is larger than that of the second cycle. Furthermore, the difference in the degree of saturation between the wetting and drying paths decreases with each successive cycle, even under the same matric suction. This can be attributed to the presence of air bubbles in the sample's pores, which inhibit the infiltration of free water. However, with repeated drying and wetting cycles, the number of bubbles gradually stabilizes, reducing their influence on the overall process.

The impact of wetting-drying cycles on the pore structure of loess diminishes as the number of cycles increases. At a certain point, further cycles have little effect on the structure. The influence of the number of cycles primarily concerns the spatial arrangement and porosity of pores within the soil. Dense loess is generally more stable in terms of pore structure than other types of loess.

5.3.3 Model fitting

This study presents the findings of drying and wetting processes conducted under various conditions across a broad range of imposed suction levels. In previous research, Brooks and Corey (1964*b*) proposed a power-law relationship between volumetric water content and suction, although this formulation is only valid for suction values greater than the air-entry value. To analyze the experimental data, Fredlund and Xing (1994) model was

also utilized. Three empirical models were used to fit the experimental data, with each model's advantages and limitations discussed. The least-square method was employed to fit the regression model, with the Levenberg-Marquardt algorithm utilized to solve the non-linear least-square regression problem. By fitting the model to the experimental results, the model parameters were obtained.

Due to random errors in the experimental results, the coefficient of regression determination (R^2) may not always provide an accurate assessment of the model's quality, even with high values. Therefore, residual and difference analyses are useful for assessing the quality of the model and illustrating various complex aspects of the model quality. Statistical techniques, such as plots of predicted versus observed values and residual versus observed values, were used to analyze the model's representation across various suction values and to validate the models. In these plots, observed values correspond to experimental data, while predicted values correspond to calculated data.

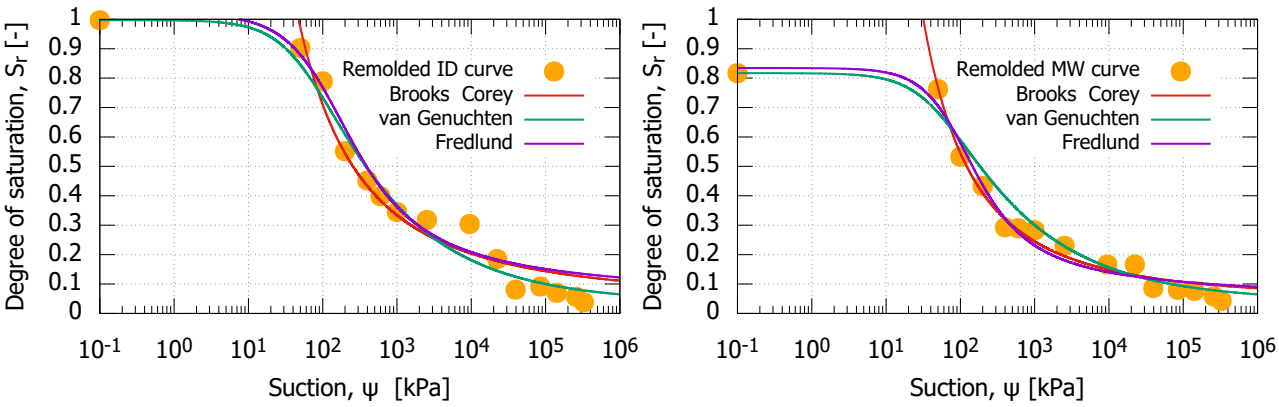

(a) (b)

Figure 5.52: Models fitting using (a) ID, and (b) MW experimental data of remolded soil.

Figs. 5.52, 5.53 and 5.54 show the determined fitting curves using the three different models for the different hydraulic paths of the remolded loess samples. Fig. 5.55, 5.56 and 5.57 show the fitting curves for the undisturbed loess samples, respectively.

As can be seen in Fig. 5.52 to Fig. 5.57, in general, the models represent well the experimental data, except the plate plateau in degree of saturation in the high suction range between about 1 MPa and 10 MPa. The reason is that the models assume a

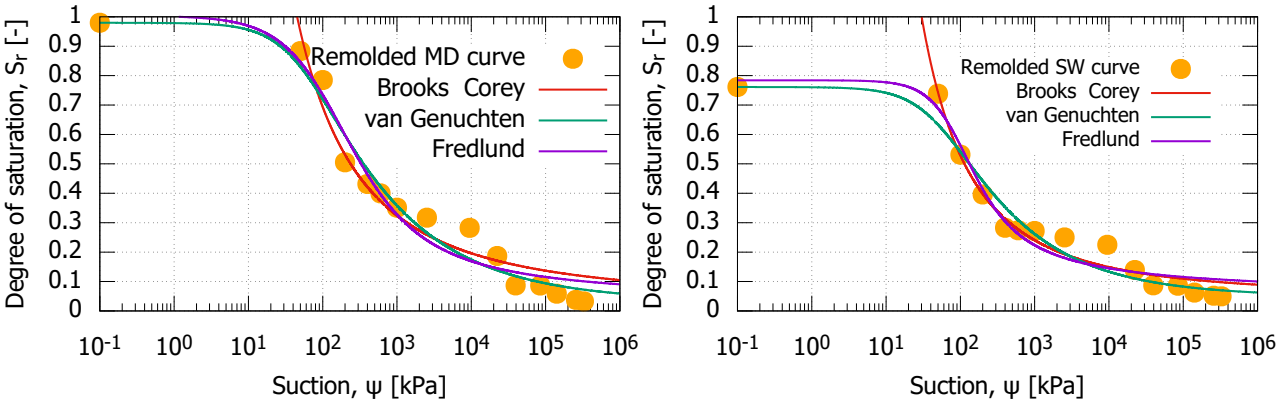

(a) (b)

Figure 5.53: Models fitting using (a) MD, and (b) SW experimental data of remolded soil.

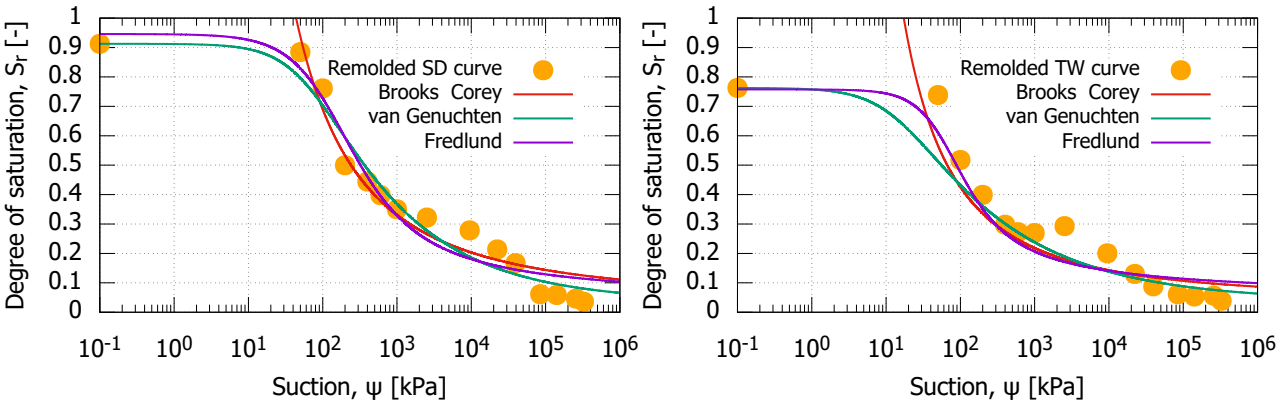

(a) (b)

Figure 5.54: Models fitting using (a) SD, and (b) TW experimental data of remolded soil.

monotonous pore size distribution of the sample, with a Gaussian distribution among single pore size values. But in reality, for typical loess soils, their pore size distribution shows double peaks (Jiang, Zhang and Hu, 2014).

Fig. 5.58, Fig. 5.59, Fig. 5.60 as well as Fig. 5.61 show observed values and the residuals plotted versus predicted values derived from the initial drying path and the main wetting path for both remolded and undisturbed loess samples, respectively. Results are given using the equations by Brooks and Corey (1964*b*), Van Genuchten (1980) with the assumption $m = 1 - 1/n$, and Fredlund and Xing (1994).

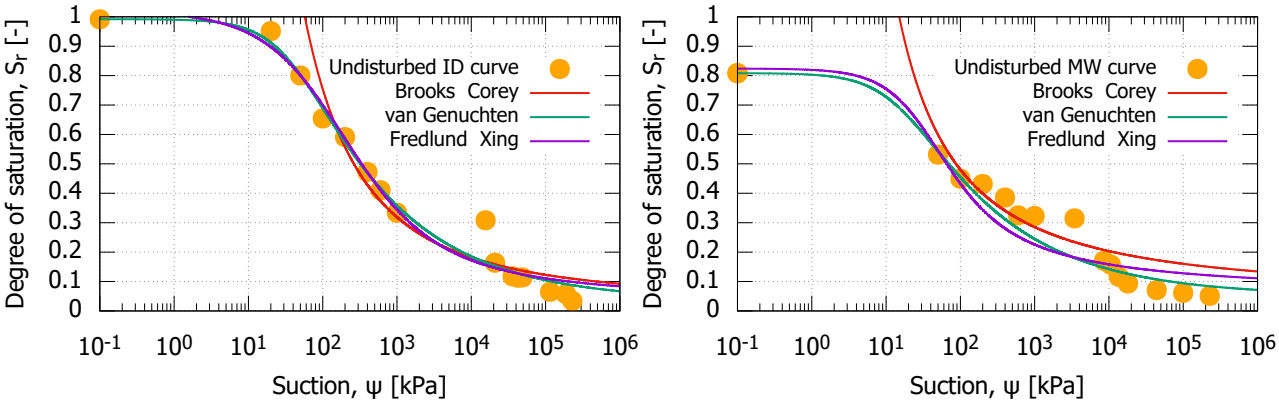

(a) (b)

Figure 5.55: Models fitting using (a) ID and, (b) MW experimental data of undisturbed soil.

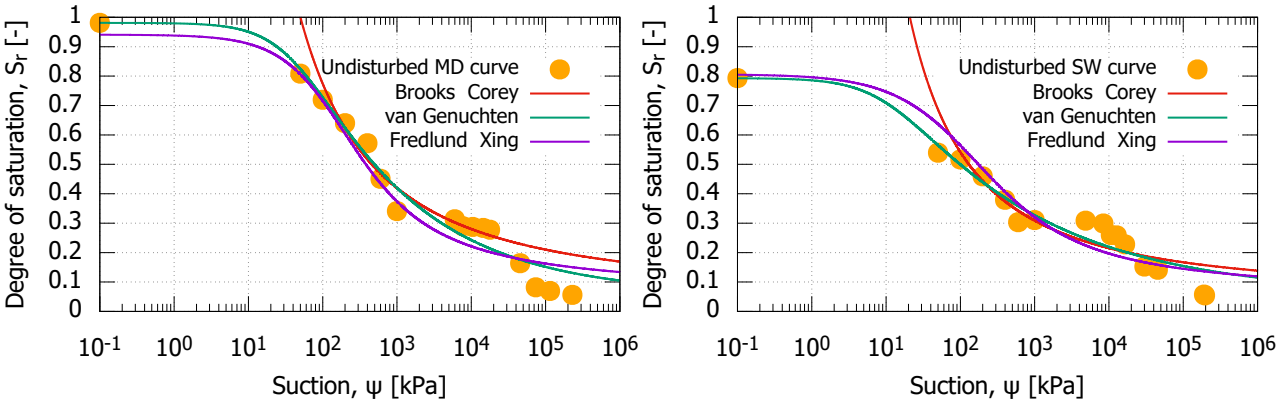

(a) (b)

Figure 5.56: Models fitting using (a) MD, and (b) SW experimental data of undisturbed soil.

Figs. 5.58(b), 5.59(b), 5.60(b), and 5.61(b) illustrate that the predicted values from the van Genuchten and Fredlund models are close to the bisection line $f(x) = x$, indicating that they are similar to the observed values from a statistical perspective. However, some points are located above the bisection line, indicating that the predicted values are underestimated. For the degree of saturation range from 0.6 to 1.0 (Fig. 5.60, 5.61), the points obtained by the Brooks and Corey model are located below the bisection line, meaning that the Brooks and Corey model overestimates the degree of saturation. The three models show no significant difference in predictions under high suction range. The

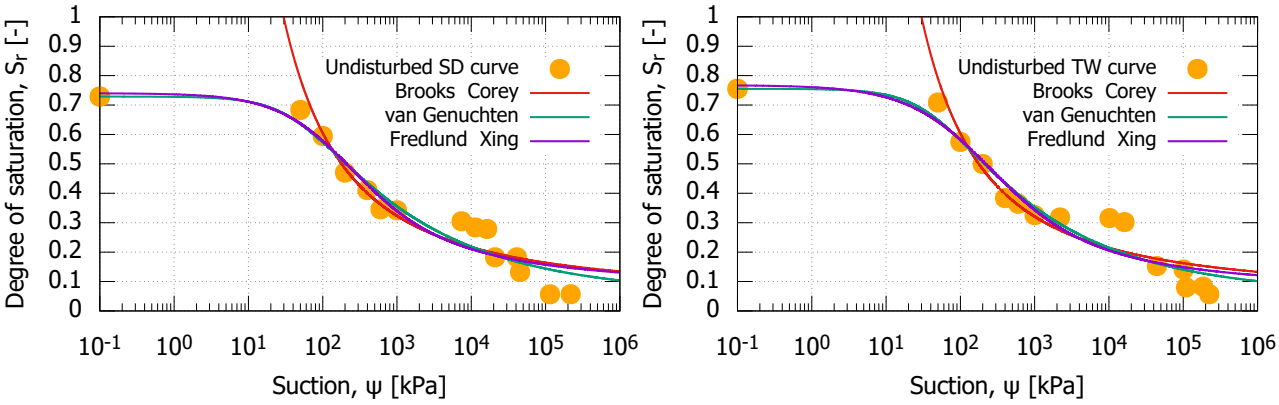

(a) (b)

Figure 5.57: Models fitting using (a) SD, and (b) TW experimental data of undisturbed soil.

residuals (see Fig. 5.58(a)) are randomly distributed above and below the line of $f(x) = 0$, which is the ideal distribution for predicted versus observed points along the $x = f(x)$ line. The coefficient of determination R^2 was also calculated to assess the quality of the models.

The analysis showed a high level of accuracy in fitting the experimental results by the three equations (Brooks and Corey, 1964*b*, Van Genuchten, 1980, and Fredlund and Xing, 1994). The equations used for the analysis were reliable in closely fitting the experimental data, particularly in the residual zone and at the inflection point of the wetting path of the SWCC.

The experimental results were analyzed statistically to assess the Soil-Water Characteristic Curve (SWCC) and model the initial drying curve of remolded loess samples. The relationship between the degree of saturation and suction suggested the need for a nonlinear function to make predictions. The conventional method to obtain model parameter values is the nonlinear regression fitting method, as presented in the former paragraphs of this section. In the following, a different approach was used to fit the experimental data. Instead of using a nonlinear model, the independent variable was first transformed into the log-scale, and then a linear model was used to fit the transformed data. This transformed the relationship between the degree of saturation and suction into a linear relationship, allowing a linear least squares regression method to be used to minimize the error when fitting the experimental data. The theoretical details of this procedure can be found in Stoimenova et al. (2003) and Stoimenova et al. (2006). To determine the best

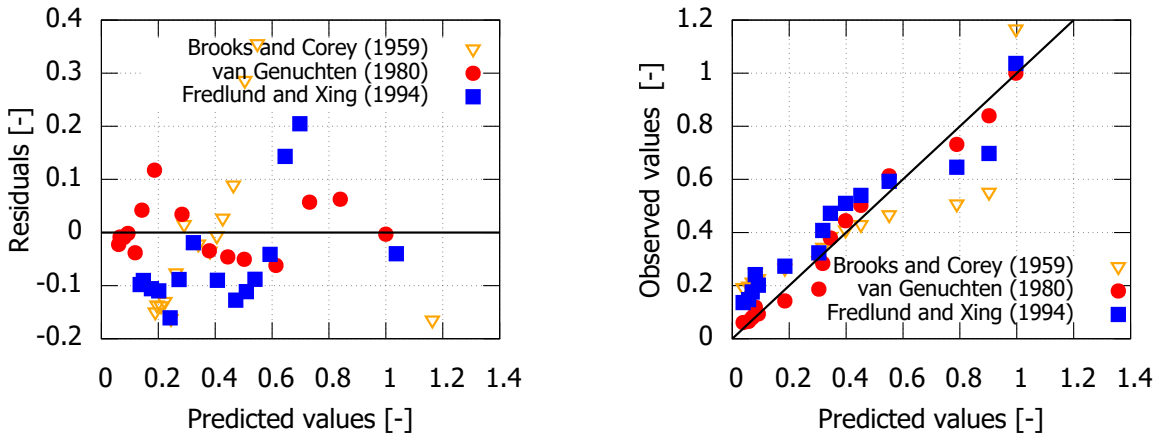

(a) (b)

Figure 5.58: Statistical assessment of the three SWCC models using ID curve of remolded loess sample, (a) Residuals, and (b) Observed vs. predicted values.

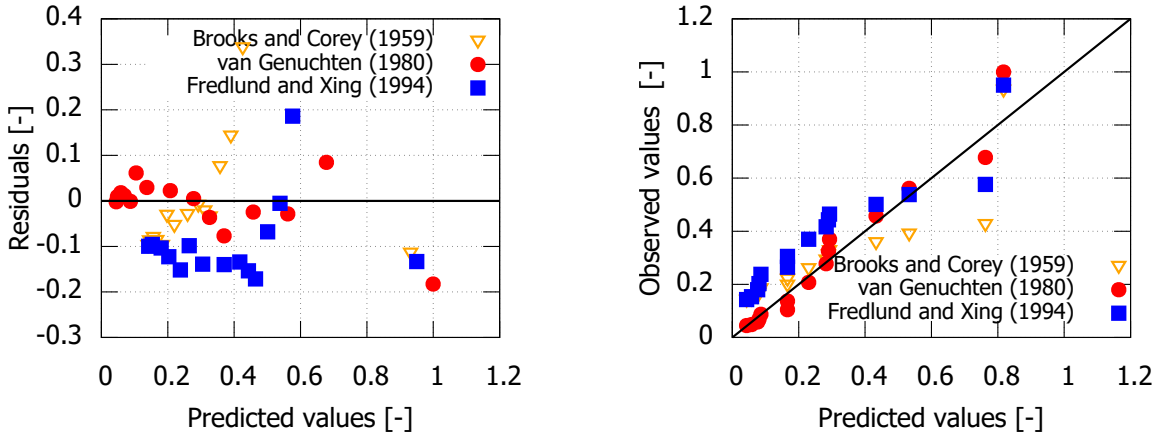

(a) (b)

Figure 5.59: Statistical assessment of the three SWCC models using the MW curve of the remolded loess sample, (a) Residuals, and (b) Observed vs. predicted values.

linear form of the experimental results, various plots of the data were examined. These plots are shown in Figs. 5.62 to 5.65. The functions of the linearized models and the results of the linear least squares regression are summarized in Tab. 5.13.

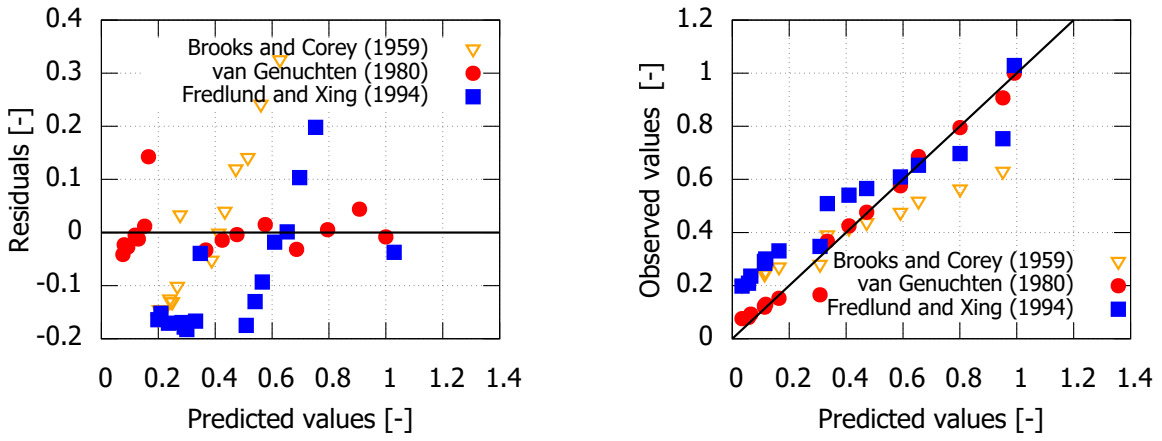

(a) (b)

Figure 5.60: Statistical assessment of the three SWCC models using the ID curve of the undisturbed loess sample, (a) Residuals, and (b) Observed vs. predicted values.

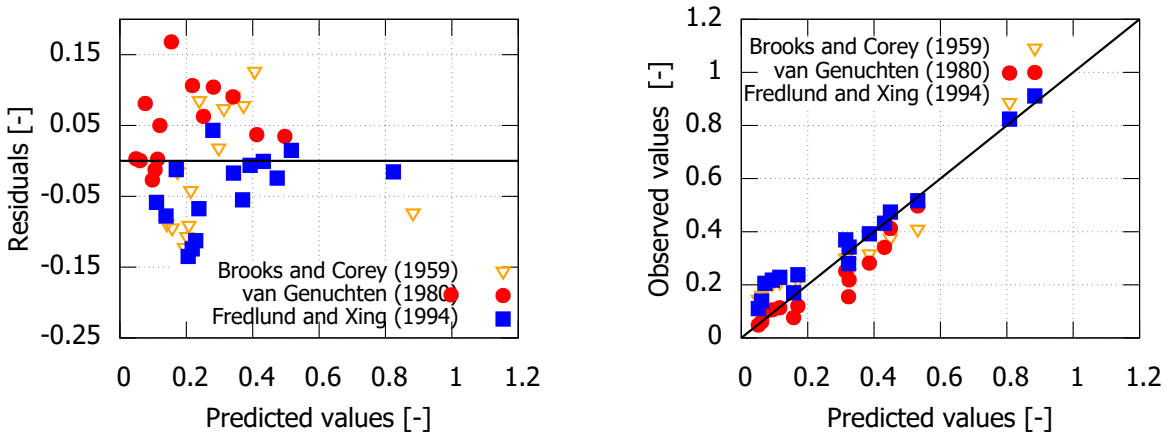

(a) (b)

Figure 5.61: Statistical assessment of the three SWCC models using MW curve of undisturbed loess sample, (a) Residuals, and (b) Observed vs. predicted values.

Table 5.13: Linearized models

Model 1: $\ln\theta = \beta_0 + \beta_1\psi + \epsilon$	y = -9E-06x - 1.5973, $R^2 = 0.67$
Model 2: $\theta = \beta_0 + \beta_1\ln\psi + \epsilon$	y= -0.0407x + 0.5119, $R^2 = 0.90$
Model 3: $\theta = \beta_0 + \beta_1\ln\ln\psi + \epsilon$	y = -0.2433x + 0.67, $R^2 = 0.84$
Model 4: $\ln\ln(1\backslash\theta) = \beta_0 + \beta_1\psi + \epsilon$	y = -0.2592x - 0.117, $R^2 = 0.83$
Model 5: $\ln\theta = \beta_0 + \beta_1\ln\psi + \epsilon$	y = -1.4209x + 0.616, $R^2 = 0.65$
Model 6: $\ln\theta = \beta_0 + \beta_1\ln\ln\psi + \epsilon$	y = 4E-06x + 0.3601, $R^2 = 0.48$
Model 7: $\ln\ln(1\backslash\theta) = \beta_0 + \beta_1\ln\psi + \epsilon$	y = 0.1438x - 0.518, $R^2 = 0.91$
Model 8: $\ln\ln(1\backslash\theta) = \beta_0 + \beta_1\ln\ln\psi + \epsilon$	y = 0.8327x - 1.0107, $R^2 = 0.80$

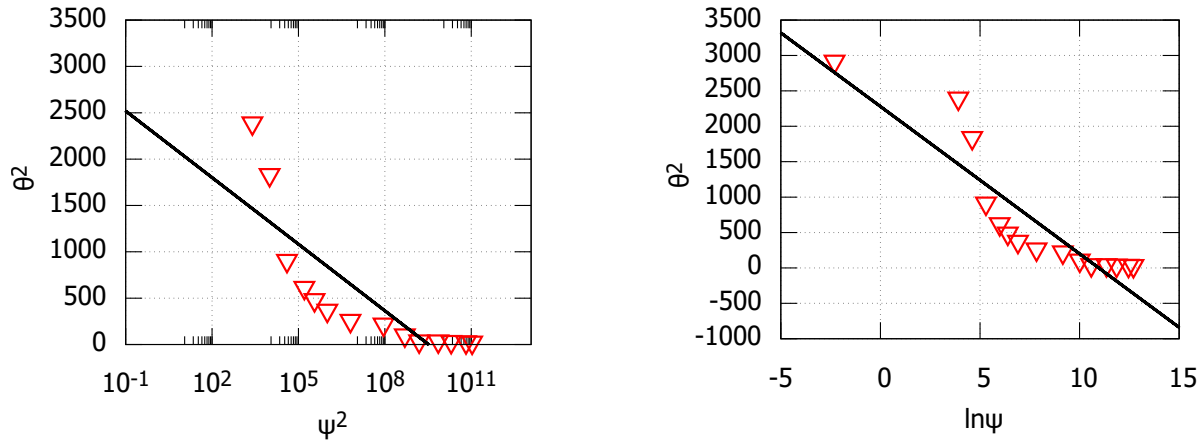

(a) (b)

Figure 5.62: Statistical model (1, 2) fitting using ID data of remolded loess sample, (a) $\psi^2 - \theta^2$, and (b) $\ln\psi - \theta^2$.

Linear transformations were applied using the square root $(\sqrt{\theta}, \sqrt{\psi})$, the power of 2 (ψ^2, θ^2), logarithm $(\ln\theta, \ln\psi)$, and even double logarithm $(\ln\ln\theta, \ln\ln\psi)$, as shown in Table 5.13. In this study, seven types of linear relationships were used to describe the initial drying curve. Regression analysis was performed to evaluate the fit of the experimental data to each model. The results showed that Model 7 and Model 2 provide the best fit to the experimental data, since they resulted in the highest R^2-value (see Tab. 5.13).

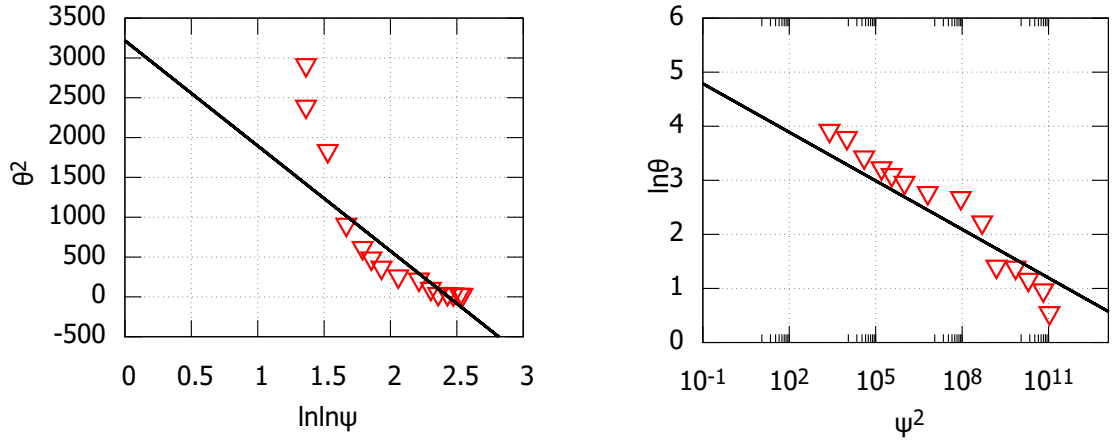

(a) (b)

Figure 5.63: Statistical model (3, 4) fitting on ID remolded data, (a) $\ln\ln\psi - \theta^2$, and (b) $\psi^2 - \ln\theta$.

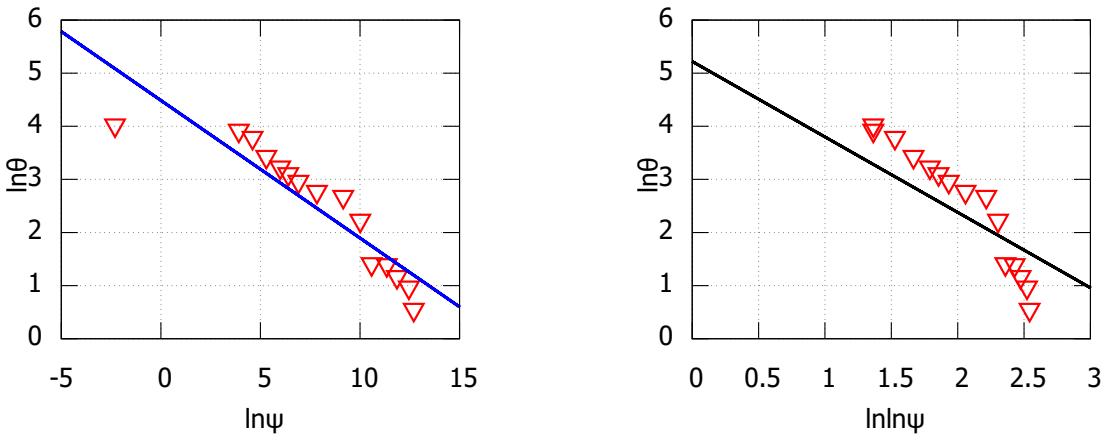

(a) (b)

Figure 5.64: Statistical model (5, 6) fitting on ID remolded data, (a) $2\ln\psi - \mathrm{lnln}\theta$, and (b) $\ln\psi - \mathrm{lnln}\theta$.

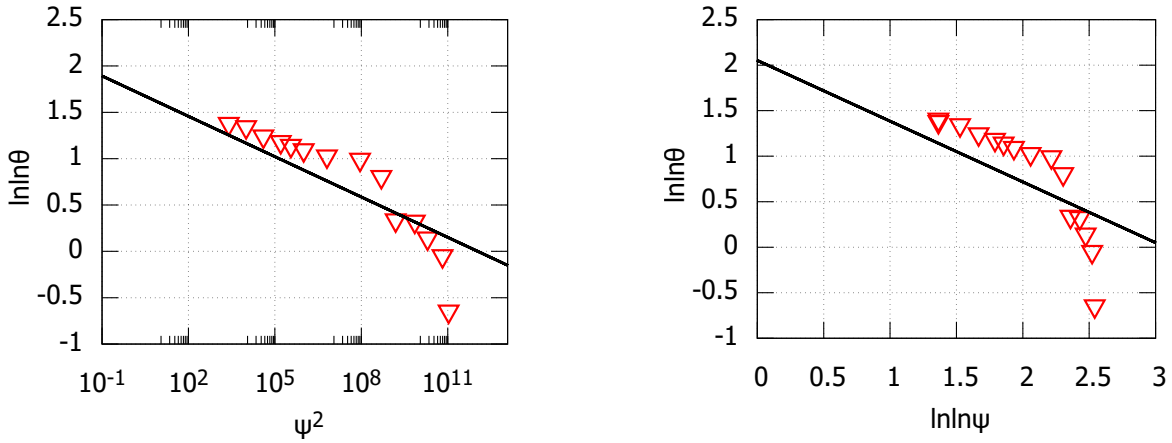

(a) (b)

Figure 5.65: Statistical model (7, 8) fitting on ID remolded data, (a) $\ln\psi - \ln\theta$, and (b) $\mathrm{lnln}\psi - \ln\theta$.

5.4 Volumetric behaviour under controlled suction

In this study, the hydro-mechanical properties of loess were investigated through experiments which were able to separately control suction and mechanical stress. Two types of tests were conducted: compression tests with constant suction and wetting-drying tests

under constant net vertical stress. The effects of soil structure, suction, and stress path on soil deformation and hardening behavior were analyzed. The results of these experiments are presented in this section. Specifically, the focus is on the experimental results obtained from one-dimensional compression and rebound tests, which are discussed in relation to the experimental program presented in Section 4.5.

5.4.1 Effect of sample structure

Void ratio versus applied vertical net stress results are presented in Fig. 5.66 for remolded loess specimens and in Fig. 5.67 for undisturbed specimens.

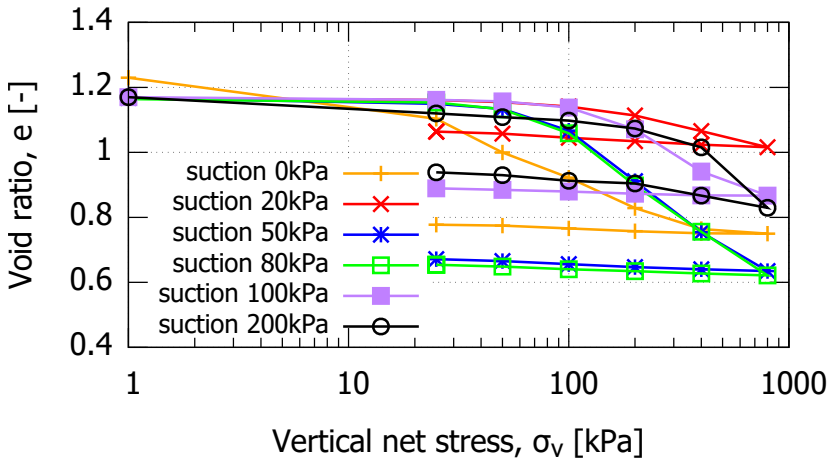

Figure 5.66: Vertical stress vs. void ratio for remolded loess samples.

Unsaturated soil exhibits complex mechanical properties compared to saturated soil due to the suction in the soil, which affects the slope of the compression curve and the yield stress. When the net stress exceeds the yield stress, the soil skeleton suffers from plastic deformations. Therefore, compared with soil samples under high suction with a corresponding greater yield stress, the final deformation of samples having smaller or zero suction is larger. This is due to the fact that the surface area and tension of the air-water interface increase with an increase in matric suction, which in turn increases the effective stress. Thus, suction decreases the compressibility of the soil sample.

However, for the remolded loess samples (see Fig. 5.66), the ordering of the curves shows that at 20 kPa suction, the compression-rebound curve exhibits the smallest deformation

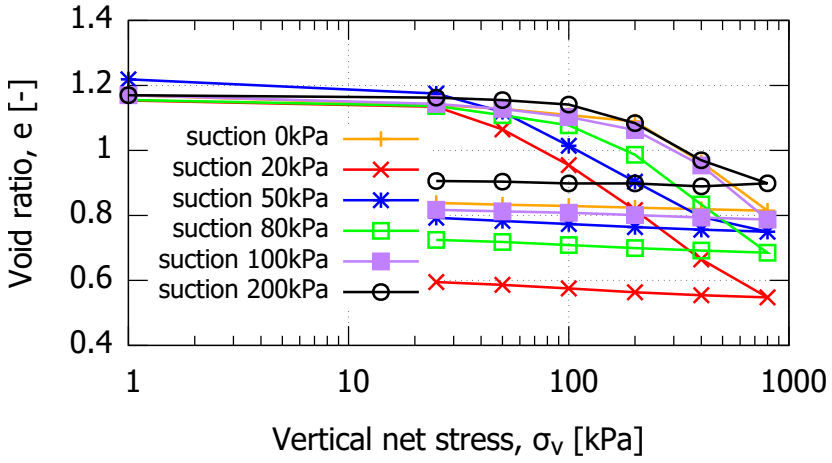

Figure 5.67: Vertical stress vs. void ratio for undisturbed loess samples.

across the entire stress range. The saturated sample lies somewhat above the curves of 50 kPa and 80 kPa, which is partly due to its greater initial void ratio. The curves of 100 kPa and 200 kPa suction show the highest yield stress (excluding the 20 kPa suction curve), as expected. In the case of undisturbed loess samples (see Fig. 5.67), the compression-rebound lines for the unsaturated samples follow a distinct pattern according to their applied suctions, with the curve of 20 kPa suction showing the greatest compression and the one of 200 kPa showing the smallest compression. However, the saturated sample lies between the curves of 200 kPa and 100 kPa and exhibits a relatively high resistance to deformation. This could be due to the prior saturation process, which may have induced compression (by collapse) in the sample, resulting in a somewhat higher density at the beginning of mechanical loading. Overall, Fig. 5.67 clearly illustrates that the deformation response of soil samples to vertical loading is influenced by the suction history and the suction of the soil sample structure. It highlights the significant impact of soil suction during vertical load application on the compression deformation characteristics of unsaturated loess.

For undisturbed loess samples, the pre-consolidation pressure accounts for both the insite stress history, the cementation bonds and the suction effect. Prior to the pre-consolidation pressure, the macrostructure within the soil sample resists the load. As the vertical stress increases beyond pre-consolidation stress, the initial structure begins to deteriorate and a new structure gradually forms. This demonstrates that loess has a high compression capacity under unsaturated conditions.

The unloading path demonstrates that the initial void ratio cannot be recovered again. The strain caused by sliding between particles or fracturing is an irreversible process that corresponds to plastic deformation. However, some small reversible deformation during unloading is observed, which corresponds to the elastic deformation of the sample. The unloading paths were approximately linear and independent of the suction applied.

Fig. 5.68 compares the results for remolded and undisturbed loess for low suction range (up to 50 kPa) and higher suction (above 50 kPa). Fig. 5.68 indicates that undisturbed loess has a higher stiffness compared to remolded loess. The difference in void ratio during loading is larger for remolded loess specimens, which further suggests a higher stiffness for undisturbed loess.

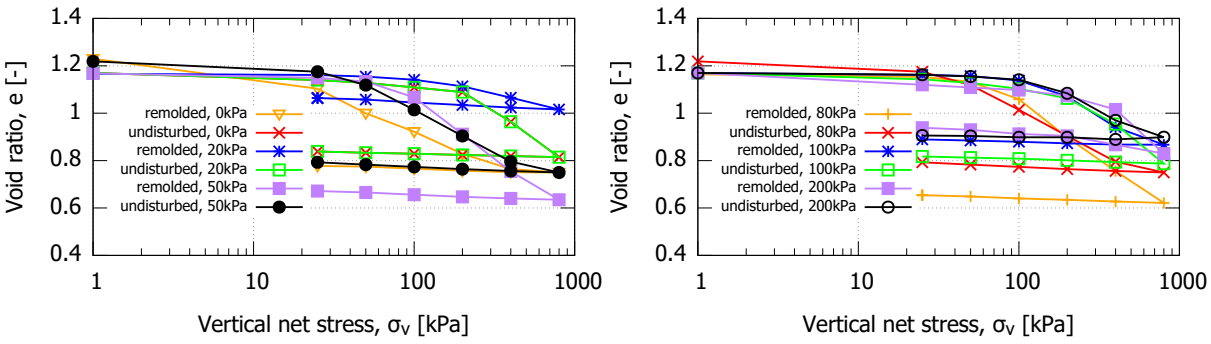

(a) (b)

Figure 5.68: Vertical stress vs. void ratio for undisturbed and remolded loess samples, (a) Low suction, and (b) High suction.

Based on the test results for both remolded and undisturbed loess specimens in Fig. 5.68, it can be observed that the change in void ratio of unsaturated specimens at suction values up to $\psi = 50$ kPa is smaller compared to the void ratio change of the saturated specimens. The test result at suction $\psi = 20$ kPa is close to the results obtained under saturated condition. It can be concluded that the stiffness increases with an increase in suction. Comparing the unloading path of all tests, it can be stated that there is similar behavior for all specimens.

The yield stress of undisturbed loess is greater than that of remolded soil because of the cementation bonding inside the undisturbed loess. As the vertical stress increases,

the cementation inside undisturbed soil is continuously destroyed and cannot be regenerated. The difference in void ratio between unsaturated remolded and undisturbed loess under small and high pressure intervals is not very significant, whereas the difference in void ratio is significant in the intermediate pressure interval. The compression curve of undisturbed soil gradually transitions to that of remolded soil, and the deformation generated in this process can be regarded as the collapse deformation of the macrostructure caused by the instability of the cementation structure.

- Loading collapse curve

The above test results were utilized to determine the characteristic parameters and calibrate the functions of the Barcelona Basic model, as described in Section 6. Various methods, including Casagrande's method (Casagrande, 1936), can be employed to determine the pre-consolidation pressure. The findings from tests conducted on unsaturated over-consolidated soil, as reported in Alonso et al. (2005), indicated the presence of two distinct zones, namely the elastic zone and the plastic zone. The pre-consolidation pressure, denoted as p_0 in partially saturated states and p_0^* in fully saturated states, separates the elastic and plastic zones based on the applied vertical stress.

Fig. 5.69 illustrates the loading-collapse line (LC), where the LC yield curves were obtained by determining the yield points from the experimental compression curves. The shape of the LC yield curves is consistent with those given by Alonso et al. (1990). The results indicate that the yield stresses at various suctions for the undisturbed loess samples are higher than those in the remolded loess samples. This suggests that the differences in the fabric of the undisturbed and remolded loess samples are reflected in the distinct LC yield curves.

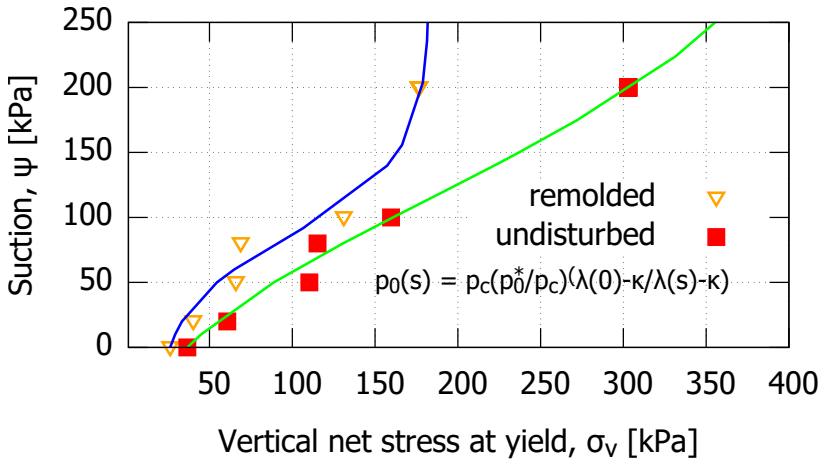

Figure 5.69: Vertical net stress at yield vs. suction.

5.4.2 Change of degree of saturation during compression

Fig. 5.70 illustrates the changes in the degree of saturation versus net vertical stress. The results show that the degree of saturation of the specimens increases with the increase in net vertical stress, and the slopes of the curves associated with different constant matric suctions are nearly identical. The degree of saturation decreases during unloading. Under high vertical stress, the macrostructure of the soil becomes densified, which reduces the pore volume and consequently increases the degree of saturation. Moreover, with an increase in applied suction, the change in the degree of saturation after the compression of unsaturated soils becomes smaller.

Under a large vertical load, according to the theory proposed by Likos and Lu (2004), the SWCC shifts to the right, causing an increase in the water content of the sample, even under constant suction conditions. This occurs due to the decrease in the curvature of the gas-liquid interface, which leads to water inflow into the sample. Additionally, as the vertical stress increases, the soil particles start to realign and move closer to each other, transforming from an unstable state to a stable state. The greater the vertical stress, the greater the effect of water content on the change of degree of saturation due to the large change of soil volume, see in Fig. 5.70.

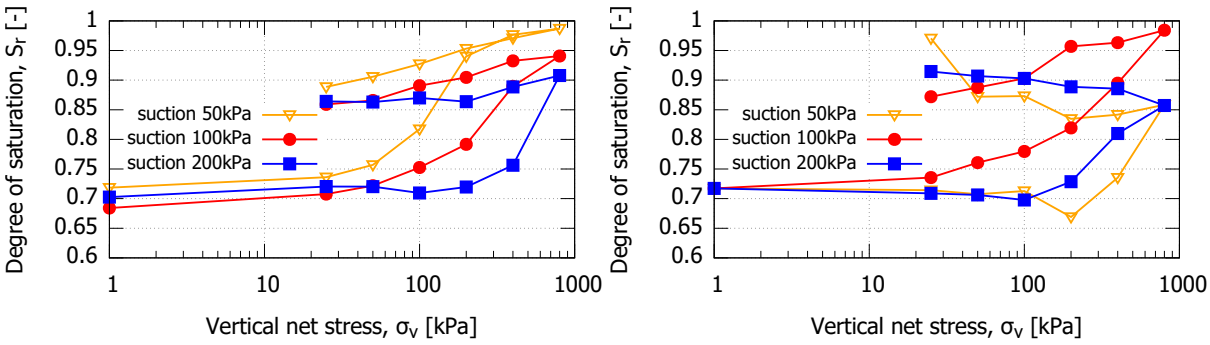

(a) (b)

Figure 5.70: Net vertical stress vs. degree of saturation for (a) Remolded loess samples, and (b) Undisturbed loess samples.

5.4.3 SWCC under various net stress conditions

- Structure effects

Fig. 5.71 illustrates the first wetting path of remolded and undisturbed loess samples under different constant applied vertical stresses. The applied suction was stepwise decreased while the applied net stress remained constant. The wetting curves of the undisturbed loess samples resulted in smaller suctions for a given degree of saturation and vertical stress, compared to the remolded loess samples, as shown in Fig. 5.71(b). This difference is attributed to the presence of large inter-aggregate pores in the undisturbed loess, which affect the wetting process under higher suctions, leading to a lower air entry value. However, at lower applied stresses of 50 and 100 kPa, the trend is less distinct, as shown in Fig. 5.71(a). Remolded loess, compared to undisturbed loess, demonstrated a higher drainage rate. Moreover, the undisturbed loess sample at 50 kPa started from a higher degree of saturation and reached a nearly saturated state with a flat increase of degree of saturation.

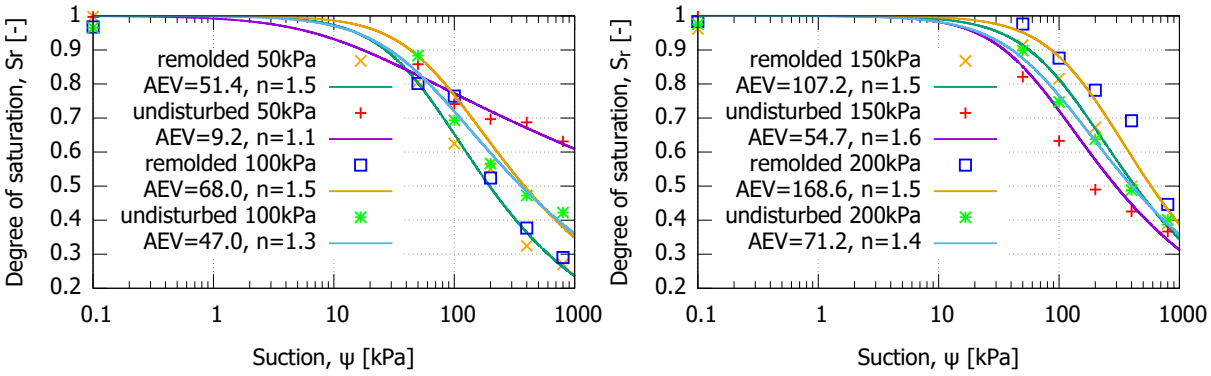

(a) (b)

Figure 5.71: Variation of degree of saturation with suction along first wetting path and under applied vertical stress of (a) 50 kPa, 100 kPa, and (b) 150 kPa, 200 kPa.

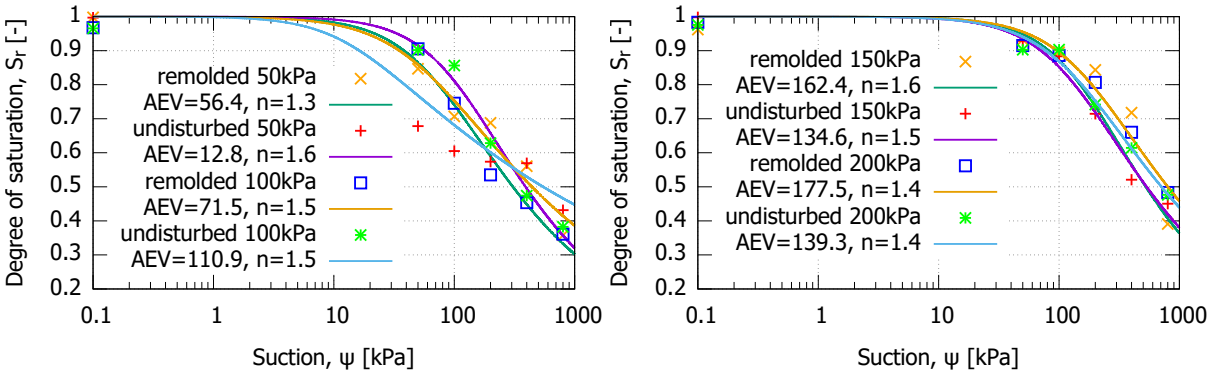

(a) (b)

Figure 5.72: Variation of degree of saturation with suction along first drying path and under applied vertical stress of (a) 50 kPa, 100 kPa, (b) 150 kPa, 200 kPa.

Fig. 5.72 displays the soil water retention curves of remolded and undisturbed soil samples under different vertical stresses, corresponding to the first drying path. As the suction increases, water content reduces due to water drainage, leading to a decrease in pore volume and the migration of liquid water within the macroscopic pores. At the lowest vertical stress, the air entry values determined by the drying curve were 56.4 kPa and 12.8 kPa for the remolded and undisturbed loess samples, respectively. However, for an applied stress of 100 kPa, the air entry value of the undisturbed loess sample was higher (111 kPa) than that of the remolded loess sample. At greater applied net stress (Fig. 5.72(b)), the undisturbed loess samples showed smaller air entry values and the corresponding curves were located to the left of the remolded ones at respective applied stresses.

- Loading effects

The impact of vertical stress on the soil water characteristic curves of loess was investigated. Fig. 5.73 illustrates the soil water retention curve of the remolded loess sample under different vertical stresses during the first wetting and first drying cycles. As the applied net stress increased, the air entry value (AEV) also increased.

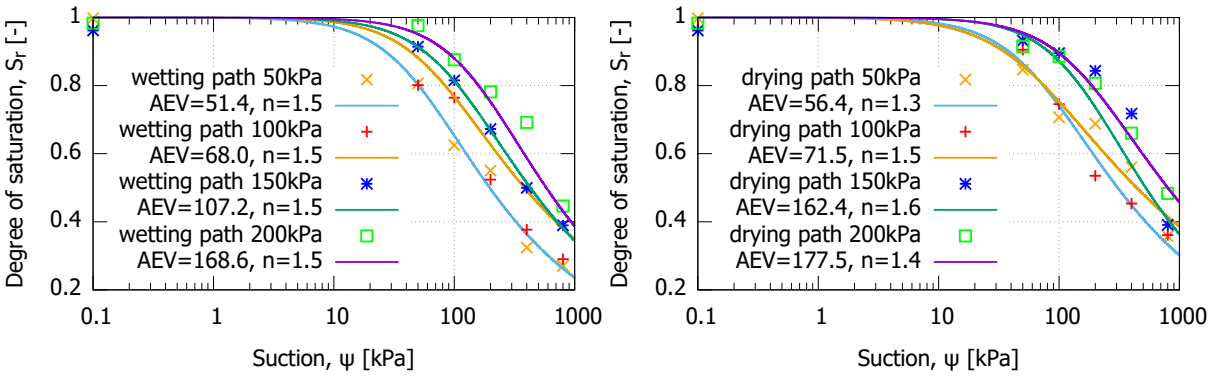

(a) (b)

Figure 5.73: Variation of degree of saturation with suction for the remolded loess sample under different vertical loading, (a) First wetting path, and (b) First drying path.

The impact of vertical loading on the SWCC of remolded loess is primarily due to changes in void ratio caused by the vertical loading. The wetting path data are arranged according to the applied stresses. As the matric suction decreases along the wetting path, the degree of soil saturation gradually increases. This increase in saturation leads to the destruction of the loess structure. The pore connectivity of the soil structure is strong, and the degree of saturation is more sensitive to changes in suction. In contrast, the ordering of the drying path data is less distinct. For instance, the respective points of 150 kPa and 200 kPa are very close and intersect with each other. Similarly, for suctions greater than 100 kPa, the drying path of 100 kPa lies below that of 50 kPa.

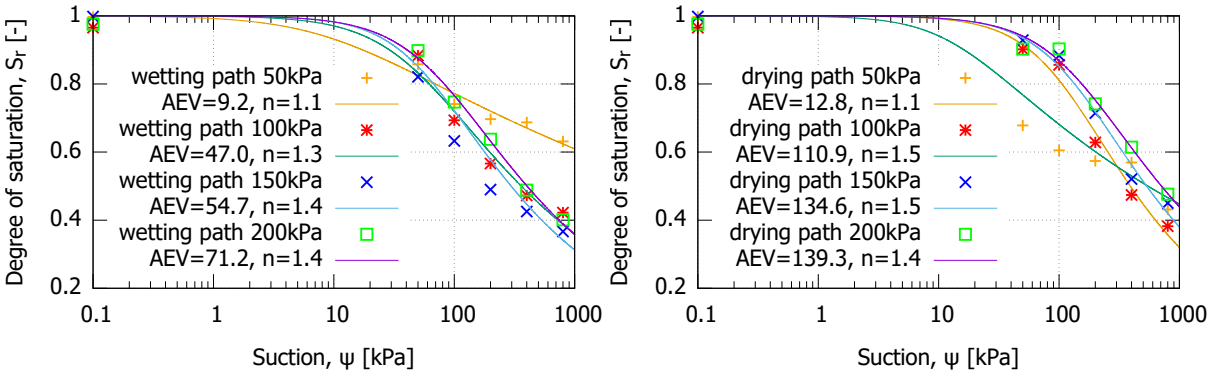

(a) (b)

Figure 5.74: Variation of degree of saturation with suction for the undisturbed loess sample under different vertical loading, (a) First wetting path, and (b) First drying path.

Fig. 5.74 illustrates the changes in the degree of saturation with applied suction under different vertical stresses for the first wetting and first drying of the undisturbed loess samples. For both the wetting and drying paths, the samples subjected to 50 kPa applied stress exhibit a distinct trend compared to those subjected to 100-200 kPa applied stresses. The curves for the 50 kPa samples are flatter because the low applied stress is not enough to compact the large macropores in the undisturbed loess samples. During wetting, the 50 kPa sample starts at a higher degree of saturation (approximately 60%) and crosses the three other curves at around 80% degree of saturation, resulting in the lowest air-entry value of approximately 9.2 kPa.

The drying path for the 50 kPa samples (Fig. 5.74(b)) is notably below those of the greater applied stresses, possibly because the large macropores allow for water drainage at low suctions. The curves and respective air-entry values for the 100, 150, and 200 kPa samples are observed according to the applied stresses, whereas for the wetting paths, no ordering with applied stress was observed. In general, the greater the applied net stress, the greater the air-entry value and suctions required for a given degree of saturation. Furthermore, the degree of saturation gradually increases with a decrease in matric suction under different vertical pressures, but the rate of increase varies.

Fig. 5.74 shows that there was a significant increase in the degree of saturation with increasing applied vertical stress under the same suction. This increase can be attributed to the fact that the undisturbed soil structure of the sample was altered by the increase

in vertical stress, and the suction helped to enhance the structural stability of the soil skeleton. With greater vertical stress, there was more rearrangement of soil particles under the same suction, resulting in better pore connectivity in the soil. As a result, the degree of saturation decreased or increased more rapidly with respect to the respective applied suction.

- Hysteresis phenomenon

From Fig. 5.75, we can observe a gap between the wetting and drying curves, which is known as the hysteresis phenomenon of the soil water characteristic curve. This phenomenon can be attributed to four factors: the bottle-neck effect caused by the uneven cross-sectional diameter of the pore channel, the entrapment of air generated during the drying and wetting process, a decrease in the influence of capillary forces on the water retention characteristic curve when suction is large, and an increase in the influence of adsorption effect of the soil surface. The adsorption effect is mainly related to the mineral composition and specific surface area of the soil.

In this study, the undisturbed and remolded loess have the same mineral composition and similar influence of adsorption force on total suction. Their initial pore size distribution differs. However, loading changed the pore size distribution, resulting in small differences in the pore size distribution between undisturbed and remolded loess samples. As suction increases, the difference in the water retention characteristic curve between undisturbed and compacted loess becomes less significant.

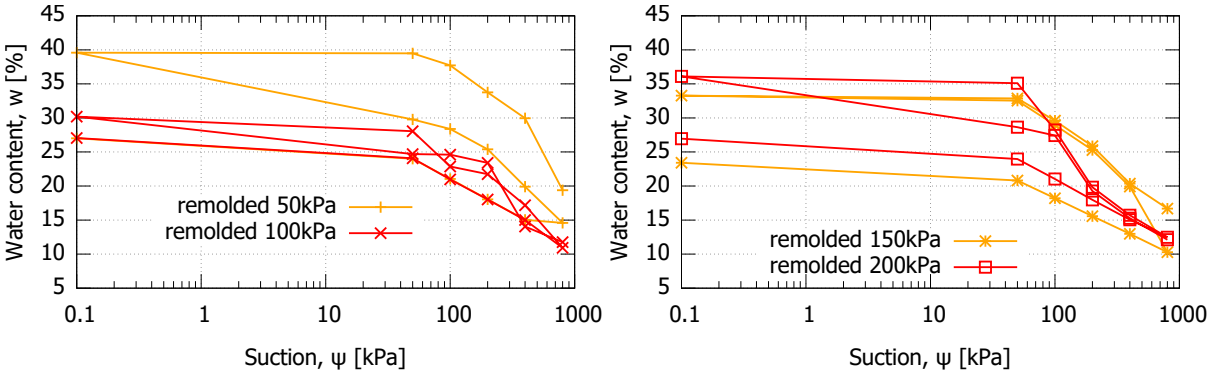

(a) (b)

Figure 5.75: Hysteresis behaviour in w-ψ plane for remolded loess sample along different hydraulic path, (a) Low vertical stress, and (b) High vertical stress.

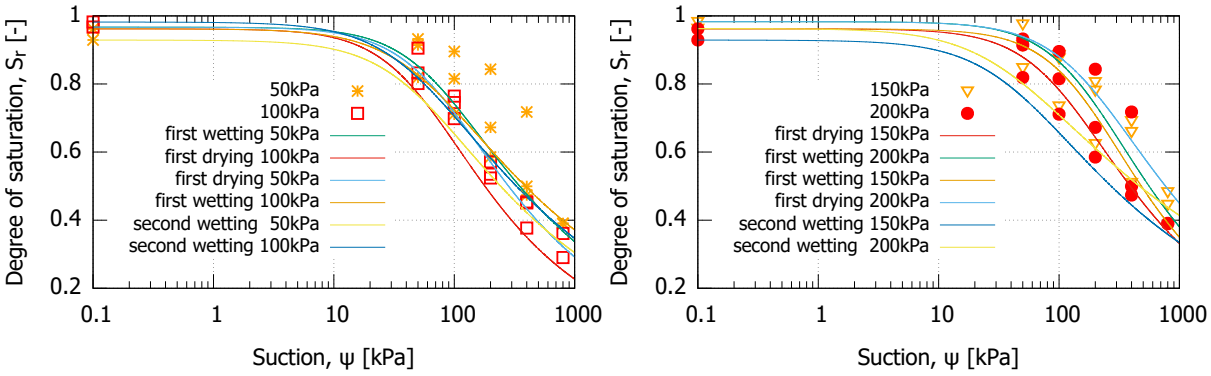

(a) (b)

Figure 5.76: Hysteresis behaviour in S_r-ψ plane for remolded loess sample along different hydraulic path, (a) Low vertical stress, and (b) High vertical stress.

In Fig. 5.75, it can be observed that at all applied stresses, the water content during the initial first wetting path remained below that of the subsequent drying path. Additionally, the water content during the following second wetting path was lower than that of the two prior paths.

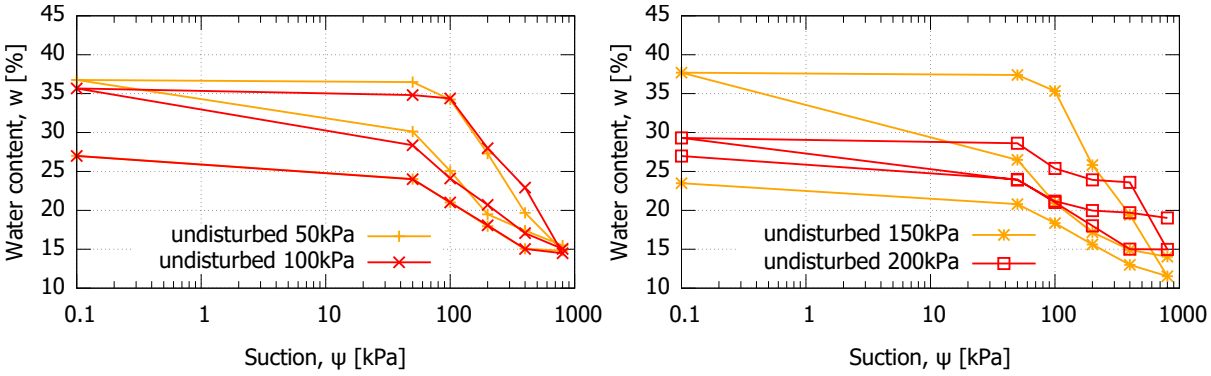

(a) (b)

Figure 5.77: Hysteresis behaviour in w-ψ plane for undisturbed loess sample along different hydraulic path, (a) Low vertical stress, and (b) High vertical stress.

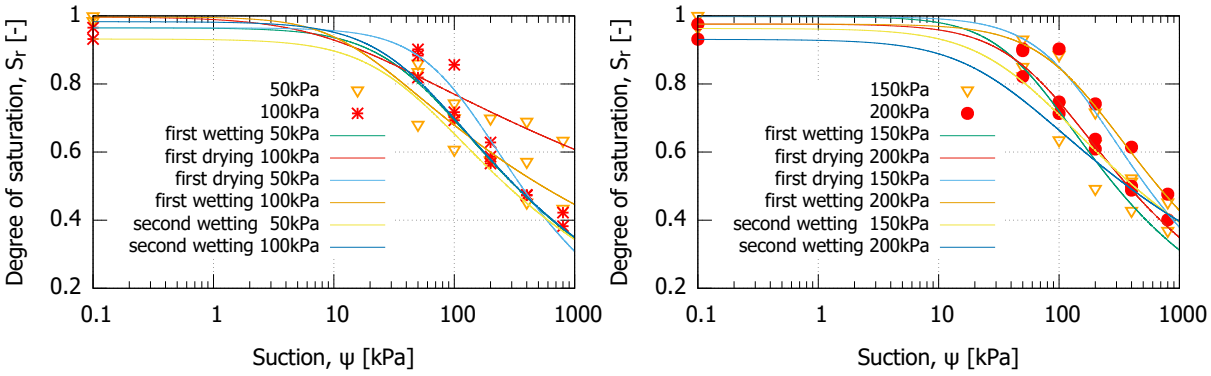

(a) (b)

Figure 5.78: Hysteresis behaviour in S_r-ψ plane for undisturbed loess sample along different hydraulic path, (a) Low vertical stress, and (b) High vertical stress.

Fig. 5.75 and Fig. 5.76 illustrate the hysteretic behavior of the remolded loess samples in terms of water content versus suction and degree of saturation versus suction, respectively. Similarly, Fig. 5.77 and Fig. 5.78 show the hysteresis behavior for the undisturbed loess samples. In all cases, the data represents the first wetting, first drying, and second wetting.

For the remolded loess samples, it can be observed that each applied stress results in a different hysteresis behavior (Fig. 5.79(a)). The hysteresis is most pronounced for 50 kPa, while it is smallest at 100 kPa. The samples at 150 kPa and 200 kPa exhibit similar behavior, with no hysteresis between the first wetting and first drying in the suction range between 50 and 800 kPa (see Fig. 5.79).

The test results also indicated that the degree of saturation of the undisturbed loess samples (Fig. 5.78) and the remolded loess samples (Fig. 5.76) reached a level between 90% and 100%. These results suggest that it was not possible to fully saturate the soil samples at zero suction, especially at low values of net vertical stress. This behavior is likely due to the presence of air bubbles trapped between the soil particles, which prevent full saturation of the soil structure.

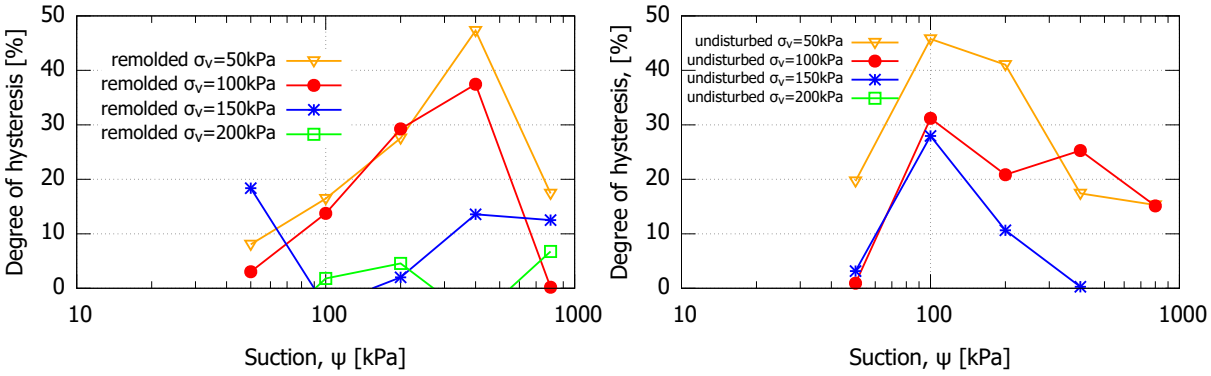

(a) (b)

Figure 5.79: The magnitude of hysteresis (D_d/w) under different vertical stress values (a) Remolded loess sample, and (b) Undisturbed loess sample.

5.4.4 Volume change during wetting and drying

Fig. 5.80(a) illustrates the variation of void ratio with applied suction during gradual wetting of the soil by multi-step suction decrease under the same constant net vertical stress. The void ratio decreases reached their maximum values at zero suction. A large collapse occurs in the suction range from 1000 kPa to 100 kPa, corresponding to the transition range under specific loading conditions. Under this range, there is a continuous seepage pathway for both pore water and pore air. The decrease in capillary force during the suction decrease process causes deformation at the macrostructural level.

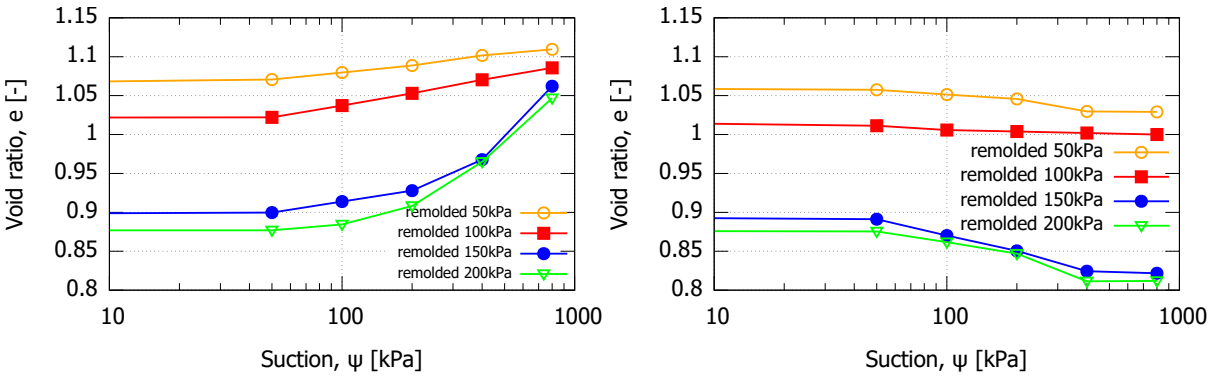

(a) (b)

Figure 5.80: Variation of void ratio with suction for the remolded loess sample along the first wetting path and first drying path, (a) First wetting path, and (b) First drying path.

As shown in Fig. 5.80(a), with an increase in the degree of saturation, the amount of wetting deformation under the same pressure gradually decreases. The soil becomes denser, its compressibility decreases, and collapsibility gradually decreases as well. The collapsibility of loess under different suction and different wetting processes varies.

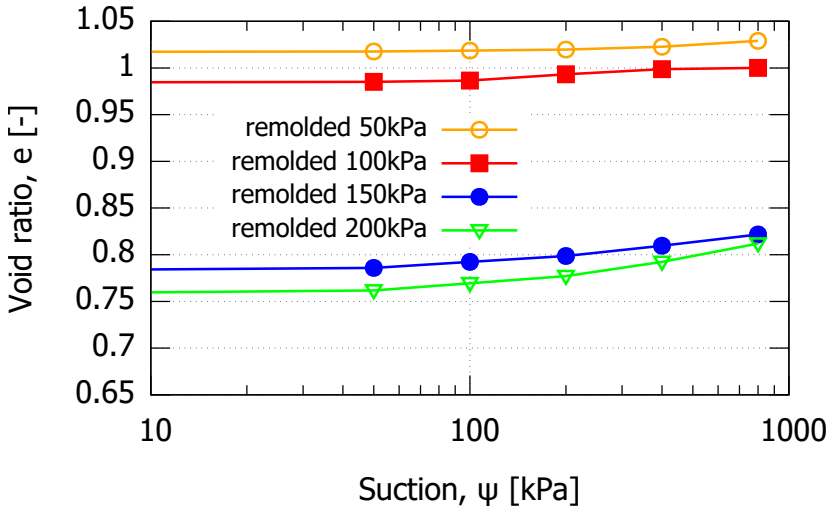

Figure 5.81: Variation of void ratio with suction for the remolded loess sample along the second wetting path.

In Fig. 5.80(a), for the lower suction range (less than 100 kPa), the e - suction curves under different vertical pressures are approximately parallel. The $e-$suction curve can be divided into two sections. Before the turning point, the void ratio rapidly decreases with decreasing suction. After the turning point, the void ratio gradually decreases with decreasing suction. The vertical pressure has a significant impact on the deformation during stepwise wetting. As the vertical pressure increases, the $e-$suction curve gradually shifts downwards, but the slopes of the curve do not change significantly. This phenomenon reflects the increase in collapsibility under greater vertical pressure.

Fig. 5.80(b) shows the variation of the void ratio with applied suction upon gradual drying of the soil. In the first drying process, as the matric suction increases, the average skeleton stress of the soil increases, the soil skeleton is compressed, the void ratio becomes smaller, and the contact area between soil particles increases. Fig. 5.80(b) indicates that the values of void ratio decreased progressively as the applied suction increased.

In the second wetting process, as the matric suction decreases, the average skeleton stress

of the soil decreases and the void ratio decreases (Fig. 5.81). However, since the sample experienced a prior wetting-drying cycle with significant void ratio decrease, the soil sample volume was only slightly compressed during the second wetting.

The data in Fig. 5.80 shows that dry-wet cycling can induce irreversible deformations in a compacted soil, with the effect varying depending on the applied vertical loading. The deformation of the compacted soil was found to be most severe under the first wetting and drying, while subsequent cycles led to a new equilibrium state with reduced deformation.

Laboratory tests revealed that dry-wet cycling resulted in collapsing properties in the compacted loess, manifesting as secondary collapsing. This may be attributed to the role of salt crystals, which are part of the soil skeleton as cementation agend. Repeated leaching during wet-dry cycling caused changes in the content and composition of soluble salts, which in turn led to a thicker diffusion layer in the electric double layer on the soil particle surfaces, weakening their connections. Hydrophilic clay minerals such as illite and montmorillonite can absorb water, causing the soil skeleton to swell, which can also contribute to the observed deformation.

As the vertical stress increases, the overhead structure of the loess changes to a surface-contact cement structure, leading to an increase in the relative sliding of the particles and a decrease in the collapsing coefficient. With an increase in the number of wet and dry cycles, remolded loess is more likely to experience wet collapse. During the drying process, the soil skeleton shrinks unevenly, resulting in the expansion of some small pores and an increase in the volume of large pores in the soil, causing the soil volume to be unable to return to its initial state before wetting. Therefore, the dry-wet cycle has the most significant influence on the compressive characteristics of the soil with the highest vertical stress. The amount of deformation has a negative correlation with the number of dry and wet cycles, i.e., it increases with increasing vertical loading and decreases with an increase in the number of dry and wet cycles.

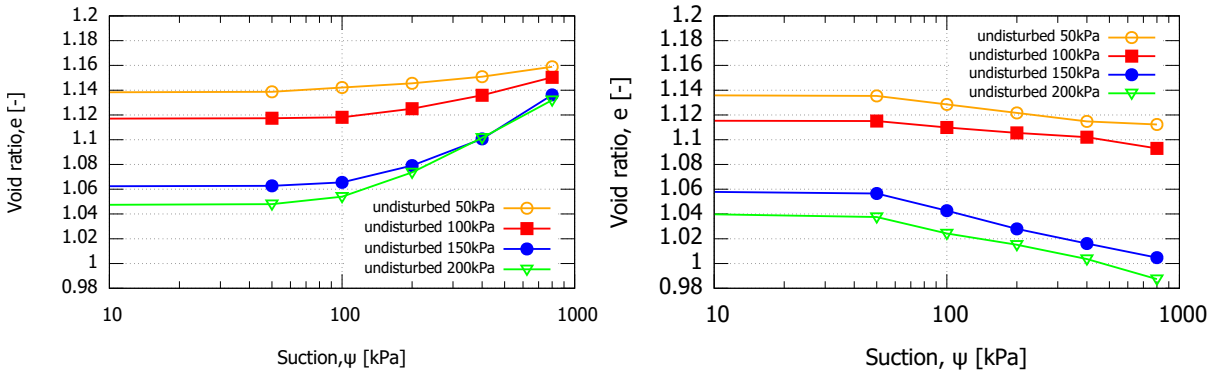

(a) (b)

Figure 5.82: Variation of void ratio with suction for the undisturbed loess sample along the first wetting path and first drying path, (a) First wetting path, and (b) First drying path.

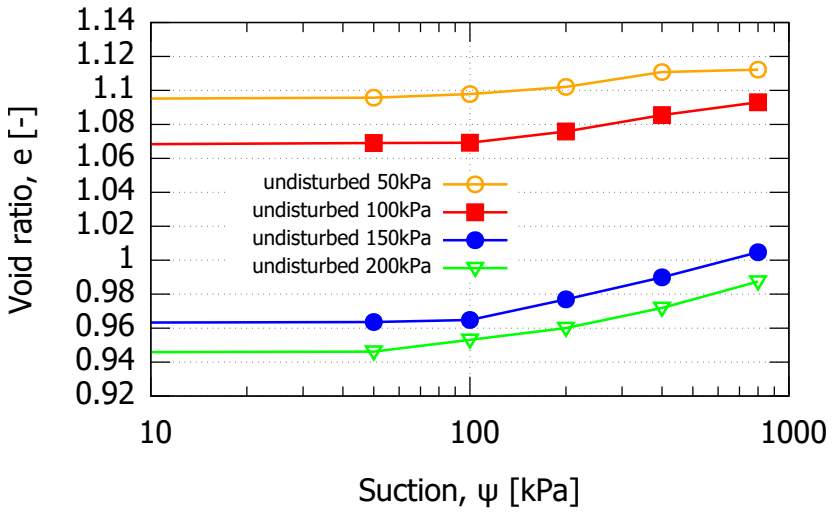

Figure 5.83: Variation of void ratio with suction for the undisturbed loess sample along the second wetting path.

In Fig. 5.82, the void ratio evolution with suction of an undisturbed soil sample is presented. The initial unsaturated state was set as the starting point for the wetting path in Fig. 5.82(a), where no further settlement was observed under a constant net vertical stress during the consolidation process. The applied suction was then decreased in multiple steps, inducing a significant reduction in void ratio and volumetric change during subsequent wetting-drying processes, as shown in Fig. 5.82(a), Fig. 5.82(b) and Fig.

5.83. When the applied vertical stress is large, the soil sample's structural strength may not withstand deformation and damage, leading to significant compression during wetting.

The wetting curve of undisturbed loess has a larger slope initially and then shows a smaller volume change after reaching a certain suction value. The sample then follows a drying path, which also induced a void ratio reduction due to shrinkage. The second wetting path induced again a wetting induced void ratio decrease, but with a lower magnitude as during first wetting. As expected, no swell was observed for all samples in Fig. 5.82. Under high vertical loading (Fig. 5.82(a)), the soil experiences greater compression deformation than at smaller load. As the soil becomes progressively saturated with water, and the degree of saturation increases with the decrease of suction, the deformation increases at a gentler rate. This is because the skeleton particles are primarily connected through cementation bonds.

Undisturbed soil samples typically exhibit cementing bonding that can support external loading at relatively low degrees of saturation. However, when suction decreases, the bonding can be broken by inflow water, resulting in collapse deformation and densification of the soil structure. This process can cause dispersion and disruption of silt-clay bridges or buttresses within the interparticle matrix, leading to a rearrangement of the soil skeleton into a more closely packed structure after the collapse of cavities and destruction of the macrostructure.

Under K_0 condition during oedometer tests, shearing forces can cause slippage between solid particles. Undisturbed loess can undergo progressive collapse after saturation, with the subsequent collapse curve overlapping with the compression curve of the saturated undisturbed loess sample. During subsequent saturation processes, the cementation between clay particles can partially fail, leading to greater collapse deformation. This is because the increase in water content decreases the cementation of clay particles in undisturbed loess, resulting in large plastic deformation under different vertical loading and significant impairment of its structure.

- Effect of structure on suction induced deformation

Fig. 5.84 compares the results of cyclic wetting and drying on remolded and undisturbed soil samples. Differences in sample preparation and sedimentation processes can result in variations in microstructure, which are more apparent under low vertical loading. Comparing the curves of undisturbed and remolded soil (Fig. 5.84), it can be observed that

the collapse line of undisturbed soil gradually approaches that of remolded soil as the vertical loading increases. At high pressure values, the difference in void ratio between remolded and undisturbed loess samples is not significant. However, at low pressure, the difference in void ratio is considerable, indicating that undisturbed soil exhibits greater resistance to collapse within this pressure range. The collapse curve of soil ultimately reaches a constant value.

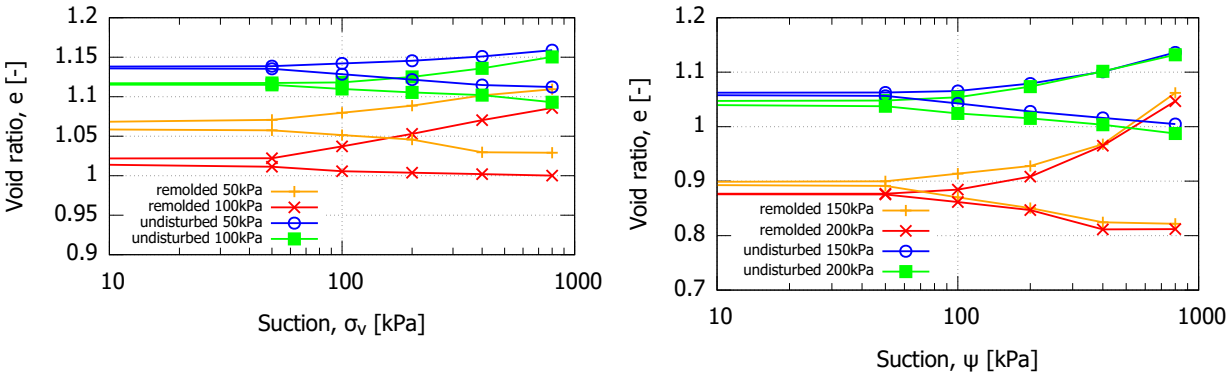

(a) (b)

Figure 5.84: Variation of void ratio with suction under different vertical stress, (a) Low vertical stress, and (b) High vertical stress.

The influence of soluble salt cementation on soil deformation is limited by low vertical pressure, with deformation mainly dependent on wetting (Fig. 5.84(a)). The decrease in suction reduces the number of cementation points in the undisturbed loess sample and increases soil deformation. However, under high vertical pressure, many cementation bonds have already been destroyed by the increase in mechanical load.

5.4.5 Comparison with single oedometer test

The collapse potential obtained by stepwise suction controlled wetting for both remolded and undisturbed soil samples is compared to those obtained using the single and double oedometer tests (Fig. 5.85). The collapse potential of the stepwise suction-controlled wetting for the remolded sample was found to be in between those determined by the single and double oedometer tests. The stepwise obtained collapse potential of the undisturbed sample was found to be very similar to the respective collapse potential obtained by single pedometer tests. The obtained values of collapse potential for the stepwise first wetting are listed in Tab. 5.14. Fig. 5.86 summarizes the measured collapse potential at

four different applied vertical stresses for the first wetting path, the first drying path and the second wetting path for the remolded and undisturbed samples. The shrinkage and collapse potential due to the first drying and second wetting are found to be significantly smaller as compared to the first wetting for both sample states.

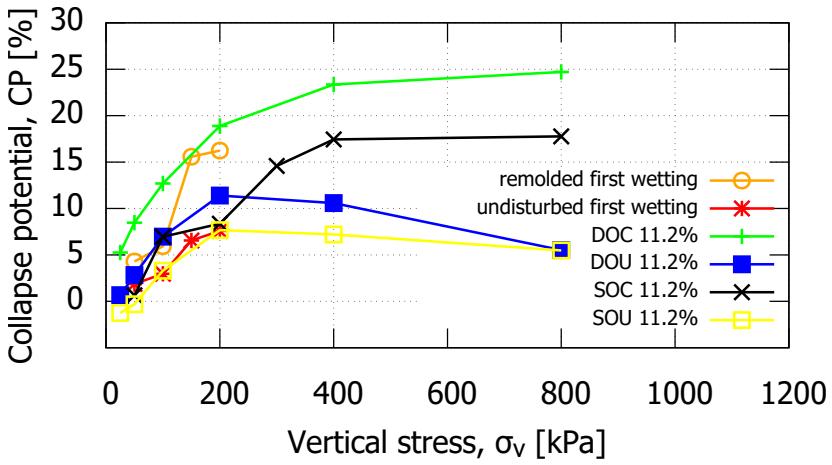

Figure 5.85: Collapse potential versus vertical stress from different test methods.

Table 5.14: Collapse potential from first wetting test (stepwise suction decrease).

Remolded loess sample (C)		Undisturbed loess sample (U)	
Vertical stress	Collapse potential	Vertical stress	Collapse potential
50	4.30	50	1.87
100	5.93	100	2.97
150	15.58	150	6.56
200	16.24	200	7.59

The collapsibility of loess is influenced by various physical properties, including its natural water content, dry density, microstructure, mineral composition, confining conditions, and hydraulic properties. The hydraulic properties, in turn, depend on factors such as the historical maximum suction, wetting degree, and wetting path. Further, as the vertical loading increases, the soil becomes more susceptible to irreversible volume collapse. The fundamental reason for the change in the soil's macroscopic deformation characteristics is the irreversible alteration of its microstructure under the influence of dry and wet cycles.

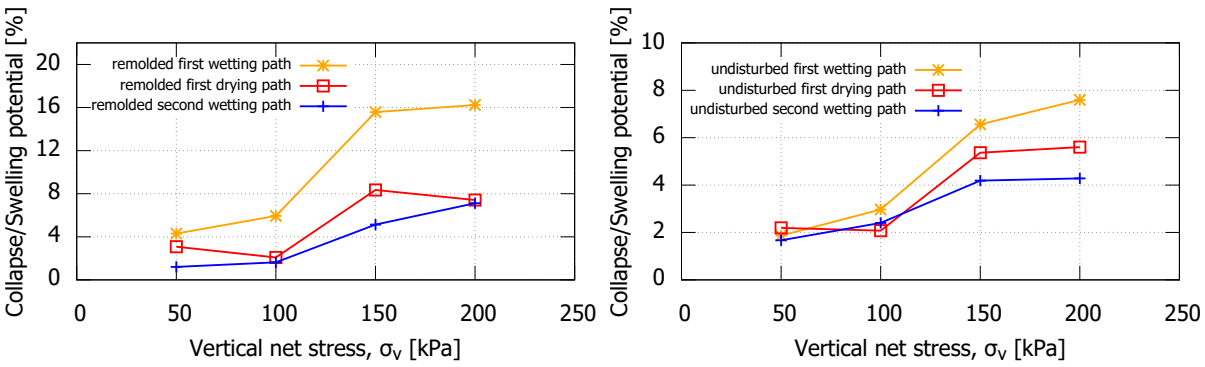

(a) (b)

Figure 5.86: Variation of collapse and shrinkage potentials with the vertical net stress value, (a) Remolded loess sample, and (b) Undisturbed loess sample.

- BBM parameters from suction controlled compression test

The model parameters for the BBM model are derived from the suction-controlled oedometer tests. Investigations carried out in the controlled-suction oedometer cell reveal that the stiffness behavior of unsaturated loess is influenced not only by the void ratio but also by the suction. The method of parameter derivation follows the guideline provided in Alonso et al. (1990).

Fig. 5.87(a) shows that the slope of the elastic part of the consolidation line (κ(s)) is slightly suction-dependent and decreases as the suction increases. κ(s) is equivalent to the unloading slope parameter, which is determined by unloading paths in a stress-specific volume plane, and can be adjusted as the suction varies. When α_i is negative, κ_i(s) will increase as the suction decreases and reach a peak when the suction equals zero. A comparison is made between the BBM parameters obtained from the results of the suction-controlled oedometer compression tests.

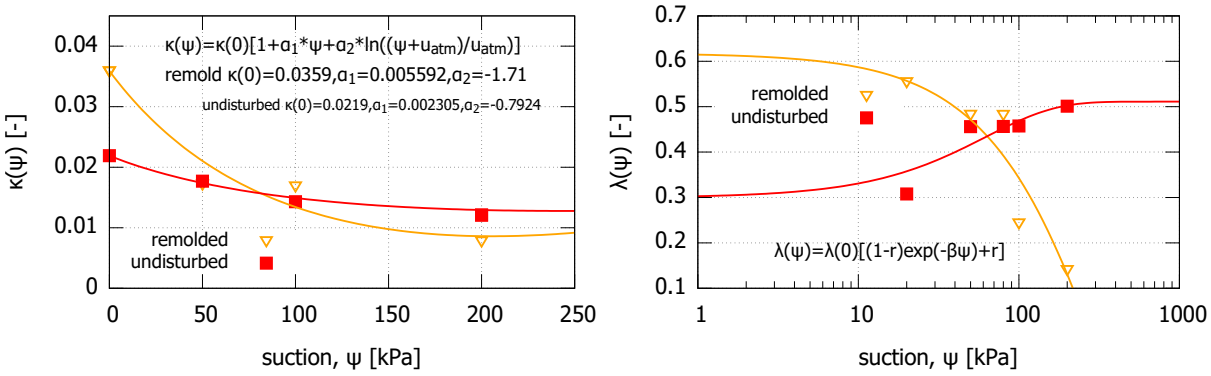

(a) (b)

Figure 5.87: κ and λ vs. suction for remolded and undisturbed loess samples from suction controlled compression test, (a) κ vs. suction, and (b) λ vs. suction.

According to the model proposed by Alonso et al. (1990), the slope of isotropic consolidation lines λ(s) decreases monotonically with the increase of suction from the saturated value $\lambda(0)$, becoming asymptotic to a value r. Fig. 5.87(b) shows the variation of λ for both types of samples with suction. Experimental results reveal that λ(s) for both undisturbed and remolded loess samples is a function of suction. For the remolded loess sample, the slope of the plastic part of the compression line λ(s) decreases with increasing suction. In contrast, the value of λ(s) increases with increasing suction from 20 to 50 MPa for undisturbed loess samples and then remains nearly constant. The reason is that the compression curves for different suction were not completely ordered according to the suction applied.

- BBM parameters from wetting and drying test

Fig. 5.88 displays the stiffness of both remolded and undisturbed soil samples under different wetting and drying paths as represented by the slope of compression line in the elastic zone $\kappa(s)$. The results indicate that $\kappa(s)$ is slightly influenced by stress path, net vertical stress, suction, and degree of saturation. The stiffness change caused by changes in suction decreases as the vertical loading increases. The first wetting path results in the lowest stiffness under various vertical loading conditions as indicated by the highest $\kappa(s)$. However, overall the suction effects on $\kappa(s)$ are not as pronounced as for λ. In case of the undisturbed samples, the effects of cyclic wetting and drying on $\kappa(s)$ are even less than for the remolded samples.

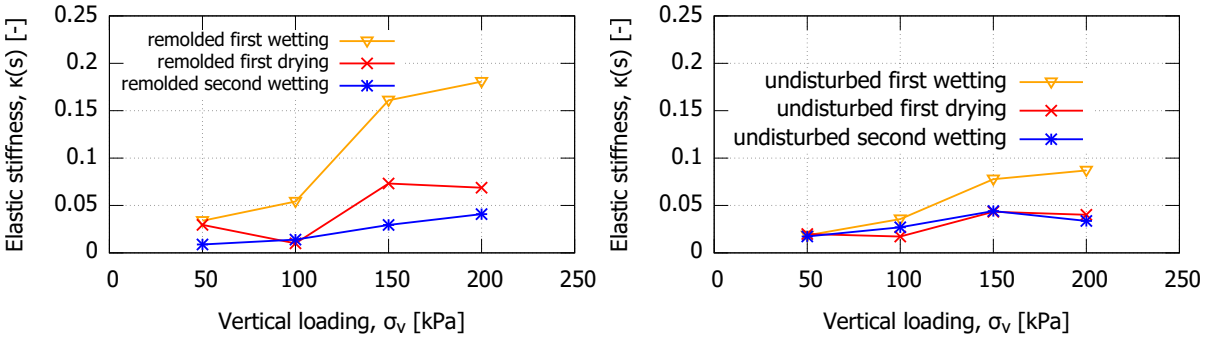

(a) (b)

Figure 5.88: Variation of κ with vertical loading along different wetting and drying paths, (a) Remolded loess sample, and (b) Undisturbed loess sample.

- Yield surface given by different stress paths.

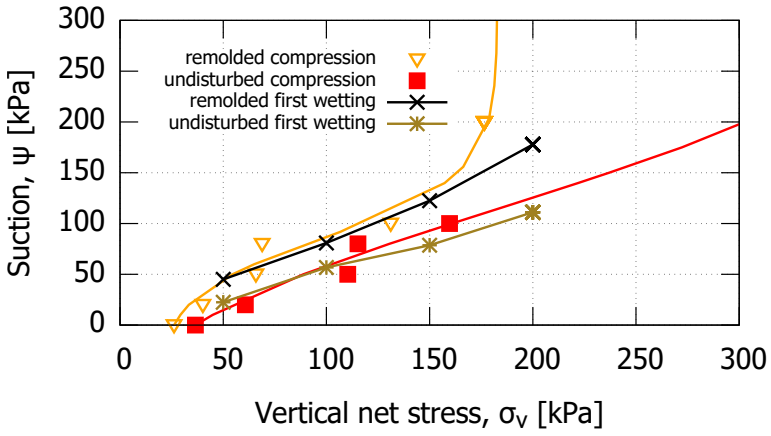

Figure 5.89: Loading collapse curves from suction controlled compression tests and first wetting tests.

The yield stress of both undisturbed and remolded soil can be represented by the LC curve when plotted on the $p - s$ plane. As shown in Fig. 5.89, the yield stress increases with increasing suction, which is attributed to the decreasing water content and the soil's increased ability to resist external loads. It can also be observed that the yield stress of undisturbed soil at a given suction is greater than that of remolded loess, indicating that undisturbed soil undergoes less deformation under increasing loads than remolded soil.

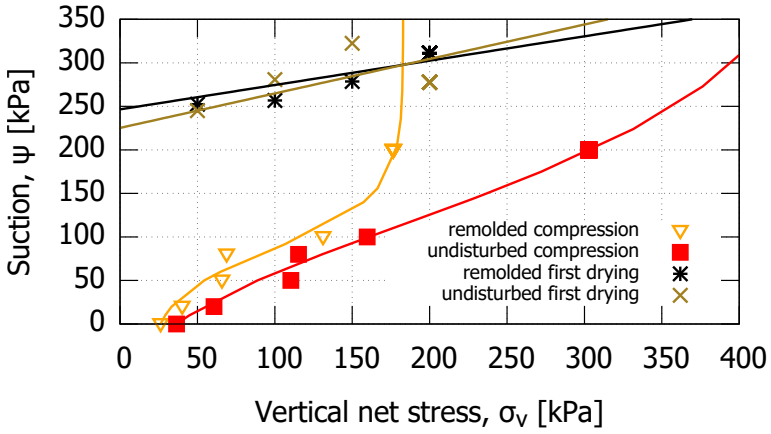

Figure 5.90: Loading collapse curves from unsaturated compression tests and first drying tests.

The elastic zone of undisturbed soil is also larger than that of remolded soil in the two-dimensional $p - s$ plane, indicating that it requires a larger suction and net mean stress to induce yielding. The presence of the soil structure in undisturbed soil contributes to its stronger ability to withstand external loads. In the suction decrease test, it was found that as the net mean stress increased, the change in yield suction was small. Therefore, it can be concluded that the yield suction of both undisturbed and remolded loess increases at a constant rate with an increase in net mean stress.

Undisturbed soil has a strong structure that can withstand external forces before plastic deformation. Under low suction, the difference in pre-consolidation pressure between the remolded and undisturbed loess samples is minimal. This is due to the damage caused to the undisturbed soil structure by wetting, causing its deformation property to shift and become similar to that of remolded soil with increasing degrees of saturation. In Fig. 5.90, the yield suction of the remolded and undisturbed loess samples obtained from the first wetting test is shown. This intersection suction marks the point at which elastic deformation shifts to plastic deformation under certain vertical loading. This finding is consistent with the collapsing tests of undisturbed and compacted loess in the single oedometer test results. In the low suction state, the collapsibility of undisturbed loess is similar to that of compacted loess. However, in conditions of low water content and high suction, the strong structure of undisturbed loess results in a significantly greater collapsibility compared to remolded loess.

- Movement of yield surface

Fig. 5.91 displays the yield suction obtained from the first and second wetting tests under various vertical loading. The yielding curve of the undisturbed loess sample is located below that of the remolded loess sample. This implies that the collapsibility of the remolded loess sample is greater than that of the undisturbed loess sample. The yield suction of the remolded and undisturbed loess samples varies linearly with loading. To induce plastic deformation, a greater decrease in suction is required for the undisturbed loess sample under the same vertical loading.

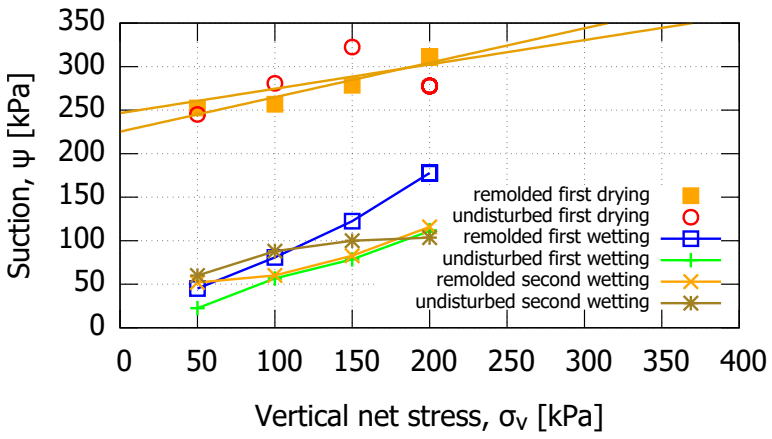

Figure 5.91: Yield suction vs. net vertical stress from suction controlled wetting and drying tests.

After cyclic wetting and drying, the yield surface shifts downwards, indicating that the structure of the sample has become more stable during the second wetting path. The elastic zone expands to a larger area. The yield suction of the soil is linked to the initial void ratio and structural state of the soil. Under different vertical stress, the yield suctions of the unsaturated undisturbed loess are equal.

5.5 Permeability test

This section focuses on the saturated permeability coefficients of remolded and undisturbed loess under different vertical loading conditions. The falling head test was employed to determine the permeability, as the loess soil requires a relatively high hydraulic

gradient to induce water flow through the soil mass due to its low permeability.

In order to perform unsaturated seepage calculations, it is necessary to determine both the soil-water characteristic curves and the coefficient of saturated permeability. The unsaturated coefficient of permeability of the collapsible soil is primarily a function of the degree of saturation, while the saturated coefficient of permeability is a function of the void ratio. Therefore, tests on the saturated permeability under different vertical loads inducing different void ratio are used to study the influence of the void ratio on permeability.

5.5.1 Effect of the sample structure and vertical loading

The results of the tests suggest that the applied vertical loading has a significant impact on the void ratio, thus, on the permeability coefficient of the soil (Fig. 5.92). This is because the size and number of voids in the soil decreases and the contact area between the soil particles increases with increasing vertical loading, resulting in lower permeability, particularly when the soil mass is confined at a high stress level. It was also found that the saturated permeability of undisturbed soil is larger than that of remolded soil due to the higher void ratio at the respective confining stresses.

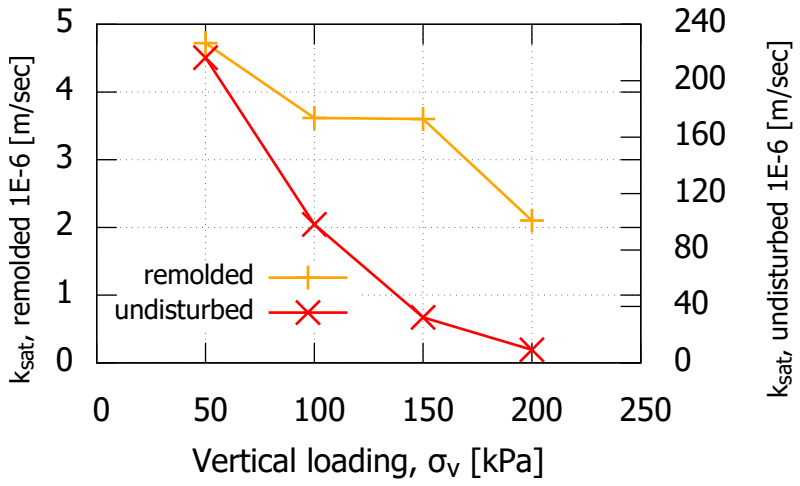

Figure 5.92: Measured saturated permeability coefficient vs. net vertical stress.

The permeability coefficient of the undisturbed sample is larger than that of the remolded sample. The undisturbed soil typically contains large pores and vertical joints that are

mostly semi-closed, which can restrict the flow of water. In contrast, the remolded soil often presents a more uniform pore structure, which can allow for easier liquid flow. However, remolded loess is more prone to collapse deformation at lower stresses, which destroys the original connected pores and results in a denser soil sample that impedes the flow of water.

5.5.2 Unsaturated permeability

The estimation of unsaturated permeability coefficients for loess soils based on SWCC and the empirical model proposed by Brooks and Corey (1964*a*) is a common practice in soil science and geotechnical engineering. The model can also estimate the unsaturated permeability coefficient by assuming a certain pore size distribution and using the pore size distribution index (n). The smaller the n value, the wider the pore size distribution, and the larger the unsaturated permeability coefficient.

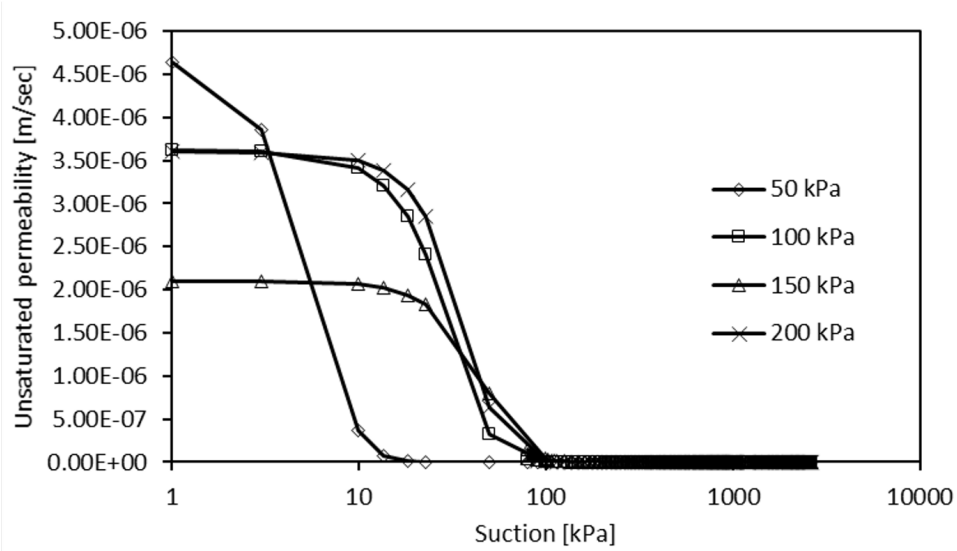

Figure 5.93: Evolution of unsaturated permeability coefficient over suction for the remolded sample.

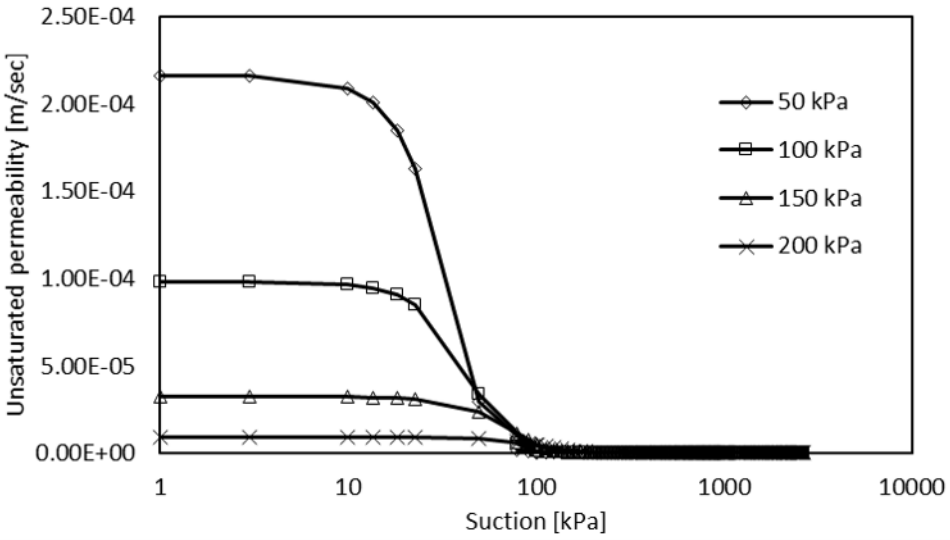

Figure 5.94: Evolution of unsaturated permeability coefficient over suction for the undisturbed sample.

The results of the permeability coefficient estimation show that the unsaturated permeability coefficient decreases as the suction increases for both remolded and undisturbed loess soils (Fig. 5.93 and Fig. 5.94). One reason is that the suction increase induces volumetric shrinkage resulting in a more narrow pore size distribution with a decrease in the effective pore size and a decrease in the unsaturated permeability coefficient. The second reason is because the movement of water through the soil is hindered by the air-filled pores, which reduce the continuity of the water flow path. The effect of suction on permeability is more pronounced at low suctions, where the decrease in water content is more significant. As the suction approaches the air entry value, the permeability coefficient decreases rapidly, indicating the transition from the liquid phase to the gas phase in the soil. The relationship between suction and permeability is often described by the relative permeability curve, which is a dimensionless function that relates the permeability of the soil under unsaturated conditions to the permeability under saturated conditions. Both suction and vertical loading affect the unsaturated permeability coefficient of loess, indicating the importance of considering the unsaturated condition in geotechnical engineering design and analysis.

5.6 Summary

This chapter presents the experimental results, analysis, and discussions of the test program conducted on both remolded and undisturbed loess soils.

- The collapse potential was studied in this thesis using both single oedometer and double oedometer tests. The collapse potential decreased as the initial water content increased. However, the collapse potential showed a non-linear relationship to the applied vertical stress at inundation with larger initial water content. Until a certain critical load, the collapse potential increased with increasing applied vertical stress at inundation. After this critical load, the collapse potential decreased with increasing applied vertical stress at inundation. The critical load depended on the pre-consolidation pressure of the sample. The collapse potential from double oedometer tests was slightly larger than that from single oedometer tests.

- The results of direct shear tests showed that the peak strength decreased as the initial water content increased. For samples with the same initial water content, the shear strength of the undisturbed samples was larger than that of the remolded samples. Under low vertical loading and high suction value, undisturbed loess behaved as a brittle material. The samples with large initial water content showed hardening behavior. The effect of confining pressure on the loess sample responses in the drained triaxial compression tests was similar to that in the direct shear tests. In general, as the confining pressure increased, the stress hardening also increased.

- The results of testing the soil water characteristics curve (SWCC) for both remolded and undisturbed loess showed that the hydraulic loading path affects the shape of the SWCC. The experimental data in this case show hysteresis in the SWCC for both types of soil, being most significant after the first drying.

- Three empirical SWCC models from the literature were used to fit the experimental data. To determine the best fit, residual analysis was used to predict the model parameters, and statistical analysis was performed to evaluate the fitting quality. Data transformation was used to find a linear relationship between the degree of saturation and suction, in order to make it easier to analyze and interpret the data.

- The constant suction oedometer tests revealed that the stiffness is higher at larger suction values, and the swelling indexes are similar for tests performed at various constant suction values. The effect of suction on the pre-consolidation pressure is significant, with an increase observed in the measured pre-consolidation pressure

with increasing suction for the defined suction range tested. The pre-consolidation pressure of the undisturbed sample is larger than that of the remolded sample.

- The results of suction-controlled wetting and drying tests show that the vertical load and direction of hydraulic loading path influence the shape of the soil water characteristic curve (SWCC). With an increase in vertical load, the curve shifts to the right of the suction value, and for a certain suction value, the degree of saturation under the drying path is larger than that under the wetting path. The air entry value of loess increases with increasing vertical load, but the SWCC located in the residual zone is less influenced by vertical load.
- The measured water content change, volume change, and controlled suction can be directly linked to the SWCC under certain confining conditions. The interpretation of the results provides insight into the behavior of unsaturated loess under different stress and suction conditions, and the factors that influence its volumetric mechanical behavior.
- The saturated permeability under different vertical loads decreases with increasing vertical load. The unsaturated coefficients of permeability of remolded loess and undisturbed loess decrease as suction increases in an unsaturated state. These findings provide insight into the behavior of loess under varying saturation and vertical load conditions, and contribute to the understanding of its permeability properties.

6 Numerical modeling and discussion

This chapter explains the mathematical equations related to the employed constitutive models and the applied boundary conditions. The thermo-hydro-mechanical model describing unsaturated soil behaviour as implemented in the CODE_BRIGHT constitutive law library is introduced. Both the constitutive models for stress-strain behaviour and hydraulic hysteresis behaviour are presented. Furthermore, the atmospheric boundary conditions are discussed and their complexity and capabilities in modeling the meteorological conditions influencing the slope behaviour are revealed.

6.1 Theoretical framework for hydro-mechanical modeling

This study applies the CODE_BRIGHT software developed by UPC. The software can consider the thermal-hydraulic-mechanical coupling under mechanical, hydraulic and thermal boundary conditions. In this section, the basics of finite element simulations considering unsaturated soil with three-phase coupling are explained. This chapter introduces the balance equations, constitutive equations, equilibrium restrictions and constraints equations used in the finite element calculations to consider the solid-liquid-thermal coupling process in unsaturated soil under various boundary conditions.

6.1.1 Balance equations

The compositional approach is adopted in CODE_BRIGHT to establish the mass balance equations (Olivella et al., 1996).

- **Mass balance of solid**

Mass balance of solid:

$$\frac{\partial(\rho_s(1-\phi))}{\partial t} + \nabla \cdot (\mathbf{j}_s) = 0 \tag{6.1}$$

ρ_s is the mass of solid per unit volume of solid, ϕ is the porosity, and $\mathbf{j}_s$ is the flux of solid. The expression for porosity variation reads:

$$\frac{D_s\phi}{Dt} = \frac{1}{\rho_s}\left[(1-\phi)\frac{D_s\rho_s}{Dt}\right] + (1-\phi)\nabla \cdot \frac{d\mathbf{u}}{dt} \tag{6.2}$$

Therein $\mathbf{u}$ is displacement and t is time. The material derivative with respect to the solid is defined as follows:

$$\frac{D_s(\bullet)}{Dt} = \frac{\partial(\bullet)}{\partial t} + \frac{d\mathbf{u}}{dt} \cdot \nabla(\bullet) \tag{6.3}$$

- **Mass balance of water**

Water can exist both in liquid and gas phases. The total mass balance of water is expressed as:

$$\frac{\partial(\rho_l^w S_l\phi + \rho_g^w S_g\phi)}{\partial t} + \nabla \cdot (\mathbf{j}_l^w + \mathbf{j}_g^w) = f^w \tag{6.4}$$

$$\phi\frac{D_s(\rho_l^w S_l + \rho_g^w S_g)}{Dt} + (\rho_l^w S_l + \rho_g^w S_g)\frac{D_s\phi}{Dt} + ((\rho_l^w S_l + \rho_g^w S_g)\phi)\nabla \cdot \frac{d\mathbf{u}}{dt} + \nabla \cdot (\mathbf{j}_l^{'w} + \mathbf{j}_g^{'w}) = f^w \tag{6.5}$$

ρ_l^w is mass content of water per unit volume of liquid phase, i.e., $\rho_l^w = \omega_l^w\rho_l$, ρ_g^w is mass content of water per unit volume of gas phase, i.e., $\rho_g^w = \omega_g^w\rho_g$. ω_l^w denotes the mass fraction of water in the liquid phase. ω_g^w denotes the mass fraction of water in the gas phase. f^w is an external supply of water. S_l is the degree of saturation of liquid phase and S_g is the degree of saturation of gas phase. ρ_l and ρ_g are the density of liquid and gas phases, respectively. $\mathbf{j}_l^w$ is the mass flux of water in the liquid phase and $\mathbf{j}_g^w$ is the mass flux of water in the gas phase.

The sum of the nonadvective and fluid motion advective fluxes is separated from the total flux in order to simplify algebraic equations. This flux is relative to the solid phase and is denoted by $j_l^{'w}$. It corresponds to the total flux minus the advective part caused by solid motion. When solid deformation is negligible, then $j' = j$. The relative contribution of each flux term to the total flux is not always the same.

- **Mass balance of air**

Air is the main component of the gas phase and it can also be dissolved in the liquid phase.

$$\phi\frac{D_s(\rho_l^a S_l+\rho_g^a S_g)}{Dt}+(\rho_l^a S_l+\rho_g^a S_g)\frac{D_s\phi}{Dt}+((\rho_l^a S_l+\rho_g^a S_g)\phi)\nabla\cdot\frac{d\mathbf{u}}{dt}+\nabla\cdot(\mathbf{j}_l^{'a}+\mathbf{j}_g^{'a})=f^a \quad (6.6)$$

ρ_l^a is the mass of air per unit volume of liquid phase, i.e., $\rho_l^a=\omega_l^a\rho_l$, ρ_g^a is the mass of air per unit volume of gas phase, i.e., $\rho_g^a=\omega_g^a\rho_g$, ω_l^a denotes the mass fraction of air in the liquid phase. ω_g^a denotes the mass fraction of air in the gas phase. $\mathbf{j}_l^a$ is the mass flux of air in the liquid phase and $\mathbf{j}_g^a$ is mass flux of air in the gas phase, and f^a denotes the external supply of air.

- **Momentum balance for the medium**

$$\nabla\cdot\boldsymbol{\sigma}+\mathbf{b}=\mathbf{0} \quad (6.7)$$

where $\boldsymbol{\sigma}$ is the stress tensor and $\mathbf{b}$ is the vector of body forces.

- **Energy balance for the medium**

The equation for internal energy balance for the porous medium is established taking into account the internal energy in the solid, liquid and gas phases (E_s, E_l, E_g), respectively:

$$\frac{\partial(E_s\rho_s(1-\phi)+E_l\rho_l S_l\phi+E_g\rho_g S_g\phi)}{\partial t}-\frac{\phi S_g p_g}{\rho_g}\frac{\partial\rho_g}{\partial t}\nabla\cdot(\mathbf{i}_c+\mathbf{j}_{Es}+\mathbf{j}_{El}+\mathbf{j}_{Eg})=f^Q \quad (6.8)$$

$\mathbf{i}_c$ is energy flux due to conduction through the porous medium, the fluxes in solid ($\mathbf{j}_{Es}$), in liquid ($\mathbf{j}_{El}$), and in gas ($\mathbf{j}_{Eg}$) are advective fluxes of energy caused by mass motions. f^Q is an internal/external energy supply.

6.1.2 Constitutive equations of the elasto-plastic model

In CODE_BRIGHT, the BBM-TEP is one of the models implemented to simulate the coupled thermo-elastoplastic behaviour of unsaturated soils (Gens et al. (1995)). Two stress variables (net stress

The soil water characteristic (SWCC) model is used to describe the relationship between water content (degree of saturation) and suction. Due to the existence of hysteresis in the relationship between the degree of saturation and suction, a SWCC model with hysteresis is used to explain the water retention behaviour of loess. Such a SWCC model can

predict the loess water retention behaviour under complex hydraulic loading paths. To build the hysteretic SWCC model, the empirical model introduced by Van Genuchten (1980) is employed for both the main drying curve and the main wetting curve under no-deformation conditions. Furthermore, a new parameter (a_{oc}) is introduced to take into account the reduction in the maximum degree of saturation due to the appearance of entrapped air during the initial drying path (Nguyen-Tuan (2014)):

$$S_{oc} = S_{ls} - a_{oc} \tag{6.9}$$

The scanning curve depends on the suction in the previous step and the trend of the capillary force in the following step. S_{oc} is used as a discriminating coefficient. The effective degree of saturation is defined as follows:

$$S_e = \frac{S_l - S_{lr}}{S_{ls} - S_{lr} - \langle S_{oc} - S_l \rangle a_{oc}/(S_{oc} - S_l)} \tag{6.10}$$

$$\begin{cases} S_{oc} - S_l = 0 & S_{oc} - S_l < 0 \\ S_{oc} - S_l = S_{oc} - S_l & S_{oc} - S_l \geq 0 \end{cases} \tag{6.11}$$

The residual liquid saturation (S_{lr}) and maximum liquid saturation (S_{ls}) determine the minimum and maximum degree of saturation possible to be reached in the soil.

The wetting scanning curves are defined as straight lines with a constant absolute value of the effective saturation increment caused by changes of suction ($dS_e/d\psi$) from the initial state to the end value at the main wetting curve (see Fig. 6.1). The drying scanning curves are described similarly, but in the opposite direction. The model for the scanning curve is initiated when the hydraulic path deviates from the first drying path. The boundary scan criterion is used to define the incremental form of the scanning curve (Beliaev and Hassanizadeh, 2001). The degree of saturation of gas is shown on the vertical axis on the left-hand side of Fig. 6.1(b). Compared to Fig. 6.1(a), Fig. 6.1(b) includes the value of entrapped air, which means the maximum degree of saturation on main wetting path is not similar to the one on initial drying curve.

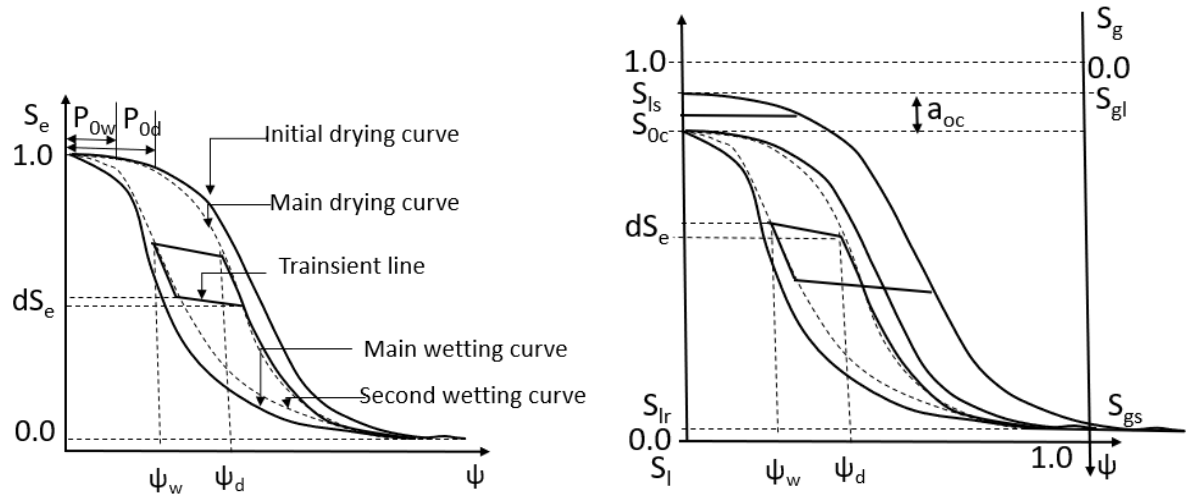

Figure 6.1: Schematic explanation of the cyclic SWCC model.

The maximum effective degree of saturation achieved in the scanning path is:

$$S_{e,w} = f(\psi_d, \lambda_d, P_{0,d}) + dS_e \tag{6.12}$$

ψ_d is the suction value on the drying path, λ_d and P_{d0} are serving as shape parameters. The index d indicates values on the initial drying curve.

The equation for the effective degree of saturation at transition state (scanning curves equation) reads:

$$S_e = \begin{cases} \frac{\psi_w - \psi}{\psi_d - \psi_w} dS_e + S_{e,w} & wetting \rightarrow drying \\ \frac{\psi_d - \psi}{\psi_d - \psi_w} dS_e + S_{e,d} & drying \rightarrow wetting \end{cases} \tag{6.13}$$

The cyclic SWCC test shows that the relationship between the degree of saturation and suction, followed by various hydraulic loading paths, is based on air-entry values and water-entry values (Likos and Lu, 2013). Following the approach in Nguyen-Tuan (2014), a parameter (n) which can consider the air occlusion during wetting and drying cycles is implemented in the model. The air entry value ($P_{0,d}$) and the water entry value ($P_{0,w}$) are modified as follows:

$$P^j_{0,w} = P_{0,w} + (S^j_{e,d})^n (P_{0,d} - P_{0,w}) \tag{6.14}$$

$$P^j_{0,d} = P_{0,d} + (1 - (S^j_{e,w})^n)(P_{0,d} - P_{0,w}) \tag{6.15}$$

$S^j_{e,d}$ and $S^j_{e,w}$ are the effective degrees of saturation at transient positions of the j^{th} drying-wetting loop.

6.1.3 Constitutive equations for the heat conduction

- Conductive flux of heat

Fourier's law is used to compute conductive heat flux:

$$\mathbf{i}_c = -\lambda_T \nabla T \tag{6.16}$$

The conductivity of the phases of the soil reads:

$$\lambda_{dry} = \lambda_{solid}^{1-\phi} \lambda_{gas}^{\phi} \tag{6.17}$$

$$\lambda_{sat} = \lambda_{solid}^{1-\phi} \lambda_{liquid}^{\phi} \tag{6.18}$$

λ_T is the soil thermal conductivity. λ_{dry} is the thermal conductivity of the dry porous medium and λ_{sat} is the thermal conductivity of the water-saturated porous medium. λ_{solid}, λ_{liquid}, λ_{gas} are solid, liquid, and gas phase thermal conductivity, respectively (Gens and Alonso, 1992). The dependence of thermal conductivity on porosity is taken into account.

The dependence of thermal conductivity on the degree of saturation is given by:

$$\lambda_T = \lambda_{sat} \sqrt{S_l} + \lambda_{dry}(1 - \sqrt{S_l}) \tag{6.19}$$

- Dispersive fluxes of mass and energy

Fick's law is applied for air or water in gas or liquid phase which reads:

$$\mathbf{i}_\alpha^i = -(\rho_\alpha \mathbf{D}'_\alpha) \nabla \omega_\alpha^i \tag{6.20}$$

ω_α^i denotes the mass fraction of 'i'-th species in α-phase, $\mathbf{D}'_\alpha$ is the mechanical dispersion tensor (α indicates the gas or liquid phase) defined as:

$$\mathbf{D}'_\alpha = d_t \mid \mathbf{q}_\alpha \mid \mathbf{I} + (d_l - d_t) \frac{\mathbf{q}_\alpha \mathbf{q}_\alpha^t}{\mid \mathbf{q}_\alpha \mid} \tag{6.21}$$

where d_l is longitudinal dispersivity and d_t is transversal dispersivity, q is the flux of the liquid phase, when α is l.

Mechanical dispersion heat flux is computed by means of Fourier's law:

$$\mathbf{i}_h = -(c_\alpha \rho_\alpha \mathbf{D}'_\alpha) \nabla T \tag{6.22}$$

where c_α is the specific heat of the α phase.

6.1.4 Atmospheric boundary conditions

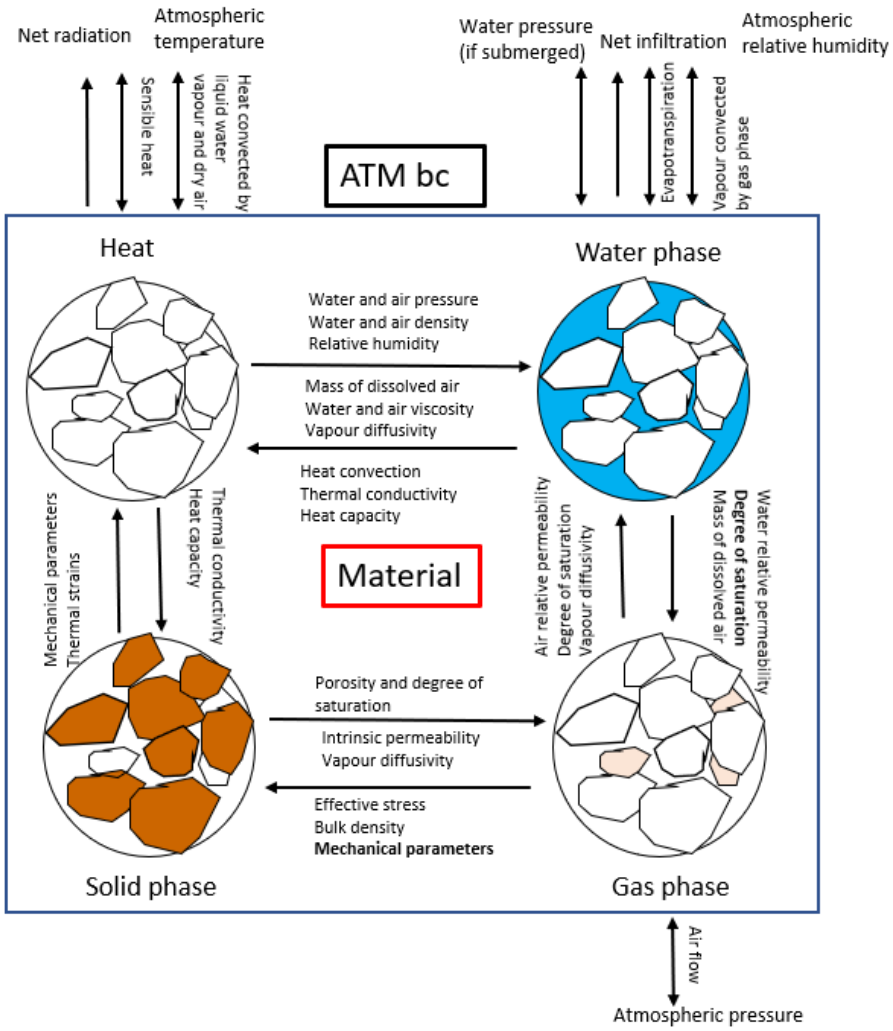

Figure 6.2: Atmospheric boundary conditions applied on three phases element (Zhang et al., 2005).

When introducing the atmospheric boundary conditions, several fluxes are to be considered, namely, the fluxes of gas and liquid phases (air and water fluxes) (see Fig. 6.2).

- Flux of air

$$j_a = w_g^a q_g = (1 - w_g^w) q_g \tag{6.23}$$

q_g is the flux of the gas phase:

$$q_g = \gamma_g (p_g - p_{ga}) \tag{6.24}$$

P_{ga} is the atmospheric pressure and γ_g is a leakage coefficient. Only the advective part in the flux of air is considered.

- Flux of water

$$j_w = k_{rain}P + k_{evap}E + j_g^w + j_{sr} \tag{6.25}$$

P is the rainfall, E is the evaporation, j_g^w is the advective flux of vapor in the gas phase, and j_{sr} is the surface runoff, where coefficients k_{rain} and k_{evap} are rain index and evaporation index.

Evaporation E is given by an aerodynamic diffusion relation:

$$E = \frac{k^2 v_a \mu}{(\ln \frac{z_a}{z_0})^2}(\rho_{va} - \rho_v) \tag{6.26}$$

ρ_{va} and ρ_v are the absolute humidity of the atmosphere and at the node of the boundary condition, respectively. A constant profile for ρ_v is assumed between this node and height z_0. k is the von Karman's constant, μ is a stability factor, v_a is the wind velocity, z_0 is the roughness length, and z_a is the screen height at which v_a and ρ_{va} are measured. The advective flux of vapour by the gas is given by:

$$\begin{cases} j_g^w = w_g^w q_g & if \quad p_g > p_{ga} \\ j_g^w = \frac{\rho_{va}}{\rho_{ga}} q_g & if \quad p_g \leq p_{ga} \end{cases} \tag{6.27}$$

where ρ_{ga} is the atmospheric gas density and q_g is the flux of the gas phase. The flux of water through the liquid phase, j_l^w is represented by the surface runoff as:

$$\begin{cases} j_{sr} = \gamma_w(p_l - p_{ga}) & p_l > p_{ga} \\ j_{sr} = 0 & p_l \leq p_{ga} \end{cases} \tag{6.28}$$

j_{sr} is the surface runoff which corresponds to the flow rate of water through the liquid phase j_l^w. γ_w is a leakage coefficient. The ponding is not explicitly simulated. When the soil is saturated ($p_l > p_{ga}$) all rainfall that cannot infiltrate will runoff.

- Total energy flux

$$j_e = k_{rad}R_n + H_s + H_c \tag{6.29}$$

k_{rad} is the radiation index.

$$R_n = R_m \tag{6.30}$$

R_n is the radiation which can be given as the measured radiation data (R_m).

H_s is the sensible heat flux, which can be calculated through an aerodynamic diffusion

relation.

$$H_s = \frac{k^2 \nu_a \mu}{(\ln \frac{z_0}{z_a})^2} \rho_{ga} C_a (T_a - T) \tag{6.31}$$

C_a is the specific heat of the gas. H_c is the convective or latent heat flux, which can be calculated by the internal energy of liquid water, vapor, and air. The convective latent heat flux H_c is calculated as:

$$H_c = h_v(E + j_w^g) + h_{la}(P + j_w^l) + h_{a0} j_a \tag{6.32}$$

h_v, h_{la} and h_{a0} are the free energies of vapor, liquid water, and air, respectively. All three of these properties depend on temperature. For h_v and h_{a0}, temperatures used are the temperatures at the node of the boundary. In terms of h_{la}, the temperature is the dew point temperature, which depends on the atmospheric vapor pressure.

6.1.5 Hydraulic constitutive equations

- Liquid advective flux

Generally, Darcy's law has been used to describe the advective flow of the water phase.

$$\mathbf{q_l} = -\frac{\mathbf{k} k_{rl}}{\mu_l} \nabla \mathtt{p}_l - \rho_l \mathbf{g} \tag{6.33}$$

μ_l is the dynamic viscosity of the pore liquid, $\mathbf{g}$ is the gravity acceleration vector, ρ_l is the liquid density, and k_{rl} is the liquid relative permeability. $\mathbf{k}$ is the tensor of intrinsic permeability that depends on porosity according to the Kozeny's model:

$$\mathbf{k} = \mathbf{k_0} \frac{\phi^3}{(1-\phi)^2} \frac{(1-\phi_0)}{2} \phi_0^3 \tag{6.34}$$

ϕ_0 is the reference porosity, $\mathbf{k_0}$ is the intrinsic permeability for a matrix with porosity ϕ_0.

The relative permeability (k_{rl}) is derived from the Mualem-van Genuchten closed-form model:

$$k_{rl} = \sqrt{S_e}(1 - (1 - S_e^{(1/\lambda)})^\lambda)^2 \tag{6.35}$$

λ is a shape parameter for the retention curve. The two-parameters van Genuchten SWCC model reads:

$$S_e = \left(1 + \left(\frac{p_g - p_l}{p}\right)^{\frac{1}{1-\lambda}}\right)^{-\lambda} \tag{6.36}$$

$$p = p_0 \left(\frac{\sigma_T}{\sigma_{T0}} \right) \tag{6.37}$$

p_0 is a model parameter which represents the air entry value in a certain hydraulic loading path. σ_T is the surface tension of the liquid. σ_{T0} is the surface tension of the liquid in which p_0 was measured.

Olivella et al. (1996) provided the empirical equation for calculating σ_T:

$$\sigma_T = 0.03059 \exp \left(\frac{252.93}{273.15 + T} \right) \tag{6.38}$$

- Gas phase relative permeability is defined as:

$$k_{rg} = A S_{eg}^{\lambda} \tag{6.39}$$

S_{eg} is the effective gas degree of saturation.

$$S_{eg} = \frac{S_g - S'_{rg}}{S_{gs} - S'_{rg}} \tag{6.40}$$

where S_{rg} is the residual gas degree of saturation and S_{gs} is the maximum gas degree of saturation.

6.2 Numerical simulations of a soil column

In this subsection, the influence of atmospheric boundary conditions on the temperature and degree of saturation, as well as water pressure distribution inside a soil column is discussed. A hysteresis model for the Soil-Water Characteristic Curve (SWCC) was employed to consider the difference caused by the hydraulic loading history, which can more reliably reproduce the reality. A Thermo-Hydraulic (TH) analysis of the problem of a soil column under atmospheric conditions was performed.

6.2.1 Geometry and discretization

Atmospheric boundary conditions were applied at the top of the 10 m high and 5 m wide soil column. Triangular finite elements were used for discretization of the geometrical model and the discretization involved in total 220 finite elements.

6.2.2 Boundary conditions

- Initial conditions for coupled TH analysis

In reality, the initial pore water pressure is influenced by the depth, hydraulic properties of the material, and the groundwater table. The calculation results are affected by the constitutive parameters and the simplified initial boundary conditions, which mainly reflect the general law of the unsaturated seepage field under atmospheric conditions. The initial conditions include the initial hydraulic and thermal conditions (see Table 6.1). The initially given suction of the soil column was linearly distributed along the height, -10 MPa at the top and 0 MPa at the bottom of the column. Zero vertical stress applies to the ground surface. The soil is considered to be homogeneous, meaning it has the same permeability in the x and y directions. Initial conditions have a great effect on the pore water pressure of the soil column.

Table 6.1: Initial values

parameter	porosity	vertical stress	pore water pressure
unit	-	MPa	MPa
value	0.46	-	-10

- Boundary conditions and simulated phases

The study defined the flux boundary conditions, porosity, liquid pressure, and gas pressure conditions for the TH type problem under atmospheric loads. The initial pore water pressure was set at the surface with -10 MPa. The water table was set at the bottom of the column, where the suction (p_g - p_l) value must be 0. The sides and bottom of the soil column are considered as impervious.

The approach to studying the influence of individual variables on the results was to change one variable at a time while keeping the others constant. When the evaporation factor was set to 0, no evaporation was calculated for liquid flux, but convective energy flux was still calculated based on evaporation. When the radiation factor was set to 0, no radiation (R_n) was calculated, but the total energy flux was not 0. That is, even when all of the factors and variables are set to 0, evaporation, gas pressure, relative humidity, and other variables still had an effect on pore water pressure. The parameter values of the atmospheric boundary conditions can be seen in Table 6.2.2:

Table 6.2: Parameters of the atmospheric boundary conditions

Atmospheric parameter	Variable	Unit	Value
Latitud	λ	Rad	0.75712
Time when autumn	t_s	s	2.28096e7
Time at noon	t_m	s	43200
Height main roughness	z_0	m	2e-2
Screen height	z_a	m	1.5
Stability factor	ϕ	kg/m^3	1.0
Atmospheric gas density	ρ_{ga}	kg/m^3	1.2
Dry albedo	A_d	-	0.2
Wet albedo	A_w	-	0.2
Gas leakage coefficient	γ_g	kg/m^2/MPa	1e6
Liquid leakage coefficient	γ_l	kg/m^2/MPa	-1e6
Rain factor	k_{rain}	-	1.0
Radiation factor	k_{rad}	-	1.0
Evaporation factor	k_{evap}	-	1.0

6.2.3 Influence of atmospheric boundary conditions

Based on meteorological data, the variations of net radiation, wind velocity, relative humidity, and air temperature with time have been prescribed at the boundaries. At top surface these values have been evaluated. The results in Fig. 6.3 to Fig. 6.7 indicate that net radiation, wind velocity, relative humidity, and air temperature all play a role in the change of pore water pressure and temperature. These changes are relatively large and within the range of observed meteorological data.

Evaporation, which is directly related to changes in surface pore water pressure and temperature, is largely determined by net solar radiation. Stronger evaporation leads to more intense changes in pore water pressure and temperature. Low air temperature slows down evaporation and results in almost no change in suction and temperature (see Fig. 6.3a). The results shown in Fig. 6.3(b) and Fig. 6.4(b) indicate that the amount of temperature changes with air temperature and relative humidity, which increases first and then decreases. Relative humidity affects the rate of change of surface suction and temperature, but its impact on temperature is smaller compared to the effect of rainfall variation (see Fig. 6.4(a) and Fig. 6.6(a)). Wind velocity accelerates the convection of air

and the circulation of air on the ground surface, affecting the change of surface pore water pressure and temperature (see Fig. 6.5(a)). The increase in wind speed and net radiation has a linear relationship with the change of pore water pressure (see Fig. 6.5(a) and Fig. 6.7(a). Net radiation has a particularly significant impact. The effect of wind velocity on evaporation was calculated based on daily wind speed. Greater net radiation leads to larger evaporation, which in turn causes a rise in suction and an increase in surface temperature (see Fig. 6.7a).

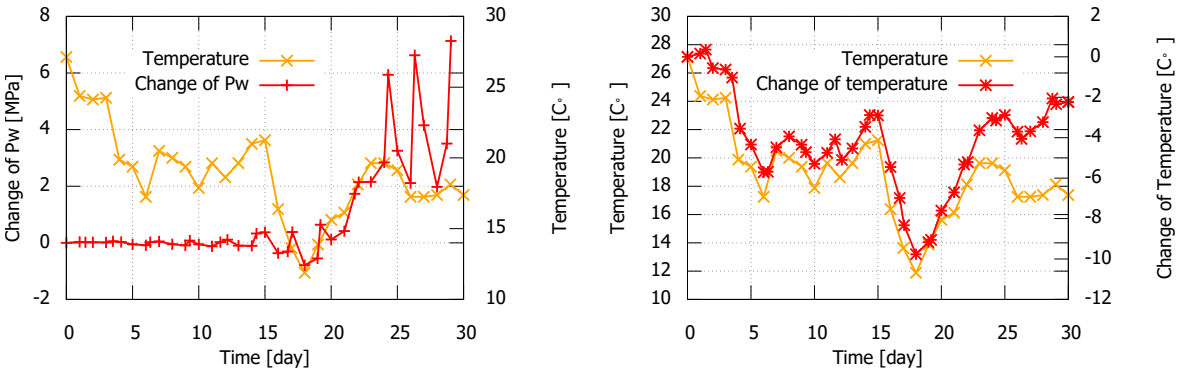

(a) (b)

Figure 6.3: Imposed temperature atmospheric boundary condition and the change of liquid pressure (a) and soil temperature (b).

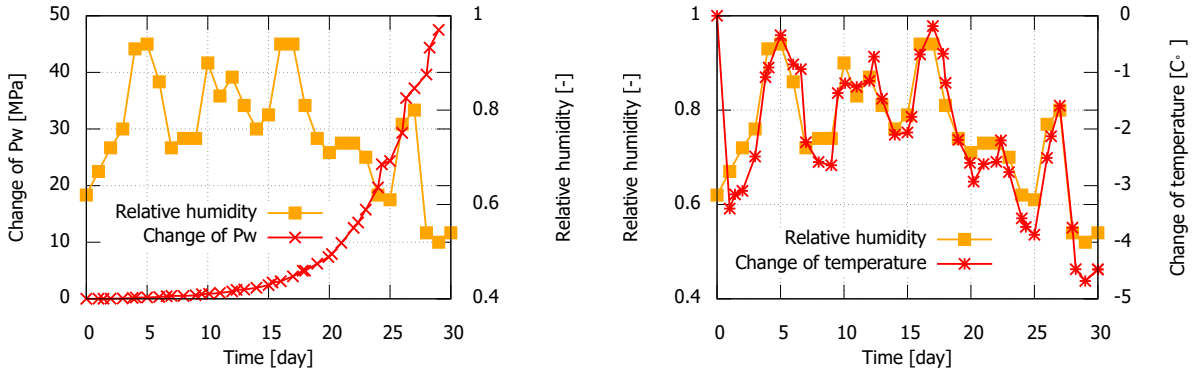

(a) (b)

Figure 6.4: Variation of the ambient relative humidity and (a) changes of the liquid pressure, and (b) soil temperature.

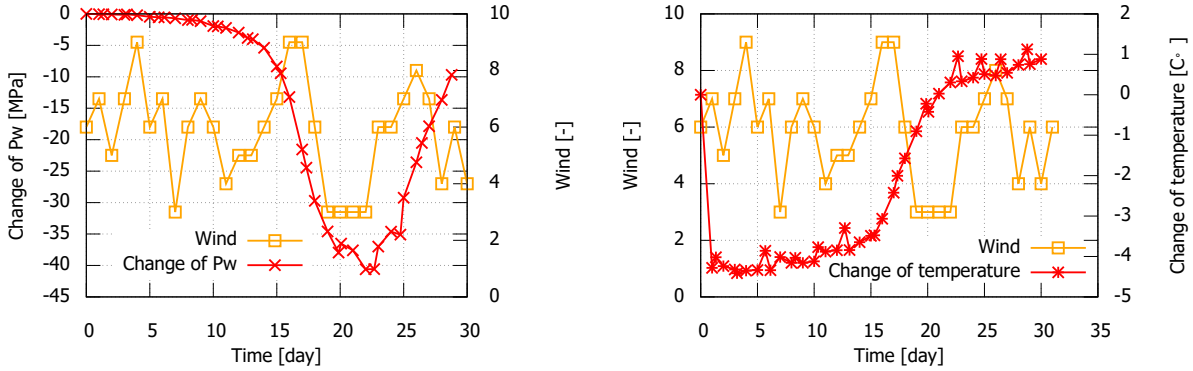

(a) (b)

Figure 6.5: Wind velocity variation and change of (a) pore water pressure and (b) soil temperature.

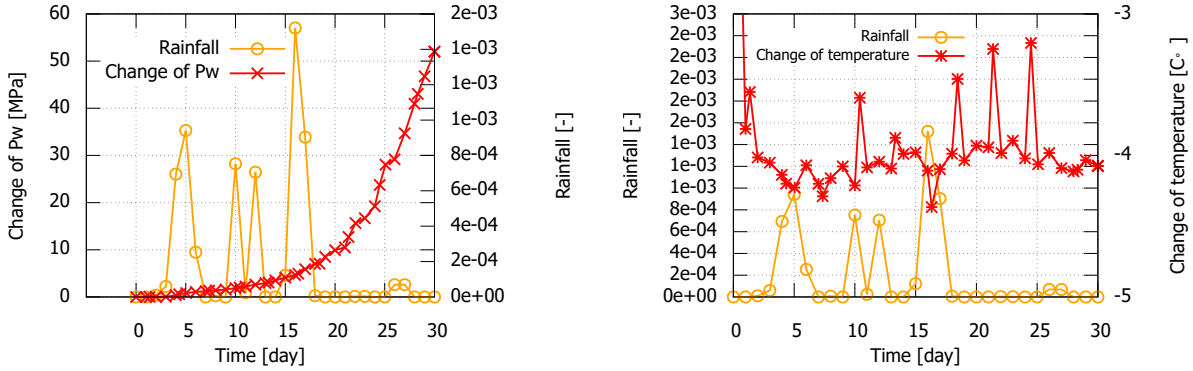

(a) (b)

Figure 6.6: Rainfall and change of (a) pore water pressure, and (b) soil temperature in the soil column.

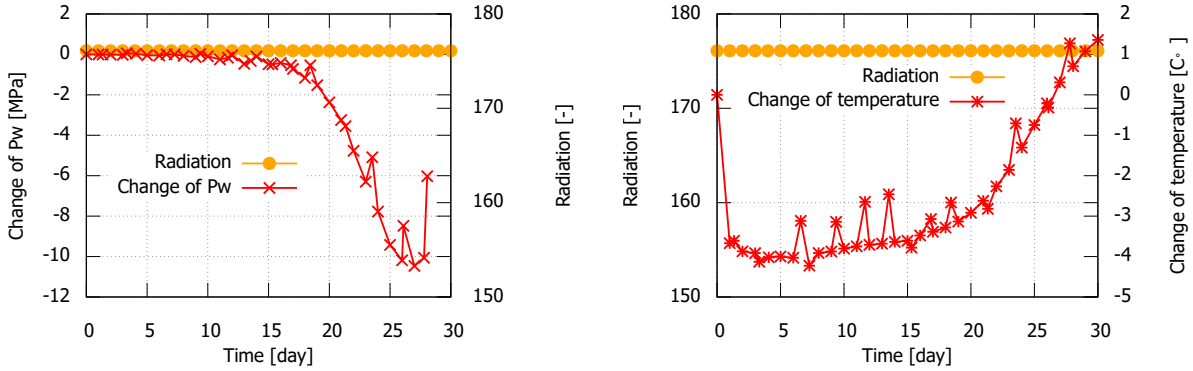

(a) (b)

Figure 6.7: Radiation and change of (a) pore water pressure, and (b) soil temperature.

All meteorological parameters have an impact on the pore water pressure in the soil, but rainfall and evaporation are the most influential factors (Fig. 6.6(b)). Wind speed, net radiation, air temperature, and relative humidity are indirect factors that affect the pore water pressure in soil through evaporation.

6.2.4 Influence of the SWCC hysteresis model

The neglect of the Soil Water Characteristic Curve (SWCC) hysteresis is only appropriate when wetting and drying conditions are monotonic, but it leads to inaccurate results in cyclic wetting and drying conditions such as intermittent precipitation and evaporation. Different hydraulic models were used to evaluate the effect of the hysteresis model on the simulation results, under the same boundary conditions, initial conditions, and material parameters. Hysteresis model 1 is explained in Eq. 6.12 and Eq. 6.13. Hysteresis model 2 is explained in Eq. 6.14 and Eq. 6.15. The simulations were performed both with and without consideration of the SWCC hysteresis.

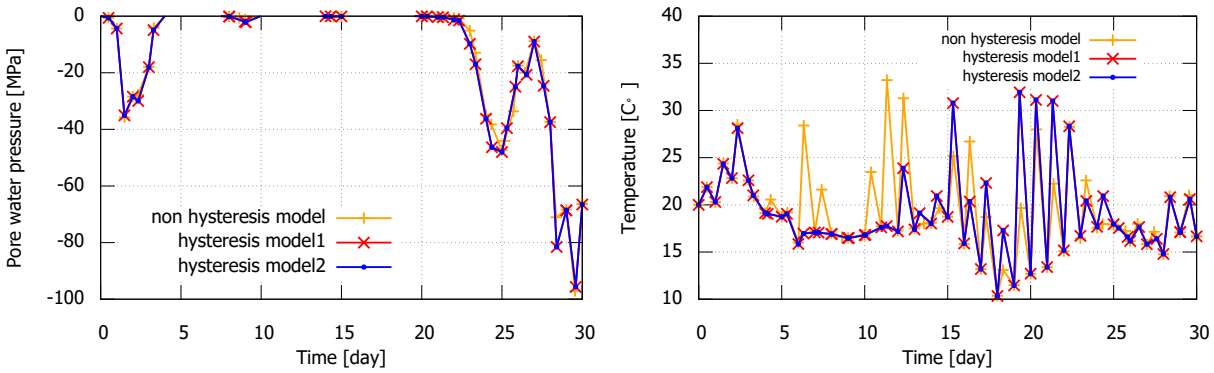

(a) (b)

Figure 6.8: Change of (a) pore water pressure, and (b) temperature by using SWCC model without and with hysteresis.

In conclusion, the results from Fig. 6.8(a) show the influence of different models on pore water pressures. Hysteresis in the soil-water characteristic curve (SWCC) results in lower infiltration and smaller changes in pore water pressure. Fig. 6.8 shows that there is only a small effect of hysteresis on temperature and less effect on pore water pressure in the

unsaturated zone (see days 0-10). This observation further highlights the importance of implementing and using appropriate models to accurately simulate the SWCC hysteresis behavior.

6.3 Summary

The following items summerize the main outcomes and the main issues discussed in this chapter:

- Firstly, the theoretical framework used for fully coupled thermo-hydro-mechanical numerical simulations is presented. Equations for mass balances are presented for a mixture of solid, water, and air phases. The equations for the balance of energy and momentum were given for the entire medium. The BBM in the form implemented in CODE_BRIGHT was introduced which in this thesis is used to model the unsaturated soil behavior. In addition, models reproducing the hysteresis of the SWCC are introduced in this chapter. The model taking air entrapment and variation of the air entry value during the drainage and wetting into account is proposed as most relevant (Nguyen-Tuan, 2014). Finally, the equations used to account for the atmospheric boundary conditions were discussed.
- One of the objectives of this study is to employ the atmospheric boundary conditions to study the instability of loess slope in a more realistic way. The influence of the atmospheric boundary conditions were firstly studied based on a soil column, where the thermal and liquid fluxes on the boundary in contact with the atmosphere were prescribed based on meterological data. It was found that the rate and magnitude of temperature and pore water pressure changes in the soil are dependent on several factors, such as the liquid flux and the heat transfer between atmospheric gas and the soil material. The model response sensitivity to the different atmospheric variables, e.g. of the results for pore water pressure and temperature, was studied. It has been found that the rainfall is the most influencing factor for pore water pressure, followed by the relative humidity and wind velocity. In terms of soil temperature, however, among atmospheric conditions, atmospheric temperature matters most. Moreover, low relative humidity may result in very low temperature change inside the soil.

- For the specific purpose of SWCC modelling, a benefit can be gained from the simulations involving cyclic evaporation and precipitation phenomena. In order to be valid along the whole loading path, including the first drying and the subsequent drying and wetting paths, a functional expression of the water retention curve with hysteresis and scanning curves was used. The effect of SWCC hysteresis on the hydraulic and thermal behaviour has been also analyzed by means of simulations of the soil column. In the simulation model, both the hysteresis in the water retention curve (hysteresis model 1) and the reduction in the maximum degree of saturation after the first drying path (hysteresis model 2) were considered. Comparison with the results obtained using various SWCC models shows that the SWCC model with hysteresis has an influence on the results for the pore water pressure and temperature distribution in the soil. In conclusion, the comparison between numerical simulation results employing different hydraulic models indicates the need to consider water retention hysteresis.

7 Loess slope simulation

In this chapter an advanced constitutive model together with atmospheric boundary conditions are employed to perform coupled THM analysis of loess slope behaviour and to study the slope failure process. The fully coupled hydro-mechanical analysis of water infiltration was performed using the finite element code CODE_BRIGHT. The numerical simulations were performed using GID as the pre-processor and post-processor for CODE_BRIGHT. A typical unsaturated loess slope in Xi'an was used as a study case.

The BBM-TEP constitutive model is used in the numerical analysis to describe the behaviour of the slope-building loess material with respect to the coupled thermo-hydro-mechanical loading. The model is based on the hydro-mechanical behavior of loess material, as described by Garakani et al., 2015. The constitutive model parameters of the BBM-TEP model were determined from the experimental data and from available data in the literature for similar soil materials. The slope geometry was taken from field measurements, while the boundary conditions were set based on meteorological data from a nearby weather station. The numerical simulation takes into account factors such as antecedent rainfall and evaporation that may impact the distribution of water pressure within the slope under atmospheric conditions. The aim of the simulation is to study the development of stresses and strains, heat transfer, and water flow in the slope.

7.1 Introduction of Baqiao slope

This section presents the study of the hydrogeology, meteorology, and geology conditions of the Baqiao slope. Furthermore, the disaster scenario which includes the occurrence time of landslide and sliding mass is discussed. Special focus is put on the antecedent rainfall and continued landslides.

7.1.1 Slope failure disaster case

The case study focuses on a catastrophic loess landslide that took place in Baqiao tableland, Xi'an, China on September 17, 2011 (see Fig. 7.1). The landslide resulted in 32 deaths. The trigger of the landslide was heavy antecedent rainfall of short duration and high daily rainfall intensity, the heaviest rainfall being 53.9 mm on 11 September (see Fig. 7.2).

Figure 7.1: Photographs of the Baqiao landslides in September 2011.

The Baqiao slope has a steep backside with an inclination angle of 78°. The sliding material is mainly composed of Malan loess (Q_3). Before the rainfall, the slope was unstable and several cracks had formed. The height of the landslide is 96 m, the width is 170 m, and the average thickness is 12 m, with the maximum thickness being 17.5 m. The sliding distance was about 150 m, with a total sliding volume of about 15×10^4 m^3. The original slope angle was 35°, but after excavation by a brick factory for construction,

the slope became 60° and the height was increased to 96 m. The topography is generally gentle in the upper part, steep in the middle, and gentle again in the foot parts.

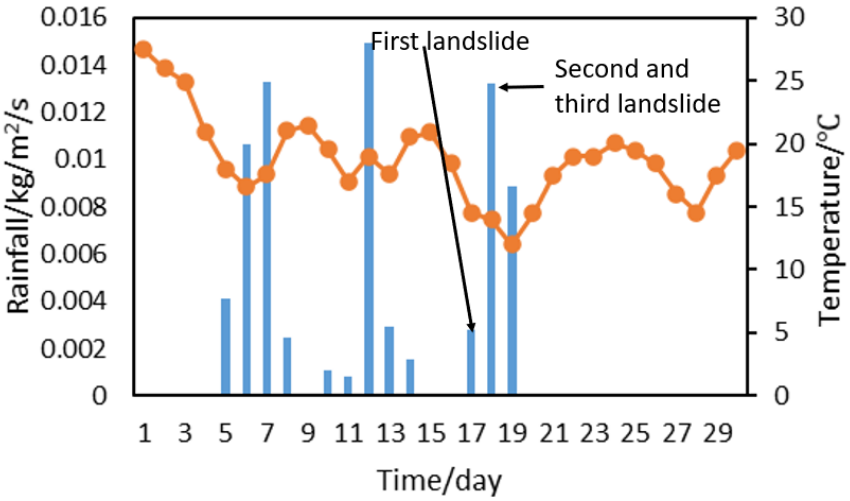

Figure 7.2: Climate data at Baqiao site during September 2011.

From September 1st to September 17th 18:00 PM, 2011, the rainfall in Xi'an city was 236.3 mm, which was 4.7 times more than the rainfall during the same period of the previous year. It was the highest amount of rain for the past 60 years. During 15-day rainfall period, there were 3 intense rainfalls. The first intense rainfall occurred from September 5th to 7th, 2011, with a total amount of 106.37 mm rainfall and a maximum single-day rainfall of 63.9 mm. The second intense rainfall occurred from September 10th to 12th, with a total rainfall of 74.2 mm and the maximum daily rainfall reaching 57.88 mm (see Fig. 7.2). The last heavy rainfall was from 17th to 19th of September. The heavy rainfall in a short period of time caused water infiltration through the cracks on the top of the slope, increasing the soil water content and the likelihood of a landslide.

7.1.2 Location and hydrological conditions

The Baqiao slope is part of the Bailu tableland in Xi'an, China. It is located in the southeast of Xi'an and is under the jurisdiction of Baqiao district (see Fig. 7.3(a)). Bailu tableland is the largest loess plateau near Xi'an and has an area of 238 km^2, a length of 28 km and a width of 7-10 km. It has an altitude that ranges from 690 to 780 m, with the highest point reaching 803.9 m. The Bailu tableland has a difference in elevation of 150 to 200 m compared to the nearby river, and there is a gully located near it.

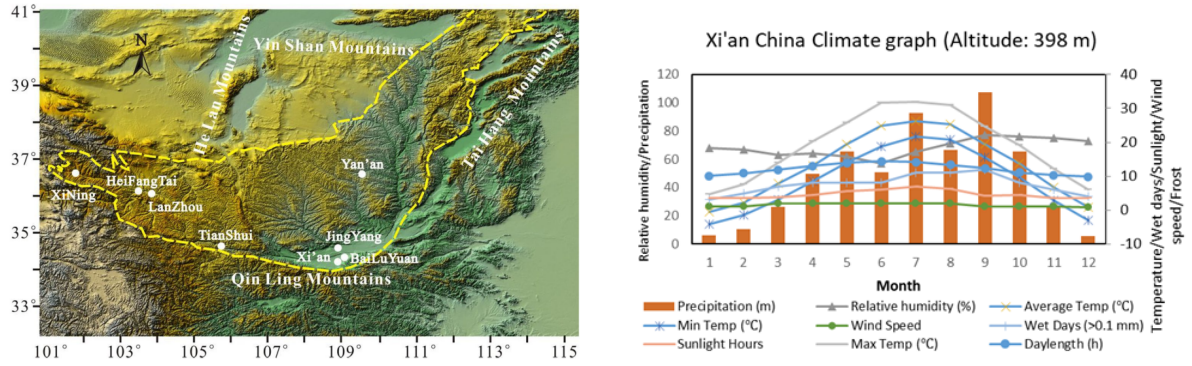

(a) (b)

Figure 7.3: Location of Baqiao slope in China (a) and climate data in Xi'an area (b).

The upper Maran loess, as determined from field investigation, is characterized by a structure with large pores and strong collapsibility. Vegetation roots grow directly into this loess and there are well-developed joints present in the layer. The topographic profile of the Bailu tableland is displayed in Fig. 7.3(a).

Bailu District has a continental monsoon climate. According to the data from the meteorological station (Fig. 7.3(b)), the average temperature over the years is 13.2°C. July is the hottest month with an average temperature of 27°C, while January is the coldest month with an average temperature of -1.4°C. The recorded minimum temperature is -17.4°C, and the maximum temperature is 43.3°C. The average absolute humidity is 11860 kPa, the relative humidity is 69.3%, and the average annual evaporation is 1376.7 mm.

In Bailu District, more than 77% of the precipitation occurs during the rainy season from May to October. The precipitation distribution is not uniform and has significant regional differences. The climate is characterized by the combined effects of the southeast monsoon and cold, dry air from the Menggu plateau to the northwest, creating an extra-tropical monsoon climate. The average annual precipitation and monthly precipitation are 584.9 mm and 53.7 mm, respectively. The maximum annual precipitation, monthly precipitation, and daily precipitation reach 1,132 mm, 259 mm, and 72 mm, respectively, as observed by meteorological observations.

The area in Bailu District is prone to geological disasters such as collapses and landslides due to its unique geological topographical and geomorphological conditions. Landslides are mostly concentrated during autumn and winter and 97.3% of landslide events occur

during the rainy season from May to October. These landslides are primarily located along the river sides. An investigation of the loess area showed that landslides mostly occur on slopes with an inclination of $35° - 55°$. Historically, these landslides have caused significant damage to the local population and their property, and have also had a direct impact on the geological environment of Xi'an.

7.1.3 Stratigraphy and geography

The stratigraphy in this study induces mainly Quaternary strata. The Quaternary loess covers the entire area by the Malan and Lishi loess deposit. The Malan loess was deposited in the Late Pleistocene, while Lishi loess was deposited in the Middle Pleistocene. In addition, the Quaternary deposits are fragmented by distribution both in the gully and on the hill slopes along the edge of the Bailu tableland. The original surface covers more than 100 m of loess. The middle part of the slope is red mud, and the lower part is sandy mudstone. The geological cross-sectional profile of the Baqiao landslide is shown in Fig. 7.4. The exposed layers in the Baqiao slope are mainly Quaternary aeolian loess deposits.

The interlayer of the slope is made up of a combination of Aeolian loess and ancient soil, with the surface layer being composed of Q_3 (Malan) loess and the middle part being composed of Q_2 (Lishi) loess. The layers of the slope include Wucheng, Lishi, and Malan loess, with the ancient soil layer being thin (less than 1m in thickness). The Aeolian loess has a loose texture, is highly collapsible, and has a unique jointing structure, along with a metastable strength characteristic.

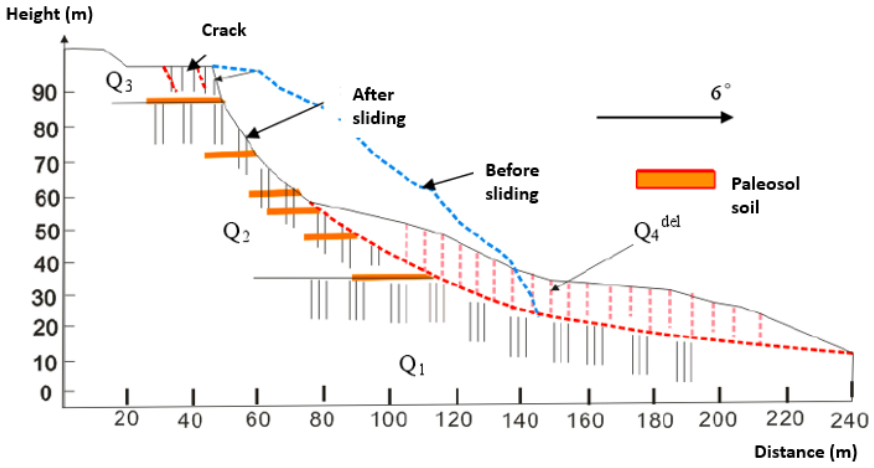

Figure 7.4: The section profile of Baqiao landslide.

There is solely an information in literature that the water level is located deep in the slope. The literature suggests that the groundwater level in the vicinity of the slope in question was found to be more than 80 meters deep. As a result, recharge of groundwater in the loess slope due to rainfall can be ignored without considering the cracks, which could provide a preferential pathway for water.

7.2 Slope modeling

This section describes the process of establishing a numerical model for the slope, including finite element discretization and the application of boundary conditions. It also provides the initial conditions and material parameter values used in the model.

7.2.1 Geometry and discretization

The numerical model for the slope was created based on the field geometrical conditions. To simplify the model and reduce computational cost, the slope structure was simplified into three different soil layers. The top layer is Q_3 loess with an average thickness of 14 meters, followed by the second and third layers which are Q_2 and Q_1 loess with a thickness of 30 m and 55 m respectively.

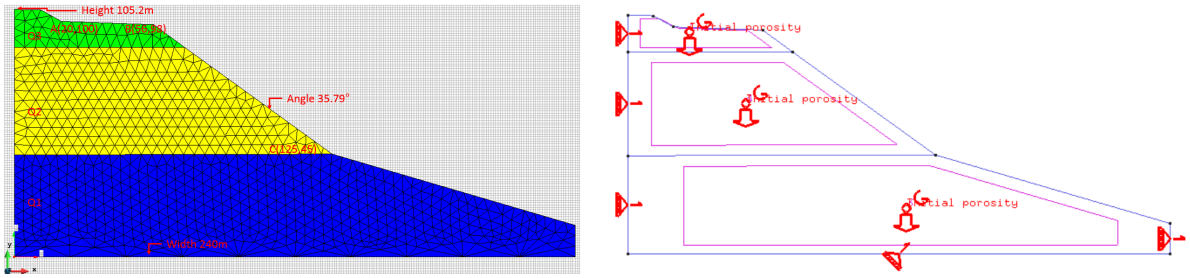

(a) (b)

Figure 7.5: Finite element discretization (a) and boundary conditions (b).

The accuracy of the numerical results can be affected by mesh discretization. To minimize the influence of discretization, a suitable mesh discretization was determined by ensuring that the model responses are not influenced by the domain size and domain discretization. A sufficiently fine finite element discretization was used to reduce discretization error during analysis (see Fig. 7.5). After evaluating the impact of various finite element sizes on the numerical results, a finite element discretization with a total of

820 triangular elements and 1430 nodes was chosen. Additionally, small time steps were selected for the finite element simulation to accurately capture the progression of pore water pressure or stress.

7.2.2 Model parameters and boundary conditions

Chapter 6 explains the atmospheric boundary conditions and the constitutive model that are foreseen to be used in the numerical simulations. The boundary conditions such as rainfall, temperature, relative humidity, wind velocity, and radiation are presented in Section 6.2.4. The model parameters and the unsaturated permeability coefficient that influences the pore water pressure are also discussed in Section 6.2.2. The balance equations and the theoretical framework for modeling two-phase flow can be found in Section 6.1.

Table 7.1: Mechanical parameters

Elastic parameter	k_{i0}	k_{s0}	K_{min}	v	α_{ss}	α_i	α_{il}	α_{sp}	p_{ref}	
unit			MPa						MPa	
Q_2	0.05	-0.3	10	0.4	0.01	-0.003	0	-0.147	0.01	
Q_1	0.21	-0.061	10	0.3	0.01	0	0	0.01	0.01	
Plastic parameter	$\lambda(0)$	r	β	k	p_{s0}	p^c	M	a	p^*_0	ϕ
unit			MPa						MPa	
Q_2	0.15	0.75	0.05	0.1	0.1	0.1	1	0.3	14	32
Q_1	0.244	0.75	80	0.1	0.01	0.1	1.2	0.99	0.05	32

Table 7.2: Hydraulic parameters

Hydraulic parameter	σ_0	S_{ls}	S_{lr}	P_0	λ	k	ϕ_0
unit	N/m	-	-	MPa	-	m^2	-
Q_2	0.072	1	0 .01	0.02	0.18	1e-16	0.44
Q_1	0.072	1	0	0.05	0.18	1e-18	0.42

Table 7.3: Gas conductivity parameters

Gas conductivity parameter	λ_k	S_{ls}	S_{lr}	A_g	λ_g	S_{rg}	S_{gs}	D	n	τ_0
unit	-	-	-	-	-	-	-	$m^2 s^{-1} K^{-n} Pa$	-	-
Q_2	0.18	1	0	1	3	1	0	$5.9*10^{-6}$	2.3	0.8
Q_1	0.18	1	0	1	3	1	0	$5.9*10^{-6}$	2.3	1.0

Table 7.4: Initial state parameters

Soil type	porosity	vertical stress	horizontal stress	p_l	p_g	T
unit	-	MPa	MPa	MPa	MPa	C
Q_2	0.42	0.02	0.02	-0.3	0.1	20
Q_1	0.40	0.03	0.03	-0.1	0.1	20

The parameters for the hydraulic and mechanical constitutive models of the top layer (Q_3) are obtained from the results of suction-controlled compression tests and are described in detail in Section 6.2.2 of the thesis. The constitutive models represent the main characteristics of the material and capture its behavior using a limited number of parameters, see Table 7.1, Table 7.2, Table 7.3, and Table 7.4.

The plane strain calculation model has fixed horizontal displacement at the side boundaries and fixed horizontal and vertical displacement at the bottom boundary. The hydraulic boundary conditions are introduced via impermeable boundaries on the side and a fixed head boundary at the bottom (see Fig. 7.5(b)). Rainfall infiltration is simulated by prescribing a liquid flux on the top slope boundary.

7.3 Results and discussion

7.3.1 Variation of pore water pressure

- Influence of antecedent rainfall

The boundary conditions were defined based on the 3-month period (July-September) and the 1-month period (September) to calculate the pore water pressure before the main rainfall event. In this case, horizontal and vertical permeability coefficients are considered

to be equal.

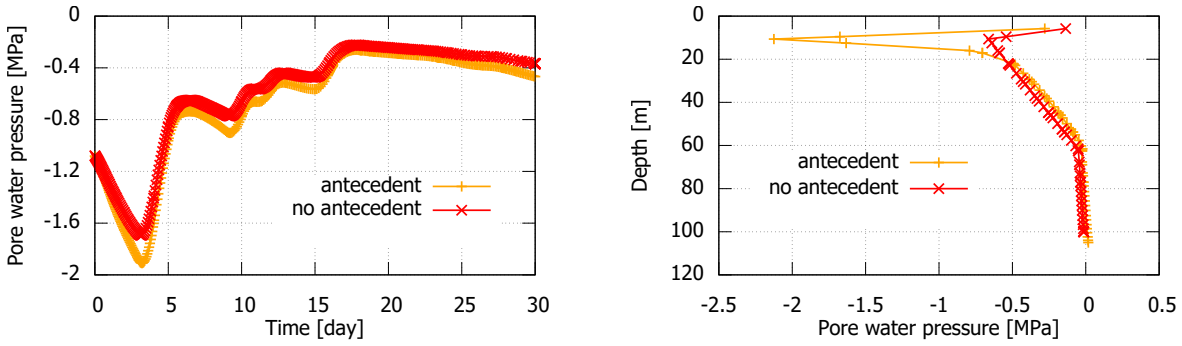

(a) (b)

Figure 7.6: The difference in pore water pressure caused by antecedent precipitation, (a) pore water pressure distribution, and (b) pore water pressure development with time along depth.

Fig. 7.6 shows that the changes in pore water pressure inside the slope are affected by the antecedent rainfall, exhibiting a higher pore water pressure when there is antecedent rainfall before the main rainfall. As rainfall duration increases, suction into the slope decreases continuously at a rate that also decreases. Simulation results indicate that antecedent rainfall plays a role in triggering landslides, with this effect diminishing over time. If there is no significant rainfall during the antecedent period, the reduction in suction typically lags behind the rainfall process (as shown in Fig. 7.6(b)). On the other hand, if there is heavy rainfall during the antecedent period, the suction decreases rapidly during the rainfall process. Antecedent rainfall is a sufficient condition for landslide development, while rainfall intensity is a necessary condition. The combination of these two factors can lead to final slope instability.

- Influence of evaporation

The infiltration process is influenced by the material properties and the atmospheric boundary conditions. Rainfall and evaporation are the most direct factors that affect the pore water pressure in the soil.

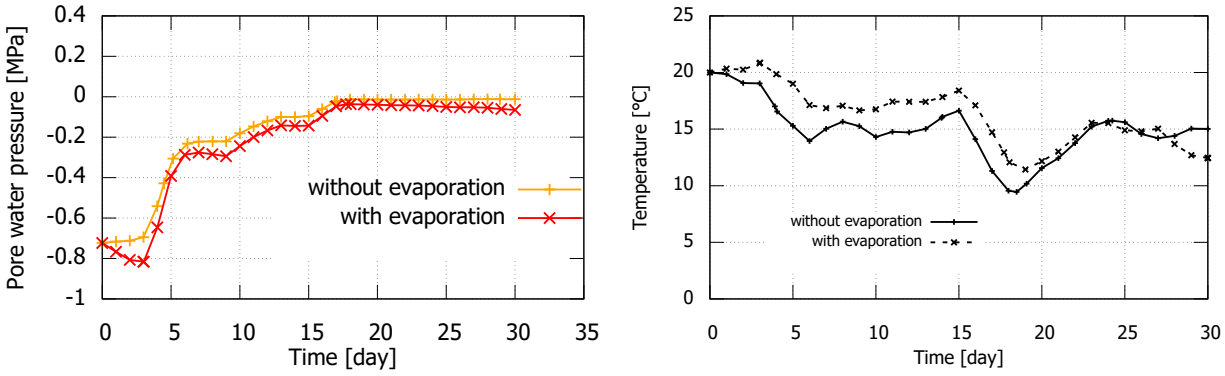

(a) (b)

Figure 7.7: The difference in pore water pressure caused by evaporation, (a) Pore water pressure development, and (b) temperature development with time.

Fig. 7.7 demonstrates how evaporation affects pore water pressure in the soil. Evaporation increases the suction and affects the seepage conditions at the slope boundary. The effect of rainfall and evaporation is limited to depths above 3 m, and pore water pressure changes mainly occur on the subsurface of the slope. Soil that is at a greater depth has a delayed response due to the infiltration rate, therefore, at the greater depth a longer suction response time is required. Infiltration of surface water affects only the upper 3 m of the intact loess. Neglecting evaporation leads to overestimation of flow flux.

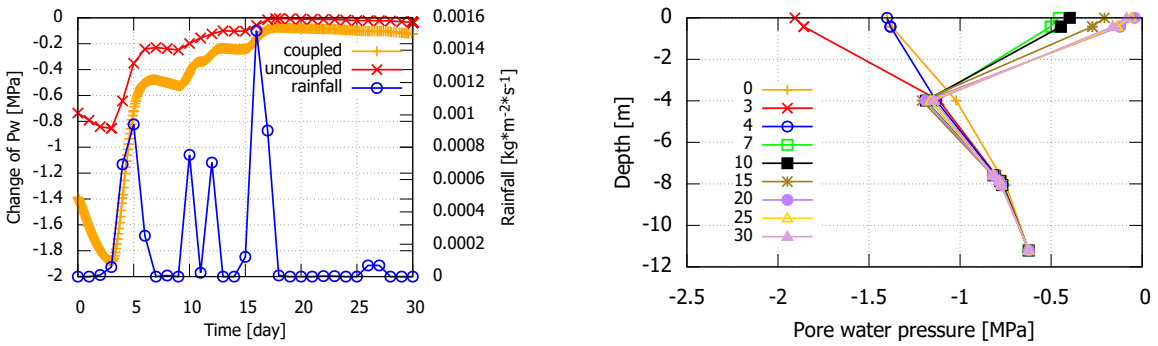

(a) (b)

Figure 7.8: The change of pore water pressure at point A under atmospheric boundary conditions (a), and pore water pressure along depth for different days (b).

The 15-minute high-intensity rainfall caused a significant reduction in matric suction, with suction increasing after the rainfall stopped, but without returning to its original

value. During the heaviest rainfall on 12th of September 2011 (194.5 mm/day), the matric suction at a depth of 1 m approached zero (see Fig. 7.8(b)). The long-duration rainfalls of low intensity (10th-15th September) had a greater effect than the short-duration, high-intensity rainfall on 12th of September (see Fig. 7.8(a)). Precipitation is the main factor that controls variations in pore pressure across the slope and hence of the suction that occurs across the portion of the slope that is immediately subject to atmospheric boundary conditions. When the suction becomes large enough, further precipitation does not cause an increase in pore water pressure.

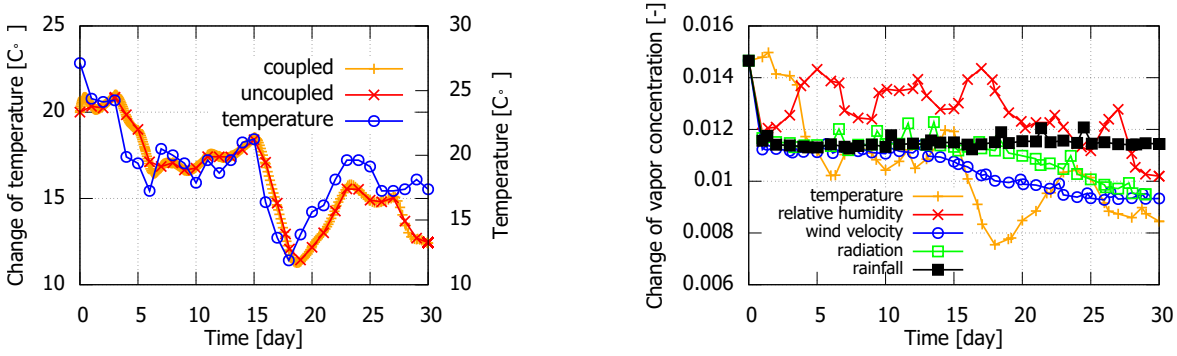

(a) (b)

Figure 7.9: Temperature (a) and vapor concentration (b) development with time under atmospheric boundary conditions.

The water pressure at observation point A located 3 meters below the surface evolves with rainfall, as shown in Fig. 7.8(a). The fully coupled THM simulation takes into account displacements, initial conditions, and changes in soil permeability due to changes in porosity. Comparing results with and without considering mechanical deformation shows the influence of coupled hydro-mechanical behavior on pore water pressure (Fig. 7.8(a)) and on temperature and vapor concentration (see Fig. 7.9). The water pressure calculated from the coupled THM model is lower than the one calculated by the TH model, indicating that the TH analysis may underestimate the stability of the slope's superficial layer. On the other hand, the temperature distribution at the observation point 5 meters below the surface does not appear to be dependent on the slope deformation (Fig. 7.9(a)).

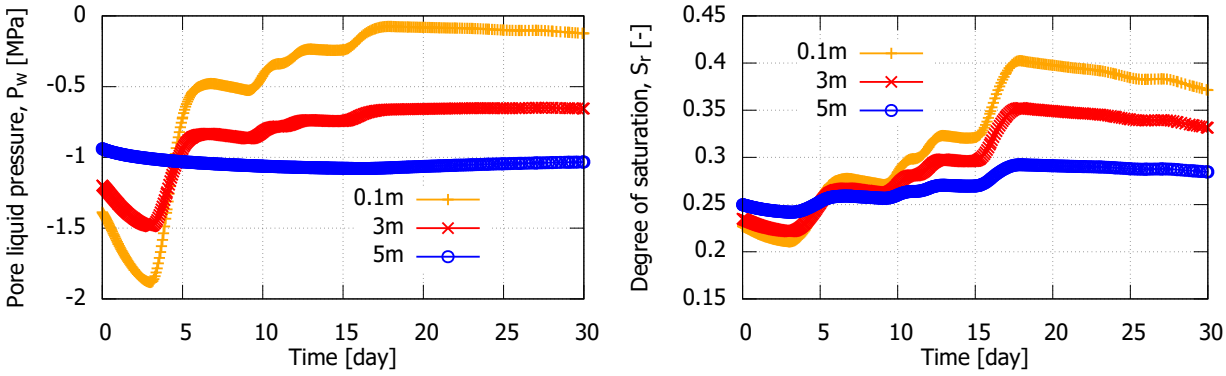

(a) (b)

Figure 7.10: Time history of pore water pressure (a) and degree of saturation (b) at different depth.

A high-intensity rainfall can increase the degree of saturation in the soil, as shown in Fig. 7.10(b). The time of 0 days corresponds to the date of 28th of August with regard to the climate data in Fig. 7.2(b). The degree of saturation firstly decreased until day 3 and subsequently increased stepwise until day 15. From day 15 to day 17, there was a significant increase in the degree of saturation, followed by a nearly constant, slightly decreasing behaviour until day 30. The total increase in the degree of saturation was greatest at a depth of 0.1 m, followed by those of 3 and 5 m depth. The pore liquid pressure as representative for the matric suction behaviour develops accordingly (Fig. 7.10(a)). Suction first increases (as shown by more negative liquid pressure), and then decreases somehow stepwise to nearly zero at 0.1 m depth and -0.7 MPa at 3 m depth.

Maximum suction variations occurred at a depth of 0.1 m, and pore pressure variations generally decrease with depth, occurring mostly in the upper 3 m. Heavy rainfall events (1st of September 2011) lead to only a slight reduction in matric suction at depths of up to 5 m. The degree of saturation is low at the onset of rainfall, but increases with the duration of rainfall, resulting in an increase in the increment of pore water pressure generated by rainfall.

The pore water pressure at the same depth but at different locations along the slope varies, with greater changes in response to rainfall at the top, middle, and toe of the slope (see Fig. 7.13). The rate of change of pore water pressure is faster closer to the slope surface and slower further away (see Fig. 7.10(a)). During the following rainfall, the pore water pressure at the top of the slope increases rapidly. The change in pore water pressure

over time inside the slope is slower due to water flow in unsaturated soil and deformation of the soil, as shown in Fig. 7.10(a). After rainfall stops, water infiltration continues, and suction on the slope surface gradually decreases. Suction in the slope decreases over time during rainfall infiltration.

Fig. 7.10(a) indicates that there is a lag in the response between the development of the pore water pressure in the soil and the change of the atmospheric conditions. The lag time increases with depth. During the initial period of rainfall, the pore water pressure at a certain depth from the surface still decreases. After a period of rainfall, the pore water pressure starts to transfer from upwards to downwards. As the distance from the ground surface increases, the lag time also increases. These observations suggest that the dynamics of pore water pressure in the slope are complex and depend on various factors.

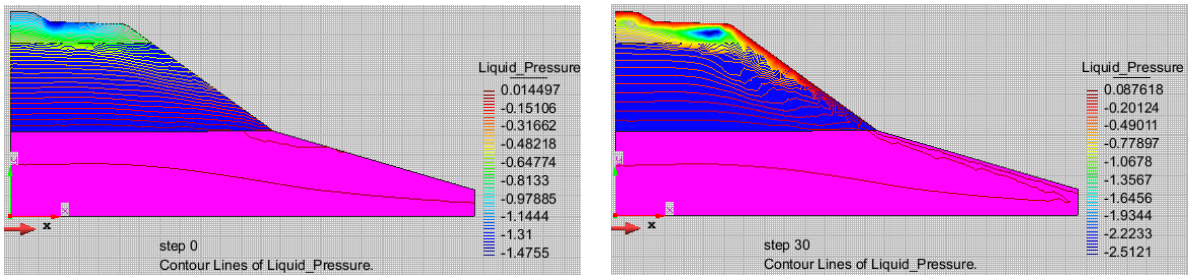

(a) (b)

Figure 7.11: The distribution of pore water pressure along the slope after 0 day (a) and 30 days (b).

As the rainfall duration increases, the matric suction inside the slope gradually decreases. The calculations for the slope pore water pressure are presented in Fig. 7.11. The influence of atmospheric conditions on pore water pressure decreases with depth. Suction near the surface is much higher than in deeper layers, and at depths below 1.5 m the suction is already very low. The rainfall leads to an increase in pore water pressure in the soil layer in the first two meters from the surface. This increase is less due to the low permeability of the soil in the case under consideration. Concluding, the change in pore water pressure occurs mainly in a shallow zone of soil close to the surface. Another conclusion is that obviously the increase in pore water pressure is closely related to the accumulated precipitation.

7.3.2 Development of displacements and plastic area

Fig. 7.12 shows the relationship between cumulative rainfall and total soil displacement at point A. Soil displacements increase with increasing rainfall intensity, and the total displacements increase over time due to increased horizontal and vertical compressive displacement. The horizontal displacements during evaporation are larger than that during precipitation. Displacements are less affected by atmospheric boundary conditions compared to water pressure and temperature.

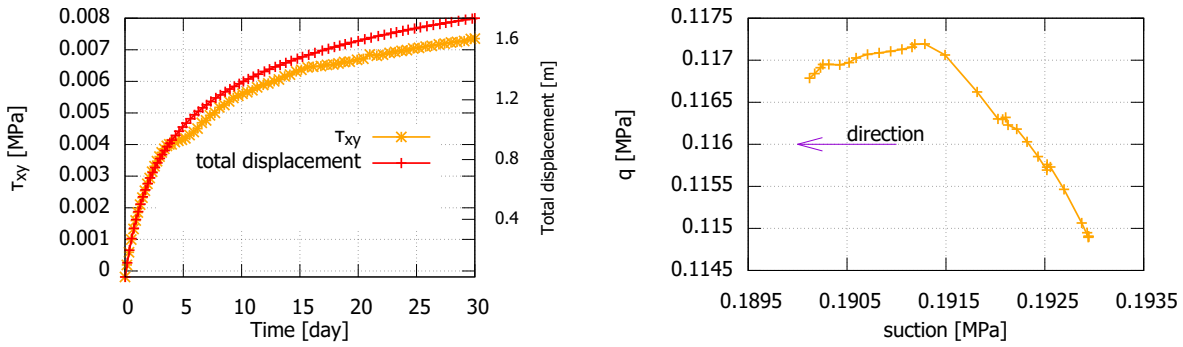

(a) (b)

Figure 7.12: Shear stress and total displacement time history (a) and stress path (q-ψ) inside the slope (b) under rainfall condition at point A.

Slope displacement is impacted by multiple factors such as soil conditions and rainfall. Changes in these variables can cause sudden changes in displacement, which is displayed as a step-like growth trend on the displacement curve (see Fig. 7.12). Rainfall has a delayed effect on landslide displacement, and the length of the lag time is influenced by different factors. The rate of displacements is proportional to the increasing rate of maximum principal stress, and the slope displacements increase due to the rainfall. However, after a prolonged period of continuous rainfall, there was a significant increase in slope displacements or slope deformations, which continued to increase at a decreasing rate as the rain persisted.

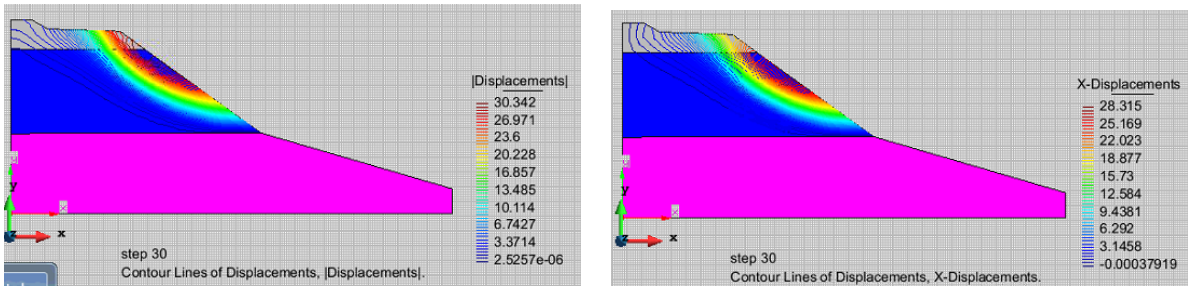

(a) (b)

Figure 7.13: Contours of total displacements (a), contours of horizontal displacements (b) under atmospheric boundary conditions.

The displacements of the slope are mainly vertical downward due to gravity, with the maximum displacements at the top of the slope. However, the contour of displacement shown in Fig. 7.13 indicates that the horizontal displacements are mainly distributed near the slope surface, with the maximum horizontal displacement appearing at the foot of the slope. The significant change in displacement gradient occurs on the foot of the slope, and the density of the displacement vector line is larger at the foot of the slope. The distribution of displacement contour decreases gradually along with the depth from the slope surface to the inside of the slope. The displacements inside the slope are small and less affected by rainfall.

7.3.3 Progress of slope failure

The process of slope failure is illustrated in Fig. 7.14, Fig. 7.15, and Fig. 7.16. When soil is locally damaged, stress is transferred to the surrounding soil and failure occurs when the shear stress exceeds the shear strength. Under continuous rainfall, the damaged area gradually expands, leading to a progressive landslide. The failure zone gradually extends from the toe to the top of the slope. The restraint effect is small along the vertical direction of the slope, and the large shear stress generates along the upward-slope direction. During rainfall, the shear stress on the slope foot increases significantly, centralizing at the foot of the slope. With sustained infiltration, loess softens, resulting in a stress concentration in weak zones and forming the saturated zone at the bottom of the loess. As the failure zone gradually extends to the surrounding soil, a failure surface is formed and a sliding body and zone develop from back to front, with the plastic zone continuing to expand. The upper part of the slope experiences greater deformation than the lower part, and the plastic shear strain before the failure of the slope is presented in Figs. 7.14 and

7.15(a), while Figs. 7.15(b) and 7.16 represent the state after the failure. Fig. 7.16 is for day 30 after failure.

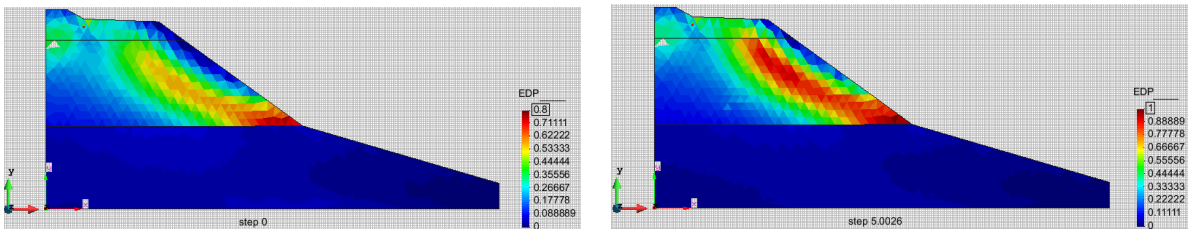

(a) (b)

Figure 7.14: Deviatoric plastic strain after 0 day (a) and 5 days (b).

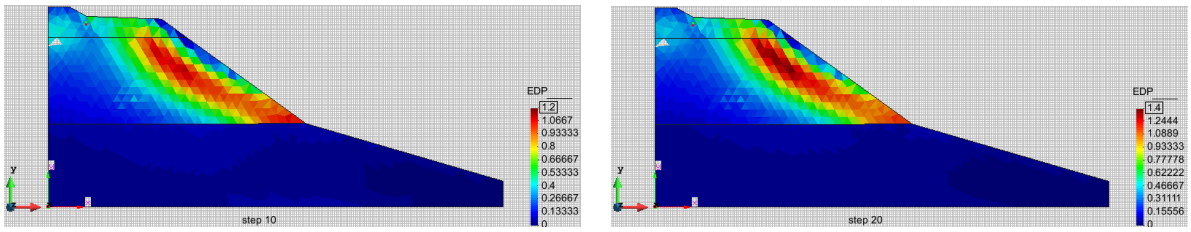

(a) (b)

Figure 7.15: Deviatoric plastic strain after 10 day (a) and 20 days (b).

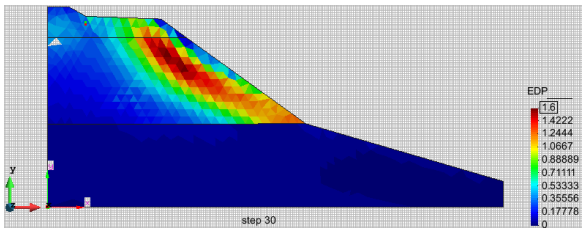

Figure 7.16: Deviatoric plastic strain after 30 days.

The instability of soil slopes is often a gradual process resulting from the accumulation of local deformation, which can be assessed using a criterion based on the distribution of plastic zones. This study uses an advanced constitutive model to investigate the development of the plastic zone of a slope under rainfall, as shown in Fig. 7.16. Rainfall infiltration causes the slope to gradually shift from local to widely distibuted large plastic deformation, leading to overall slippage failure. A shear band-type bifurcation can occur where plastic deformation is concentrated, and failure due to plastic deformation and shear strain localization can happen even without complete saturation of the sediment.

7.4 Summary

Numerical simulations using the finite element code CODE_ BRIGHT were performed to assess the processes leading to a loess landslide due to atmospheric boundary conditions. A coupled THM analysis was used with imposed atmospheric boundary conditions, and the material parameters, initial conditions, and boundary conditions are presented in Section 7.2. The influence of atmospheric boundary conditions on slope stability was investigated through a series of numerical simulations of a soil column (see Chapter 6) and employing a numerical model of a real slope. The coupled hydo-mechanical analysis was competent in fully reproducing stress strain behaviour, vapour transport, and temperature conduction in the soil. The simulations of the slope were based on model parameters derived from testing of loess samples performed as part of the thesis.

This study considers the failure mechanism of loess slope under unsaturated soil conditions and examines the effects of antecedent rainfall and evaporation on slope stability under atmospheric boundary conditions. The research done in this thesis involved performing a number of analyses to determine the relationship between changes in atmospheric boundary conditions and the slope response. Based on the results of the numerical simulations several conclusions can be drawn:

- The historical Baqiao slope failure was not caused by a single rainfall event, so this study compares the results of the simulations of landslide processes with and without accounting for antecedent rainfall. It was found that the antecedent rainfall had a significant effect on the water pressure in the top surface layer of the slope. However, the more distant in time the preceding precipitation events are, the less impact they have on slope stability.
- The study found that evaporation has a significant impact on the water pressure within the slope. Ignoring evaporation can lead to underestimation of slope stability because the negative water pressure is smaller. Suction in the slope decreases rapidly during rainfall. The fluctuations in the atmospheric boundary conditions cause changes in evaporation and infiltration, leading to fluctuations in water pressure.
- The hydraulic characteristics of the soil significantly affect the water pressure in the slope. The influence of atmospheric conditions on water pressure and temperature in the slope becomes less significant as depth increases. For a loess soil slope, atmospheric conditions have a significant impact up to a depth of 5 meters. Over

time, the water pressure reaches a steady state with minimal variation, and this time is mainly dependent on factors such as rainfall intensity, duration, soil depth, initial water pressure, and loess initial saturation.

- The calculation of water pressure in the slope using a coupled THM analysis, which takes into account slope deformation caused by water infiltration, shows a smaller suction value compared to calculations that do not consider slope deformation. The amount of deformation is influenced by soil hydraulic and mechanical characteristics as well as precipitation, and lower soil permeability improves slope stability against more intense and prolonged rainfall. To investigate the impact of infiltration on slope deformation, the contribution of negative pore water pressure needs to be examined.
- Section 7.3.3 presents the results of the analysis of the slope failure process and the depth of the soil mass affected by the failure, leading to a conclusion about the relationship between rainfall events and the cause of slope failure due to infiltration. The numerical simulation results are consistent with field observations for the hydrological conditions studied. In general, shallower failures are associated with plastic deformation, while deeper failures are linked to changes in effective stress throughout the slope. However, the depth of failure is not only influenced by the mechanical characteristics of loess material but also by the hydraulic characteristics of the soil. Furthermore, this chapter gives a qualitative assessment of the location of the failure zones depending on the atmospheric boundary conditions.

In conclusion, the use of rigorous finite element analysis can be considered as an effective method for studying the behaviour of slopes that yields relatively accurate results. This approach is particularly useful for analysing processes in loess slopes and for identifying the mechanisms that cause loess slope failure during rainfall events.

8 Conclusions and outlook

8.1 Conclusions

The main objective of the thesis is to investigate the coupled hydro-mechanical behaviour of unsaturated loess and the loess slope instability mechanism. Due to the complex behaviour of unsaturated loess soils, the focus of the thesis was mainly on approaches and solutions to selected problems related to the response of loess slopes to the changes in the atmospheric conditions. The approaches employed in this study include experimental and numerical methods. In the experimental part, different devices, measurement methods and test procedures are used and in the numerical part mathematical models and finite element simulations are applied. The effects of hydraulic loading history and the loess structure on the deformation and shear strength of loess were experimentally investigated. An advanced constitutive model, the Barcelona basic model, was employed in loess slope simulations. The finite element method was used to solve the posed boundary value problems for simulating the loess slope instability with the emphasis on the atmospheric boundary conditions. The numerical models and approaches developed to simulate the loess slope behaviour have been shown to be capable of describing the stress-strain relationship of unsaturated soil under hydromechanical loading and have proved to be useful for simulating complex loess landslide behaviour under atmospheric boundary conditions. Based on the results obtained within this thesis the following conclusions can be drawn.

8.1.1 Experimental work

Determining the physical and chemical properties of the specific loess material through MIP and SEM studies is an important part of characterizing and understanding the loess material behavior. The results showed that the pore structure of loess is heterogeneous. The comparison of the microstructure of remolded and undisturbed loess samples showed that the presence of clay particles and soluble salts in the undisturbed loess samples creates bridging and cementation between the solid particles, which underlies the significant

differences between the two types of loess samples.

The results of the collapse tests showed that the collapsibility has the largest value at a critical vertical stress, which is dependent on the soil condition (remolded or undisturbed) and the soil initial state. Both single and double oedometer tests showed that before the maximum collapsing pressure, the collapsibility coefficient decreased with an increase in initial water content, and increased with an increase in pressure (Fig. 5.6). After passing the maximum collapsing pressure, the collapsibility coefficient decreased with an increase in the applied vertical stress at inundation. However, the quantitative collapsibility obtained by the two methods was different for the two types of loess samples, indicating that the stress path affects the collapsibility coefficient of the remolded sample. Specifically, the collapsibility coefficient value obtained from a single oedometer test was less than that obtained from a double oedometer test (Fig. 5.5). The results also showed that there were significant differences in engineering properties between remolded and undisturbed loess samples, with the collapsibility of the remolded loess sample being larger than that of the undisturbed loess sample (Fig. 5.7).

The presented results of single-stage and multi-stage shear tests conducted to investigate the influence of initial water content, test method and soil structure on the unsaturated shear strength parameters allow the following conclusions to be drawn. Undisturbed loess exhibits greater unsaturated shear strength compared to remolded loess (see Fig. 5.19). The shear strength of loess decreases nonlinearly with an increase in water content (see Fig. 5.26). During shear deformation, loess exhibits dilatancy at low vertical load and low initial water content, and contraction at high vertical load and high initial water content. Moreover, it shows visible brittleness at low water content and ductility at high water content (see Fig. 5.9). The influence of water content on the unsaturated shear strength of undisturbed loess is due to two factors, namely, the cohesive force that is present in the remolded sample, and the additional cohesive force provided by the cementation bond in the undisturbed sample (see Fig. 5.26).

As described in Chapter 5.2.5, the results of testing the soil-water characteristic curve (SWCC) of loess under various wetting-drying cycles indicate that the maximum degree of saturation cannot be achieved after subsequent wetting due to entrapped air within the sample, resulting in hysteresis between the drying and wetting curves (see Fig. 5.36). The degree of hysteresis is influenced by the degree of homogeneity and changes after different drying-wetting cycles, as reported in the literature. The effect of the hydraulic

loading history disappears once the suction reaches the residual suction value (see Fig. 5.45 to Fig. 5.50). The air entry value tends to increase as the number of dry and wet cycles increases. The permeability coefficient of loess decreases with the increase in vertical load (see Fig. 5.92), while the unsaturated coefficients of permeability decrease with the increase in suction (see Fig. 5.94). Overall, the results of the experiments conducted to determine the dependence between suction and pore water content reveal the specificity of the loess's SWCC, which is influenced not only by the applied mechanical stress but also by the suction history and the hydraulic loading path.

The suction-controlled compression tests presented in Section 5.3.3 reveal that the compressibility of loess decreases with increasing suction, while the pre-consolidation pressure increases with increasing suction. The undisturbed loess is found to be in an over-consolidated state. The reloading process in the compression test under different suction values shows that the rebound coefficient of loess does not depend much on suction. The test also reveals that the collapse deformation of loess has three stages with changes in suction, but the amount of collapse is not significantly different from that recorded in the single odometer test (see Fig. 5.85). During the entire process of wetting, there is both elastic compression and plastic collapsing under the saturation process. The constant suction compression experiment shows that the SWCC is affected by the stress state, and the relationship between suction and saturation changes when mechanical load is applied. The air entry value increases with the increase of vertical stress. The LC line obtained from the suction-controlled compression experiment and the LC line obtained by the constant load wetting test do not coincide, indicating the stress path dependence of the remolded loess behavior (see Fig. 5.89). Soil hydraulic and mechanical behavior influence each other in a complex way, with pore water pressure causing soil deformation and altering its hardening behavior, while deformation alters the relationship between degree of saturation and suction.

8.1.2 Numerical work

Unlike using a single relationship between the degree of saturation and suction, the model used in this thesis can accurately capture the hysteresis of the soil hydraulic characteristics, which is essential for reliable predictions. The implication is that neglecting hysteresis in hydraulic behavior can lead to unrealistic simulations and, therefore, the recommen-

dation is to use an adequate soil water relationship model to reflect the realistic field conditions.

The results in this dissertation from the use of a coupled hydromechanical (THM and HM) constitutive model that accounts for the interaction between pore water pressure and stress demonstrate the large capacity of the coupled THM and HM simulations to adequately model processes in unsaturated soils. The CODE_BRIGHT finite element code developed by the Polytechnic University of Catalonia (UPC) used here to simulate and analyze the behavior of the Baqiao slope under atmospheric boundary conditions has proven to be a very good tool for analyzing such problems. Rainfall-initiated loess landslides involve complex processes that are influenced by different meteorological conditions. In this study, several atmospheric parameters including evaporation and precipitation, ambient temperature, relative humidity and wind speed are considered to comprehensively study the distribution of pore water pressure, soil temperature and displacements based on the Baqiao slope example. Chapter 6.1.5 shows that the pore water pressure inside the slope is strongly influenced by the considered atmospheric variables (see Fig. 6.3 - Fig. 6.7). Therefore, in addition to precipitation, other atmospheric conditions play a significant role in the stability of loess slopes.

It can be confidently concluded that the results of the numerical analysis carried out in the dissertation helped to better understand the progressive failure of the Baqiao landslide due to rainfall. By using the soil-water characteristic curve model with hysteresis and by employing the BBM model as implemented in CODE_BRIGHT, the distribution and variation of pore water pressure inside the loess slope under atmospheric boundary conditions and the development of the plastic zone in the slope body were effectively simulated and the obtained numerical solutions proved to be reliable. Furthermore, based on the results in the thesis, it can be concluded that the coupled thermo-hydromechanical (THM) simulation, which takes atmospheric boundary conditions into account, gives more adequate results in predicting slope instability than those obtained from the coupled thermo-hydro simulation. As a final conclusion, the research findings of this dissertation can be the basis for developing a methodology to analyze actual landslide problems in loess areas and help to understand the mechanism of its occurrence.

8.2 Outlook

Based on the findings of this study, the following recommendations are proposed for further research on undisturbed unsaturated loess to improve the understanding and solution to geotechnical engineering problems:

Suction-controlled triaxial tests can provide valuable information on the hydro-mechanical behavior of unsaturated loess under various stress paths. Advanced techniques, such as those for directly obtaining unsaturated coefficients of permeability, can be employed. However, further research is needed to develop a hydro-mechanical coupled model that considers variables such as suction, net pressure, and degree of saturation, in order to accurately represent undisturbed loess. Furthermore, a new constitutive model with structural parameters must be developed to specifically represent the mechanical behavior of undisturbed loess. Microstructure properties of undisturbed loess under different conditions should also be investigated, and a connection should be made between the changing microstructure and hydro-mechanical behavior.

The study proposes that probabilistic analysis can be utilized to consider the spatial anisotropy of the material within the slope and to investigate the landslide under rainfall. Additionally, a new hysteresis hydraulic model can be incorporated into the finite element method to simulate the material's behavior under different hydraulic paths. To further investigate the failure of loess slopes induced by rainfall, the simulation should consider fissures and cracks that create preferential infiltration paths. Although appropriate model parameters are necessary to accurately capture the unique hydraulic coupling characteristics of undisturbed loess, the finite element method can be improved to study the loess landslide under rainfall with a deep-set sliding surface.

Bibliography

Acharya, G., Cochrane, T., Davies, T. and Bowman, E. (2011), 'Quantifying and modeling post-failure sediment yields from laboratory-scale soil erosion and shallow landslide experiments with silty loess', *Geomorphology* **129**(1-2), 49–58.

Agus, S. (2005), An experimental study on hydro-mechanical characteristics of compacted bentonite-sand mixtures, PhD thesis, Faculty of Civil Eng., Bauhaus-Universitaet, Weimar, Germany.

Agus, S. and Leong, E. & Schanz, T. (2003), 'Assessment of statistical models for indirect determination of permeability functions from soil–water characteristic curves', *Géotechnique* **53**(2), 279–282.

Al-Badran, Y. (2011), Volumetric yielding behavior of unsaturated fine-grained soils, PhD thesis, Ruhr-Universitaet Bochum.

Al-Mukhtar, M., Qi, Y., Alcover, F. and Bergaya, F. (1999), 'Oedometric and water-retention behaviour of highly compacted unsaturated smectites', *Canadian Geotechnical Journal* **36**(4), 675–684.

Al-Obaidi, Q. (2015), Hydro-mechanical behaviour of collapsible soils, PhD thesis, Ruhr-Universitaet Bochum.

Alonso, E., Gens, A. and Delahaye, H. (2003), 'Influence of rainfall on the deformation and stability of a slope in overconsolidated clays: a case study', *Hydrogeology Journal* **11**(1), 174–192.

Alonso, E., Gens, A. and Josa, A. (1990), 'A constitutive model for partially saturated soils', *Géotechnique* **40**(3), 405–430.

Alonso, E. and Pinyol, M. (2008), Unsaturated soil mechanics in earth and rockfill dam engineering, *in* 'Unsaturated Soils. Advances in Geo-Engineering', CRC Press, pp. 19–48.

Alonso, E., Romero, E., Hoffmann, C. and García-Escudero, E. (2005), 'Expansive bentonite–sand mixtures in cyclic controlled-suction drying and wetting', *Engineering Geology* **81**(3), 213–226.

Alonso, E., Zervos, A. and Pinyol, M. (2016), 'Thermo-poro-mechanical analysis of landslides: from creeping behaviour to catastrophic failure', *Géotechnique* **66**(3), 202–219.

Alsherif, N. A. and McCartney, J. S. (2016), 'Yielding of silt at high temperature and suction magnitudes', *Geotechnical and Geological Engineering* **34**(2), 501–514.

An, S., Kukla, G., Porter, C. and Xiao, L. (1991), 'Late Quaternary dust flow on the Chinese loess plateau', *Catena* **18**(2), 125–132.

Anderson, A. and Sitar, N. (1995), 'Analysis of rainfall-induced debris flows', *Journal of Geotechnical Engineering* **121**(7), 544–552.

Arnone, E., Noto, V., Lepore, C. and Bras, L. (2011), 'Physically-based and distributed approach to analyze rainfall-triggered landslides at watershed scale', *Geomorphology* **133**(3-4), 121–131.

Askarinejad, A. (2015), *Failure mechanisms in unsaturated silty sand slopes triggered by rainfall*, Vol. 248, vdf Hochschulverlag AG.

Assallay, M., Rogers, F. and Smalley, J. (1997), 'Formation and collapse of metastable particle packings and open structures in loess deposits', *Engineering Geology* **48**(1-2), 101–115.

ASTMD2216 (2010), *Standard test methods for laboratory determination of water (moisture) content of soil and rock by mass*, Vol. Annual Book of ASTM Standards, Vol.04.08, ASTM International, Philadelphia,PA, ASTM,USA, ASTM International, 100 Barr Harbor Drive, PO Box C700, West Conshohocken, PA 19428-2959, United States.

ASTMD2435 (1996), *Standard test method for one-dimensional consolidation properties of soils*, Vol. Annual Book of ASTM Standards, Vol.04.08, ASTM International, Philadelphia,PA, ASTM,USA, ASTM International, 100 Barr Harbor Drive, PO Box C700, West Conshohocken, PA 19428-2959, United States.

ASTMD2937 (2000), *Standard test method for density of soil in place by the drive cylinder method*, Vol. Annual Book of ASTM Standards, Vol.04.08, ASTM International, Philadelphia,PA, ASTM,USA, ASTM International, 100 Barr Harbor Drive, PO Box C700, West Conshohocken, PA 19428-2959, United States.

ASTMD3080 (2011), *Standard test method for direct shear test of soils under consolidated drained conditions*, Vol. Annual Book of ASTM Standards, Vol.04.08, ASTM International, Philadelphia,PA, ASTM,USA, ASTM International, 100 Barr Harbor Drive, PO Box C700, West Conshohocken, PA 19428-2959, United States.

ASTMD422 (1963), *Standard test method for particle-size analysis of soils*, Vol. Annual Book of ASTM Standards, Vol.04.08, ASTM International, Philadelphia,PA, ASTM,USA, ASTM International, 100 Barr Harbor Drive, PO Box C700, West Conshohocken, PA 19428-2959, United States.

ASTMD4318 (2000), *Standard test methods for liquid limit, plastic limit, and plasticity index of soils*, Vol. Annual Book of ASTM Standards, Vol.04.08, ASTM International, Philadelphia,PA, ASTM,USA, ASTM International, 100 Barr Harbor Drive, PO Box C700, West Conshohocken, PA 19428-2959, United States.

ASTMD5084 (2007), *Standard test methods for measurement of hydraulic conductivity of saturated porous materials using a flexible wall permeameter*, Vol. Annual Book of ASTM Standards, Vol.04.08, ASTM International, Philadelphia,PA, ASTM,USA, ASTM International, 100 Barr Harbor Drive, PO Box C700, West Conshohocken, PA 19428-2959, United States.

ASTMD5333 (1996), *Standard test method for measurement of collapse potential of soils*, Vol. Annual Book of ASTM Standards, Vol.04.08, ASTM International, Philadelphia,PA, ASTM,USA, ASTM International, 100 Barr Harbor Drive, PO Box C700, West Conshohocken, PA 19428-2959, United States.

ASTMD6836 (2008), *Standard test methods for determination of the soil water characteristic curve for desorption using a hanging column, pressure extractor, chilled mirror hygrometer, and/or centrifuge*, Vol. Annual Book of ASTM Standards, Vol.04.08, ASTM International, Philadelphia,PA, ASTM,USA, ASTM International, 100 Barr Harbor Drive, PO Box C700, West Conshohocken, PA 19428-2959, United States.

ASTMD7181 (2011), *Method for consolidated drained triaxial compression test for soils*, Vol. Annual Book of ASTM Standards, Vol.04.08, ASTM International, Philadelphia,PA, ASTM,USA, ASTM International, 100 Barr Harbor Drive, PO Box C700, West Conshohocken, PA 19428-2959, United States.

ASTMD854 (2010), *Standard test methods for specic gravity of soil solids by water pycnometer*, Vol. Annual Book of ASTM Standards, Vol.04.08, ASTM International,

Philadelphia,PA, ASTM,USA, ASTM International, 100 Barr Harbor Drive, PO Box C700, West Conshohocken, PA 19428-2959, United States.

ASTME104 (1997), *Maintaining constant relative humidity by means of aqueous solutions*, Vol. Annual Book of ASTM Standards, Vol.04.08, ASTM International, Philadelphia,PA, ASTM,USA, ASTM International, 100 Barr Harbor Drive, PO Box C700, West Conshohocken, PA 19428-2959, United States.

Baoping, W., Sijing, W., Enzhi, W., Jianmin, Z., Yugeng, W. and Xinglin, W. (2005), 'Deformation characteristics of loess landslide along the contact between loess and neocene red mudstone', *Acta Geologica Sinica-English Edition* **79**(1), 139–151.

Barden, L., McGown, A. and Collins, K. (1973), 'The collapse mechanism in partly saturated soil', *Engineering Geology* **7**(1), 49–60.

Bear, J. and Braester, C. (1972), 'On the flow of two immscible fluids in fractured porous media', **2**, 177–202.

Beckwith, H. and Hansen, A. (1982), 'Calcareous soils of the southwestern United States'.

Beliaev, Y. and Hassanizadeh, M. (2001), 'A theoretical model of hysteresis and dynamic effects in the capillary relation for two-phase flow in porous media', *Transport in Porous Media* **43**(3), 487–510.

Bishop, W. (1955), 'The use of the slip circle in the stability analysis of slopes', *Geotechnique* **5**(1), 7–17.

Brideau, M., Pedrazzini, A., Stead, D., Froese, C., Jaboyedoff, M. and van Zeyl, D. (2011), 'Three-dimensional slope stability analysis of South Peak, Crowsnest Pass, Alberta, Canada', *Landslides* **8**(2), 139–158.

Brinkgreve, J. and Bakker, L. (1991), Non-linear finite element analysis of safety factors, *in* 'Proc. 7th Int. Conf. on Comp. Methods and Advances in Geomechanics, Cairns, Australia', pp. 1117–1122.

Brooks, H. and Corey, T. (1964*a*), 'Hydraulic properties of porous media and their relation to drainage design', *Transactions of the ASAE* **7**(1), 26–0028.

Brooks, R. and Corey, T. (1964*b*), 'HYDRAU uc properties of porous media', *Hydrology Papers, Colorado State University* **24**, 37.

Bulut, R. & Leong, C. (2008), 'Indirect measurement of suction', pp. 21–32.

Burdine, N. (1953), 'Relative permeability calculations from pore size distribution data', *Journal of Petroleum Technology* **5**(3), 71–78.

Burton, J., Sheng, D. and Campbell, C. (2014), 'Bimodal pore size distribution of a high-plasticity compacted clay', *Géotechnique Letters* **4**(2), 88–93.

Cai, F. and Ugai, K. (2004), 'Numerical analysis of rainfall effects on slope stability', *International Journal of Geomechanics* **4**(2), 69–78.

Campbell, S. (1974), 'A simple method for determining unsaturated conductivity from moisture retention data', *Soil science* **117**(6), 311–314.

Canone, D., Ferraris, S., Sander, G. and Haverkamp, R. (2008), 'Interpretation of water retention field measurements in relation to hysteresis phenomena', *Water Resources Research* **44**(4).

Capparelli, G. and Versace, P. (2011), 'FLaIR and SUSHI: two mathematical models for early warning of landslides induced by rainfall', *Landslides* **8**(1), 67–79.

Cardoso, R., Fernandes, V., Ferreira, M. and Teixeira, P. F. (2012), Settlement prediction of high speed railway embankments considering the accumulation of wetting and drying cycles, *in* 'Unsaturated Soils: Research and Applications', Springer, pp. 291–298.

Casadei, M., Dietrich, E. and Miller, L. (2003), 'Testing a model for predicting the timing and location of shallow landslide initiation in soil-mantled landscapes', *Earth Surface Processes and Landforms: The Journal of the British Geomorphological Research Group* **28**(9), 925–950.

Casagrande, A. (1936), The determination of the preconcolidation load and its practical influence., *in* 'Pro, Ist International Conf. on Soil; Mech. And Found. Eng., Boston, Discussion D-34. Vol. 3'.

Cascini, L., Calvello, M. and Grimaldi, M. (2010), 'Groundwater modeling for the analysis of active slow-moving landslides', *Journal of Geotechnical and Geoenvironmental Engineering* **136**(9), 1220–1230.

Cascini, L., Cuomo, S. and Della Sala, M. (2011), 'Spatial and temporal occurrence of rainfall-induced shallow landslides of flow type: A case of Sarno-Quindici, Italy', *Geomorphology* **126**(1-2), 148–158.

Castro, G. (1975), 'Liquefaction and cyclic mobility of saturated sands', *Journal of Geotechnical and Geoenvironmental Engineering* **101**(ASCE# 11388 Proceeding).

Castro, G.and Poulos, S. J. (1977), 'Factors affecting liquefaction and cyclic mobility', *Journal of Geotechnical and Geoenvironmental Engineering* **103**(6).

Chatzis, I. and Dullien, L. (1983), 'Dynamic immiscible displacement mechanisms in pore doublets: theory versus experiment', *Journal of Colloid and Interface Science* **91**(1), 199–222.

Chen, C., He, J. and Yang, P. (2007), 'Constitutive relationship of intact loess considering structural effect', *Yantu Lixue (Rock and Soil Mechanics)* **28**(11), 2284–2290.

Chen, H., Chen, P., Chen, S. and Zhung, B. (2009), 'Simulation of a slope failure induced by rainfall infiltration', *Environmental Geology* **58**(5), 943–952.

Chen, P., Mirus, B., Lu, N. and Godt, W. (2017), 'Effect of hydraulic hysteresis on stability of infinite slopes under steady infiltration', *Journal of Geotechnical and Geoenvironmental Engineering* **143**(9), 04017041.

Chen, Y., Irfan, M., Uchimura, T. and Zhang, K. (2018), 'Feasibility of using elastic wave velocity monitoring for early warning of rainfall-induced slope failure', *Sensors* **18**(4), 997.

Cheng, M., Lansivaara, T. and Wei, B. (2007), 'Two-dimensional slope stability analysis by limit equilibrium and strength reduction methods', *Computers and Geotechnics* **34**(3), 137–150.

Childs, C. and Collis-George, N. (1950), 'The permeability of porous materials', *Proceedings of the Royal Society of London. Series A. Mathematical and Physical Sciences* **201**(1066), 392–405.

Chiu, F. and Ng, W. (2003), 'A state-dependent elasto-plastic model for saturated and unsaturated soils', *Géotechnique* **53**(9), 809–829.

Cho, E. and Lee, R. (2001), 'Instability of unsaturated soil slopes due to infiltration', *Computers and Geotechnics* **28**(3), 185–208.

Cho, E. and Lee, R. (2002), 'Evaluation of surficial stability for homogeneous slopes considering rainfall characteristics', *Journal of Geotechnical and Geoenvironmental Engineering* **128**(9), 756–763.

Coleman, D. (1962), 'Stress strain relations for partly saturated soil', *Corespondence to Geotechnique* **12**(4), 348–350.

Collins, D. and Znidarcic, D. (2004), 'Stability analyses of rainfall induced landslides', *Journal of Geotechnical and Geoenvironmental Engineering* **130**(4), 362–372.

Croney, D. and Coleman, D. (1954), 'Soil structure in relation to soil suction (pF)', *Journal of Soil Science* **5**(1), 75–84.

Crosta, B. and Frattini, P. (2008), 'Rainfall-induced landslides and debris flows', *Hydrological Processes: An International Journal* **22**(4), 473–477.

Crosta, B., Imposimato, G. and Roddeman, G. (2006), Continuum numerical modelling of flow-like landslides, *in* 'Landslides from Massive Rock Slope Failure', Springer, pp. 211–232.

Cruden, M. and Varnes, J. (1996), *Landslides: investigation and mitigation. Chapter 3-Landslide types and processes*, number 247.

Cui, J., Loiseau, C. and Delage, P. (2002), Microstructure changes of a confined swelling soil due to suction, *in* 'Unsaturated Soils: Proceedings of the Third International Conference on Unsaturated Soils, UNSAT 2002, 10-13 March 2002, Recife, Brazil', Vol. 2, CRC Press, p. 593.

Cui, J., Lu, F., Delage, P. and Riffard, M. (2005), 'Field simulation of in situ water content and temperature changes due to ground-atmospheric interactions', *Géotechnique* **55**(7), 557–568.

Cui, S.-h., Pei, X.-j., Wu, H.-y. and Huang, R. (2018), 'Centrifuge model test of an irrigation-induced loess landslide in the Heifangtai loess platform, Northwest China', *Journal of Mountain Science* **15**(1), 130–143.

Cui, Y. J. and Delage, P. (1996), 'Yeilding and plastic behaviour of an unsaturated compacted silt', *Géotechnique* **46**(2), 291–311.

Dane, H. and Wierenga, J. (1975), 'Effect of hysteresis on the prediction of infiltration, redistribution and drainage of water in a layered soil', *Journal of Hydrology* **25**(3-4), 229–242.

Das, P. and Thyagaraj, T. (2018), 'Collapse behaviour of compacted red soil', *International Journal of Geotechnical Engineering* **12**(1), 20–27.

Dawson, M., Roth, H. and Drescher, A. (1999), 'Slope stability analysis by strength reduction', *Geotechnique* **49**(6), 835–840.

Delage, P. & Romero, E. and Tarantino, A. (2008), 'Recent developments in the techniques of controlling and measuring suction in unsaturated soils', pp. 49–68.

Delage, P., Cui, J. and Antoine, P. (2008), 'Geotechnical problems related with loess deposits in Northern France', *arXiv preprint arXiv:0803.1435* .

Deng, H., Shao, J., Chen, L. and She, T. (2012), 'A structural parameter reflecting coupling action between shear stress and spherical stress', *Rock and Soil Mechanics* **33**(8), 2310–2314.

Derbyshire, E., Dijkstra, A., Smalley, J. and Li, Y. (1994), 'Failure mechanisms in loess and the effects of moisture content changes on remoulded strength', *Quaternary International* **24**, 5–15.

Derbyshire, E. and Mellors, W. (1988), 'Geological and geotechnical characteristics of some loess and loessic soils from China and Britain: a comparison', *Engineering Geology* **25**(2-4), 135–175.

Derbyshire, E. and Meng, X. (1995), 'Collapsible loess on the loess plateau of China', pp. 267–293.

Derbyshire, E., Meng, X. and Dijkstra, T. A. (2000), *Landslides in the thick loess terrain of north-west China*, John Wiley & Sons Incorporated.

Dijkstra, A. (2001), 'Geotechnical thresholds in the Lanzhou loess of China', *Quaternary International* **76**, 21–28.

Dijkstra, A., Smalley, J. and Rogers, F. (1995), 'Particle packing in loess deposits and the problem of structure collapse and hydroconsolidation', *Engineering Geology* **40**(1-2), 49–64.

Dijkstra, T., Rogers, F., Smalley, J., Derbyshire, E., Li, J. and Meng, M. (1994), 'The loess of north-central China: geotechnical properties and their relation to slope stability', *Engineering Geology* **36**(3-4), 153–171.

DIN18129 (1996), 'Baugrund, untersuchung von bodenproben-kalkgehaltsbestimmung'.

Duncan, M., Wright, G. and Brandon, L. (2014), *Soil strength and slope stability*, John Wiley & Sons.

Ebel, A., Loague, K. and Borja, R. I. (2010), 'The impacts of hysteresis on variably saturated hydrologic response and slope failure', *Environmental Earth Sciences* **61**(6), 1215–1225.

El-Ehwany, M. and Houston, S. L. (1990), 'Settlement and moisture movement in collapsible soils', *Journal of Geotechnical Engineering* **116**(10), 1521–1535.

Elia, G., Cotecchia, F., Pedone, G., Vaunat, J., Vardon, J., Pereira, C., Springman, M., Rouainia, M., Van Esch, J. and Koda, E. (2017), 'Numerical modelling of slope–vegetation–atmosphere interaction: an overview', *Quarterly Journal of Engineering Geology and Hydrogeology* **50**(3), 249–270.

Everett, H. and Smith, W. (1954), 'A general approach to hysteresis. Part 2: Development of the domain theory', *Transactions of the Faraday Society* **50**, 187–197.

Everett, H. and Whitton, W. I. (1952), 'A general approach to hysteresis', *Transactions of the Faraday Society* **48**, 749–757.

Feda, J., Bohac, J. and Herle, I. (1995), 'K0-compression of reconstituted loess and sand with stress prturbations', *Soils and Foundations* **35**(3), 97–104.

Fell, R., Corominas, J., Bonnard, C., Cascini, L., Leroi, E. and Savage, Z. (2008), 'Guidelines for landslide susceptibility, hazard and risk zoning for land-use planning', *Engineering Geology* **102**(3-4), 99–111.

Feng, M. and Fredlund, G. (1999), Hysteretic influence associated with thermal conductivity sensor measurements, *in* 'Proceedings from Theory to the Practice of Unsaturated Soil Mechanics in Association with the 52nd Canadian Geotechnical Conference and the Unsaturated Soil Group, Regina, Sask', Vol. 14, pp. 14–20.

Fleureau, J.-M., Kheirbek-Saoud, S., Soemitro, R. and Taibi, S. (1993), 'Behavior of clayey soils on drying–wetting paths', *Canadian geotechnical journal* **30**(2), 287–296.

Fleureau, M., Verbrugge, C., Huergo, J., Correia, G. and Kheirbek-Saoud, S. (2002), 'Aspects of the behaviour of compacted clayey soils on drying and wetting paths', *Canadian Geotechnical Journal* **39**(6), 1341–1357.

Fourie, B. (1996), Predicting rainfall-induced slope instability, *in* 'Proceedings of the institution of civil engineers: geotechnical engineering', Vol. 119.

Fourie, B., Rowe, D. and Blight, E. (1999), 'The effect of inffiltration on the stability of the slopes of a dry ash dump', *Geotechnique* **49**(1), 1–13.

Frechen, M., Oches, A. and Kohfeld, K. E. (2003), 'Loess in Europeâmass accumulation rates during the Last Glacial Period', *Quaternary Science Reviews* **22**(18-19), 1835–1857.

Fredlund, D. G. and Rahardjo, H. (1993), *Soil Mechanics for Unsaturated Soils*, John Wiley & Sons.

Fredlund, G. (2000), 'The 1999 RM Hardy Lecture: The implementation of unsaturated soil mechanics into geotechnical engineering', *Canadian Geotechnical Journal* **37**(5), 963–986.

Fredlund, G. and Gan, M. (1995), The collapse mechanism of a soil subjected to one-dimensional loading and wetting, *in* 'Genesis and properties of collapsible soils', Springer, pp. 173–205.

Fredlund, G. and Morgenstern, R. (1977), 'Stress state variables for unsaturated soils', *Journal of Geotechnical and Geoenvironmental Engineering* **103**(ASCE 12919).

Fredlund, G., Morgenstern, R. and Widger, A. (1978), 'The shear strength of unsaturated soils', *Canadian geotechnical journal* **15**(3), 313–321.

Fredlund, G. and Xing, A. (1994), 'Equations for the soil-water characteristic curve', *Canadian geotechnical journal* **31**(4), 521–532.

Gallipoli, D., Wheeler, J. and Karstunen, M. (2003), 'Modelling the variation of degree of saturation in a deformable unsaturated soil.', *Géotechnique.* **53**(1), 105–112.

Garakani, A., Haeri, M., Khosravi, A. and Habibagahi, G. (2015), 'Hydro-mechanical behavior of undisturbed collapsible loessial soils under different stress state conditions', *Engineering geology* **195**, 28–41.

Gardner, R. (1956), 'Calculation of capillary conductivity from pressure plate outflow data 1', *Soil Science Society of America Journal* **20**(3), 317–320.

Gardner, R. (1958), 'Some steady-state solutions of the unsaturated moisture flow equation with application to evaporation from a water table', *Soil Science* **85**(4), 228–232.

Gasmo, M., Rahardjo, H. and Leong, C. (2000), 'Infiltration effects on stability of a residual soil slope', *Computers and Geotechnics* **26**(2), 145–165.

Gens, A. and Alonso, E. (1992), 'A framework for the behaviour of unsaturated expansive clays', *Canadian Geotechnical Journal* **29**(6), 1013–1032.

Gens, A., Alonso, E. and Lloret, A. (1995), Effect of structure on the volumetric behaviour of a compacted soil, *in* 'PROCEEDINGS OF THE FIRST INTERNATIONAL CONFERENCE ON UNSATURATED SOILS/UNSAT'95/PARIS/FRANCE/6-8 SEPTEMBER 1995. VOLUME 1'.

Gerhard, I. and Kueper, H. (2003), 'Influence of constitutive model parameters on the predicted migration of DNAPL in heterogeneous porous media', *Water Resources Research* **39**(10).

Gerscovich, S., Vargas Jr, A. and De Campos, P. (2006), 'On the evaluation of unsaturated flow in a natural slope in Rio de Janeiro, Brazil', *Engineering Geology* **88**(1-2), 23–40.

Gibbs, J. and Holland, L. (1960), 'Subsidence characteristics of low-density silty soils in areas of Upper Meeker Canal-Missouri River basin project and lateral PE 41.2 Columbia basin project: Denver, Colorado, US Bureau of Reclamation, Division of Engineering Laboratory', *Earth Laboratory Report No. EM-608* .

Greenspan, L. (1977), 'Humidity fixed points of binary saturated aqueous solutions', *Journal of Research of The National Bureau of Standards* **81**(1), 89–96.

Griffiths, V. and Lane, A. (1999), 'Slope stability analysis by finite elements', *Geotechnique* **49**(3), 387–403.

Griffiths, V. and Lu, N. (2005), 'Unsaturated slope stability analysis with steady infiltration or evaporation using elasto-plastic finite elements', *International Journal for Numerical and Analytical Methods in Geomechanics* **29**(3), 249–267.

Guan, G. S., Rahardjo, H. and Choon, L. E. (2009), 'Shear strength equations for unsaturated soil under drying and wetting', *Journal of Geotechnical and Geoenvironmental Engineering* **136**(4), 594–606.

Guo-rui, G. (1984), 'Microstructures of expansive soil and swelling potential', *Chinese Jounal of Geotechnical Engineering* **2**.

Guorui, G. (1988), 'Formation and development of the structure of collapsing loess in China', *Engineering Geology* **25**(2-4), 235–245.

Guorui, G. (1994), 'The formation of collapsibility of loess soils in China', *Journal of Nanjing Architectural and Civil Engineering Institute* **2**.

Haeri, M., Khosravi, A., Garakani, A. A. and Ghazizadeh, S. (2017), 'Effect of soil structure and disturbance on hydromechanical behavior of collapsible loessial soils', *International Journal of Geomechanics* **17**(1), 04016021.

Haines, B. (1930), 'Studies in the physical properties of soil. V. The hysteresis effect in capillary properties, and the modes of moisture distribution associated therewith', *The Journal of Agricultural Science* **20**(1), 97–116.

Hamrouni, F., Trabelsi, H., El Ghezal, L. and Jamei, M. (2015), 'Numerical simulation of rainfall test on small-scale model', *UNSAT, BATNA* pp. 138–146.

Hanks, J., Klute, A. and Bresler, E. (1969), 'A numeric method for estimating infiltration, redistribution, drainage, and evaporation of water from soil', *Water Resources Research* **5**(5), 1064–1069.

Hilf, W. (1956), 'An investigation of pore water pressure in compacted cohesive soils'.

Hoffmann, C., Meler, N., Pinyol, M. and Alonso, E. (2014), 'Small scale slope failure benchmark test. Modelling and prediction', *Procedia Earth and Planetary Science* **9**, 201–205.

Hossain, A. and Yin, J. H. (2010), 'Shear strength and dilative characteristics of an unsaturated compacted completely decomposed granite soil', *Canadian Geotechnical Journal* **47**(10), 1112–1126.

Houston, L., Houston, N., Zapata, E. and Lawrence, C. (2001), *Geotechnical engineering practice for collapsible soils*, Springer.

Hovarth, L. (1985), 'Handbook of aqueous electrolyte solutions: physical properties, estimation, and correlation methods', *New York: Ellis Horwood* .

Hu, L., Yeung, R., Lee, F. and Wang, J. (2001), 'Mechanical behavior and microstructural variation of loess under dynamic compaction', *Engineering Geology* **59**(3-4), 203–217.

Hu, R., Hong, M., Chen, F. and Zhou, B. (2018), 'Hydraulic hysteresis effects on the coupled flow–deformation processes in unsaturated soils: Numerical formulation and slope stability analysis', *Applied Mathematical Modelling* **54**, 221–245.

Hu, Z.-Q., Shen, Z.-J. and Xie, D.-Y. (2005), 'Constitutive model of structural loess.', *Yanshilixue Yu Gongcheng Xuebao/Chin. J. Rock Mech. Eng.* **24**(4), 565–569.

Huang, B., Fredlund, G. and Fredlund, D. (2010), 'Comparison of measured and PTF predictions of SWCCs for loess soils in China', *Geotechnical and Geological Engineering* **28**(2), 105–117.

Huang, J., Zhang, W., Zuo, Q., Bi, R., Shi, S., Wang, X., Chang, L., Huang, W., Yang, S. and Zhang, B. (2008), 'An overview of the semi-arid climate and environment research observatory over the Loess Plateau', *Advances in Atmospheric Sciences* **25**(6), 906.

Huang, Q. and Li, L. (2011), 'Formation, distribution and risk control of landslides in China', *Journal of Rock Mechanics and Geotechnical Engineering* **3**(2), 97–116.

Huat, K., Ali, J. and Low, H. (2006), 'Water infiltration characteristics of unsaturated soil slope and its effect on suction and stability', *Geotechnical & Geological Engineering* **24**(5), 1293–1306.

Isakov, A. and Moryachkov, Y. (2013), 'Estimation of slope stability using two-parameter criterion of stability', *International Journal of Geomechanics* **14**(3), 06014004.

Iwata, S. (1995), 'Interaction between particles through water', *Soil–water interactions: mechanisms and applications. Marcel Dekker Inc., New York* pp. 154–228.

Jaynes, B. (1984), 'Comparison of soil-water hysteresis models', *Journal of Hydrology* **75**(1-4), 287–299.

Jennings, B. and Burland, B. (1962), 'Limitations to the use of effective stresses in partly saturated soils', *Géotechnique* **12**(2), 125–144.

Jennings, E. & Knight, K. (1957), 'The prediction of total heave from the double oedometer test', *Transactions of the South African Institution of Civil Engineers* **7**(9), 285–291.

Jiang, M. J., Li, T., Hu, H. J. and Thornton, C. (2014), 'DEM analyses of one-dimensional compression and collapse behaviour of unsaturated structural loess', *Computers and Geotechnics* **60**, 47–60.

Jiang, M. J., Zhang, G. and Hu, H. (2014), 'Structural characterization of natural loess and remolded loess under triaxial tests', *Engineering geology* **181**, 249–260.

Jiang, Y., Chen, W., Wang, G., Sun, G. and Zhang, F. (2017), 'Influence of initial dry density and water content on the soil–water characteristic curve and suction stress of a reconstituted loess soil', *Bulletin of Engineering Geology and the Environment* **76**(3), 1085–1095.

Jotisankasa, A. and Mairaing, W. (2009), 'Suction-monitored direct shear testing of residual soils from landslide-prone areas', *Journal of Geotechnical and Geoenvironmental engineering* **136**(3), 533–537.

Kawai, K., Kato, S. and Karube, D. (2000), The model of water retention curve considering effects of void ratio., *in* 'Unsaturated soils for Asia. Proceedings of the Asian Conference on Unsaturated Soils, UNSAT-ASIA 2000, Singapore, 18-19 May, 2000', AA Balkema, pp. 329–334.

Kayadelen, C., Tekinsoy, A. and Taşkıran, T. (2007), 'Influence of matric suction on shear strength behavior of a residual clayey soil', *Environmental Geology* **53**(4), 891.

Khalili, N., Geiser, F. and Blight, E. (2004), 'Effective stress in unsaturated soils: Review with new evidence', *International journal of Geomechanics* **4**(2), 115–126.

Khalili, N., Habte, A. and Zargarbashi, S. (2008), 'A fully coupled flow deformation model for cyclic analysis of unsaturated soils including hydraulic and mechanical hystereses', *Computers and Geotechnics* **35**(6), 872–889.

Khalili, N. and Khabbaz, H. (1998), 'A unique relationship of chi for the determination of the shear strength of unsaturated soils', *Geotechnique* **48**(5).

Khalili, N. and Zargarbashi, S. (2010), 'Influence of hydraulic hysteresis on effective stress in unsaturated soils', *Géotechnique* **60**(9), 729.

Khoshghalb, A. and Khalili, N. (2013), 'A meshfree method for fully coupled analysis of flow and deformation in unsaturated porous media', *International Journal for Numerical and Analytical Methods in Geomechanics* **37**(7), 716–743.

Khosravi, A., Salam, S., McCartney, S. and Dadashi, A. (2016), 'Suction-induced hardening effects on the shear modulus of unsaturated silt', *International Journal of Geomechanics* **16**(6), D4016007.

Kie, T. T. (1988), 'Fundamental properties of loess from Northwestern China', *Engineering Geology* **25**(2-4), 103–122.

Kim, J., Jeong, S. and Regueiro, R. A. (2012), 'Instability of partially saturated soil slopes due to alteration of rainfall pattern', *Engineering Geology* **147**, 28–36.

Klukanova, A. and Frankovska, J. (1995), *The Slovak Carpathians loess sediments, their fabric and properties*, Springer.

Klukanova, A. and Sajgalik, J. (1994), 'Changes in loess fabric caused by collapse: an experimental study', *Quaternary International* **24**, 35–39.

Kool, B. and Parker, C. (1987), 'Development and evaluation of closed-form expressions for hysteretic soil hydraulic properties', *Water Resources Research* **23**(1), 105–114.

Kosugi, K. (1999), 'General model for unsaturated hydraulic conductivity for soils with lognormal pore-size distribution', *Soil Science Society of America Journal* **63**(2), 270–277.

Kozeny, J. (1927), 'Uber Kapillare Leitung Des Wassers in Boden: Sitzungsberichte der Wiener Akademie der Wissenschaften'.

Lawton, C., Fragaszy, J. and Hardcastle, H. (1989), 'Collapse of compacted clayey sand', *Journal of Geotechnical Engineering* **115**(9), 1252–1267.

Lawton, C., Fragaszy, J. and Hetherington, D. (1992), 'Review of wetting-induced collapse in compacted soil', *Journal of geotechnical engineering* **118**(9), 1376–1394.

Le, H., Gallipoli, D., Sanchez, M. and Wheeler, J. (2012), 'Stochastic analysis of unsaturated seepage through randomly heterogeneous earth embankments', *International Journal for Numerical and Analytical Methods in Geomechanics* **36**(8), 1056–1076.

Ledesma, A., Gens, A. and Alonso, E. (1996), 'Parameter and variance estimation in geotechnical backanalysis using prior information', *International Journal for Numerical and Analytical Methods in Geomechanics* **20**(2), 119–141.

Lefebvre, G. (1995), Collapse mechanisms and design considerations for some partly saturated and saturated soils, *in* 'Genesis and Properties of Collapsible Soils', Springer, pp. 361–374.

Leong, C., Tripathy, S. and Rahardjo, H. (2003), 'Total suction measurement of unsaturated soils with a device using the chilled-mirror dew-point technique', *Geotechnique* **53**(2), 173–182.

Li, P., Xie, L., Pak, S. and Vanapalli, K. (2019), 'Microstructural evolution of loess soils from the Loess Plateau of China', *Catena* **173**, 276–288.

Li, S. (2005), 'Modelling of hysteresis response for arbitrary wetting/drying paths', *Computers and Geotechnics* **32**(2), 133–137.

Li, X. and Li, C. (2017), 'Quantification of the pore structures of Malan loess and the effects on loess permeability and environmental significance, Shaanxi Province, China: an experimental study', *Environmental Earth Sciences* **76**(15), 523.

Li, Y. and Mo, P. (2019), 'A unified landslide classification system for loess slopes: A critical review', *Geomorphology* .

Liang, C., Cao, C. and Wu, S. (2018), 'Hydraulic-mechanical properties of loess and its behavior when subjected to infiltration-induced wetting', *Bulletin of Engineering Geology and the Environment* **77**(1), 385–397.

Lide, R. & Frederikse, R. (1994), *Handbook of chemistry and physics, chemical*, Rubber Publishing Co.(CRC), USA.

Likos, J. and Lu, N. (2004), 'Hysteresis of capillary stress in unsaturated granular soil', *Journal of Engineering Mechanics* **130**(6), 646–655.

Likos, J. and Lu, N. (2013), 'Hysteresis and uncertainty in soil water-retention curve parameters', *Journal of Geotechnical and Geoenvironmental Engineering* **140**(4), 04013050.

Lin, G. (1995), *Variation in collapsibility and strength of loess with age*, Springer.

Lin, G. and Liang, M. (1982), 'Engineering properties and zoning of loess and loess-like soils in China', *Canadian Geotechnical Journal* **19**(1), 76–91.

Lin, G., Xu, J. and Zhang, S. (2008), Loess in China and landslides in loess slopes, *in* 'Proceedings of the Tenth International Symposium on Landslides and Engineered Slopes. Balkema, Christchurch', pp. 129–144.

Lins, Y. (2010), Hydro-mechanical properties of partially saturated sand, PhD thesis, Ruhr-Universitaet Bochum.

Lins, Y., Schanz, T. and Fredlund, D. G. (2009), 'Modified pressure plate apparatus and column testing device for measuring SWCC of sand', *Geotechnical Testing Journal* **32**(5), 450–464.

Liu, D. and Carter, P. (2002), 'A structured Cam Clay model', *Canadian Geotechnical Journal* **39**(6), 1313–1332.

Liu, Y., Fu, B., Lü, Y., Wang, Z. and Gao, G. (2012), 'Hydrological responses and soil erosion potential of abandoned cropland in the Loess Plateau, China', *Geomorphology* **138**(1), 404–414.

Liu, Z., Liu, F., Ma, F., Wang, M., Bai, X., Zheng, Y., Yin, H. and Zhang, G. (2015), 'Collapsibility, composition, and microstructure of loess in China', *Canadian Geotechnical Journal* **53**(4), 673–686.

LLoret, A. and Alonso, E. (1980), 'Consolidation of unsaturated soils including swelling and collapse behaviour', *Géotechnique* **30**(4), 449–477.

Lu, N. (2008), 'Is matric suction a stress variable?', *Journal of Geotechnical and Geoenvironmental Engineering* **134**(7), 899–905.

Lu, N. & Likos, J. (2004), *Unsaturated soil mechanics*, John Wiley & Sons, Hoboken, New Jersey.

Lu, N., Anderson, T., Likos, J. and Mustoe, W. (2008), 'A discrete element model for kaolinite aggregate formation during sedimentation', *International Journal for Numerical and Analytical Methods in Geomechanics* **32**(8), 965–980.

Lu, N. and Godt, J. (2008), 'Infinite slope stability under steady unsaturated seepage conditions', *Water Resources Research* **44**(11).

Lu, N., Godt, W. and Wu, T. (2010), 'A closed-form equation for effective stress in unsaturated soil', *Water Resources Research* **46**(5).

Lu, N. and Griffiths, V. (2004), 'Profiles of steady-state suction stress in unsaturated soils', *Journal of Geotechnical and Geoenvironmental Engineering* **130**(10), 1063–1076.

Lu, Z.-h., Chen, Z.-h., Fang, X.-w., Guo, J.-f. and Zhou, H.-q. (2006), 'Structural damage model of unsaturated expansive soil and its application in multi-field couple analysis on expansive soil slope', *Applied Mathematics and Mechanics* **27**(7), 891–900.

Luo, H., Wu, F., Chang, J. and Xu, J. (2018), 'Microstructural constraints on geotechnical properties of Malan Loess: a case study from Zhaojiaan landslide in Shaanxi province, China', *Engineering Geology* **236**, 60–69.

Luo, S., Xie, Y., Shao, J. and Zhang, J. (2004), 'Variation characteristics of soil structure of unsaturated loess', *J Northwest Sci Tech Univ Agri For* **8**(5), 114–117.

Luo, Y., Wang, T., Liu, X. and Zhang, H. (2014), 'Laboratory study on shear strength of loess joint', *Arabian Journal for Science and Engineering* **39**(11), 7549–7554.

Mahinroosta, R., Alizadeh, A. and Gatmiri, B. (2015), 'Simulation of collapse settlement of first filling in a high rockfill dam', *Engineering Geology* **187**, 32–44.

Maqsoud, A., Bussière, B., Aubertin, M. and Mbonimpa, M. (2012), 'Predicting hysteresis of the water retention curve from basic properties of granular soils', *Geotechnical and Geological Engineering* **30**(5), 1147–1159.

Marcial, D., Delage, P. and Cui, J. (2002), 'On the high stress compression of bentonites', *Canadian Geotechnical Journal* **39**(4), 812–820.

Meyer, S., Tan, S., Barrs, D. and Smith, G. (1990), 'Root growth and water uptake by wheat during drying of undisturbed and repacked soil in drainage lysimeters', *Australian Journal of Agricultural Research* **41**(2), 253–265.

Miao, T., Liu, Z. and Niu, Y. (2002), 'Unified catastrophic model for collapsible loess', *Journal of Engineering Mechanics* **128**(5), 595–598.

Miller, M. P., Singer, M. J. and Nielsen, D. R. (1988), 'Spatial variability of wheat yield and soil properties on complex hills', *Soil Science Society of America Journal* **52**(4), 1133–1141.

Mualem, Y. (1974), 'A conceptual model of hysteresis', *Water Resources Research* **10**(3), 514–520.

Mualem, Y. (1976), 'A new model for predicting the hydraulic conductivity of unsaturated porous media', *Water Resources Research* **12**(3), 513–522.

Mualem, Y. (1984), 'A modified dependent-domain theory of hysteresis', *Soil Science* **137**(5), 283–291.

Mualem, Y. and Beriozkin, A. (2009), 'General scaling rules of the hysteretic water retention function based on Mualemâs domain theory', *European Journal of Soil Science* **60**(4), 652–661.

Muñoz-Castelblanco, J., Delage, P., Pereira, J. and Cui, Y. (2013), The relationship between the microstructure and the water retention properties of a natural loess from northern france, *in* 'Proceeding of the 5th Asia-Pacific Conference on Unsaturated Soils', Vol. 1, pp. 357–362.

Munoz-Castelblanco, J., Delage, P., Pereira, J.-M. and Cui, Y.-J. (2011), 'Some aspects of the compression and collapse behaviour of an unsaturated natural loess', *Géotechnique Letters* pp. 1–6.

Ng, W., Sadeghi, H., Hossen, B., Chiu, F., Alonso, E. and Baghbanrezvan, S. (2016), 'Water retention and volumetric characteristics of intact and re-compacted loess', *Canadian Geotechnical Journal* **53**(8), 1258–1269.

Ng, W., Xu, J. and Yung, Y. (2009), 'Effects of wetting–drying and stress ratio on anisotropic stiffness of an unsaturated soil at very small strains', *Canadian Geotechnical Journal* **46**(9), 1062–1076.

Nguyen-Tuan, L. (2014), Coupled thermo-hydro-mechanical analysis, PhD thesis, Ruhr-Universitaet Bochum.

Nimmo, J. R. (1992), 'Semiempirical model of soil water hysteresis', *Soil Science Society of America Journal* **56**(6), 1723–1730.

Nouaouria, S., Guenfoud, M. and Lafifi, B. (2008), 'Engineering properties of loess in Algeria', *Engineering Geology* **99**(1-2), 85–90.

Nuth, M. and Laloui, L. (2008), 'Advances in modelling hysteretic water retention curve in deformable soils', *Computers and Geotechnics* **35**(6), 835–844.

Olivella, S., Gens, A., Carrera, J. and Alonso, E. (1996), 'Numerical formulation for a simulator (CODE_BRIGHT) for the coupled analysis of saline media', *Engineering Computations* **13**(7), 87–112.

Osipov, I. and Sokolov, N. (1995), Factors and mechanism of loess collapsibility, *in* 'Genesis and properties of collapsible soils', Springer, pp. 49–63.

Parker, C., Lenhard, J. and Kuppusamy, T. (1987), 'A parametric model for constitutive properties governing multiphase flow in porous media', *Water Resources Research* **23**(4), 618–624.

Pavlakis, G. and Barden, L. (1972), 'Hysteresis in the moisture characteristics of clay soil', *Journal of Soil Science* **23**(3), 350–361.

Pécsi, M. (1990), 'Loess is not just the accumulation of dust', *Quaternary International* **7**, 1–21.

Peng, D., Xu, Q., Liu, F., He, Y., Zhang, S., Qi, X., Zhao, K. and Zhang, X. (2018), 'Distribution and failure modes of the landslides in Heitai terrace, China', *Engineering Geology* **236**, 97–110.

Peng, D., Xu, Q., Qi, X., Fan, X., Dong, X., Li, S. and Ju, Y. (2016), 'Study on early recognition of loess landslides based on field investigation', *International Journal of Georesources and Environment-IJGE (formerly Int'l J of Geohazards and Environment)* **2**(2), 35–52.

Peng, J., Fan, Z., Wu, D., Zhuang, J., Dai, F., Chen, W. and Zhao, C. (2015), 'Heavy rainfall triggered loess–mudstone landslide and subsequent debris flow in Tianshui, China', *Engineering Geology* **186**, 79–90.

Pham, Q., Fredlund, G. and Barbour, L. (2003), 'A practical hysteresis model for the soil-water characteristic curve for soils with negligible volume change', *Geotechnique* **53**(2), 293–298.

Pham, Q., Fredlund, G. and Barbour, L. (2005), 'A study of hysteresis models for soil-water characteristic curves', *Canadian Geotechnical Journal* **42**(6), 1548–1568.

Pham, V. and Fredlund, G. (2003), 'The application of dynamic programming to slope stability analysis', *Canadian Geotechnical Journal* **40**(4), 830–847.

Phien-Wej, N., Pientong, T. and Balasubramaniam, S. (1992), 'Collapse and strength characteristics of loess in Thailand', *Engineering Geology* **32**(1-2), 59–72.

Philip, R. and De Vries, A. (1957), 'Moisture movement in porous materials under temperature gradients', *Eos, Transactions American Geophysical Union* **38**(2), 222–232.

Pintado, X. and Lloret, A. & Romero, E. (2009), 'Assessment of the use of the vapour equilibrium technique in controlled-suction tests', *Canadian Geotechnical Journal* **46**(4), 411–423.

Pinyol, M., Alonso, E., Corominas, J. and Moya, J. (2012), 'Canelles landslide: modelling rapid drawdown and fast potential sliding', *Landslides* **9**(1), 33–51.

Porter, C. (2001), 'Chinese loess record of monsoon climate during the last glacial–interglacial cycle', *Earth-Science Reviews* **54**(1-3), 115–128.

Poulos, S. J. (1981), 'The steady state of deformation', *Journal of Geotechnical and Geoenvironmental Engineering* **107**(ASCE 16241 Proceeding).

Poulos, S. J., Castro, G. and France, J. W. (1985), 'Liquefaction evaluation procedure', *Journal of Geotechnical Engineering* **111**(6), 772–792.

Poulovassilis, A. (1970), 'Hysteresis of pore water in granular porous bodies', *Soil Science* **109**(1), 5–12.

Poulovassilis, A. and Childs, E. (1971), 'The hysteresis of pore water: the non-independence of domains', *Soil Science* **112**(5), 301–312.

Prapaharan, S., Altschaeffl, G. and Dempsey, J. (1985), 'Moisture curve of compacted clay: mercury intrusion method', *Journal of Geotechnical Engineering* **111**(9), 1139–1143.

Price, E. and Morgenstern, R. (1965), 'The analysis of the stability of general slip surfaces'.

Qi, S. (2017), Numerical investigation for slope stability of expansive soils and large strain consolidation of soft soils, PhD thesis, Université d'Ottawa/University of Ottawa.

Qi, S. and Vanapalli, S. K. (2016), 'Influence of swelling behavior on the stability of an infinite unsaturated expansive soil slope', *Computers and Geotechnics* **76**, 154–169.

Qiu, J., Regmi, D., Cui, P., Cao, M., Lee, Z. and Zhu, H. (2016), 'Size distribution of loess slides in relation to local slope height within different slope morphologies', *Catena* **145**, 155–163.

Qiu, J., Wang, X., Lai, J., Zhang, Q. and Wang, B. (2018), 'Response characteristics and preventions for seismic subsidence of loess in Northwest China', *Natural Hazards* **92**(3), 1909–1935.

Rahardjo, H., Lee, T., Leong, C. and Rezaur, B. (2005), 'Response of a residual soil slope to rainfall', *Canadian Geotechnical Journal* **42**(2), 340–351.

Rahardjo, H., Leong, C. and Rezaur, B. (2008), 'Effect of antecedent rainfall on pore-water pressure distribution characteristics in residual soil slopes under tropical rainfall', *Hydrological Processes: An International Journal* **22**(4), 506–523.

Rahardjo, H., Lim, T., Chang, F. and Fredlund, G. (1995), 'Shear-strength characteristics of a residual soil', *Canadian Geotechnical Journal* **32**(1), 60–77.

Rahardjo, H. and Rezaur, R. (2008), *Monitoring and modeling of slope response to climate changes*, CRC Press.

Rahardjo, H., Satyanaga, A. and Leong, C. (2013), 'Effects of flux boundary conditions on pore-water pressure distribution in slope', *Engineering Geology* **165**, 133–142.

Reeve, J., Smith, D. and Thomasson, J. (1973), 'The effect of density on water retention properties of field soils', *Journal of Soil Science* **24**(3), 355–367.

Richards, A. (1931), 'Capillary conduction of liquids through porous mediums', *Physics* **1**(5), 318–333.

Richards, A. and Weaver, R. (1944), 'Moisture retention by some irrigated soils as related to soil moisture tension', *Journal of Agricultural Research* **69**(6), 215–235.

Rodrigues, A. and Vilar, M. (2006), Relationship between collapse and soil-water retention curve of a sandy soil, *in* 'Unsaturated Soils 2006', pp. 1025–1036.

Rogers, F. (1995), *Types and distribution of collapsible soils*, Springer.

Rogers, F., Dijkstra, A. and Smalley, J. (1994), 'Hydroconsolidation and subsidence of loess: studies from China, Russia, North America and Europe: in memory of Jan Sajgalik', *Engineering Geology* **37**(2), 83–113.

Romero, E., Gens, A. and Lloret, A. (1999), 'Water permeability, water retention and microstructure of unsaturated compacted Boom clay', *Engineering Geology* **54**(1-2), 117–127.

Romero, E. and Vaunat, J. (2000), Retention curves of deformable clays, *in* 'Experimental evidence and theoretical approaches in unsaturated soils', CRC Press, pp. 99–114.

Salter, J. and Williams, B. (1965), 'The influence of texture on the moisture characteristics of soils: II. Available-water capacity and moisture release characteristics', *Journal of Soil Science* **16**(2), 310–317.

Sassa, K., Fukuoka, H., Wang, F. and Wang, G. (2005), 'Dynamic properties of earthquake-induced large-scale rapid landslides within past landslide masses', *Landslides* **2**(2), 125–134.

Schaap, G. and Bouten, W. (1996), 'Modeling water retention curves of sandy soils using neural networks', *Water Resources Research* **32**(10), 3033–3040.

Schaap, G. and Leij, J. (1998), 'Database-related accuracy and uncertainty of pedotransfer functions', *Soil Science* **163**(10), 765–779.

Schaap, G., Leij, J. and Van Genuchten, M. T. (1998), 'Neural network analysis for hierarchical prediction of soil hydraulic properties', *Soil Science Society of America Journal* **62**(4), 847–855.

Schaap, G., Leij, J. and Van Genuchten, M. T. (2001), 'Rosetta: A computer program for estimating soil hydraulic parameters with hierarchical pedotransfer functions', *Journal of Hydrology* **251**(3-4), 163–176.

Seiphoori, A. and Ferrari, A. & Laloui, L. (2014), 'Water retention behaviour and microstructural evolution of MX-80 bentonite during wetting and drying cycles', *Géotechnique* **64**(9), 721–734.

Seiphoori, A., Laloui, L., Ferrari, A. and Hassan, M. & Khushefati, W. (2016), 'Water retention and swelling behaviour of granular bentonites for application in Geosynthetic Clay Liner (GCL) systems', *Soils and Foundations* **56**(3), 449–459.

Sharma, R. S. (1998), Mechanical behaviour of unsaturated highly expansive clays, PhD thesis, University of Oxford.

Sheng, C., Fredlund, G. and Gens, A. (2008), 'A new modelling approach for unsaturated soils using independent stress variables', *Canadian Geotechnical Journal* **45**(4), 511–534.

Shi, S., Wu, Z., Wu, R., Li, B., Wang, T. and Xin, P. (2016), 'Analysis of the causes of large-scale loess landslides in Baoji, China', *Geomorphology* **264**, 109–117.

Sivakumar Babu, L., Srivastava, A. and Murthy, N. (2006), 'Reliability analysis of the bearing capacity of a shallow foundation resting on cohesive soil', *Canadian Geotechnical Journal* **43**(2), 217–223.

Sivakumar, V. & Wheeler, J. (2000), 'Influence of compaction procedure on the mechanical behaviour of an unsaturated compacted clay. Part 1: Wetting and isotropic compression', *Géotechnique* **50**(4), 359–368.

Skempton, W. (1954), 'The pore-pressure coefficients A and B', *Geotechnique* **4**(4), 143–147.

Smalley, I. (1995), 'Making the material: the formation of silt sized primary mineral particles for loess deposits', *Quaternary Science Reviews* **14**(7-8), 645–651.

Smalley, J. and Jary, Z. (2005), 'Maps of worldwide loess distribution: from Keilhack to Kriger and beyond', *New Zealand Soil News* **53**, 45–9.

Smalley, J., Jefferson, F., Dijkstra, A. and Derbyshire, E. (2001), 'Some major events in the development of the scientific study of loess', *Earth-Science Reviews* **54**(1-3), 5–18.

Sorbino, G. and Nicotera, M. V. (2013), 'Unsaturated soil mechanics in rainfall-induced flow landslides', *Engineering Geology* **165**, 105–132.

Spencer, E. (1967), 'A method of analysis of the stability of embankments assuming parallel inter-slice forces', *Geotechnique* **17**(1), 11–26.

Stoimenova, E., Datcheva, M. and Schanz, T. (2003), 'Statistical modeling of the soil water characteristic curve for geotechnical data', pp. 356–366.

Stoimenova, E., Lins, Y., Datcheva, M. and Schanz, T. (2006), 'Inverse modelling of soil hydraulic characteristic functions'.

Suebsuk, J., Horpibulsuk, S. and Liu, D. (2010), 'Modified Structured Cam Clay: A generalised critical state model for destructured, naturally structured and artificially structured clays', *Computers and Geotechnics* **37**(7-8), 956–968.

Sun, A., Sheng, C., Cui, B. and Li, J. (2006), Effect of density on the soil-water-retention behaviour of compacted soil, *in* 'Unsaturated Soils 2006', pp. 1338–1347.

Sun, A., Sheng, C. and Sloan, W. (2007), 'Elastoplastic modelling of hydraulic and stress–strain behaviour of unsaturated soils', *Mechanics of Materials* **39**(3), 212–221.

Sun, D., Sheng, D., Xiang, L. and Sloan, S. W. (2008), 'Elastoplastic prediction of hydro-mechanical behaviour of unsaturated soils under undrained conditions', *Computers and Geotechnics* **35**(6), 845–852.

Sun, D., Sheng, D. and Xu, Y. (2007), 'Collapse behaviour of unsaturated compacted soil with different initial densities', *Canadian Geotechnical Journal* **44**(6), 673–686.

Tadepalli, R. and Fredlund, G. (1991), 'The collapse behavior of a compacted soil during inundation', *Canadian Geotechnical Journal* **28**(4), 477–488.

Tang, M., Xue, Q., Li, G. and Feng, W. (2015), 'Three modes of rainfall infiltration inducing loess landslide', *Natural Hazards* **79**(1), 137–150.

Taylor, D. (1951), 'A triaxial shear investigation on a partially saturated soil'.

Topp, C. (1969), 'Soil-Water Hysteresis Measured in a Sandy Loam and Compared with the Hysteretic Domain Model', *Soil Science Society of America Journal* **33**(5), 645–651.

Topp, C. (1971), 'Soil water hysteresis in silt loam and clay loam soils', *Water Resources Research* **7**(4), 914–920.

Tsaparas, I., Rahardjo, H., Toll, G. and Leong, C. (2002), 'Controlling parameters for rainfall-induced landslides', *Computers and Geotechnics* **29**(1), 1–27.

Tsiampousi, A., Smith, C. and Potts, M. (2017), 'Coupled consolidation in unsaturated soils: From a conceptual model to applications in boundary value problems', *Computers and Geotechnics* **84**, 256–277.

Tsiampousi, A., Zdravkovic, L. and Potts, M. (2016), 'Numerical study of the effect of soil–atmosphere interaction on the stability and serviceability of cut slopes in London clay', *Canadian Geotechnical Journal* **54**(3), 405–418.

Tu, X., Kwong, A., Dai, F., Tham, L. and Min, H. (2009), 'Field monitoring of rainfall infiltration in a loess slope and analysis of failure mechanism of rainfall-induced landslides', *Engineering Geology* **105**(1-2), 134–150.

Van Asch, W. and Malet, J. (2009), 'Flow-type failures in fine-grained soils: an important aspect in landslide hazard analysis', *Natural Hazards and Earth System Sciences* **9**(5), 1703–1711.

Van Genuchten, T. (1980), 'A closed-form equation for predicting the hydraulic conductivity of unsaturated soils 1', *Soil Science Society of America Journal* **44**(5), 892–898.

Vanapalli, K., Fredlund, G., Pufahl, E. and Clifton, W. (1996), 'Model for the prediction of shear strength with respect to soil suction', *Canadian Geotechnical Journal* **33**(3), 379–392.

Vaunat, J., Cante, C., Ledesma, A. and Gens, A. (2000), 'A stress point algorithm for an elastoplastic model in unsaturated soils', *International Journal of Plasticity* **16**(2), 121–141.

Wang, G., Li, T., Xing, X. and Zou, Y. (2015), 'Research on loess flow-slides induced by rainfall in July 2013 in Yanâan, NW China', *Environmental earth sciences* **73**(12), 7933–7944.

Wang, G. and Sassa, K. (2001), 'Factors affecting rainfall-induced flowslides in laboratory flume tests', *Geotechnique* **51**(7), 587–599.

Wang, G., Suemine, A. and Schulz, H. (2010), 'Shear-rate-dependent strength control on the dynamics of rainfall-triggered landslides, Tokushima Prefecture, Japan', *Earth Surface Processes and Landforms* **35**(4), 407–416.

Wang, G., Zhang, J., Xuan, Y., Liu, J., Jin, J., Bao, Z. and He, R. (2013), 'Simulating the impact of climate change on runoff in a typical river catchment of the Loess Plateau, China', *Journal of Hydrometeorology* **14**(5), 1553–1561.

Wang, J., Liang, Y., Zhang, H., Wu, Y. and Lin, X. (2014), 'A loess landslide induced by excavation and rainfall', *Landslides* **11**(1), 141–152.

Wang, W., Sassa, K. and Wang, G. (2002), 'Mechanism of a long-runout landslide triggered by the August 1998 heavy rainfall in Fukushima Prefecture, Japan', *Engineering Geology* **63**(1-2), 169–185.

Wang, Y., Shao, M., Zhu, Y. and Liu, Z. (2011), 'Impacts of land use and plant characteristics on dried soil layers in different climatic regions on the Loess Plateau of China', *Agricultural and Forest Meteorology* **151**(4), 437–448.

Wen, B.-P. and Yan, Y.-J. (2014), 'Influence of structure on shear characteristics of the unsaturated loess in Lanzhou, China', *Engineering Geology* **168**, 46–58.

Wheeler, J., Sharma, S. and Buisson, R. (2003), 'Coupling of hydraulic hysteresis and stress–strain behaviour in unsaturated soils', *Géotechnique* **53**(1), 41–54.

Wheeler, J. and Sivakumar, V. (1995), 'An elasto-plastic critical state framework for unsaturated soil', *Géotechnique* **45**(1), 35–53.

Wu, L., Zhou, Y., Sun, P., Shi, J., Liu, G. and Bai, L. (2017), 'Laboratory characterization of rainfall-induced loess slope failure', *Catena* **150**, 1–8.

Xiaokun, H., Vanapalli, K. and Tonglu, L. (2018), 'Water infiltration characteristics in loess associated with irrigation activities and its influence on the slope stability in Heifangtai loess highland, China', *Engineering Geology* **234**, 27–37.

Xie, W.-l., Li, P., Zhang, M.-s., Cheng, T.-e. and Wang, Y. (2018), 'Collapse behavior and microstructural evolution of loess soils from the Loess Plateau of China', *Journal of Mountain Science* **15**(8), 1642–1657.

Xie, W. and Li, P. (2018), 'Prediction of the wetting-induced collapse behaviour using the soil-water characteristic curve', *Journal of Asian Earth Sciences* **151**, 259–268.

Xiong, Y., Bao, X., Ye, B. and Zhang, F. (2014), 'Soil–water–air fully coupling finite element analysis of slope failure in unsaturated ground', *Soils and Foundations* **54**(3), 377–395.

Xu, J. and Liao, J. (2007), 'Original and secondary high-frequency sandstorm zones in the loess plateau region, china', *Geografiska Annaler: Series A, Physical Geography* **89**(2), 121–127.

Xu, L., Dai, C., Gong, M., Tham, G. and Min, H. (2012), 'Irrigation-induced loess flow failure in Heifangtai Platform, north-west China', *Environmental Earth Sciences* **66**(6), 1707–1713.

Xu, L., Dai, F., Tham, L., Tu, X., Min, H., Zhou, Y., Wu, C. and Xu, K. (2011), 'Field testing of irrigation effects on the stability of a cliff edge in loess, North-west China', *Engineering Geology* **120**(1-4), 10–17.

Xu, Q. and Zhang, L. (2010), 'The mechanism of a railway landslide caused by rainfall', *Landslides* **7**(2), 149–156.

Xu, Y., Leung, C., Yu, J. and Chen, W. (2018), 'Numerical modelling of hydro-mechanical behaviour of ground settlement due to rising water table in loess', *Natural Hazards* **94**(1), 241–260.

Yang, H., Rahardjo, H., Leong, E. and Fredlund, D. (2004), 'Factors affecting drying and wetting soil-water characteristic curves of sandy soils', *Canadian Geotechnical Journal* **41**(5), 908–920.

Ye, G., Zhang, F., Yashima, A., Sumi, T. and Ikemura, T. (2005), 'Numerical analyses on progressive failure of slope due to heavy rain with 2D and 3D FEM', *Soils and Foundations* **45**(2), 1–15.

Zandarín, M. T., Oldecop, A., Rodríguez, R. and Zabala, F. (2009), 'The role of capillary water in the stability of tailing dams', *Engineering Geology* **105**(1-2), 108–118.

Zhang, C., Kröhn, K. and Rothfuchs, T. (2005), Applications of CODE-BRIGHT to thermal-hydro-mechanical experiments on clays, *in* 'Unsaturated Soils: Numerical and Theoretical Approaches', Springer, pp. 341–357.

Zhang, D. and Wang, G. (2007), 'Study of the 1920 Haiyuan earthquake-induced landslides in loess (China)', *Engineering Geology* **94**(1-2), 76–88.

Zhang, F., Pei, X., Chen, W., Liu, G. and Liang, S. (2014), 'Spatial variation in geotechnical properties and topographic attributes on the different types of shallow landslides in a loess catchment, China', *European Journal of Environmental and Civil Engineering* **18**(4), 470–488.

Zhang, F. Y., Wang, G. H., Kamai, T. and Chen, W. W. (2013), 'Undrained shear behavior of loess saturated with different concentrations of sodium chloride solution', *Engineering Geology* **155**, 69–79.

Zhang, M. and Liu, J. (2010), 'Controlling factors of loess landslides in western China', *Environmental Earth Sciences* **59**(8), 1671–1680.

Zhou, A., Sheng, D., Sloan, W. and Gens, A. (2012), 'Interpretation of unsaturated soil behaviour in the stress–saturation space, I: volume change and water retention behaviour', *Computers and Geotechnics* **43**, 178–187.

Zhou, X., Zhu, Y., Zheng, M., Wang, X. and Liu, H. (2002), 'Landslide disaster in the loess area of China', *Journal of Forestry Research* **13**(2), 157–161.

Zhou, Y., Tham, L., Yan, W., Dai, F. and Xu, L. (2014), 'Laboratory study on soil behavior in loess slope subjected to infiltration', *Engineering Geology* **183**, 31–38.

Zhu, J. and Anderson, S. (1998), 'Determination of shear strength of Hawaiian residual soil subjected to rainfall-induced landslides', *Géotechnique* **48**(1), 73–82.

Zhuang, J., Peng, J., Wang, G. and Iqbal, J. (2017), 'Prediction of rainfall-induced shallow landslides in the Loess Plateau, Yan'an, China, using the TRIGRS model', *Earth Surface Processes and Landforms* **42**(6), 915–927.

Schriftenreihe des Instituts für Grundbau, Wasserwesen und Verkehrswesen der Ruhr-Universität Bochum

Herausgeber: H.L. Jessberger

1 (1979) **Hans Ludwig Jessberger**
Grundbau und Bodenmechanik an der Ruhr-Universität Bochum

2 (1978) **Joachim Klein**
Nichtlineares Kriechen von künstlich gefrorenem Emschermergel

3 (1979) **Heinz-Joachim Gödecke**
Die Dynamische Intensivverdichtung wenig wasserdurchlässiger Böden

4 (1979) **Poul V. Lade**
Three Dimensional Stress-Strain Behaviour and Modeling of Soils

5 (1979) **Roland Pusch**
Creep of soils

6 (1979) **Norbert Diekmann**
Zeitabhängiges, nichtlineares Spannungs-Verformungsverhalten von gefrorenem Schluff unter triaxialer Belastung

7 (1979) **Rudolf Dörr**
Zeitabhängiges Setzungsverhalten von Gründungen in Schnee, Firn und Eis der Antarktis am Beispiel der deutschen Georg-von-Neumayer- und Filchner-Station

8 (1984) **Ulrich Güttler**
Beurteilung des Steifigkeits- und Nachverdichtungsverhaltens von ungebundenen Mineralstoffen

9 (1986) **Peter Jordan**
Einfluss der Belastungsfrequenz und der partiellen Entwässerungsmöglichkeiten auf die Verflüssigung von Feinsand

10 (1986) **Eugen Makowski**
Modellierung der künstlichen Bodenvereisung im grundwasserdurchströmten Untergrund mit der Methode der finiten Elemente

11 (1986) **Reinhard A. Beine**
Verdichtungswirkung der Fallmasse auf Lastausbreitung in nichtbindigem Boden bei der Dynamischen Intensivverdichtung

12 (1986) **Wolfgang Ebel**
Einfluss des Spannungspfades auf das Spannungs-Verformungsverhalten von gefrorenem Schluff im Hinblick auf die Berechnung von Gefrierschächten

13 (1987) **Uwe Stoffers**
Berechnungen und Zentrifugen-Modellversuche zur Verformungsabhängigkeit der Ausbaubeanspruchung von Tunnelausbauten in Lockergestein

14 (1988) **Gerhard Thiel**
Steifigkeit und Dämpfung von wassergesättigtem Feinsand unter Erdbebenbelastung

15 (1991) **Mahmud Thaher**
Tragverhalten von Pfahl-Platten-Gründungen im bindigen Baugrund,
Berechnungsmodelle und Zentrifugen-Modellversuche

Schriftenreihe des Instituts für Grundbau der Ruhr-Universität Bochum

Herausgeber: H.L. Jessberger

16 (1992) **Rainer Scherbeck**
Geotechnisches Verhalten mineralischer Deponieabdichtungsschichten
bei ungleichförmiger Verformungswirkung

17 (1992) **Martin M. Bizialiele**
Torsional Cyclic Loading Response of a Single Pile in Sand

18 (1993) **Michael Kotthaus**
Zum Tragverhalten von horizontal belasteten Pfahlreihen aus langen Pfählen in Sand

19 (1993) **Ulrich Mann**
Stofftransport durch mineralische Deponieabdichtungen:
Versuchsmethodik und Berechnungsverfahren

20 (1992) **Festschrift anlässlich des 60. Geburtstages von**
Prof. Dr.-Ing. H. L. Jessberger
20 Jahre Grundbau und Bodenmechanik an der Ruhr-Universität Bochum

21 (1993) **Stephan Demmert**
Analyse des Emissionsverhaltens einer Kombinationsabdichtung im Rahmen der
Risikobetrachtung von Abfalldeponien

22 (1994) **Diethard König**
Beanspruchung von Tunnel- und Schachtausbauten in kohäsionslosem Lockergestein
unter Berücksichtigung der Verformung im Boden

23 (1995) **Thomas Neteler**
Bewertungsmodell für die nutzungsbezogene Auswahl von Verfahren zur Altlastensanierung

24 (1995) **Ralph Kockel**
Scherfestigkeit von Mischabfall im Hinblick auf die Standsicherheit von Deponien

25 (1996) **Jan Laue**
Zur Setzung von Flachfundamenten auf Sand unter wiederholten Lastereignissen

26 (1996) **Gunnar Heibrock**
Zur Rissbildung durch Austrocknung in mineralischen Abdichtungsschichten
an der Basis von Deponien

27 (1996) **Thomas Siemer**
Zentrifugen-Modellversuche zur dynamischen Wechselwirkung zwischen Bauwerken
und Baugrund infolge stoßartiger Belastung

28 (1996) **Viswanadham V. S. Bhamidipati**
Geosynthetic Reinforced Mineral Sealing Layers of Landfills

29 (1997) **Frank Trappmann**
Abschätzung von technischem Risiko und Energiebedarf bei Sanierungsmaßnahmen für Altlasten

30 (1997) **André Schürmann**
Zum Erddruck auf unverankerte flexible Verbauwände

31 (1997) **Jessberger, H. L. (Herausgeber)**
Environment Geotechnics, Report of ISSMGE Technical Committee TC 5 on Environmental Geotechnics

Schriftenreihe des Instituts für Grundbau und Bodenmechanik der Ruhr-Universität Bochum

Herausgeber: Th. Triantafyllidis

32 (2000) **Triantafyllidis, Th. (Herausgeber)**
Boden unter fast zyklischer Belastung: Erfahrung und Forschungsergebnisse (Workshop)

33 (2002) **Christof Gehle**
Bruch- und Scherverhalten von Gesteinstrennflächen mit dazwischenliegenden Materialbrücken

34 (2003) **Andrzej Niemunis**
Extended hypoplastic models for soils

35 (2004) **Christiane Hof**
Über das Verpressankertragverhalten unter kalklösendem Kohlensäureangriff

36 (2004) **René Schäfer**
Einfluss der Herstellungsmethode auf das Verformungsverhalten von Schlitzwänden in weichen bindigen Böden

37 (2005) **Henning Wolf**
Zur Scherfugenbänderung granularer Materialien unter Extensionsbeanspruchung

38 (2005) **Torsten Wichtmann**
Explicit accumulation model for non-cohesive soils under cyclic loading

39 (2008) **Christoph M. Loreck**
Die Entwicklung des Frischbetondruckes bei der Herstellung von Schlitzwänden

40 (2008) **Igor Arsic**
Über die Bettung von Rohrleitungen in Flüssigböden

41 (2009) **Anna Arwanitaki**
Über das Kontaktverhalten zwischen einer Zweiphasenschlitzwand und nichtbindigen Böden

Schriftenreihe des Lehrstuhls für Grundbau, Boden- und Felsmechanik der Ruhr-Universität Bochum

Herausgeber: T. Schanz

42 (2009) **Yvonne Lins**
Hydro-Mechanical Properties of Partially Saturated Sand

43 (2010) **Tom Schanz (Herausgeber)**
Geotechnische Herausforderungen beim Umbau des Emscher-Systems
Beiträge zum RuhrGeo Tag 2010

44 (2010) **Jamal Alabdullah**
Testing Unsaturated Soil for Plane Strain Conditions: A New Double-Wall Biaxial Device

45 (2011) **Lars Röchter**
Systeme paralleler Scherbänder unter Extension im ebenen Verformungszustand

46 (2011) **Yasir Al-Badran**
Volumetric Yielding Behavior of Unsaturated Fine-Grained Soils

47 (2011) **Usque ad finem**
Selected research papers

48 (2012) **Muhammad Ibrar Khan**
Hydraulic Conductivity of Moderate and Highly Dense Expansive Clays

49 (2014) **Long Nguyen-Tuan**
Coupled Thermo-Hydro-Mechanical Analysis: Experimental and Back Analysis

50 (2014) **Tom Schanz (Herausgeber)**
Ende des Steinkohlenbergbaus im Ruhrrevier: Realität und Perspektiven für die Geotechnik Beiträge zum RuhrGeo Tag 2014

51 (2014) **Usque ad finem**
Selected research papers

52 (2014) **Houman Soleimani Fard**
Study on the Hydro-Mechanical Behaviour of Fiber Reinforced Fine Grained Soils with Application to the Preservation of Historical Monuments

53 (2014) **Wiebke Baille**
Hydro-Mechanical Behavior of Clays - Significance of Mineralogy

54 (2014) **Qasim Abdulkarem Jassim Al-Obaidi**
Hydro-Mechanical Behavior of Collapsible Soils

55 (2015) **Veselin Zarev**
Model Identification for the Adaption of Numerical Simulation Models - Application to Mechanized Shield Tunneling

56 (2015) **Meisam Goudarzy**
Micro and Macro Mechanical Assessment of Small and Intermediate Strain Properties of Granular Material

57 (2016) **Oliver Detert**
Analyse einer selbstregulierenden interaktiven Membrangründung für Schüttkörper auf geringtragfähigen Böden

58 (2016) **Yang Yang**
Analyses of Heat Transfer and Temperature-induced Behaviour in Geotechnics

59 (2016) **Alborz Pourzargar**
Application of suction stress concept to partially saturated compacted soils

60 (2017) **Hanna Haase**
Multiscale analysis of clay-polymer composites for Geoenvironmental applications

61 (2017) **Kavan Khaledi**
Constitutive modeling of rock salt with application to energy storage caverns

62 (2017) **Nina Silvia Müthing**
On the consolidation behavior of fine-grained soils under cyclic loading

63 (2017) **Elham Mahmoudi**
Probabilistic analysis of a rock salt cavern with application to energy storage systems

64 (2017) **Negar Rahemi**
Evaluation of liquefaction behavior of sandy soils using critical state soil mechanics and instability concept

65 (2018) **Chenyang Zhao**
A contribution to modeling of mechanized tunnel excavation

66 (2019) **Tom Schanz (Herausgeber)**
Innovationen im Spezialtiefbau und in der Umweltgeotechnik
Geotechnik Beiträge zum RuhrGeo Tag 2014

67 (2019) **Linzhi Lang**
Hydro-Mechanical Behaviour of Bentonite-Based Materials Used for Disposal of Radioactive Wastes

68 (2019) **Usama Al-Anbaki**
Hydraulic Interaction of Soil and Nonwoven Geotextiles under Unsaturated Conditions

69 (2019) **Abhishek Rawat**
Coupled Hydro-mechanical Behavior of a Compacted Bentonite-Sand Mixture: Experimental and Numerical Investigations

Schriftenreihe des Lehrstuhls für Bodenmechanik, Grundbau und Umweltgeotechnik der Ruhr-Universität Bochum

Herausgeber: T. Wichtmann

70 (2019) **Mahmoud Qarmout**
Tunnel face stability using Kinematical Element Method (KEM)

71 (2021) **Raoul Hölter**
Optimal Experimental Design in Geotechnical Engineering.

72 (2022) **Wolfgang Lieske**
Impact of polymer constitution on the hydro-mechanical behaviour of modified bentonite for the application in geotechnical and geoenvironmental engineering

73 (2022) **Patrick Staubach**
Contributions to the numerical modeling of pile installation processes and high-cyclic loading of soils

74 (2022) **Lingyun Li**
On the hydromechanical behaviour of loess and its effect on slope stability under rainfall infiltration